Characterisation of granular flows using multiscale modelling

Daniel Anthony Foden Clarke

A thesis submitted in partial fulfilment of the requirements for the Degree
of Doctor of Philosophy in Chemical and Process Engineering
University of Canterbury

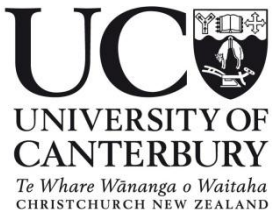

Christchurch, New Zealand

October 2018

"You could find out most things, if you knew the right questions to ask. Even if you didn't, you could still find out a lot."

— Iain M. Banks, *The Player of Games*, (1988).

Abstract

Granular materials are ubiquitous in industry and nature. The performance of industrial granular processes is highly sensitive to operating conditions, which poses a challenge for designing process equipment. Granular flow modelling is an area of interest since it offers a predictive insight into process behaviour prior to commissioning full-scale operations. A continuum description is the only technically feasible approach for modelling granular flows for industrial-scale applications. However, closure models for the system of equations governing the motion of granular materials are still an emerging area of research. To this end, magnetic resonance imaging (MRI) and multiscale computer simulations are useful techniques for understanding spatially resolved motion in opaque granular flows.

This thesis consists of three aspects. First, simulations of gas flow coupled with discrete particle motion of a laboratory-scale bubbling fluidised bed were performed. The purpose of these simulations was to investigate the effect that a modified drag model and different void fraction schemes have on simulated fluidisation hydrodynamics. Second, a theoretical model that described the effect of granular rotation dynamics on the MR signal was derived. Simulations of MRI pulse gradient spin echo experiments were performed on discrete element simulations of an annular shear cell to validate this new model. This approach proposes for the first time an experimental framework by which the angular velocity distribution in granular flows can be measured by MRI. Furthermore, MRI simulation was also used to show that MRI experiments could quantitatively measure the solid volume fraction in flowing granular materials. Third, discrete element simulations of an annular shear cell were used to validate nonlocal kinetic theory and fluidity continuum models.

Deputy Vice-Chancellor's Office
Postgraduate Office

UNIVERSITY OF CANTERBURY
Te Whare Wānanga o Waitaha
CHRISTCHURCH NEW ZEALAND

Co-Authorship Form

This form is to accompany the submission of any thesis that contains research reported in co-authored work that has been published, accepted for publication, or submitted for publication. A copy of this form should be included for each co-authored work that is included in the thesis. Completed forms should be included at the front (after the thesis abstract) of each copy of the thesis submitted for examination and library deposit.

Please indicate the chapter/section/pages of this thesis that are extracted from co-authored work and provide details of the publication or submission from the extract comes:

Chapter 4 of this thesis contains work published in: Clarke, D.A.,Sederman, A.J., Gladden, L.F. and Holland, D.J. Investigation of Void Fraction Schemes for Use with CFD-DEM Simulations of Fluidized Beds. Industrial and Engineering Chemistry Research, 2018. 57(8): p. 3002-3013

Please detail the nature and extent (%) of contribution by the candidate:

All simulation work and writing the manuscript were performed by the candidate. The experiment and refinement of the manuscript are attributed to the co-authors.

Certification by Co-authors:

If there is more than one co-author then a single co-author can sign on behalf of all
The undersigned certifys that:

- The above statement correctly reflects the nature and extent of the PhD candidate's contribution to this co-authored work
- In cases where the candidate was the lead author of the co-authored work he or she wrote the text

Name: *Daniel Holland* Signature: *Daniel Holland* Date: *30/10/2018*

Acknowledgements

As I contemplate my thesis journey over the past three-and-a-half years, I am reminded of the support I received from many magnificent people. Without them, this thesis would be considerably diminished. Here, I would like to extend my gratitude to everybody who helped me along the way.

Firstly, I would like to thank Daniel Holland for the supervisory support he has given during this project. His unwavering encouragement was an inspiring source of motivation, especially at times when things looked difficult. I appreciate the attention to detail that he gave in his feedback on my writing. Our discussions led to many intriguing lines of inquiry that I have enjoyed pursuing over the course of this thesis.

Thanks to my co-supervisor Ken Morison for his support during this project. I am grateful that he was willing to stand in as my primary supervisor at the start of the project. I found his feedback on my oral presentations to be extremely valuable for delivering talks to larger audiences.

I have enjoyed working on computer simulations. They are safe, tidy and require little supervision! However, simulation results are of little value without confirmation that they are an accurate representation of reality. For that reason, I am greatly indebted to the experimentalists who designed and performed the MRI experiments that were used to validate the simulation results presented in this thesis. Those people are: Hilary Fabich, Tim Brox, Petrik Galvosas, Sarah Codd, Joe Seymour, Jennifer Brown, Andy Sederman, and Lynn Gladden.

I appreciate the many interesting discussions that I had with Luke Fullard, who helped me grasp the concepts involved in continuum modelling and coarse graining. During my studies, it has been encouraging to watch the small group of New Zealand-based granular flow researchers grow in numbers and start to collaborate more closely.

It was a pleasure to assist Jamie Roverts, Jane Holt, Julian Annett Chee, and Kristina Aust on their final-year and masters research projects. Their findings were the source of many new ideas that positively influenced the direction of my thesis.

I would like to acknowledge the producers of the open source software that was used during this project. These groups include: the National Energy Technology Laboratory (NETL), DCS Computing, and the Pöschel group at FAU Erlangen-Nürnburg.

Many of the simulations performed during this project were run on the University of Auckland Pan cluster. I would like to thank the National eScience Infrastructure (NeSI) for hosting my project. One downside of running simulations on other peoples' computers is that there are many annoying barriers to building software! Many thanks to Daniel Lagrava for his assistance in getting the CFDEM code working on Pan. I would also like to thank Paul Walmsley, Sung Bae and Constantine Zakkaroff at UC HPC for running the very educational parallel computing courses.

I would like to acknowledge the financial support I received during this project. This included funding from the Department of Chemical and Process Engineering (CAPE), the UC Doctoral scholarship, a travel grant from the Canterbury Branch of the Royal Society of New Zealand, and conference expenses covered by the organisers of the 14th International Conference on Magnetic Resonance Microscopy.

I would like to pay tribute to my fellow CAPE postgrads whose great spirit of companionship helped me through the troublesome times that are an inevitable part of research. The walking trips, group dinners, and quiz nights (where we won on two occasions) were especially memorable. Thanks to Leatham Landon-Lane, Tom Meaclem, Harshal Panidepu, and Ben Reynolds for their help proofreading this thesis.

Finally, I would like to thank my parents and wider family for their support, kind words, and their boundless optimism.

Table of Contents

1. Introduction 1

1.1. Multiscale modelling of fluid –particle systems 2

1.2. Magnetic resonance imaging of granular flow 4

1.3. Objectives and thesis outline 4

1.4. References 6

2. Literature review 7

2.1. Fluidisation and the scale-up method 7

2.2. Two-fluid models of gas-solid flow 10

2.3. Unresolved discrete particle modelling of gas-particle flow 16

2.4. Magnetic resonance imaging of granular materials 23

2.4.1 Background to NMR 24

2.4.2 Background to MRI 26

2.4.3 Measuring velocity using MRI 28

2.5. Summary 30

2.6. References 32

3. Validation of CFD-DEM codes and the effective diameter drag model 37

3.1. Introduction 37

3.2. Method 40

3.2.1 Mesh design 40

3.2.2 Effective diameters to approximate nonsphericity 41

3.2.3 Additional simulation details 43

3.3. Results and discussion 45

3.3.1 Investigating mesh effect 45

3.3.2 Effective diameters 48

3.4. Conclusions 51

3.5. References 52

4. Investigation of void fraction schemes for use with CFD-DEM simulations of fluidised beds 55

4.1. Introduction 55

4.2. Method 58

4.2.1 Experiment 58

4.2.2 Simulation setup 59

4.2.3 Implementation of Void Fraction Schemes 64

4.2.4 Post-processing and analysis 69

4.3. Results and discussion 71

4.3.1 Evaluation of void fraction schemes 71

4.3.2 Analysis of computation time 73

4.3.3 Comparison with experiment 75

4.4. Conclusions 81

4.5. References 83

5. Measurement of rotational granular dynamics with MRI 85

5.1. Introduction 85

5.2. Theory 87

5.2.1 Evaluation of volume integral 91

5.3. Method 93

5.3.1 MRI experiment 93

5.3.2 Simulation details 93

5.3.3 MRI simulation algorithm 95

5.3.4 DEM averaging post-processing algorithm 96

5.4. Results and discussion 99

5.4.1 DEM post-processing methods 99

5.4.2 Verification of signal model for rotation 100

5.4.3 Couette flow verification and validation 102
5.5. Conclusions 112
5.6. References 113
6. Quantitative validation of MRI volume fraction measurements for granular flow 116
6.1. Introduction 116
6.1.1 Theory 119
6.2. Method 121
6.2.1 Discrete element method 121
6.2.2 MRI simulations 123
6.2.3 MRI experiments 125
6.3. Results and discussion 126
6.3.1 Validation of MRI 126
6.3.2 Correcting for Gibbs ringing 130
6.3.3 Comparison with experiment 132
6.4. Conclusions 134
6.5. References 135
7. Validation of nonlocal granular rheology using the discrete element method 137
7.1. Introduction 137
7.1.1 Theory 139
7.2. Method 144
7.2.1 Discrete element method simulations 144
7.2.2 Coarse-graining 145
7.2.3 Continuum model parameters 148
7.3. Results and discussion 150
7.3.1 DEM simulations 150
7.3.2 Coarse-graining 152
7.3.3 Bocquet model 155

7.3.4 Gradient expansion model 157
7.3.5 Cooperative model 158
7.3.6 Microscale definition for fluidity 160
7.4. Conclusions 161
7.5. References 162
8. Conclusions and future work 164
8.1. Summary of findings 164
8.2. Future work 167
8.3. References 169
9. Appendices 170
9.1. Appendix A: MFIX input script for fluidised bed simulation 170
9.2. Appendix B: CFDEM scripts for fluidised bed simulation 175
9.3. Appendix C: LIGGGHTS input script for Couette cell simulations 182
9.4. Appendix D: Matlab code for satellite point MRI simulation 185
9.5. Appendix E: Matlab codes for DEM averaging and coarse-graining 189
9.6. Appendix F: Microscale fluidity for planar shear with gravity 195

Nomenclature

The symbols and abbreviations used in this thesis are presented in this section in alphabetical order. For each quantity a brief description is provided and the SI unit is denoted.

$\boldsymbol{a}_g$	Acceleration due to gravity	m s^{-2}
A	Parameter in cooperative nonlocal fluidity model	
b	Parameter in $\mu(I)$ rheology model	
$\boldsymbol{B}$	Magnetic field	T
B_0	Applied static magnetic field	T
c	Cut-off width for coarse-graining	m
d_p	Particle diameter	m
$d_{p,d}$	Particle diameter for drag force calculation	m
$d_{p,v}$	Particle diameter for void fraction calculation	m
D	Velocity gradient tensor	s^{-1}
D_b	Fluidised bed diameter	m
e_n	Normal coefficient of restitution	
e_t	Tangential coefficient of restitution	
E	Elastic modulus	Pa
$\boldsymbol{f}_c$	Total contact force acting on a particle	N
$\boldsymbol{f}_d$	Drag force acting on a particle	N
$\boldsymbol{f}_{ij}$	Contact force exerted on particle *i* by *j*	N
F	Dimensionless granular fluidity	
F_0	Dimensionless drag force at Stokes limit	
F_r	Parameter in Johnson & Jackson frictional stress model	
F_{st}	Drag force for Stokes flow	kg m^{-3} s^{-1}
FOV	Field of view	m
g	Granular fluidity	s^{-1}
$\boldsymbol{g}$	Magnetic field gradient	T m^{-1}
g_{loc}	Granular fluidity for local rheology	s^{-1}
g_s	Slice gradient strength	T m^{-1}
g_0	Radial distribution function	
G	Shear modulus	Pa
h	Planck constant	J s

h_w	Averaging width in MFIX DPVM void fraction model	m
H	Gap width in annular shear cell	m
I	Inertial number	
I_{MR}	Spatially resolved signal intensity of MR image	
I_0	Parameter in $\mu(I)$ rheology model	
$\boldsymbol{I}_{gs}$	Interphase momentum transfer	kg m^{-2} s^{-2}
$\boldsymbol{I}_p$	Moment of inertia	kg m^2
$\boldsymbol{J}$	Impulse vector	kg m s^{-2}
$\boldsymbol{k}$	Reciprocal space vector (k-space)	m^{-1}
k_n	Normal spring constant	N m^{-1}
k_t	Tangential spring constant	N m^{-1}
Δk	Increment in k-space	m^{-1}
L	Fluidised bed height	m
m	Exponent that describe stress-shear scaling relation	
m_p	Particle mass	kg
M_0	Magnetisation at equilibrium	A m^{-1}
$\boldsymbol{M}$	Magnetisation	A m^{-1}
$\boldsymbol{n}_{ij}$	Normal unit vector between particles *i* and *j*	
N_c	Number of particles in contact	
N_p	Number of particles	
N_s	Number of samples	
N_{SP}	Number of satellite points	
$\boldsymbol{p}$	Reciprocal velocity space vector	s m^{-1}
p_g	Fluid phase pressure	Pa
p_s	Granular pressure	Pa
Δp	Pressure drop across fluidised bed	Pa
P	Probability distribution function	
$\boldsymbol{q}$	Fluctuating kinetic energy flux	kg s^{-3}
r	Radial coordinate	m
r_i	Radius of inner wall for annular shear flow	m
r_w	Parameter in Bocquet KTGF model	m
R	Particle radius	m
Re	Reynolds number	
S	MRI signal	
S_c	Characteristic length for fluid cell	m

S_d	Characteristic length for fluid domain	m
S_0	MRI signal for zero gradient	
t	Time	s
t_c	Collision time	s
t_d	Delay time	s
t_D	Pseudo-time used for diffusive void fraction scheme	s
t_p	Time interval between RF pulses	s
t_R	Rayleigh time	s
$\boldsymbol{t}_{ij}$	Tangential unit vector between particles *i* and *j*	
Δt	Numerical time step size	s
Δt_f	Fluid phase numerical time step size	s
T	Granular temperature	$m^2\ s^{-2}$
$\boldsymbol{T}_c$	Torque exerted on particle by contacts	N m
T_0	Parameter in Bocquet KTGF model	$m^2\ s^{-2}$
T_1	Spin-lattice (longitudinal) relaxation time	s
T_2	Spin-spin (transverse) relaxation time	s
T_2^*	Overall transverse relaxation time	s
$\boldsymbol{u}$	Particle velocity relative to local mean	$m\ s^{-1}$
$\langle u^2 \rangle$	Variance of velocity fluctuations	$m^2\ s^{-2}$
U	Velocity of inner moving wall in annular shear cell	$m\ s^{-1}$
U_{mf}	Superficial gas velocity at minimum fluidisation	$m\ s^{-1}$
$\boldsymbol{v}_g$	Fluid phase velocity	$m\ s^{-1}$
$\boldsymbol{v}_p$	Velocity of an individual particle	$m\ s^{-1}$
$\boldsymbol{v}_s$	Granular velocity	$m\ s^{-1}$
V	Volume	m^3
V_{cell}	Volume of computational cell	m^3
V_p	Particle volume	m^3
V_w	Volume of coarse-graining region	m^3
w	Spatial averaging length scale	m
W	Weighting applied to coarse-graining	
x	x-coordinate of position vector	m
$\boldsymbol{x}$	Position vector	m
$\boldsymbol{x}_b$	Position of boundary	m
$\boldsymbol{x}_{ij}$	Distance between particles *i* and *j*	m
$\boldsymbol{x}_0$	Initial position	m

$\delta \boldsymbol{x}$	Overlap between particle and averaging region	m
y	y-coordinate of position vector	m
y^f	Parameter in Johnson & Jackson frictional stress model	
Y	Yield parameter	
z	z-coordinate of position vector	m
Δz	Slice thickness	m

Greek letters

α	Parameter in Beetstra drag model	
β_d	Drag coefficient	kg m^{-3} s^{-1}
β	Exponent in Bocquet KTGF model	
γ	Gyromagnetic ratio	rad s^{-1} T^{-1}
$\dot{\gamma}$	Shear rate	s^{-1}
γ_n	Normal viscous dissipation rate	kg s^{-1}
γ_t	Tangential viscous dissipation rate	kg s^{-1}
Γ	Granular temperature loss rate in Ding & Gidaspow KTGF	kg m^{-1} s^{-3}
δ	Gradient pulse time	s
δ_B	Decay length parameter in Bocquet KTGF model	m
δ_n	Normal overlap between granules	m
$\boldsymbol{\delta}_t$	Tangential overlap between granules	m
Δ	Gradient pulse delay time	s
ϵ	Granular temperature loss rate in Bocquet KTGF model	kg m^{-3} s^{-1}
ϵ_0	Parameter in Bocquet KTGF model	
ε_g	Void fraction	
$\varepsilon_{g,mf}$	Void fraction at minimum fluidisation	
ε_s	Solid volume fraction	
$\varepsilon_{s,c}$	Solid volume fraction at random close packing	
η_g	Fluid shear viscosity	Pa·s
η_s	Granular shear viscosity	Pa·s
θ	Phase shift in MR signal	
θ_c	Phase shift associated with particle centre	
θ_i	Angular displacement about axis *i*	
λ	Fluctuating kinetic energy conductivity in Bocquet KTGF model	kg m^{-1} s^{-1}
λ_0	Parameter in Bocquet KTGF model	

μ	Ratio between shear and normal stress	
μ_i	Stress ratio at inner wall of shear cell	
μ_f	Coefficient of friction	
μ_s	Ratio between shear and normal stress at yield point	
μ_M	Magnetic moment	A m^2
$\Delta\mu$	Parameter in $\mu(I)$ rheology model	
ν	Poisson ratio	
ν_l	Nonlocal parameter in gradient expansion nonlocal rheology	
ξ	Cooperativity length	m
ρ	Spin density	m^{-3}
ρ_g	Fluid density	kg m^{-3}
ρ_s	Granule density	kg m^{-3}
ρ_0	Parameter in Bocquet KTGF model	kg m^{-3}
σ^g	Fluid stress tensor	Pa
σ^s	Granular stress tensor	Pa
τ	Shear stress	Pa
ϕ_{cube}	Volume fraction of cube inside a computational cell	
ϕ^f	Internal angle of friction	
ϕ_p	Volume fraction of a particle inside a computational cell	
$\chi(I)$	Function in the gradient expansion fluidity model	
$\psi(r)$	Function in the Bocquet flow model	
$\boldsymbol{\omega}_p$	Angular velocity of an individual particle	rad s^{-1}
$\langle\omega^2\rangle$	Angular velocity variance	rad^2 s^{-2}
ω_M	Precession frequency	Hz
$\omega_{M,0}$	Lamor frequency	Hz
$\Delta\omega_s$	RF range for slice selection	Hz

Abbreviations

CFD	Computational fluid dynamics
CFD-DEM	Computational fluid dynamics-discrete element method (unresolved)
CPMG	Carr-Purcell-Meiboom-Gill RF pulse sequence
DBM	Discrete bubble method
DEM	Discrete element method
DMRS	Dynamic magnetic resonance scattering
DPM	Discrete particle method
DPVM	Divided particle volume method
ECVT	Electrical capacitance volume tomography
FCC	Face-centred cubic
FID	Free induction decay
KTGF	Kinetic theory of granular flow
LB	Lattice Boltzmann
LBM	Lattice Boltzmann method
LIGGGHTS	LAMMPS improved for general granular and granular heat transfer simulations
MD	Molecular dynamics
MFIX	Multiphase flow with interphase exchange
MR	Magnetic resonance
MRI	Magnetic resonance imaging
MPT	Magnetic particle tracking
NMR	Nuclear magnetic resonance
PCM	Particle centred method
PDE	Partial differential equation
PEPT	Positron emission particle tracking
PFG	Pulsed field gradient
PGSE	Pulse gradient spin echo
PIV	Particle image velocimetry
PSD	Particle size distribution
RDF	Radial distribution function
RF	Radiofrequency
TFM	Two-fluid model

1. Introduction

Granular materials are assemblies of distinct solid particles where inter-particle interactions are chracterised by a loss of kinetic energy. Given their ubiquity, an understanding of flow behaviour is important for understanding natural and industrial processes. Granular flows are highly varied and complex, they exhibit states which are analogous to solids, liquids and gases. The bulk flow is sensitive to features occuring on the scale of the granules, and the granule properties; while the local flow depends on flow in other regions.

Fluid-particle fluidisation is one example of a unit operation that is challenging to understand due to the complexity of granular materials. Fluidised beds have a crucial role in process such as fluid catalytic cracking of hydrocarbons, combustion of conventional and renewable fuels, polymerisation reactions, drying, and freezing of food products. Fluidisation was first used in the 1920s for coal gasification, yet until the 1950s fluidised processes were operated with little knowledge of the flow, heat transfer, or reaction kinetics. This was problematic since fluidised beds display many different flow regimes, some of which hinder performance. Early experimental studies using bubbling fluidised beds erroneously predicted the heat transfer coefficient because the flow was assumed to follow plug or mixed flow models when in fact neither flow model was applicable as evidenced by the low conversion in reaction kinetics studies [1]. To optimise industrial scale fluidised bed performance, scale-up is used, where the process is performed at laboratory and pilot scales to inform the design of the full-scale process. The uncertainty surrounding the scale dependence of flow parameters means that industrial scale fluidised beds may exhibit inferior performance compared to pilot scale studies [2, 3]. Therefore, there is interest in simulating the fluidisation hydrodynamics to complement the scale-up process such that the behaviour of the commissioned process is predictable.

Computational fluid dynamics (CFD) simulations of fluidised beds have been the subject of research for the past four decades. A full-scale fluidised bed contains such a large number of particles that it is not possible to track the individual trajectories. Thus, it is assumed that the continuum description holds true for the granular material. However, granular rheology is currently described by a disparate set of models applicable under different flow conditions. This framework makes it challenging to understand granular flows that simultaneously

consist of dilute and dense packing which are found in the process industries. A strategy to resolve inter-particle interactions at the continuum scale is presented in the following section.

1.1. Multiscale modelling of fluid –particle systems

The equations governing the distribution of mass and motion of a continuous granular flow require closure by specifying a constitutive equation to describe the stress tensor of the granular phase. As the granular stress is dependent on a multitude of factors, such as other continuum variables and the physical properties of the granules, it was proposed that closure relations are developed from simulations that resolve contacts between individual granules. This concept forms part of the modelling hierarchy commonly referred to as multiscale modelling [4] and was introduced by researchers at the University of Twente in the early 2000s. The principle of multiscale modelling is that closure relations for models at one particular length scale are derived from data obtained by models at a smaller length scale. For fluidised bed simulations, van der Hoef et al. [4] identify five pertinent length scales, illustrated in Figure 1.1. At the smallest scale, the fluid phase and the granules are modelled as discrete entities. The interaction between the fluid and solid phases is resolved by fluid molecules colliding with solid particles. Such models are only feasible at very small length scales and thus are not widely studied within the multiscale framework, since the rheology of liquids and gases is already well understood. At the length scale of ~1 cm, resolved discrete particle method (DPM) simulations are feasible. Here, the continuum assumption is made for the fluid phase and the fluid-particle interaction is handled by imposing a no-slip boundary condition at the surface of the granules. Data from these simulations is useful for developing models for drag under a variety of flow regimes, particle packings and particle shapes with greater precision than is possible with experiments. Next in the hierarchy is the unresolved discrete particle method, referred to as computational fluid dynamics-discrete element method (CFD-DEM) in this thesis. Larger scale simulations are feasible because the numerical grid over which the fluid phase volume-averaged Navier-Stokes equations are solved is coarser. As the fluid cells are several particle diameters in length, it is not possible to resolve the fluid-particle interactions. Instead, drag equations (such as those derived from resolved DPM simulations) are used to estimate the drag force acting on each granule. This method is suitable for simulating laboratory scale systems containing up to ~30 million granules [5]. For pilot scale systems, the number of particle exceeds this amount by orders of magnitude, hence it is not feasible to model particles as discrete entities. Instead, the continuum assumption is applied to the granular phase, introducing another set of volume-

averaged Navier-Stokes equations. For this reason, the method is referred to as a two-fluid model (TFM). An additional closure is required in the form of a constitutive equation for the stress tensor of the granular phase.

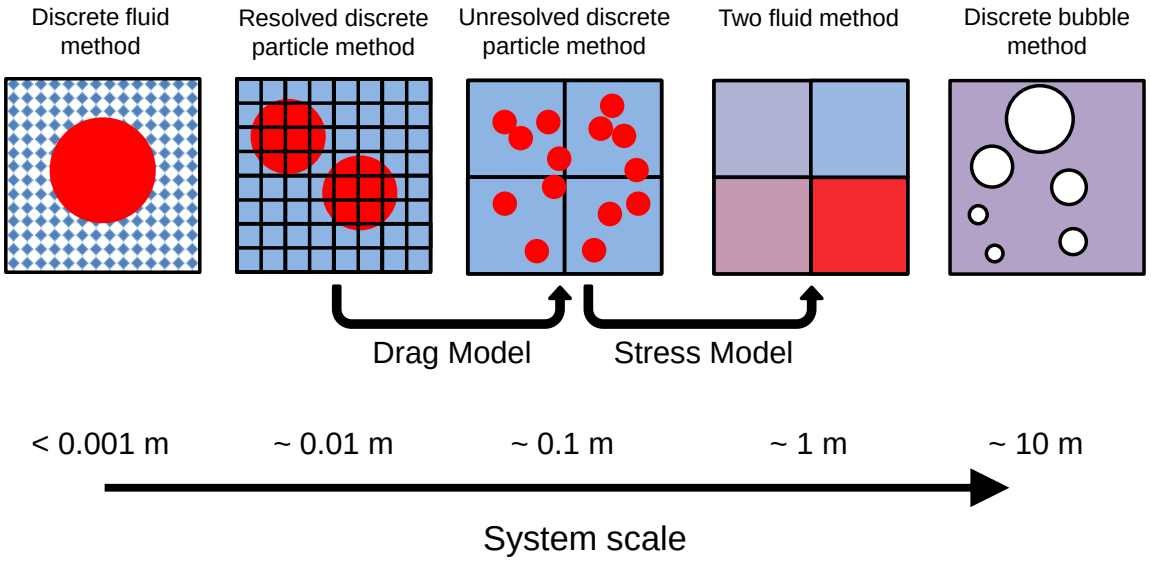

Figure 1.1. Schematic outlining the different simulation techniques that make up the multiscale modelling framework for fluid-particle flows.

Multiscale modelling postulates that CFD-DEM simulation data can be used to derive an appropriate form for the stress tensor. For full-scale systems, the TFM is challenging as the size of the numerical grid has an influence on the simulation result. A grid-independent result may require an unfeasibly high number of nodes at which the model is solved. Another simulation method suitable for full-scale systems is the discrete bubble method (DBM). Here, bubbles are modelled as discrete entities travelling through a fluid-particle emulsion phase. Only one set of Navier-Stokes equations needs to be solved and the number of bubbles in the system is sufficiently low to facilitate discrete modelling. The DBM is not widely used owing to improvements in computer performance and the development of filtered models for the TFM that account for sub-grid scale flow features while running coarse grids [6].

Figure 1.1 shows the connectivity between the modelling approaches. The fluid particle interaction term in the CFD-DEM model can be ascertained by calculating the drag forces acting on each granule in resolved DPM simulations. Drag equations developed by this approach [7-9] are now widely accepted alternatives to well-established empirical correlations. Similarly, expressions (or model parameters) for the stress tensor in TFM can be found by spatial averaging of the contact stresses between discretely modelled granules [10-12]. The efficacy of this strategy depends on the smaller scale model providing an accurate

description of the flow behaviour, otherwise inaccuracies propagate through to the larger scale model. Hence, this thesis investigates the role that the interphase coupling has on the results of CFD-DEM simulations.

1.2. Magnetic resonance imaging of granular flow

To test the validity of these modelling approaches, it is necessary to compare the model predictions to data collected from physical experiments. If the simulations agree with experiments, then closure relations derived from the model can be treated with confidence. Experimental measurements of granular flows are challenging as many regions of interest are optically inaccessible. Several measurement techniques are able to study opaque systems, yet MRI is unique as it is able to collect spatially-resolved, time averaged measurements of the solid volume fraction and the local velocity distribution. MRI exploits the phenomenon where nuclei have distinct spin states whose energy gap is proportional to the magnetic field. By placing the flow in a spatially varying magnetic field and exciting the sample with a radiofrequency pulse, a signal is recovered from which an image of the spin density can be reconstructed. Velocity images can be created by applying a pair of opposite gradient pulses which do not perfectly rephase moving spins, leading to attenuation of the signal [13]. Current MRI velocimetry theory assumes that rotational motion of granules about their centres of mass makes no contribution towards the signal attenuation. Therefore, the extent which granule rotation affects the measurements is unquantified. The effect of motion on the signal makes quantitative measurements of the solid volume fraction difficult as the signal intensity is influenced by the local flow. However, this effect can be minimised with careful design of the gradient sequence. In this thesis, an attempt at quantifying the signal attenuation caused by granule rotation was made. MRI simulations were designed to validate the rotation theory and a gradient sequence designed for quantitative volume fraction measurements.

1.3. Objectives and thesis outline

The objective of this thesis is to use CFD-DEM simulations that are validated by comparison with MRI experiments to help develop continuum models of granular flow. To achieve this objective, the coupling between the fluid and particles in CFD-DEM, and the ability of MRI to measure continuum variables for granular flow are also investigated. Chapter 2 reviews the existing work performed in simulations of fluidised beds, development of granular rheology models and magnetic resonance imaging of granular flows. Chapter 3 gives an overview of the calculation of the drag acting on the particles and explores an effective diameter method

to approximate the effects of nonsphericity. Chapter 3 also compares the predictive accuracy of two different open-source CFD-DEM programs. Chapter 4 performs CFD-DEM simulations of a square fluidised bed using different void fraction schemes and assesses their influence on the results. Different levels of grid refinement were performed to investigate the effect of the inlet boundary condition. Chapter 5 investigated the effect of granule rotation on MRI velocity measurements. A theoretical model was developed to predict the signal attenuation as a function of the angular velocity distribution. MRI experiments were simulated using DEM of an annular shear cell. Chapter 6 performed MRI simulations of an annular shear cell using a velocity compensated gradient pulse sequence to attain quantitative measurements of the solid volume fraction. Chapter 7 investigates granular rheology models by applying them to coarse-grained DEM simulations of a 3D annular shear cell. Chapter 8 provides the main findings from the work conducted in this thesis and identifies areas where future work is required.

1.4. References

1. Levenspiel, O., *Difficulties in trying to model and scale-up the Bubbling Fluidized Bed (BFB) reactor*. Industrial and Engineering Chemistry Research, 2008. **47**(2): p. 273-277
2. Knowlton, T.M., S.B.R. Karri, and A. Issangya, *Scale-up of fluidized-bed hydrodynamics.* Powder Technology, 2005. **150**(2): p. 72-77
3. Rüdisüli, M., et al., *Scale-up of bubbling fluidized bed reactors - A review.* Powder Technology, 2012. **217**: p. 21-38
4. van der Hoef, M.A., et al., *Numerical simulation of dense gas-solid fluidized beds: A multiscale modeling strategy*, in *Annual Review of Fluid Mechanics*. 2008. p. 47-70.
5. Ozel, A., et al., *Fluid and particle coarsening of drag force for discrete-parcel approach.* Chemical Engineering Science, 2016. **155**: p. 258-267
6. Igci, Y., et al., *Filtered two-fluid models for fluidized gas-particle suspensions.* AIChE Journal, 2008. **54**(6): p. 1431-1448
7. Hill, R.J., D.L. Koch, and A.J.C. Ladd, *Moderate-Reynolds-number flows in ordered and random arrays of spheres.* Journal of Fluid Mechanics, 2001. **448**: p. 243-278
8. Beetstra, R., M.A. Van Der Hoef, and J.A.M. Kuipers, *Drag force of intermediate reynolds number flow past mono- And bidisperse arrays of spheres.* AIChE Journal, 2007. **53**(2): p. 489-501
9. Tang, Y., E.A.J.F. Peters, and J.A.M. Kuipers, *Direct numerical simulations of dynamic gas-solid suspensions.* AIChE Journal, 2016
10. Chialvo, S., J. Sun, and S. Sundaresan, *Bridging the rheology of granular flows in three regimes.* Physical Review E - Statistical, Nonlinear, and Soft Matter Physics, 2012. **85**(2)
11. Chialvo, S. and S. Sundaresan, *A modified kinetic theory for frictional granular flows in dense and dilute regimes.* Physics of Fluids, 2013. **25**(7)
12. Kamrin, K. and G. Koval, *Effect of particle surface friction on nonlocal constitutive behavior of flowing granular media.* Computational Particle Mechanics, 2014. **1**(2): p. 169-176
13. Fukushima, E., *Nuclear magnetic resonance as a tool to study flow.* Annual Review of Fluid Mechanics, 1999. **31**: p. 95-123

2. Literature review

The research fields relevant to the objectives of this thesis were grouped into four categories. First, fluidisation and the scale-up design approach are reviewed. Second, two-fluid modelling of fluid-particle flows and developments in granular rheology are reviewed. Third, discrete modelling of granular flow is reviewed, where the coupling between the fluid and particle phases is unresolved. Finally, the operating principles of nuclear magnetic resonance (NMR) and magnetic resonance imaging (MRI) are reviewed. In particular, flow measurement techniques using MRI are explored. From this review, the topics to be investigated in the following chapters of this thesis were identified.

2.1. Fluidisation and the scale-up method

Fluidisation describes the phenomenon where an assembly of granules transitions from a solid-like to a fluid-like state when fluid is passed through the granular packing. If the fluid velocity is sufficiently low, then the gravitational force acting on the granules is greater than the drag force. In this case, the granules are stationary, and the system operates in a fixed bed regime. Fixed beds have excellent fluid-solid contact, however for applications such as exothermic reactions, regions of high temperature (known as hot spots) can form, which can prove problematic in terms of reaction product quality, catalyst deactivation, and runaway reactions. The formation of hot spots can be prevented by agitating the bed material to distribute heat more evenly. Agitation can be introduced by increasing the gas velocity such that the bed material becomes fluidised. Fluidisation occurs when the drag force acting on the granules exceeds the gravitational force. The bed of particles expands and behaves like a liquid due to the increased mobility of the granules.

The exact nature of the flow is sensitive to the superficial gas velocity and the particle properties. First considering the role of particles, the experiments of Geldart [1] categorised particles according to their mean diameter and relative density. Four distinct categories were observed as shown in Figure 2.1. Group A particles display significant bed expansion above minimum fluidisation, followed by the onset of bubbling. For group B particles the minimum gas velocity required to form bubbles is equal to the minimum fluidisation velocity. Group C particles fluidise poorly or not at all due to the dominance of cohesive forces between fine

particles. The material flows as a plug, or channels in the bed form through which most of the fluid flows. Group D particles can form spouted beds and differ from Group B in that the bubble rise velocity is lower than the gas velocity in the dense phase, facilitating bypassing of the fluidising gas through the bubble. These classifications are important since each group demonstrates different fluidisation behaviour, which has a significant effect on performance. The following fluidisation regimes are observed with increasing superficial fluid velocity: Below the minimum fluidisation velocity, U_{mf}, the system is a fixed bed. For Group A particles, exceeding U_{mf} causes the bed to expand without the formation of bubbles, a regime known as smooth fluidisation. Above the minimum bubbling velocity, voids of excess gas form bubbles that erupt at the bed surface. For narrow fluidised beds, such as laboratory or pilot-scale processes, the bubbles can span the bed diameter, leading to a slugging regime. At higher gas velocities, a turbulent regime exists where voids and particle clusters move chaotically. Further increasing the gas velocity, the particles are entrained by the gas and leave the system. The fluidised bed is in a lean phase with pneumatic transport [2]. The smooth and turbulent regimes offer good gas solids contact, however smooth fluidisation has poor mixing and the turbulent regime is unstable. Bubbling and slugging regimes are the most common operating regime in industry. However, there is the potential for poor gas-solids contacts due to the gas bypassing in the form of large bubbles or slugs. Therefore, it is important that fluidised beds operate in the correct flow regime for optimised process performance.

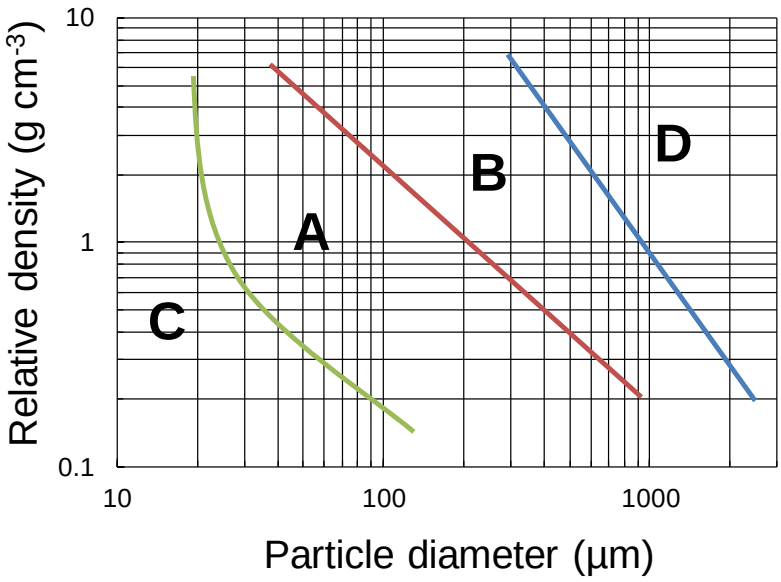

Figure 2.1. Classification chart for granular materials indicating typical particle properties for each of the groups identified by Geldart [1]. The solid lines indicate approximate boundaries between the groups.

Industrial scale fluidised beds were traditionally designed using scale-up methods [3]. The objective of scale-up is to obtain hydrodynamic similarity between processes at different length scales. Scaling laws postulate that hydrodynamic similarity can be achieved by maintaining the values of a series of dimensionless groups derived from the governing equations of the system. Scaling laws were derived by Glicksman [4] from the governing equations of Anderson and Jackson [5], where the Ergun equation [6] describes the momentum transfer between the fluid phase and the particles. These dimensionless groups include the Reynolds number, Froude number, gas to solid density ratio, bed diameter to bed height ratio, particle diameter to bed diameter ratio, sphericity and the particle size distribution (PSD). Hydrodynamic similarity is most commonly measured by analysis of the fluid pressure fluctuations, either as a power spectrum or a probability distribution. If these functions are within a prescribed tolerance for differently scaled systems, then the scaling is considered successful. Dimensionless scaling is complicated by the possibility that infeasible properties may be required to maintain the values of these groups for a different length scale, for example, unphysically high particle density. It is possible that the Geldart classification could differ between different systems where the scaling laws are satisfied, leading to dissimilar flow behaviour. Furthermore, the scaling laws do not consider the contact properties of granules, which were found to strongly influence pressure fluctuations [7] with all other factors being equal. It has also been observed that supposedly simplified scaling laws [8] are better able to achieve hydrodynamic similarity owing to the additional degrees of

freedom offered by such models. Considering the limited predictive ability of the scale-up process, there is interest in directly modelling the hydrodynamics of the full-scale fluidised bed prior to commissioning.

Two-phase fluid particle flows may be modelled with several different approaches. The first category of models describe the granular phase as a collection of discrete entities. This category can be further divided into resolved and unresolved models which describes how the fluid and particle motion is coupled. The resolved discrete model imposes no slip between the fluid and particles [9]. The unresolved discrete model uses a drag equation that is a function of the relative velocity between the particle and the locally averaged fluid [10]. It is not possible to model an industrial scale system with these methods using current computing technology. For this reason, the granular phase is approximated as a continuous medium. The details of this so called "two-fluid" modelling approach are illustrated in Section 2.2 and the unresolved discrete particle model is described in Section 2.3.

2.2. Two-fluid models of gas-solid flow

The volume averaged mass and momentum conservation equations for gas-solid flows were derived by Anderson and Jackson [5]. While the form of the equations may appear to be an *ad-hoc* modification to incorporate the phase volume fractions as coefficients, it is in fact the result of an assumed distinction between features of the flow at different length scales. The local averaging process involves multiplying the equation by a weighting function, followed by integration across the system volume. This approach assumes that there is a "separation of scales", that is fluctuations in the values of point variables occur at length scales smaller than, or larger than, the radius of the weighting function; fluctuations on the length scale of the weighting function are not significant. The form of the gas phase continuity and momentum conservation equation are given by:

$$\rho_g \frac{\partial \varepsilon_g}{\partial t} + \rho_g \nabla \cdot \left(\varepsilon_g \boldsymbol{v}_g\right) = 0 \tag{2.1}$$

$$\rho_g \frac{\partial}{\partial t} \varepsilon_g \boldsymbol{v}_g + \rho_g \nabla \cdot \left(\varepsilon_g \boldsymbol{v}_g^2\right) = -\varepsilon_g \nabla p_g + \nabla \cdot \left(\varepsilon_g \sigma^g\right) + \varepsilon_g \rho_g \boldsymbol{a}_g - \boldsymbol{I}_{gs} \tag{2.2}$$

where ρ_g is the solid phase density, ε_g is the void fraction, $\boldsymbol{v}_g$ is the local gas velocity, p_g is the gas pressure, σ^g is the shear stress tensor, $\boldsymbol{a}_g$ is the acceleration due to gravity, and $\boldsymbol{I}_{gs}$ represents the momentum transfer from the gas phase to the particles. The stress tensor is the difference between the local mean stress tensor and a Reynolds stress that arises from spatial

fluctuations in the fluid velocity over the averaging region, however it is common practice to ignore the Reynolds stresses and assume that the gas phase stress tensor follows Newton's law of viscosity. The continuity and momentum conservation equations for the particle phase were derived from the equation of motion for a single particle, and are given by:

$$\rho_s \frac{\partial \varepsilon_s}{\partial t} + \rho_s \nabla \cdot (\varepsilon_s \boldsymbol{v}_s) = 0 \tag{2.3}$$

$$\rho_s \frac{\partial}{\partial t} \varepsilon_s \boldsymbol{v_s} + \rho_s \nabla \cdot (\varepsilon_s \boldsymbol{v_s^2}) = -\nabla p_g + \nabla \cdot \sigma^s + \rho_s \boldsymbol{a}_g + \boldsymbol{I}_{gs} \tag{2.4}$$

where ρ_s is the granule density, ε_s is the solid volume fraction, $\boldsymbol{v}_s$ is the local solids velocity, and σ^s is the solid phase stress tensor. Closure relations are required for the interphase momentum transfer and the solid phase stress tensor. The interphase momentum transfer consists of buoyancy, drag, and Magnus forces. For gas solid flows, drag represents the largest contribution to the momentum transfer, thus this term may be described by:

$$\boldsymbol{I}_{gs} = \frac{\beta_d V_p}{\varepsilon_s} \left(\boldsymbol{v}_s - \boldsymbol{v}_g \right) \tag{2.5}$$

where V_p is the particle volume and β_d is the drag coefficient.

The introduction of high-performance computers enabled these model equations to be solved. One of the challenges facing researchers was the need to close the system of equations with a constitutive model for the solid phase stress tensor. Like the volume averaged fluid phase stress tensor, the solid phase stress tensor contains a contribution from Reynolds stresses associated with spatial fluctuations in the velocity of the particle phase. These Reynolds stresses can be included or neglected depending on the type of rheology model. As the dependence of the solid phase stress on the viscosity was unknown, early work assumed that the granular material was inviscid. The assumption of inviscid gas and solid flows produced results that were in good qualitative agreement with experimental bubble dynamics [11], and in good quantitative agreement with time averaged velocity profiles [12]. However, the assumption of an inviscid granular material was problematic as it does not allow for investigating the forces exerted on internal components by the granules. Thus, the kinetic theory of granular flow (KTGF) model was incorporated into the model equations, the computed void fraction profile and void fraction oscillation frequency were in good quantitative agreement with experiments [13]. Kinetic theory is particularly useful as it describes the granular viscosity in terms of the particle properties with few empirical

correlations. Such models offer useful insights into the role that particle properties have on the bed hydrodynamics.

The KTGF draws analogies to similar models for dense gases. It is assumed that particles were perfectly spherical, and involved in instantaneous, binary elastic collisions. Mass, momentum and fluctuation energy conservation equations are derived from the Maxwell transport equation [14] which gives the Boltzmann equation. The Boltzmann equation is simplified by using the Enskog approximation; where the pair distribution function is the product of two single-particle velocity distribution functions and the radial distribution function [13]. The Boltzmann equation is solved using Chapman-Enskog theory [15], which describes the velocity distribution function as a perturbation expansion. The zeroth-order solution is the Maxwellian velocity distribution function. The first-order perturbation function is also solved [16]. With a definition for the velocity distribution function and hence the pair distribution function, equations for the transport properties can then be found. Alternatively, the velocity distribution function may be assumed to be Maxwellian [13], or the form of the first order perturbation function may be assumed [17]. A model that takes higher order moments of the velocity distribution function has been developed [18]. However, this approach is only currently suitable for dilute systems and has higher computational costs than low-order models. The low-order models all yield similar expressions for the transport coefficients: pressure, shear viscosity, bulk viscosity, pseudo-thermal conductivity and dissipation rate. The model developed by Ding and Gidaspow [13] is presented here. Under Chapman-Enskog theory, the transport coefficients are a function of granular temperature. Granular temperature is defined as the ensemble average of the particle phase fluctuation velocity.

$$T = \frac{\langle u_x^2 \rangle}{3} + \frac{\langle u_y^2 \rangle}{3} + \frac{\langle u_z^2 \rangle}{3} \tag{2.6}$$

where $\boldsymbol{u} = \boldsymbol{v}_p - \boldsymbol{v}_s$. Therefore, the KTGF incorporates an additional transport equation for fluctuating kinetic energy which enables the granular temperature to be calculated throughout the system.

$$\frac{3}{2}\left[\rho_s \frac{\partial}{\partial t}(\varepsilon_s T) + \rho_s \nabla \cdot (\varepsilon_s \boldsymbol{v}_s T)\right] = -p_s \nabla \cdot \boldsymbol{v}_s - \varepsilon_s \sigma^s : \nabla \boldsymbol{v}_s - \nabla \cdot (\varepsilon_s \boldsymbol{q}) - 3\beta_d T - \Gamma \tag{2.7}$$

where p_s is the granular pressure, and is equal to:

$$p_s = (1 + 2(1 + e_n) g_0) \varepsilon_s \rho_s T \tag{2.8}$$

where e_n is the normal restitution coefficient, and g_0 is the radial distribution function (RDF). Notable versions of the RDF are those of Carnahan and Starling [19], Ogawa [20], and Ma and Ahmadi [21]. The pseudo-thermal energy flux, $\boldsymbol{q}$ is described by the Fourier law $\boldsymbol{q} = \lambda \nabla T$, where the pseudo-thermal conductivity, λ describes the diffusive transport of fluctuating kinetic energy by collisions and is described by:

$$\lambda = 2\rho_s \varepsilon_s^2 g_0 d_p (1 + e_n)\sqrt{T/\pi} \tag{2.9}$$

The constitutive equation for the collisional stress is assumed to be Newtonian and consists of kinetic and collisional components. The kinetic component describes the contribution that particle velocity fluctuations have towards the transport of momentum. The collisional component describes how binary particle collisions influence the transport of momentum. The granular shear viscosity is equal to:

$$\eta_s = \frac{4}{5}\varepsilon_s \rho_s d_p g_0 (1 + e_n)\sqrt{T/\pi} \tag{2.10}$$

The pseudo-thermal dissipation rate, Γ accounts for the loss in fluctuating kinetic energy due to inelastic collisions between particles and is calculated by:

$$\Gamma = 3(1 - e_n)^2 \varepsilon_s^2 \rho_s g_0 T \left(\frac{4}{d_p}\sqrt{\frac{T}{\pi}} - \nabla \boldsymbol{v}_s \right) \tag{2.11}$$

Kinetic theory predictions agree well with DEM simulations [22, 23] and experimental data for dilute, gas-like granular flows where the assumptions are valid. However, for dense granular flows, contacts involve multiple particles and may involve enduring, frictional contacts. Kinetic theory is unsuitable for describing dense flows as the kinetic energy dissipation rate and the granular pressure are overestimated because the granule velocities are correlated [24]. The state of the art for kinetic theory models is the extended kinetic theory [25], which incorporates a length scale into the dissipation rate that models enduring contacts between chains of granules. This model was in good agreement with discrete element simulations of frictionless dense planar shear flow [26] provided that the walls were of low roughness. Advanced kinetic theory models incorporate the role of interparticle friction by introducing angular momentum and rotational granular temperature conservation equations [27-29]. However, these models do not capture the solid volume fraction dependence of the ratio of the rotational velocity variance to the linear velocity variance.

For systems such as fluidised beds where dense and dilute conditions exist simultaneously, part of the challenge has been how to completely describe the rheology while incorporating

these distinct models. One approach is to use a "global equation of state". The development of a "global equation of state" has been a focus of research efforts where a single model is able to adequately describe the granular media at dilute, intermediate and dense states. Khain [30] and Luding [31] developed models from hard-sphere planar shear molecular dynamics (MD) simulations. These global equations of state are limited by the fact that they were fitted to MD simulation data. By doing so, they reflect the assumptions made by the hard-sphere MD simulations. Soft-sphere MD simulations of particles under shear showed that the phenomenon where viscosity diverges at volume fractions below the random close packing volume fraction did not occur [32], illustrating that discrete particle simulations must be representative of reality if they are to be used to derive continuum models.

Another approach for correcting the limitations in kinetic theory stress models is the frictional stress model. The first model was proposed by Johnson and Jackson [33] and was inspired by previous work in the field of soil mechanics.

$$\sigma^{s,f} = p_s^f \delta_{ij} - p_s^f \sin\phi^f \, D \tag{2.12}$$

where δ_{ij} is the Kronecker delta, ϕ^f is the internal angle of friction, and D is the shear rate tensor. In contrast to the kinetic stress equation, the form of the frictional stress equation was largely empirical. Other frictional stress models were proposed by Schaeffer [34] and by Srivastava and Sundaresan [35], the latter incorporated the effect of fluctuations in the strain rate. All of these models required an additional *ad-hoc* equation to describe the frictional pressure p_s^f at volume fractions above $\varepsilon_{s,m}$, such as the equation of Johnson and Jackson [33] given below:

$$p_s^f = \frac{F_r}{\left(\varepsilon_{s,m} - \varepsilon_s\right)^{y_f}} \tag{2.13}$$

Where F_r and y_f are parameters. For systems such as fluidised beds where both conditions exist simultaneously, part of the challenge has been how to completely describe the rheology while incorporating these distinct models. The models have been combined in a piecewise fashion, where the solid volume fraction is the criterion for transition. This total stress equation is input to the momentum and granular temperature conservation equations. Validation studies of joint KTGF-frictional stress rheology models have been performed for bubbling fluidised beds [36-38]. These studies demonstrated that the bubble size was underestimated by simulations with frictional stress models and was highly sensitive to the minimum void fraction at which the frictional stress model contributed.

The failure of joint KTGF-frictional stress models to accurately describe fluidised bed behaviour is in part due to the different flow regimes that exist within dense granular flows. These regimes were illustrated by the DEM simulations of Chialvo et al. [39]. Each regime is classified by the scaling of pressure against shear rate ($p_s \propto \dot{\gamma}^m$). At low shear rate and low volume fraction, the material is in the inertial regime where the scaling follows the Bagnold relation where $m = 2$. At volume fractions above a critical value, the system is quasistatic where the pressure is insensitive to the shear rate ($m = 0$). At higher shear rates, the distinction between the quasistatic and inertial regime disappears to form an intermediate regime ($m = ½$) that exists above and below the critical volume fraction. Hence, descriptions for the inertial and intermediate regimes are required for a complete granular rheology.

A well-known rheology for dense inertial granular flows is the local $\mu(I)$ law [40]. The model introduces a shear stress ratio, $\mu(I) = \tau/p$ that is a function of the inertial number, *I*:

$$I = \frac{\dot{\gamma}}{\sqrt{p_s/(\rho_s d^2)}}. \tag{2.14}$$

The inertial number is a measure of the relative dominance of inertial effects in the flow and may be considered as a ratio of two different timescales: (1) A characteristic deformation time $1/\dot{\gamma}$ that describes the time required for one layer of granules to travel distance *d* relative to the layer below it; (2) A confinement time $\sqrt{p_s/(\rho_s d^2)}$ that describes the time for a layer to return to its position after it has moved over a particle [41]. The stress ratio is calculated by:

$$\mu(I) = \mu_s + \frac{\mu_2 - \mu_s}{I_0/I + 1} \tag{2.15}$$

where μ_s is a yield parameter, μ_2 is an upper limit to the friction, and I_0 is a constant. Values for these parameters have been determined by experimentation [42, 43] and simulation [44]. The velocity profile predictions of the local $\mu(I)$ rheology are in excellent agreement with experimental and discrete data of inclined granular flows in 2D and 3D [40, 45], where the model recovers the velocity profiles derived by Bagnold [46, 47]. It has been shown that the $\mu(I)$ model is only well-posed for a narrow range of inclination angles and that simulations set outside this window diverge [48].

The local rheology also does not capture non-local effects observed in experiments. Continuing with the example of inclined flow, experiments have shown that the angle of repose (the angle at which the material stops flowing) decreases with increasing depth of the

granule layer [49] whereas the local rheology predicts a repose angle independent of layer depth. Nonlocality occurs due to cooperative effects between grains and involves long-distance transportation of momentum at a time scale shorter than either of the timescales described by the inertial number [50]. The state of the art granular rheology models describe nonlocality by introducing an additional state variable known as the granular fluidity, the distribution of which is controlled by an independent transport equation. The cooperative nonlocal granular fluidity model proposed by Kamrin and Koval [51] is itself a modification of the kinetic elastoplastic model by Bocquet et al. [52] where the fluidity is a ratio of the local shear rate and stress ratio. Parallel to this model, a gradient expansion model [53] was developed that took the inertial number as the fluidity. A detailed description of these models is provided in Chapter 7. Outstanding challenges for nonlocal rheology involve developing an understanding of the microscopic origins of fluidity. Simulations suggest that there is a relationship between fluidity, the particle packing and velocity fluctuations that is independent of system geometry [54]. A microphysical description for granular fluidity bears a resemblance to the philosophy behind kinetic theory for dilute granular flows. Furthermore, the introduction of a fluidity transport equation necessitates additional boundary conditions for the fluidity. The exact form of the boundary conditions is not clear. However, discrete element simulations have shown that wall friction and roughness have a strong influence on the shear profile [55-57], indicating that these features should be considered when developing boundary conditions for continuum models.

2.3. Unresolved discrete particle modelling of gas-particle flow

This section describes models where the gas phase is treated as a continuous medium resolved on a length scale of several particle diameters in length, as described by Equations 2.1 and 2.2. The particles are resolved as distinct entities whose interaction with the gas phase is controlled by a drag law. The first such CFD-DEM simulations were performed by Tsuji et al. [10]. Particle contacts may be resolved using either a hard-sphere or soft-sphere approach. Contacts in hard-sphere simulations are modelled as binary and instantaneous, the change in the velocity from a collision is calculated by [58]:

$$m_i(\boldsymbol{v}_i - \boldsymbol{v}_{i,0}) = -m_j(\boldsymbol{v}_j - \boldsymbol{v}_{j,0}) = \boldsymbol{J} \tag{2.16}$$

where $\boldsymbol{v}_{i,0}$ is the pre-collision velocity of particle *i*, $\boldsymbol{v}_i$ is the post-collision velocity of particle *i*, m_i is the mass of particle *i*, and $\boldsymbol{J}$ is the impulse vector, which consists of a normal component determined by:

$$J_n = -(1 + e_n) m_{ij} \boldsymbol{v}_{ij,0} \cdot \boldsymbol{n}_{ij} \tag{2.17}$$

where e_n is the normal coefficient of restitution, $m_{ij} = \left(m_i^{-1} + m_j^{-1}\right)^{-1}$, $v_{ij,0}$ is the relative velocity between particles *i* and *j* prior to collision, and $\boldsymbol{n}_{ij}$ is the unit vector along the normal direction which goes through the centres of particle *i* and particle *j*. The tangential component of the impulse vector is given by:

$$J_t = \max\left(-\frac{2}{7}(1 + e_t) \times m_{ij} \boldsymbol{v}_{ij,0} \boldsymbol{t}_{ij}\, , -\mu_f J_n\right) \tag{2.18}$$

where e_t is the tangential restitution coefficient, $\boldsymbol{t}_{ij}$ is the tangential unit vector, orthogonal to the normal unit vector, and μ_f is the interparticle dynamic friction coefficient. The rotational motion after the collision is calculated according to:

$$\frac{I_i}{R_i}\left(\boldsymbol{\omega}_i - \boldsymbol{\omega}_{i,0}\right) = -\frac{I_j}{R_j}\left(\boldsymbol{\omega}_j - \boldsymbol{\omega}_{j,0}\right) = -\boldsymbol{n}_{ij} \times \boldsymbol{J} \tag{2.19}$$

Where I_i is the moment of inertia for the particle *i*, which is $2/5\, m_i R_i^2$ for a sphere. The pre-collision angular velocity is $\boldsymbol{\omega}_{i,0}$, and the post-collision angular velocity is $\boldsymbol{\omega}_i$. Hard-sphere simulations are computationally efficient as they are driven by the occurrence of collision events rather than time. However, hard-sphere models are poorly suited for dense granular flows where simulations may fail if the particle concentration is too high due to a divergence in the number of collisions, a phenomenon known as inelastic collapse [59]. Intermediate and quasistatic flow regimes do not form in the rigid particle limit, hence hard-sphere models cannot describe features of interest in physical granular flows [39]. The soft-sphere Discrete Element Method originally developed by Cundall and Strack [60] does not suffer from the aforementioned disadvantage of the hard-sphere method and the additional computational cost has become less important with improvements in computer hardware.

The discrete element method resolves the positions and velocities of individual particles by numerical integration of Newton's second law of motion with respect to time. For particles in gas-solid flow, Newton's 2nd law takes the form:

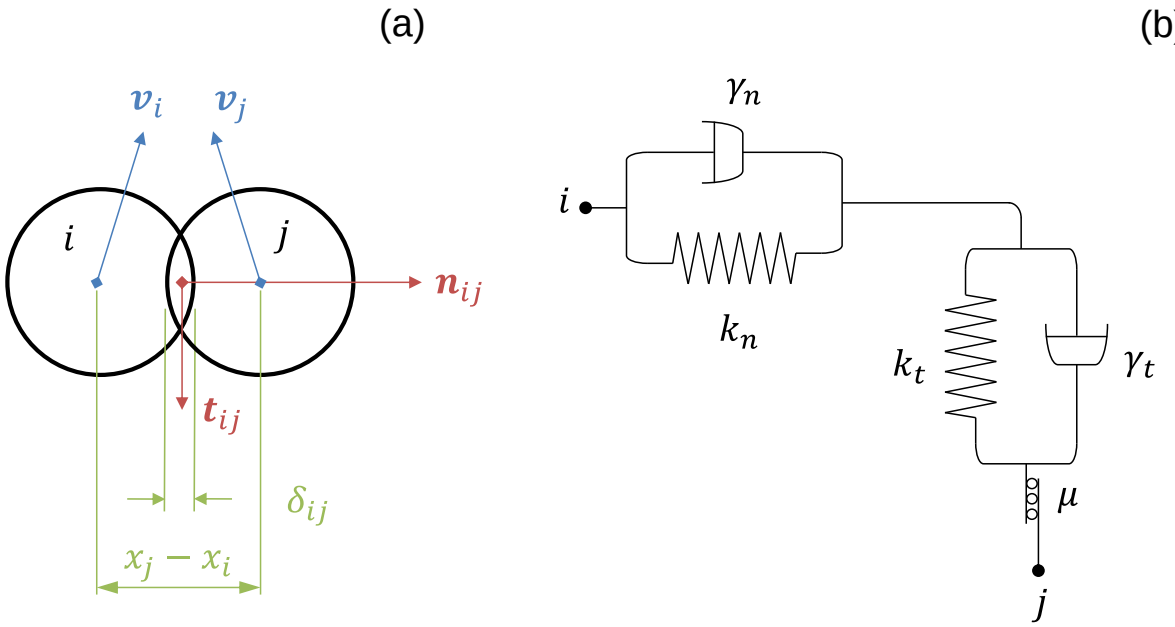

Figure 2.2 (a) Diagram of contacting particles illustrating the variables involved in determining the contact force. (b) Schematic of contact force scheme consisting of elastic and viscous contributions along the normal and tangential directions, and Coulomb friction along the tangential direction.

$$m_p \frac{d\boldsymbol{v}_p}{dt} = \boldsymbol{f}_c + \boldsymbol{f}_{d,p} + m_p \boldsymbol{a}_g \tag{2.20}$$

where v_p is the velocity of a particle, $\boldsymbol{f}_c$ is the total contact force acting on the particle due to physical contacts from other particles as illustrated in Figure 2.2(a). Rotational motion of the particles is modelled using an analogous approach. The torque balance for a particle is equal to:

$$I_p \frac{d\boldsymbol{\omega}_p}{dt} = \boldsymbol{T}_c \tag{2.21}$$

where ω_p is the angular velocity vector of particle p, $\boldsymbol{T}_c$ is the total torque induced by tangential contact forces:

$$\boldsymbol{T}_c = \sum_{j \neq i}^{N} R\boldsymbol{n}_{ij} \times \boldsymbol{F}_{t,ij}. \tag{2.22}$$

The total contact force is equal to the sum of normal and tangential forces from the N_c particles in contact with particle i:

$$\boldsymbol{f}_c = \sum_{j \neq i}^{N_c} \left(\boldsymbol{F}_{n,ij} + \boldsymbol{F}_{t,ij} \right) \tag{2.23}$$

where the normal force between particle *i* and its neighbour *j* is described by a contact force scheme. The contact forces consist of elastic and viscous components as shown by Figure 2.2(b). The two most widely used contact force schemes are the linear spring-dashpot model and the Hertzian model. The basic form of both models is as follows:

$$\boldsymbol{F}_{n,ij} = k_n \delta_n \boldsymbol{n}_{ij} - \gamma_n \boldsymbol{v}_{n,ij} \tag{2.24}$$

$$\boldsymbol{F}_{t,ij} = \begin{cases} k_t \boldsymbol{\delta}_t - \gamma_t \boldsymbol{v}_{t,ij} & \text{if } F_{t,ij} \le \mu_f \left| F_{n,ij} \right| \\ -\mu_f \left| \boldsymbol{F}_{n,ij} \right| \boldsymbol{t}_{ij} & \text{otherwise.} \end{cases} \tag{2.25}$$

where k_n is the normal spring stiffness, k_t is the tangential spring stiffness, δ_n is the normal overlap between particles *i* and *j*, $\boldsymbol{\delta}_t$ is the tangential displacement, and is calculated by the method described by Deen [58]. The normal relative velocity between particles *i* and *j* is denoted by $\boldsymbol{v}_{n,ij}$, and $\boldsymbol{v}_{t,ij}$ is the relative tangential velocity. γ_n is the normal viscous damping coefficient, which is given by:

$$\gamma_n = \frac{2\sqrt{m_{\text{eff}} k_n}\, |\ln e_n|}{\sqrt{\pi^2 + \ln^2 e_n}} \tag{2.26}$$

where $m_{\text{eff}} = m^2/(2m)$ and the tangential damping coefficient γ_t is:

$$\gamma_t = \frac{2\sqrt{m_{\text{eff}} k_t}\, |\ln e_t|}{\sqrt{\pi^2 + \ln^2 e_t}} \tag{2.27}$$

where e_t is the tangential restitution coefficient. For the linear spring-dashpot model, the spring constants are fixed values, while for the Hertzian model, they are a function of the overlap:

$$k_n = \frac{4}{3} E^* \sqrt{R^* \delta_n} \tag{2.28}$$

$$k_t = 8 G^* \sqrt{R^* \delta_n} \tag{2.29}$$

where$1/R^*$ is equal to $1/R_i + 1/R_j$, and $1/E^*$ is $(1-\nu_i)/E_i + \left(1-\nu_j\right)/E_j$. E_i is the elastic modulus of particle *i* and ν_i is the Poisson ratio of particle *i*. The effective shear modulus is denoted by G^*, and is found by:

$$\frac{1}{G^*} = \frac{2(2-\nu_i)(1+\nu_i)}{E_i} + \frac{2\left(2-\nu_j\right)\left(1+\nu_j\right)}{E_j}. \tag{2.30}$$

The Hertzian damping coefficients are calculated by:

$$\gamma_n = -2\sqrt{\frac{10 E^* m^*}{6}} \frac{\ln e_n \, (R^* \delta_n)^{\frac{1}{4}}}{\sqrt{\ln^2 e_n + \pi^2}} \tag{2.31}$$

$$\gamma_t = -2\sqrt{\frac{40G^*m^*}{6}}\frac{\ln e_n\,(R^*\delta_n)^{\frac{1}{4}}}{\sqrt{\ln^2 e_n + \pi^2}} \tag{2.32}$$

where$1/m^*$ is equal to $1/m_i + 1/m_j$. Identifying which particles are in contact is a computationally expensive task that is handled by a neighbour search algorithm. The N^2 algorithm is a crude method where for each particle, the relative position of the remaining particles is checked to identify overlaps. The number of logical tests required increases with the square of the number of particles in the system. Since there is little utility in checking particles several diameters apart, the cell-linked list method [61] is a more widely used alternative. This method groups particles into spatial bins and then detects contacts between particles with envelopes located within the same bin. The computation time for the cell-linked list method scales approximately linearly with the number of particles. However, for systems with size distributions, a cell-linked list returns too many unnecessary potential contacts for small particles. To optimise searching for bidisperse and polydisperse materials, the search is divided into levels [62] where on each level contacts between similarly sized particles are detected. Next, contacts between differently sized particles that belong to different levels are detected. This cross-level detection is only performed between a given level and levels containing smaller granules to avoid unnecessary double counting. With this detection method, it is possible to simulate polydisperse systems with a similar run time to a monodisperse equivalent [63].

The granule velocities are found by numerical integration of Equation 2.20 with respect to time. Particle positions were updated by numerical integration of the velocity with respect to time. Numerical integration schemes such as the Euler method, Adams-Bashforth [64] and velocity Verlet [65, 66] methods are commonly used. The Euler method takes the position and velocity at time t and calculates the position and velocity at time $t + \Delta t$ by:

$$\boldsymbol{v}_p(t + \Delta t) = \boldsymbol{v}_p(t) + \Delta t \left.\frac{d\boldsymbol{v}_p}{dt}\right|_t \tag{2.33}$$

$$\boldsymbol{x}_p(t + \Delta t) = \boldsymbol{x}_p(t) + \boldsymbol{v}_p(t + \Delta t)\Delta t \tag{2.34}$$

$$\boldsymbol{\omega}_p(t + \Delta t) = \boldsymbol{\omega}_p(t) + \Delta t \left.\frac{d\boldsymbol{\omega}_p}{dt}\right|_t \tag{2.35}$$

where Δt is the time interval between steps. The Euler method is first-order accurate. The global truncation error is proportional to the step size. As the simulation run time is controlled by the number of steps performed, it is advantageous to make the step size as large as possible. However, the first order accuracy of the Euler method means that the truncation

error is prohibitively high as the step size increases. Alternatives to the Euler method include the second order Adams Bashforth method which calculates the position and velocity at $t + \Delta t$ according to:

$$\boldsymbol{v}_p(t + \Delta t) = \boldsymbol{v}_p(t) + 0.5\left(3\frac{d\boldsymbol{v}_p}{dt}\Big|_t + \frac{d\boldsymbol{v}_p}{dt}\Big|_{t-\Delta t}\right)\Delta t \tag{2.36}$$

$$\boldsymbol{x}_p(t + \Delta t) = \boldsymbol{x}_p(t) + 0.5\left(3\boldsymbol{v}_p(t) + \boldsymbol{v}_p(t - \Delta t)\right)\Delta t \tag{2.37}$$

$$\boldsymbol{\omega}_p(t + \Delta t) = \boldsymbol{\omega}_p(t) + 0.5\left(3\frac{d\boldsymbol{\omega}_p}{dt}\Big|_t + \frac{d\boldsymbol{\omega}_p}{dt}\Big|_{t-\Delta t}\right)\Delta t. \tag{2.38}$$

The velocity Verlet method calculates the position at $t + \Delta t$ by:

$$\boldsymbol{x}_p(t + \Delta t) = \boldsymbol{x}_p(t) + \boldsymbol{v}_p(t)\Delta t + 0.5\frac{d\boldsymbol{v}_p}{dt}\Big|_t \Delta t^2. \tag{2.39}$$

The position at $t + \Delta t$ is used to calculate the acceleration at $t + \Delta t$ using Equation 2.20, which is used to calculate the velocity at $t + \Delta t$ by:

$$\boldsymbol{v}_p(t + \Delta t) = \boldsymbol{v}_p(t) + 0.5 * \left(\frac{d\boldsymbol{v}_p}{dt}\Big|_t + \frac{d\boldsymbol{v}_p}{dt}\Big|_{t+\Delta t}\right)\Delta t. \tag{2.40}$$

Analogously, the angular velocity is found according to:

$$\boldsymbol{\omega}_p(t + \Delta t) = \boldsymbol{\omega}_p(t) + 0.5 * \left(\frac{d\boldsymbol{\omega}_p}{dt}\Big|_t + \frac{d\boldsymbol{\omega}_p}{dt}\Big|_{t+\Delta t}\right)\Delta t. \tag{2.41}$$

The Adams-Bashforth method and the velocity Verlet methods are second order accurate, that is, the global truncation error is proportional to the square of the step size. For example, halving the time step reduces the global truncation error by a factor of 4. Another additional factor that controls the maximum allowable step size is contact resolution. The transfer of energy during a contact should occur on a timescale similar to that of reality. For the linear spring-dashpot model, the collision time, t_c, is determined by:

$$t_c = \pi \Big/ \sqrt{\frac{k_n}{m_{\text{eff}}} - \frac{\gamma_n^2}{m_{\text{eff}}^2}}. \tag{2.42}$$

The step size is set to a fraction of t_c, such as 1/50 [67]. For the Hertzian contact model, the criterion is the Rayleigh time, which is a measure of the travel time of Rayleigh waves across the granule surface, and is equal to [68]:

$$t_R = \frac{\pi R\sqrt{\rho_s/G}}{0.8766 + 0.1631\nu}. \tag{2.43}$$

In practice, the step size is advised to be 25% of the Rayleigh time, although this factor should be lower for instances where contacts involve large relative velocities [69]. For this reason, it is common practice to model fluidised beds with particles that have low values of k_n, or E as it increases the permissible time step and was found to have minimal influence on the bed hydrodynamics [70].

The governing equations for the fluid phase require knowledge of the fluid volume fraction (also known as void fraction) and the interphase momentum transfer. To determine the proportion of each computational cell that is occupied by the fluid phase, local spatial averaging of the DEM data is required. In general, the local void fraction over a region of space such as a CFD cell is calculated according to:

$$\varepsilon_g = 1 - \frac{\sum_{p=1}^{N_\mathrm{p}} \phi_p V_p}{V_{cell}} \tag{2.44}$$

where ϕ_p is a weighting of the particle volume within the cell, and V_{cell} is the volume of the cell. The weightings used may reflect the amount of particle volume in the cell, or involve smoothing for numerical stability. A detailed review of common void fraction schemes is provided in Chapter 4. The interphase momentum term is the total drag force acting on the particles within the computational cell, that is:

$$\boldsymbol{I}_{gs} = \frac{\sum_{p=1}^{N_\mathrm{particles}} \boldsymbol{f}_{d,p} \phi_p}{V_{cell}} \tag{2.45}$$

is handled using a drag law as with the TFM, however it is calculated on a per-particle basis by:

$$\boldsymbol{f}_{d,p} = -V_p \nabla p_g + \beta_d V_p \left(\boldsymbol{v}_g - \boldsymbol{v}_p\right). \tag{2.46}$$

The exact form of the drag coefficient has been an intense area of research as it is highly sensitive to the Reynolds number and the void fraction. Early drag models were derived empirically, such as the Ergun [6] model for dense particle flows, or the model of Wen and Yu [71] for dilute flows. The model of Di Felice [72] related the drag coefficient for particle packings to that experienced by an isolated single particle. Advancements in computer processing facilitated simulations of fully-resolved gas flow coupled with discrete particles. The gas phase is modelled using either CFD or LBM where the gas velocity at the particle surface is described by the no-slip boundary condition. These simulations have been used to develop drag models for collections of spheres in regular and random packing arrangements [73] at low to intermediate Reynolds numbers. The model developed from simulations by

Beetstra et al. [74] is widely used due to its validity over a wider range of void fractions and Reynolds numbers than the preceding empirical models. Recent work by Tang et al. [75] investigated the hitherto ignored effect of velocity fluctuations on the drag coefficient, which were responsible for the Beetstra model underestimating the drag coefficient when used in CFD-DEM simulations [76]. Developments for nonspherical drag models are reviewed in Chapter 3.

2.4. Magnetic resonance imaging of granular materials

Simulations of granular flow require validation against experiments such that model predictions can be applied to industrial systems with confidence. Different experimental techniques have been developed to measure the solid volume fraction and the velocity distribution. The solid volume fraction in the bed can be measured with radiation attenuation methods such as x-ray [77] or gamma ray densitometry [78]. Radiation is introduced to the system by a source and the intensity of the radiation leaving the system is recorded by a detector positioned opposite to the source. The intensity of the detected radiation is inversely related to the density of the matter through which the radiation has travelled [79]. By positioning the source and detector at different positions around the system, image reconstruction is used to produce a spatially resolved density map through a cross-section of the sample [80]. The solid volume fraction has also been measured with electrical capacitance volume tomography (ECVT) [81]. In ECVT, the electrical capacitance field is measured by an array of electrodes placed around the exterior of the system. From these capacitance data, the spatially resolved density of the system is attained by image reconstruction [82]. Accurate image reconstruction is challenging and limits the resolution that can be achieved by this method [83]. Furthermore, ECVT is not able to measure the velocities of the granules. Particle tracking methods measure the particle trajectory of granules by collecting series of discrete position measurements. Particle image velocimetry (PIV) [84] measures particle positions by the analysis of optical images, and hence is limited to optically accessible systems. Positron emission particle tracking (PEPT) [85] infers the positions of tracer particles by detecting radiation emitted by radionuclides. This method requires long experiments and the accuracy is limited by the ~1 mm uncertainty in the tracer position [86]. These methods do not measure the solid volume fraction directly; instead it is inferred by assuming that the system is ergodic. Magnetic resonance (MR) is an experimental technique that exploits the behaviour of spin-active nuclei in magnetic fields. Notable applications include chemical analysis using nuclear magnetic resonance (NMR) spectroscopy and non-

invasive imaging for research and clinical purposes, known as magnetic resonance imaging (MRI). Of particular interest in this thesis is the use of MRI for spatially resolved velocity measurements in opaque systems. In this section, the pertinent theory of MR is reviewed and its application to imaging and velocimetry.

2.4.1 Background to NMR

Spin is a quantum mechanical property of nuclei that is analogous to angular momentum in classical physics. Spin-active nuclei have an odd mass number or an odd atomic number. Common spin-active nuclei have a spin quantum number of ½. A nucleus with a spin quantum number of ½ rotating about its axis in the presence of a magnetic field (denoted by B_0) in the z-direction induces a magnetic moment described by:

$$\mu_{M,z} = \pm\frac{\gamma h}{4\pi} \tag{2.47}$$

The nuclei occupy two energy states: a low-energy state $-\frac{\gamma h B_0}{4\pi}$ (parallel to B_0), and a high-energy state $+\frac{\gamma h B_0}{4\pi}$ (antiparallel to B_0). This phenomenon is known as Zeeman splitting, first demonstrated for nuclear spin by Stern and Gerlach [87]. The net magnetisation, $\boldsymbol{M}$, is defined as the sum of the magnetic moments of the nuclei in a sample and follows Boltzmann's equation. At room temperature, the parallel state is several orders of magnitude more populous than the antiparallel state. Electromagnetic radiation is used to promote nuclei from the parallel state to the antiparallel state, first performed on molecular beams by Rabi [88]. This method was extended independently by Bloch [89, 90] and Purcell [91] for liquids and solids. The required energy of the photon is equal to the energy gap between the two states. The frequency of the photon is related to the magnetic field by:

$$\omega_{M,0} = \gamma B_0 \tag{2.48}$$

The radiofrequency (RF) pulse is applied perpendicularly to B_0, meaning that the net magnetisation has a component perpendicular to B_0. When the RF field is no longer applied, this component of magnetisation precesses at an angular frequency ω_0 (known as the Lamor frequency) equal to the angular frequency of the RF pulse. In the absence of the RF field, the sample returns to its equilibrium magnetisation state, M_0, a process known as relaxation. The change in time of the net magnetisation components is described by the Bloch equations:

$$\frac{dM_{x,y}}{dt} = \gamma(\boldsymbol{M} \times \boldsymbol{B})_{x,y} - \frac{M_{x,y}}{T_2} \tag{2.49}$$

$$\frac{dM_z}{dt} = \gamma(\boldsymbol{M} \times \boldsymbol{B})_z - \frac{(M_z - M_0)}{T_1} \tag{2.50}$$

The relaxation process consists of two main mechanisms described by distinct timescales The decay of the component parallel to B_0 is described by T_1, while the decay of the perpendicular component is described by T_2. Inhomogeneities in the sample of the applied magnetic field also contribute to the decay of the perpendicular magnetisation components, thus an overall transverse relaxation time T_2^* is defined. The transient magnetic field produced by the precessing nuclei induces a voltage in the RF coil, the profile of the induced voltage over time is known as the free induction decay (FID). Fourier transformation of the FID returns a peak at the Lamor frequency.

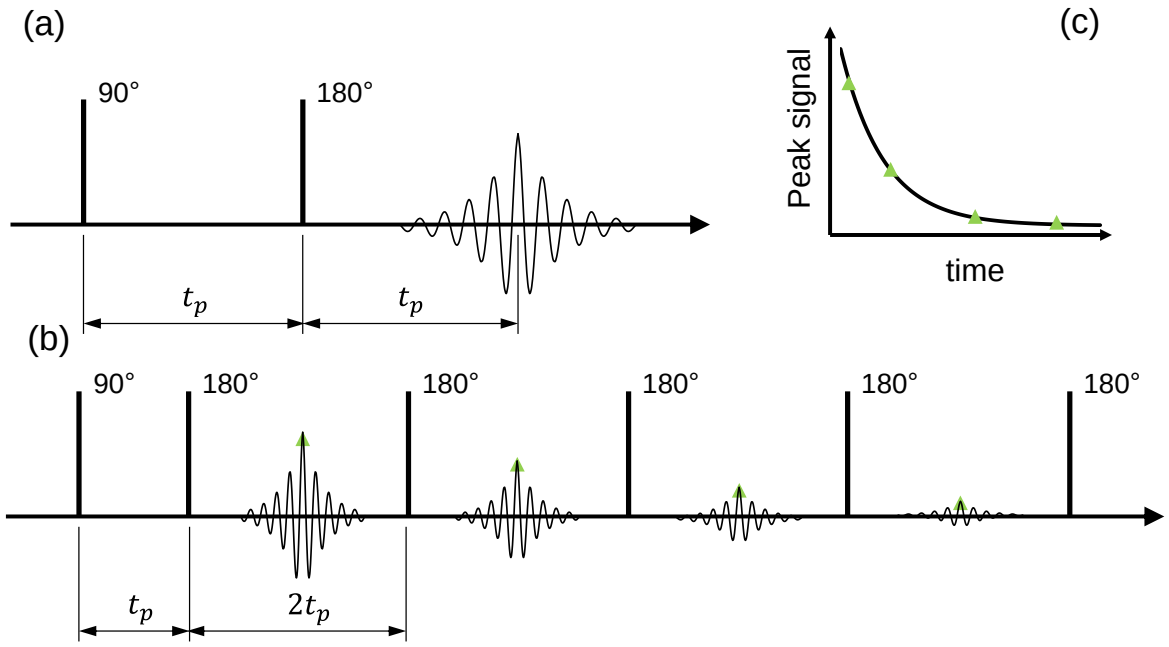

Figure 2.3. (a) pulse schematic for spin-echo experiment. (b) pulse sequence for CPMG experiment. (c) Decay of the peak signal with time.

In spin echo experiments [92] such as the one illustrated by Figure 2.3(a), the magnetisation is rotated into the transverse plane by a 90° RF pulse. Inhomogeneities in the magnetic field cause the magnetisation of some spins to precess faster than others, causing the net magnetisation to decay. The application of a 180° RF pulse at time t_p flips the magetisations, such that the slower spins lead the faster spins. Amplification in the signal is observed once the magnetisation vectors of all the spins realign with the net magnetisation. The refocusing of the signal is not perfect due to spin-spin relaxation. A repeating sequence of 180° RF pulses separated by $2t_p$, shown in Figure 2.3(b) produces a sequence of echos, of which the

peak signal intensity decreases exponentially with time. The time constant for this decay curve shown in Figure 2.3(c) is the spin-spin relaxation time T_2 in the absence of any imhomogeneous effects. Such an experiment is known as a Carr-Purcell-Meiboom-Gill (CPMG) pulse sequence [93, 94].

2.4.2 Background to MRI

The signal can encode information about the position of the nuclei by introducing a spatially varying magnetic field [95, 96]. Gradient coils create a magnetic field that varies linearly with position. In the case of a gradient along the z-direction, the precession frequency in the laboratory frame of reference depends on the z-coordinate according to:

$$\omega_{M,z} = \gamma(B_0 + zg_z) \tag{2.51}$$

Fourier transformation of the signal returns the frequency distribution of the precession frequencies in the sample. This distribution is known as the spin density $\rho(z)$ and is a relative measure of the number of spin-active nuclei within a region of space. It is common practice to study the precession of spins about B_0 in a rotating reference frame such that the spin motion can be more easily understood. In a rotating frame with a frequency of γB_0, the complex signal from a sample is given by:

$$S(\tau) = \iiint \rho(\boldsymbol{x}) \exp\left(i\gamma \int_0^\tau \boldsymbol{g}(t) \cdot \boldsymbol{x}\, dt\right) dV \tag{2.52}$$

where $\boldsymbol{x}$ is the position vector, and V is the sample domain. By convention the term within the exponential function is defined in terms of reciprocal space, more commonly known as k-space:

$$\boldsymbol{k} = \frac{\gamma}{2\pi} \int \boldsymbol{g}(t)\, dt \tag{2.53}$$

Collecting signal data for different values of $\boldsymbol{k}$ in the frequency domain, followed by Fourier transformation produces a spatial domain spin density map. k-space is traversed using either frequency encoding or phase encoding. Frequency encoding traverses k-space by maintaining a constant gradient strength while changing the time used to acquire the signal. A spin-echo sequence is performed in the presence of an applied gradient. Following the 180° RF pulse, data at many points along the signal are collected, where each point is separated by the dwell time. Frequency encoding is advantageous as multiple points in k-space are sampled during a single excitation. Spins with the same spatial coordinate along the frequency encoding axis, but different positions orthogonal to the frequency encoding gradient have the same

frequency, thus the orthogonal direction is spatially unresolved. These spins are distinguished by changing the phase angle of the precession frequency orthogonal to the direction of frequency encoding. This process is performed with the use of another gradient to encode for phase angle, where the phase angle θ is defined by:

$$\theta = \int \boldsymbol{g}(t) \cdot \boldsymbol{x}(t)\, dt \tag{2.54}$$

With phase encoding, *k*-space is traversed by keeping the duration of the gradient encoding fixed and by varying the strength of the gradient. The gradient is applied to approximate a square pulse prior to the refocusing 180° RF pulse. Unlike frequency encoding only one point in k-space can be sampled per excitation, which increases the time required to run experiments. Pulse sequence diagrams for frequency and phase encoding are shown by Figure 2.4.

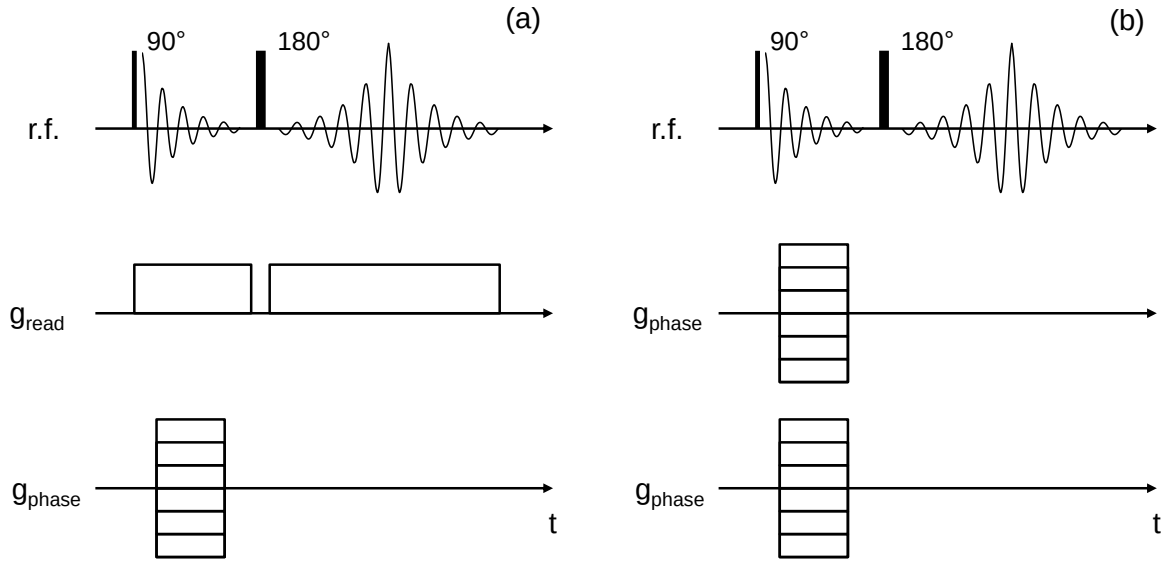

Figure 2.4. Spin echo gradient sequences for 2D imaging using (a) frequency-phase encoding, and (b) phase-phase encoding.

Due to the often long experiment times required to generate 3D images, pseudo 2D images are produced instead by isolating the spin echo to nuclei within a narrow region of the sample. An RF pulse is applied in conjunction with the slice selection gradient to rotate only the magnetisation vectors of nuclei precessing within this frequency window onto the transverse plane. The thickness of a slice along the z-direction, Δz is estimated by:

$$\Delta z = \frac{\Delta \omega_s}{\gamma G_z} \tag{2.55}$$

where $\Delta\omega_s$ is the range of frequencies in the RF pulse, and G_z is the slice gradient. 2D imaging sequences can consist of frequency encoding combined with phase encoding, or with phase encoding along both spatial dimensions. Measuring the solid volume fraction is complicated by the signal attenuation induced by flow. Gradient sequences can be designed to compensate for this effect. These sequences are reviewed in Chapter 6. The collected signal data are in the frequency domain, the image is obtained by converting the data to the spatial domain via discrete Fourier transform.

2.4.3 Measuring velocity using MRI

The MR signal is sensitive to flow, which if uncorrected leads to distortions in images. However, this feature is useful from the perspective of measuring flow. MRI measurements of velocity are classified into two categories: time-of-flight and phase contrast [97]. Time-of-flight experiments measure flow by first tagging nuclei within a planar slice. Tagging involves rotating the magnetisation vector along the transverse plane such that the signal from the selected slice is close to fully attenuated. If there is a time delay between tagging and imaging, the tag is distorted due to the motion of the nuclei. Assuming that the slice is along the x-y plane, the velocity in the z direction is obtained by [98]:

$$v_z = \frac{1}{t_d}\frac{\int z I_{MR}\, dz}{\iiint I_{MR}\, dxdydz} \tag{2.57}$$

It is possible to perform time-of-flight experiments for motion parallel to the slice plane by tagging nuclei in a grid pattern [99]. Quantitative velocity measurements are obtained by measuring the deformation of the grid for images separated by a delay time. Thus, the resolution of the velocity information is limited by the resolution of the grid, not the resolution of the image. Subsequently, the phase contrast method has become more popular in recent decades owing to improvements in the resolution and accuracy. Consider a spin with constant velocity, where the position is described by $\boldsymbol{x} = \boldsymbol{x}_0 + \boldsymbol{v}t$, the precession frequency in the laboratory frame becomes:

$$\omega_M = \gamma\big(B_0 + \boldsymbol{g}\cdot(\boldsymbol{x}_0 + \boldsymbol{v}t)\big). \tag{2.58}$$

In the rotating frame of reference with a frequency of γB_0, the complex signal is:

$$S = \iiint \rho(\boldsymbol{x}) \exp\left(i\gamma \int_0^{\tau} \boldsymbol{g}(t)\cdot(\boldsymbol{x_0} + \boldsymbol{v}t)\, dt\right) dV. \tag{2.59}$$

Thus, the phase angle of the signal is described by:

$$\theta = \gamma\left(\boldsymbol{x}_0 \cdot \int_0^{\tau} \boldsymbol{g}(t)\,dt + \boldsymbol{v} \cdot \int_0^{\tau} t\boldsymbol{g}(t)\,dt\right). \tag{2.60}$$

To remove the contribution of the position at the start of the imaging sequence, the time integral of the gradient sequence should be set to zero. Thus, the phase angle can be expressed by $\theta = \boldsymbol{p} \cdot \boldsymbol{v}$, where the inverse velocity variable $\boldsymbol{p}$ is defined as:

$$\boldsymbol{p} = \gamma \int t\boldsymbol{g}(t)\,dt. \tag{2.61}$$

Any combination of gradient pulses equal in strength and duration, but in opposite directions meets the criteria that $\int_0^{\tau} \boldsymbol{g}(t)\,dt = 0$. If there is a single pair of flow encoding gradient pulses, with pulse duration δ, magnitude $\boldsymbol{g}$, and separated by Δ, then:

$$\boldsymbol{p} = \gamma \boldsymbol{G}\delta\Delta. \tag{2.62}$$

Therefore, the local mean velocity can be found by the ratio of the phase angle of the signal measured by experiments to the known inverse variable. This imaging sequence is referred to as pulse gradient spin echo (PGSE) and was first performed by Stejskal and Tanner [100] to measure the diffusion coefficients of liquids. The pulse sequence is shown by Figure 2.5.

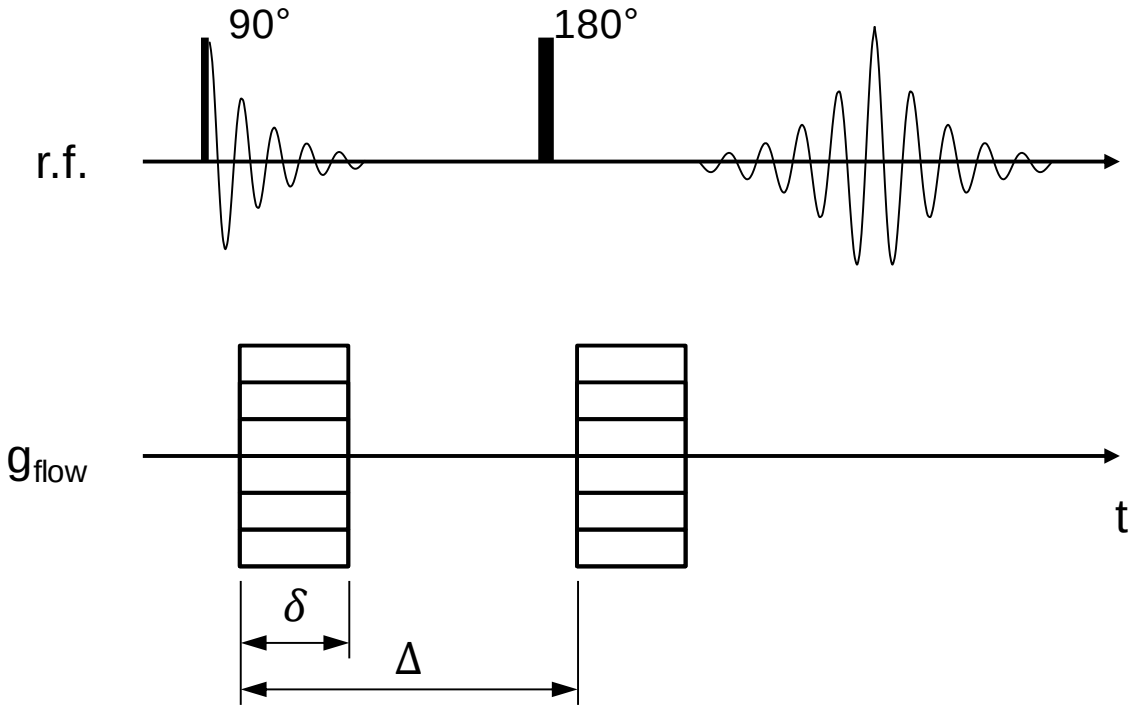

Figure 2.5. Pulse diagram for pulse gradient spin echo sequence.

For granular flow, Caprihan and Seymour [101] measured the velocity variance in rotating drum flow by measuring the apparent diffusion coefficient using a series of gradient

sequences, which were used to calculate the diffusion coefficient and the mean collision time. The velocity variance was inferred from the assumed theoretical velocity autocorrelation function. Holland et al. [102] measured spatially resolved components of the velocity variance in a fluidised bed. Their experimental technique is explained in detail in Chapter 5 and utilises the PGSE sequence used in phase contrast velocity imaging. Both these approaches neglect the contribution from rotating granules. There is evidence to suggest that MRI is capable of resolving granule rotation. Time-of-flight velocity measurements of a Couette cell containing mustard seeds were performed by Mueth et al. [103]. Near the moving inner wall, ordering was observed where the granules form concentric layers. For perfectly ordered granules, the local mean velocity profile is expected to take the form of a staircase, where rapid shear occurs at the interfaces of the layers, and the velocity within the granule is constant. This staircase profile was disrupted by disordering of granules and rotational motion which caused the nuclei within the granule to displace by differing amounts. Using optical velocimetry (which does not measure rotational motion), it was found that disordering of the granules alone was insufficient to account for the non-zero shear inside the layers. The difference between the shear profiles measured optically and with MRI was used to infer the mean angular velocity in each layer. Besides their work, granule rotation has not been explored further with MRI.

2.5. Summary

The scale-up method is difficult to apply to fluidised bed processes and the performance of full-scale equipment is often inferior to expectations. Computer modelling of full-scale fluidised beds offers the potential to predict the hydrodynamics prior to commissioning. Due to computational limitations, it is only possible to model full-scale fluidised beds by describing the granular phase as a continuous medium. This assumption requires knowledge of how the granular stress depends on the shear, particle properties, solid volume fraction and velocity distribution. Several approaches have been proposed including kinetic theory methods, frictional stress equations, local viscoplastic, and nonlocal rheological models. These models require validation, which is performed by discrete element method simulations and physical experiments.

Discrete element simulations resolve the trajectories of individual granules and are related to continuum models by spatial averaging of discrete data. For systems such as fluidised beds, where particle motion is heavily influenced by drag exerted by the fluid flow, the DEM is

coupled with CFD modelling of the fluid phase. For this approach to be feasible for laboratory scale fluidised beds, the CFD grid must be several particle diameters in size. This stipulation necessitates the use of a drag equation to resolve the interaction between the fluid and the particles. Drag equations are derived from experiments and resolved CFD-DEM simulations and are not always representative of systems to which they are applied. Drag equations also require knowledge of the local particle packing for which exact solutions are not easily attainable. The influence of these features is not understood. Therefore, systematic investigations of the Beetstra drag model and several void fraction schemes were performed.

MRI is able to measure the velocity distribution within granular materials. Past research has indicated that granule rotation has an influence on the mean velocity measured using a time-of-flight technique. However, the significance of this effect on the phase contrast velocity technique has not been studied. MRI experiments were simulated to validate a theoretical analysis of rotational motion effects. Furthermore, there is uncertainty in quantitative solid volume fraction measurements due to flow related artifacts. Simulated MRI experiments were performed to determine if the MR image intensity was an accurate analogue for the phase concentration by validating a velocity compensated imaging sequence.

2.6. References

1. Geldart, D., *Types of gas fluidization.* Powder Technology, 1973. **7**(5): p. 285-292
2. Kunii, D. and O. Levenspiel, *Fluidization engineering*. 2013: Elsevier.
3. Rüdisüli, M., et al., *Scale-up of bubbling fluidized bed reactors - A review.* Powder Technology, 2012. **217**: p. 21-38
4. Glicksman, L.R., *Scaling relationships for fluidized beds.* Chemical Engineering Science, 1984. **39**(9): p. 1373-1379
5. Anderson, T.B. and R. Jackson, *A Fluid Mechanical Description of Fluidized Beds.* Industrial & Engineering Chemistry Fundamentals, 1967. **6**(4): p. 527-539
6. Ergun, S., *Fluid flow through packed columns.* Chemical Engineering Progress, 1952. **48**: p. 89-94
7. Goldschmidt, M.J.V., J.A.M. Kuipers, and W.P.M. Van Swaaij, *Hydrodynamic modelling of dense gas-fluidised beds using the kinetic theory of granular flow: Effect of coefficient of restitution on bed dynamics.* Chemical Engineering Science, 2001. **56**: p. 571-578
8. Glicksman, L.R., M. Hyre, and K. Woloshun, *Simplified scaling relationships for fluidized beds.* Powder Technology, 1993. **77**(2): p. 177-199
9. Ladd, A.J., *Numerical Simulations of Particulate Suspensions Via a Discretized Boltzmann Equation. Part 1. Theoretical Foundation.* Journal of Fluid Mechanics, 1994. **271**: p. 285-309
10. Tsuji, Y., T. Kawaguchi, and T. Tanaka, *Discrete particle simulation of two-dimensional fluidized bed.* Powder Technology, 1993. **77**(1): p. 79-87
11. Gidaspow, D. and B. Ettehadieh, *Fluidization in Two-Dimensional Beds with a Jet. 2. Hydrodynamic Modeling.* Industrial and Engineering Chemistry Fundamentals, 1983. **22**(2): p. 193-201
12. Gidaspow, D., *Hydrodynamics of fiuidizatlon and heat transfer: Supercomputer modeling.* Applied Mechanics Reviews, 1986. **39**(1): p. 1-23
13. Ding, J. and D. Gidaspow, *A Bubbling Fluidization Model Using Kinetic Theory of Granular Flow.* AIChE Journal, 1990. **36**(4): p. 523-538
14. Gidaspow, D., *Multiphase Flow and Fluidization: Continuum and Kinetic Theory Descriptions*. 1994: Elsevier Science.
15. Chapman, S. and T.G. Cowling, *The Mathematical Theory of Non-uniform Gases: An Account of the Kinetic Theory of Viscosity, Thermal Conduction and Diffusion in Gases*. 1970: Cambridge University Press.
16. Nieuwland, J.J., et al., *Hydrodynamic Modeling of Gas/Particle Flows in Riser Reactors.* AIChE Journal, 1996. **42**(6): p. 1569-1582
17. Lun, C.K.K., et al., *Kinetic theories for granular flow: inelastic particles in Couette flow and slightly inelastic particles in a general flowfield.* Journal of Fluid Mechanics, 1984. **140**: p. 223-223
18. Passalacqua, A., et al., *A fully coupled quadrature-based moment method for dilute to moderately dilute fluid-particle flows.* Chemical Engineering Science, 2010. **65**(7): p. 2267-2283
19. Carnahan, N.F. and K.E. Starling, *Equation of state for nonattracting rigid spheres.* The Journal of Chemical Physics, 1969. **51**(2): p. 635-636
20. Ogawa, S., A. Umemura, and N. Oshima, *On the equations of fully fluidized granular materials.* Zeitschrift für angewandte Mathematik und Physik ZAMP, 1980. **31**(4): p. 483-493
21. Ma, D. and G. Ahmadi, *An equation of state for dense rigid sphere gases.* The Journal of Chemical Physics, 1986. **84**(6): p. 3449-3450

22. Goldschmidt, M.J.V., R. Beetstra, and J.A.M. Kuipers, *Hydrodynamic modelling of dense gas-fluidised beds: Comparison of the kinetic theory of granular flow with 3D hard-sphere discrete particle simulations.* Chemical Engineering Science, 2002. **57**(11): p. 2059-2075
23. Saitoh, K. and H. Hayakawa, *Rheology of a granular gas under a plane shear.* Physical Review E - Statistical, Nonlinear, and Soft Matter Physics, 2007. **75**(2)
24. Mitarai, N. and H. Nakanishi, *Velocity correlations in dense granular shear flows: Effects on energy dissipation and normal stress.* Physical Review E - Statistical, Nonlinear, and Soft Matter Physics, 2007. **75**(3)
25. Jenkins, J.T., *Dense shearing flows of inelastic disks.* Physics of Fluids, 2006. **18**(10)
26. Vescovi, D., et al., *Plane shear flows of frictionless spheres: Kinetic theory and 3D soft-sphere discrete element method simulations.* Physics of Fluids, 2014. **26**(5)
27. Jenkins, J.T. and M.W. Richman, *Kinetic theory for plane flows of a dense gas of identical, rough, inelastic, circular disks.* Physics of Fluids, 1985. **28**(12): p. 3485-3494
28. Lun, C.K.K., *Kinetic theory for granular flow of dense, slightly inelastic, slightly rough spheres.* Journal of Fluid Mechanics, 1991. **233**(539): p. 539-559
29. Jenkins, J.T. and C. Zhang, *Kinetic theory for identical, frictional, nearly elastic spheres.* Physics of Fluids, 2002. **14**(3): p. 1228-1235
30. Khain, E., *Hydrodynamics of fluid-solid coexistence in dense shear granular flow.* Physical Review E - Statistical, Nonlinear, and Soft Matter Physics, 2007. **75**(5)
31. Luding, S., *Global equation of state of two-dimensional hard sphere systems.* Physical Review E - Statistical, Nonlinear, and Soft Matter Physics, 2001. **63**(4 I): p. 422011-422014
32. Otsuki, M., H. Hayakawa, and S. Luding, *Behavior of pressure and viscosity at high densities for two-dimensional hard and soft granular materials.* Progress of Theoretical Physics Supplement, 2010(184): p. 110-133
33. Johnson, P.C. and R. Jackson, *Frictional-collisional constitutive relations for granular materials, with application to plane shearing.* Journal of Fluid Mechanics, 1987. **176**: p. 67-93
34. Schaeffer, D.G., *Instability in the evolution equations describing incompressible granular flow.* Journal of Differential Equations, 1987. **66**(1): p. 19-50
35. Srivastava, A. and S. Sundaresan, *Analysis of a frictional–kinetic model for gas–particle flow.* Powder Technology, 2003. **129**(1–3): p. 72-85
36. Passalacqua, A. and L. Marmo, *A critical comparison of frictional stress models applied to the simulation of bubbling fluidized beds.* Chemical Engineering Science, 2009. **64**(12): p. 2795-2806
37. Farzaneh, M., et al., *The crucial role of frictional stress models for simulation of bubbling fluidized beds.* Powder Technology, 2015. **270**(PA): p. 68-82
38. Schneiderbauer, S., A. Aigner, and S. Pirker, *A comprehensive frictional-kinetic model for gas-particle flows: Analysis of fluidized and moving bed regimes.* Chemical Engineering Science, 2012. **80**: p. 279-292
39. Chialvo, S. and S. Sundaresan, *A modified kinetic theory for frictional granular flows in dense and dilute regimes.* Physics of Fluids, 2013. **25**(7)
40. Jop, P., Y. Forterre, and O. Pouliquen, *A constitutive law for dense granular flows.* Nature, 2006. **441**(7094): p. 727-730
41. GDR MiDi, *On dense granular flows.* The European Physical Journal E, 2004. **14**(4): p. 341-365
42. Fall, A., et al., *Dry granular flows: Rheological measurements of the μ (I) -rheology.* Journal of Rheology, 2015. **59**(4): p. 1065-1080

43. Jop, P., Y. Forterre, and O. Pouliquen, *Crucial role of sidewalls in granular surface flows: Consequences for the rheology.* Journal of Fluid Mechanics, 2005. **541**: p. 167-192
44. Da Cruz, F., et al., *Rheophysics of dense granular materials: Discrete simulation of plane shear flows.* Physical Review E - Statistical, Nonlinear, and Soft Matter Physics, 2005. **72**(2)
45. Chauchat, J. and M. Médale, *A three-dimensional numerical model for dense granular flows based on the μ(I) rheology.* Journal of Computational Physics, 2014. **256**: p. 696-712
46. Bagnold, R.A., *Experiments on a gravity-free dispersion of large solid spheres in a Newtonian fluid under shear.* Proceedings of the Royal Society of London. Series A. Mathematical and Physical Sciences, 1954. **225**(1160): p. 49
47. Lagrée, P.Y., L. Staron, and S. Popinet, *The granular column collapse as a continuum: Validity of a two-dimensional Navier-Stokes model with a Î(I)-rheology.* Journal of Fluid Mechanics, 2011. **686**: p. 378-408
48. Barker, T., et al., *Well-posed and ill-posed behaviour of the μ-rheology for granular flow.* Journal of Fluid Mechanics, 2015. **779**: p. 794-818
49. Pouliquen, O., *Scaling laws in granular flows down rough inclined planes.* Physics of Fluids, 1999. **11**(2-3): p. 542-548
50. Bouzid, M., et al., *Non-local rheology in dense granular flows: Revisiting the concept of fluidity.* European Physical Journal E, 2015. **38**(11): p. 1-15
51. Kamrin, K. and G. Koval, *Nonlocal constitutive relation for steady granular flow.* Physical Review Letters, 2012. **108**(17)
52. Bocquet, L., A. Colin, and A. Ajdari, *Kinetic theory of plastic flow in soft glassy materials.* Physical Review Letters, 2009. **103**(3)
53. Bouzid, M., et al., *Nonlocal rheology of granular flows across yield conditions.* Physical Review Letters, 2013. **111**(23)
54. Zhang, Q. and K. Kamrin, *Microscopic Description of the Granular Fluidity Field in Nonlocal Flow Modeling.* Physical Review Letters, 2017. **118**(5)
55. Artoni, R. and P. Richard, *Effective Wall Friction in Wall-Bounded 3D Dense Granular Flows.* Physical Review Letters, 2015. **115**(15)
56. Weinhart, T., et al., *Closure relations for shallow granular flows from particle simulations.* Granular Matter, 2012. **14**(4): p. 531-552
57. Bharathraj, S. and V. Kumaran, *Effect of base topography on dynamics and transition in a dense granular flow.* Journal of Fluid Mechanics, 2017. **832**: p. 600-640
58. Deen, N.G., et al., *Review of discrete particle modeling of fluidized beds.* Chemical Engineering Science, 2007. **62**: p. 28-44
59. McNamara, S. and W.R. Young, *Inelastic collapse and clumping in a one-dimensional granular medium.* Physics of Fluids A, 1992. **4**(3): p. 496-504
60. Cundall, P.A. and O.D.L. Strack, *A discrete numerical model for granular assemblies.* Géotechnique, 1979. **29**(1): p. 47-65
61. Cundall, P.A., *Formulation of a three-dimensional distinct element model—Part I. A scheme to detect and represent contacts in a system composed of many polyhedral blocks.* International Journal of Rock Mechanics and Mining Sciences & Geomechanics Abstracts, 1988. **25**(3): p. 107-116
62. Iwai, T., C.W. Hong, and P. Greil, *Fast particle pair detection algorithms for particle simulations.* International Journal of Modern Physics C, 1999. **10**(5): p. 823-837
63. Ogarko, V. and S. Luding, *A fast multilevel algorithm for contact detection of arbitrarily polydisperse objects.* Computer Physics Communications, 2012. **183**(4): p. 931-936

64. Butcher, J.C., *Numerical Methods for Ordinary Differential Equations*. Numerical Methods for Ordinary Differential Equations. 2016. 1-513.
65. Verlet, L., *Computer "experiments" on classical fluids. I. Thermodynamical properties of Lennard-Jones molecules.* Physical review, 1967. **159**(1): p. 98-103
66. Swope, W.C., et al., *A computer simulation method for the calculation of equilibrium constants for the formation of physical clusters of molecules: Application to small water clusters.* The Journal of Chemical Physics, 1982. **76**(1): p. 637-649
67. Garg, R., et al., *Documentation of open-source MFIX-DEM software for gas-solids flows*. 2012.
68. Li, Y., Y. Xu, and C. Thornton, *A comparison of discrete element simulations and experiments for 'sandpiles' composed of spherical particles.* Powder Technology, 2005. **160**(3): p. 219-228
69. Rackl, M. and K.J. Hanley, *A methodical calibration procedure for discrete element models.* Powder Technology, 2017. **307**: p. 73-83
70. Kaneko, Y., T. Shiojima, and M. Horio, *DEM simulation of fluidized beds for gas-phase olefin polymerization.* Chemical Engineering Science, 1999. **54**(24): p. 5809-5821
71. Wen, C.Y. and Y.H. Yu, *A generalized method for predicting the minimum fluidization velocity.* AIChE Journal, 1966. **12**(3): p. 610-612
72. Di Felice, R., *The voidage function for fluid-particle interaction systems.* International Journal of Multiphase Flow, 1994. **20**(1): p. 153-159
73. Hill, R.J., D.L. Koch, and A.J.C. Ladd, *Moderate-Reynolds-number flows in ordered and random arrays of spheres.* Journal of Fluid Mechanics, 2001. **448**: p. 243-278
74. Beetstra, R., M.A. Van Der Hoef, and J.A.M. Kuipers, *Drag force of intermediate reynolds number flow past mono- And bidisperse arrays of spheres.* AIChE Journal, 2007. **53**(2): p. 489-501
75. Tang, Y., E.A.J.F. Peters, and J.A.M. Kuipers, *Direct numerical simulations of dynamic gas-solid suspensions.* AIChE Journal, 2016
76. Kriebitzsch, S.H.L., M.A. Van Der Hoef, and J.A.M. Kuipers, *Fully resolved simulation of a gas-fluidized bed: A critical test of DEM models.* Chemical Engineering Science, 2013. **91**: p. 1-4
77. Miller, A. and D. Gidaspow, *Dense, vertical gas-solid flow in a pipe.* AIChE Journal, 1992. **38**(11): p. 1801-1815
78. Gidaspow, D., C. Lin, and Y.C. Seo, *Fluidization in Two-Dimensional Beds with a Jet. 1. Experimental Porosity Distributions.* Industrial and Engineering Chemistry Fundamentals, 1983. **22**(2): p. 187-193
79. Bartholomew, R.N. and R.M. Casagrande, *Measuring Solids Concentration in Fluidized Systems by Gamma-Ray Absorption.* Industrial and Engineering Chemistry, 1957. **49**(3): p. 428-431
80. Azzi, M., et al., *Mapping solid concentration in a circulating fluid bed using gammametry.* Powder Technology, 1991. **67**(1): p. 27-36
81. Moucheront, P., et al., *MRI investigation of granular interface rheology using a new cylinder shear apparatus.* Magnetic Resonance Imaging, 2010. **28**(6): p. 910-918
82. Fasching, G.E. and N.S. Smith Jr, *A capacitive system for three-dimensional imaging of fluidized beds.* Review of Scientific Instruments, 1991. **62**(9): p. 2243-2251
83. Holland, D.J., et al., *Comparison of ECVT and MR Measurements of Voidage in a Gas-Fluidized Bed.* Industrial & Engineering Chemistry Research, 2009. **48**(1): p. 172-181

84. Bokkers, G.A., M. Van Sint Annaland, and J.A.M. Kuipers, *Mixing and segregation in a bidisperse gas-solid fluidised bed: A numerical and experimental study.* Powder Technology, 2004. **140**: p. 176-186
85. Leadbeater, T.W., D.J. Parker, and J. Gargiuli, *Positron imaging systems for studying particulate, granular and multiphase flows.* Particuology, 2012. **10**(2): p. 146-153
86. Wildman, R.D. and J.M. Huntley, *Experimental measurements and modelling of rapid granular flows.* Powder Technology, 2008. **182**(2): p. 182-191
87. Gerlach, W. and O. Stern, *Der experimentelle Nachweis der Richtungsquantelung im Magnetfeld.* Zeitschrift für Physik, 1922. **9**(1): p. 349-352
88. Rabi, I.I., et al., *A new method of measuring nuclear magnetic moment.* Physical review, 1938. **53**(4): p. 318
89. Bloch, F., *Nuclear induction.* Physical review, 1946. **70**(7-8): p. 460-474
90. Bloch, F., W.W. Hansen, and M. Packard, *The nuclear induction experiment.* Physical review, 1946. **70**(7-8): p. 474-485
91. Purcell, E.M., H.C. Torrey, and R.V. Pound, *Resonance absorption by nuclear magnetic moments in a solid [7]*. Physical review, 1946. **69**(1-2): p. 37-38
92. Hahn, E.L., *Spin echoes.* Physical review, 1950. **80**(4): p. 580-594
93. Carr, H.Y. and E.M. Purcell, *Effects of diffusion on free precession in nuclear magnetic resonance experiments.* Physical review, 1954. **94**(3): p. 630-638
94. Meiboom, S. and D. Gill, *Modified spin-echo method for measuring nuclear relaxation times.* Review of Scientific Instruments, 1958. **29**(8): p. 688-691
95. Lauterbur, P.C., *Image formation by induced local interactions: Examples employing nuclear magnetic resonance.* Nature, 1973. **242**(5394): p. 190-191
96. Mansfield, P. and P.K. Grannell, *Nmr 'diffraction' in solids?* Journal of Physics C: Solid State Physics, 1973. **6**(22): p. L422-L426
97. Fukushima, E., *Nuclear magnetic resonance as a tool to study flow.* Annual Review of Fluid Mechanics, 1999. **31**: p. 95-123
98. Majors, P.D., R.C. Givler, and E. Fukushima, *Velocity and concentration measurements in multiphase flows by NMR.* Journal of Magnetic Resonance, 1989. **85**(2): p. 235-243
99. Axel, L. and L. Dougherty, *MR imaging of motion with spatial modulation of magnetization.* Radiology, 1989. **171**(3): p. 841-845
100. Stejskal, E.O. and J.E. Tanner, *Spin diffusion measurements: Spin echoes in the presence of a time-dependent field gradient.* The Journal of Chemical Physics, 1965. **42**(1): p. 288-292
101. Caprihan, A. and J.D. Seymour, *Correlation Time and Diffusion Coefficient Imaging: Application to a Granular Flow System.* Journal of Magnetic Resonance, 2000. **144**(1): p. 96-107
102. Holland, D.J., et al., *Spatially resolved measurement of anisotropic granular temperature in gas-fluidized beds.* Powder Technology, 2008. **182**(2): p. 171-181
103. Mueth, D.M., et al., *Signatures of granular microstructure in dense shear flows.* Nature, 2000. **406**(6794): p. 385-389

3. Validation of CFD-DEM codes and the effective diameter drag model

In unresolved CFD-DEM simulations, particle trajectories depend strongly on the interphase momentum transfer between the fluid and granular phases. Momentum transfer in these simulations is controlled by the drag equation. State of the art drag models are currently derived from resolved CFD-DEM simulations of spherical particles, which is not an accurate representation of many real granular systems. Furthermore, momentum transfer is also influenced by features of the numerical simulation such as the grid resolution, and the interval at which the momentum transfer term is updated. In this chapter, CFD-DEM simulations of a cylindrical fluidised bed were performed using two open-source multiphase flow solvers. The effect of the grid resolution, fluid phase time step size, and the coupling interval between the phases were investigated. The effective diameter approach was used to estimate suitable particle diameters to account for nonsphericity when calculating voidage and drag. This approach improved the agreement with MRI experiments in the lower half of the bed, but only offered marginal improvements in the upper half of the bed. These results demonstrated that the effective diameters method is an efficient approach to approximate the effects of nonsphericity.

3.1. Introduction

For CFD-DEM simulations to become useful for deriving closure relations for two-fluid models of fluidised beds, it is necessary to validate CFD-DEM simulations against laboratory scale experimental data. There are technical challenges involved with designing CFD-DEM simulations to offer suitable agreement with experiments. These concern the meshing of the fluid domain and coupling the fluid and particle phases appropriately.

Discretising the domain is challenging for unresolved CFD-DEM simulations due to the assumed separation of scales used to derive the volume-averaged conservation equations of the fluid phase [1]. Local averaging of the point variable conservation equations assumes that the fluctuations in the values of point variables are not large at the fluid cell length scale. This assumption is not met when the fluid cells are below the scale of the particle or orders of magnitude greater than the particle diameter. Grid sizing below 1.6 times the particle

diameter has been shown to produce unphysical solutions due to the breakdown of the volume averaging assumption [2]. Furthermore, if cells are too small, the void fraction may not be accurately estimated. Conversely, fluid cells that exceed several diameters cannot capture flow features at subscales, which require filtered forms of the conservation equations to account for unresolved features [3-5]. In general, it is advised that cells are sized to between 3-4 particle diameters [2, 6-8]. A consequence of these grid sizing restrictions is that inflation layers, where boundary layers are resolved while bulk flow is less resolved are unsuitable for CFD-DEM simulations.

The nature of the flow domain introduces the additional consideration of the coordinate system. Here, the system of interest is a three-dimensional cylindrical fluidised bed. Cylindrical coordinates are a useful basis for discretising this system. However, cylindrical grids are limited by the requirement of a boundary along the centreline of the bed. The gas velocity was found to decrease near the centre if the boundary is not handled appropriately [9], although the void fraction is insensitive to the boundary used [10]. There are also a wide range of cell volumes within the grid; cells near the centre are small, while cells along the circumference are large. Alternatively, Cartesian grids with the cut-cell method can generate meshes for domains with sloped or curving boundaries [11]. Fluid cells are modified to have boundaries which are curved or sloped to closely follow the form of the target geometry [12]. This method also has problematic small cells; however these are located at the outer boundary of the domain where they have less effect on the main flow. A hybrid approach was developed by Boyce et al. [13] where the mesh consisted of equal volume cylindrical wedges. This method is particularly challenging to implement as fluxes must be divided between adjacent cells. Alternatively, unstructured grids consisting of tetrahedrons, hexahedra and wedges have also been incorporated into the CFD-DEM framework [14] and allow for uniform grid sizing, although unstructured grids are not a common feature in open-source CFD-DEM solvers.

Open-source CFD solvers are an attractive alternative as the public availability of the source code enables users to understand the underlying physics of the solution algorithm. Furthermore, modifications can be made to the source code to simulate specialised systems. Several codes are available to simulated fluid-particle flow. This chapter focuses on two: MFIX and CFDEM. MFIX is an open-source multiphase flow solver produced by the National Energy Technology Laboratory, US Department of Energy [15]. It has been used by researchers to model multiphase flow phenomena occurring in processes involving granular

materials. The MFIX software includes three kinds of models to describe the particle phase. These are the CFD-DEM, TFM, and multiphase particle-in-cell. Only the MFIX CFD-DEM component of the MFIX package was used during this investigation. The MFIX CFD-DEM software was validated by Li et al. [16]. The test cases studied were: (1) The narrow three-dimensional bubbling fluidised bed of Müller et al. [17] and (2) the rectangular spout-fluidised bed of Link et al. [18]. The test case for (1) has also been validated in serial and distributed-memory-parallel modes [19]. The CFDEM® Project develops the open-source DEM simulation software known as LIGGGHTS [20]. To simulate gas-solid flows, LIGGGHTS source code is combined with the open-source CFD solver OpenFOAM [21], and code that calculates gas-particle interaction terms, such as the void fraction and the drag. This software package is known as CFDEM-Coupling [22]. CFDEM has been validated by Kloss et al. [20]. The test cases were: (1) a packed bed, where conductive and convective heat transfer were studied and (2) the pseudo-2D rectangular spout-fluidised bed of Link et al. [23].

CFD-DEM simulations often approximate particles as spheres for the purposes of simplicity and reducing computational expense. However, many physical systems do not consist of spherical particles, which limits the suitability of CFD-DEM of spheres for continuum model development unless nonspherical behaviour can be reliably approximated. The calculation of the drag force on spherical particles was introduced in Section 2.3. DEM simulations involving nonspherical particles are more challenging since more complex contact detection algorithms are required. Contact detection between nonspherical particles has been achieved using polyhedra [24], multispheres [25], the Gilbert-Johnson-Keerthi algorithm [26], and superquadrics [27-29]. Additional considerations need to be made to calculate the drag force acting on nonspherical particles. For spheres, symmetry means that the frontal area is the cross-sectional area of a sphere and is independent of orientation. For nonspherical particles, the frontal area is a function of the orientation of the particle relative to the flow and requires more intricate calculation. Hilton et al. [28] used Gram-Schmidt orthogonalisation to numerically calculate the projected area for superquadric particles. While drag induces rotational motion in real systems, it can be neglected in simulations since the gas flow is generally parallel to the particle motion [28]. The effect of the particle shape is captured by the drag coefficient. Drag coefficient models for nonspherical particles have been developed from experiments [30] and fully resolved LB simulations [31-33]. Non-spherical particles may increase the run time of the simulation by up to a factor of 6 [26]. Given this additional

complication of modelling nonspherical behaviour, it is advantageous if the drag and packing effects can be approximated while running CFD-DEM simulations of spherical particles. One such method is effective diameter method described by Boyce et al. [34]. In brief, different particle diameters are used to calculate the void fraction and drag forces to mimic the packing and drag acting on nonspherical particles.

In this chapter, MFIX and CFDEM were validated against MRI velocimetry experiments using a 3D laboratory scale bubbling fluidised bed. While both programmes have been validated previously, the reference systems were different to the system of interest for this project. The importance of the meshing of the fluid grid was tested by simulating the cylindrical domain with cut-cell and Cartesian-cylindrical hybrid meshes. The interphase coupling was verified by varying the frequency of the particle drag force calculations. Finally, suitable effective diameters for the studied system were identified using CFD-DEM simulations and fluidisation theory. These effective diameters were applied to the cylindrical fluidised bed system to assess the efficacy of this method for modelling nonspherical particles.

3.2. Method

3.2.1 Mesh design

The OpenFOAM functionality within CFDEM is capable of generating grids with general hexahedral elements, allowing for the possibility of generating grids that have cells that are more uniform in volume than either the Cartesian cut-cell method, or cylindrical coordinates. Figure 3.1(a) shows a hybrid grid that uses distorted hexahedral cells around the outer edge of the bed to avoid the small cells created by the cut-cell method and Cartesian cells in the centre to avoid the small cells inherent to cylindrical coordinate grids. The Cartesian cut-cell method is the only practical option for simulating cylinders with the MFIX DEM since cylindrical coordinates are not yet fully implemented for CFD-DEM simulations. For a fair comparison between the two solvers, the grids used in each simulation needed to be similar. Hence an approximation to the cut-cell grid was developed for CFDEM shown by Figure 3.1(b). The MFIX Cartesian cut-cell grid is shown in Figure 3.1(c).

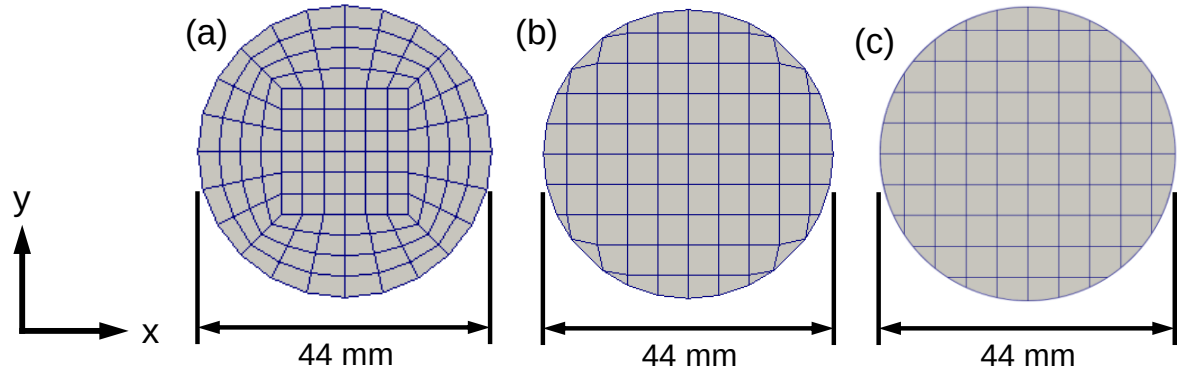

Figure 3.1. Horizontal cross-sections of fluid meshes used to compare MFIX and CFDEM. (a) Imitation of the MFIX cut-cell for CFDEM. (b) Hybrid grid for CFDEM. (c) MFIX cut-cell.

The diameter of the bed was 44 mm, while the inlet gas distributor was 40 mm in diameter. There was a 2 mm wide annulus around the circumference of the base where there was no gas flow. The mass flow inlet boundary condition replicated the flow of gas in the inner 40 mm of the base. The mean gas velocity at the inlet required to achieve a superficial velocity of 0.6 m s^{-1} was 0.73 m s^{-1}. Since some cells contained part of the inlet and the outer rim, the gas velocity in each cell was calculated by multiplying the mean inlet velocity by the area fraction of the cell that was within the inner 40 mm of the inlet face.

3.2.2 Effective diameters to approximate nonsphericity

Given the technical challenges and performance costs associated with direct modelling of nonspherical particles, it is advantageous to approximate nonspherical behaviour while simulating with spheres as described by Boyce et al. [34]. This approximation involves adjusting the particle diameter to alter the void fraction and drag calculations. The diameter used to calculate the particle volume is adjusted such that the volume fraction matches that measured for nonspherical particles. For example, the void fraction at minimum fluidisation is adjusted by changing the diameter (denoted as $d_{p,v}$ for clarity) to match $\varepsilon_{g,mf,exp}$ observed in experiments. The diameter used to calculate the void fraction is determined by:

$$d_{p,v} = d_p \left(\frac{\varepsilon_{g,mf,sim}}{\varepsilon_{g,mf,exp}} \right)^{\frac{1}{3}} \tag{3.1}$$

where $\varepsilon_{g,mf,sim}$ is the void fraction at minimum fluidisation observed in simulations of spherical particles. It is expected that for spheres this void fraction is close to the random close packing fraction of 0.37.

The diameter used in the drag force (denoted by $d_{p,d}$) is adjusted to account for the effects of frontal area and shape on the drag coefficient. The drag force acting on a particle is given by:

$$\boldsymbol{f}_d = \beta_d V_p(\boldsymbol{v}_g - \boldsymbol{v}_p) \tag{3.2}$$

where β_d is the drag coefficient, V_p is the particle volume, $\boldsymbol{v}_g$ is the local gas velocity, and $\boldsymbol{v}_p$ is the particle velocity. At minimum fluidisation, the gas velocity is $U_{mf}/\varepsilon_{g,mf}$ and the particle velocity is zero. For the Beetstra model, the drag coefficient takes the sum of the limit in Stokes flow and an inertial term:

$$\beta_d = F_{st}(F_0(\varepsilon_s) + \alpha \mathrm{Re}_{mf}) \tag{3.3}$$

where the Reynolds number at minimum fluidisation is defined by:

$$\mathrm{Re}_{mf} = \frac{\rho_g U_{mf} d_{p,d}}{\eta_g} \tag{3.4}$$

The dimensionless drag at the Stokes limit, $F_0(\varepsilon_s)$ is described by:

$$F_0(\varepsilon_s) = \frac{10\varepsilon_s}{\varepsilon_g^2} + \varepsilon_g^2(1 + 1.5\sqrt{\varepsilon_s}) \tag{3.5}$$

The coefficient α was derived empirically from the LB simulations from [35], and is equal to:

$$\alpha = \frac{0.413}{24\varepsilon_g^2}\left[\frac{1/\varepsilon_g + 3\varepsilon_s\varepsilon_g + 8.4\mathrm{Re}^{-0.343}}{1 + 10^{3\varepsilon_s}\mathrm{Re}^{-(1+4\varepsilon_s)/2}}\right] \tag{3.6}$$

The drag coefficient is multiplied by F_{st}, the drag force for Stokes flow, which is defined by:

$$F_{st} = \frac{18\eta_g\varepsilon_g}{d_{p,d}^2} \tag{3.7}$$

To approximate the packing of nonspherical particles, the void fraction, ε_g is estimated using the void fraction diameter calculated from Equation 3.1. In this chapter, the drag diameter is only applied to Equation 3.3 and its dependents. The particle volume term in Equation 3.2 is calculated using the true particle diameter. The value of $d_{p,d}$ was found by running CFD-DEM simulations for a fixed value of $d_{p,v}$ at $U_{mf,exp}$ and a series of different $d_{p,d}$. In this study the effective diameter method was only simulated in MFIX due to the simplicity of modifying the source code with time dependent drag diameters. For the system studied here, $U_{mf,exp} = 0.3$ m s^{-1}. The appropriate value of $d_{p,d}$ was found from the fluctuations in the pressure drop. Pressure drop fluctuations indicate the presence of bubbles that form when the drag force exerted on the particles exceeds the weight force of the bed. Thus, in simulations with decreasing gas velocity, the appropriate value of $d_{p,d}$ was found when the pressure

fluctuations stopped. Thus, a combination of ($d_{p,d}$, $d_{p,v}$) was found that yielded ($\varepsilon_{mf,exp}$, $U_{mf,exp}$) when simulated in CFD-DEM.

An alternative theoretical approach to estimate the effective drag diameter utilises the balance between particle drag and weight forces at minimum fluidisation. The pressure drop, Δp across the bed in terms of the drag force is described by:

$$\Delta p = \frac{\varepsilon_{s,mf,exp} \boldsymbol{f}_d L}{\varepsilon_{g,mf,exp} V_p} \tag{3.8}$$

Where L is the height of the bed and $\boldsymbol{f}_d = \beta V_p U_{mf} / \varepsilon_{g,mf,exp}$. At minimum fluidisation, the pressure drop due to particle drag is balanced by the weight of the particles in the bed, thus the pressure drop is equal to:

$$\Delta p = \frac{2 N_p \rho_s d_p^3 \boldsymbol{a_g}}{3 D_b^2} \tag{3.9}$$

where the true particle diameter is used in this equation. The number of particles is denoted by N_p, the bed diameter by D_b and gravitational acceleration by $\boldsymbol{a_g}$. For known values of U_{mf}, ρ_g, η_g, and a specified void fraction diameter, the corresponding drag diameter is found by equating the pressure drop from Equation 3.8 to Equation 3.9.

3.2.3 Additional simulation details

In order to match the experiment, 42,670 particles with a diameter of 1.07 mm each were simulated, giving a settled bed height of 30 mm. The initial particle positions used in both MIFX and CFDEM simulations were generated by LIGGGHTS; particles were poured in and left to settle for 500,000 time steps (0.5 s) in the absence of gas flow. The results were not sensitive to the initial packing arrangement.

With regard to the fluid phase, the spatial discretisation schemes used in each of the simulations were second-order accurate. The superbee scheme was used in MFIX . Since the superbee scheme is not available in CFDEM, a Gaussian integration discretisation scheme with a linear interpolation scheme was used. The first-order Euler temporal discretisation scheme was used in both simulations. For the DEM, the second-order Adams-Bashforth time integration scheme was used for MFIX, while the velocity Verlet scheme [36] was used by CFDEM.

Both codes included a particle-centred void fraction scheme; however the particle-centred method is not effective for describing the dynamic behaviour of this bed due to the level of

grid refinement [2]. Instead, divided particle volume methods were used. As will be described in Chapter 4, the MFIX DPVM weighted the contribution of each particle towards the voidage within a cell by the distance between the particle and the cell boundary. For the CFDEM simulation, the satellite point method was used [37]. Given that more computation time was required for the satellite point code developed for MFIX compared to the MFIX DPVM, the MFIX DPVM was selected for this study. It will be shown in Chapter 4 that both schemes predicted similar instantaneous void fraction fields and did not have a significant effect on the averaged particle velocity field for the tested system. Therefore, it was assumed that the void fraction scheme did not influence the results collected during this comparison.

The linear spring-dashpot contact force scheme was used in both programmes. The specified contact parameters are given in Table 3.1. Equivalent contact parameters were used by each simulation.

Table 3.1. Linear spring-dashpot contact parameters as implemented for MFIX and CFDEM.

MFIX Contact Parameters		CFDEM Contact Parameters	
Normal particle spring constant (N m^{-1})	1000	Normal particle spring constant (N m^{-1})	1000
Coefficient of normal restitution (-)	0.93	Tangential particle spring constant (N m^{-1})	285.7
tangential/normal damping coefficients (-)	0.5	Normal viscous damping coefficient (kg s^{-1})	9.32×10^{-4}
Coefficient of friction (-)	0.1	Tangential viscous damping coefficient (kg s^{-1})	4.66×10^{-4}
		Coefficient of friction (-)	0.1

The time step should normally be equal to about 20% of the Rayleigh time [38]. For this set of contact parameters, the Rayleigh time was 8.75×10^{-6} s and therefore, the DEM time step size was set to 1×10^{-6}s for the CFDEM software. The time step size for the fluid phase was set to 5×10^{-4}s. The MFIX DEM time step was 1.15×10^{-6}s, or $1/50^{th}$ of the minimum collision time [39]. In MFIX, the fluid time step size was adaptive. If the solution to the fluid phase conservation equations does not converge at a particular time step size, the time step value is reduced. The maximum time step size that was allowed was 5×10^{-4}s. For most of the simulations, this time step was sufficient to achieve convergence. MFIX simulations were performed on a cloud computer that consisted of a single Intel Xeon E5-2670 v2 CPU, with 3.75 GB of memory and a clock frequency of 2.5 GHz. The CFDEM simulations were run in parallel over four Intel x86 CPUs, each with 8 GB of memory and a clock frequency of 2.7 GHz. Since each code was run with different hardware, no analysis of the computation time was performed.

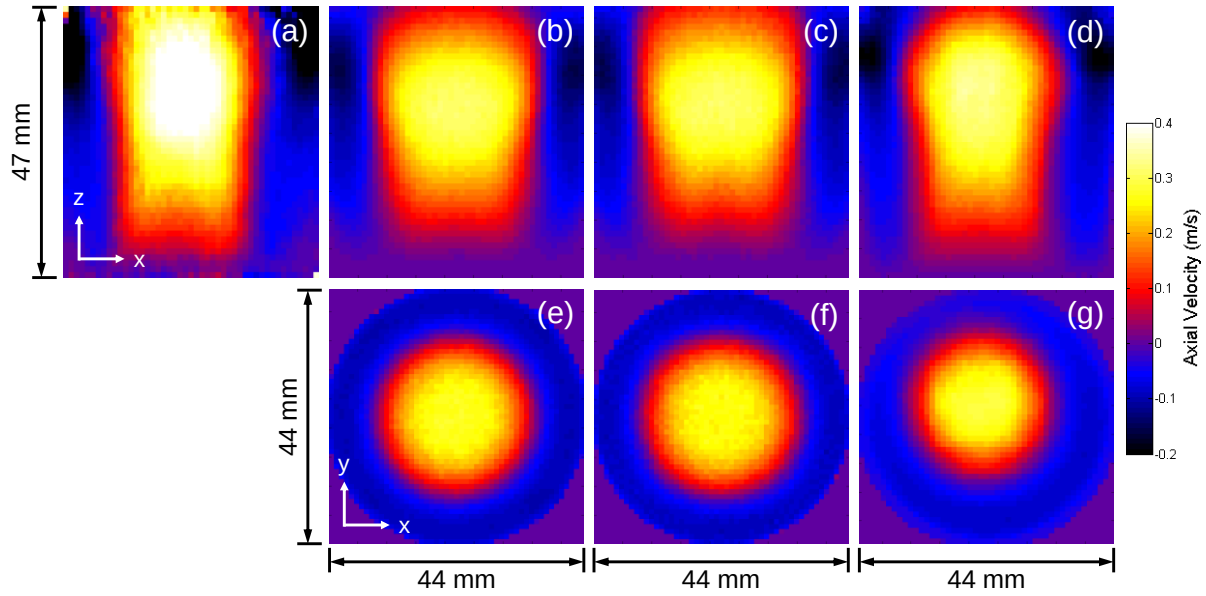

Figure 3.2. Particle-weighted time-averaged vertical velocity maps along the *x-z* plane for: (a) experiment, (b) CFDEM with cut-cell grid, (c) CFDEM with hybrid grid, (d) MFIX. The maps along the *x-y* plane are: (e) CFDEM with cut-cell grid, (f) CFDEM with hybrid grid, (g) MFIX.

3.3. Results and discussion

In this section, the simulation results from each solver using the fluid grids shown in Figure 3.1 are compared to data from the MRI experiment. The effect of decreasing the fluid phase time step and decreasing the calculation interval for the void fraction and drag forces of the MFIX simulation are compared to the original settings detailed in the previous section. Next, the effective drag diameter is estimated using CFD-DEM simulations, the results from this method are compared against the theoretical approach in Section 3.2.2. Finally, the effective diameters are applied to the cylindrical fluidised bed CFD-DEM simulation, compared against the experiment and discussed with consideration to the previous effective diameter study [34].

3.3.1 Investigating mesh effect

Figure 3.2 gives the particle-weighted time-averaged vertical velocity maps for each of the simulations with the uniform inlet boundary condition along a 5 mm thick slice in the centre of the bed along the *x-z* plane. All the simulations could replicate the correct particle circulation pattern seen in experiments shown by Figure 3.2(a) where particles ascended rapidly in the centre and moved downwards slowly near the circumference of the bed. While the qualitative agreement is good, the quantitative agreement is comparatively poor. The velocities predicted by the simulations along the centre of the bed are shown in Figure 3.3(a).

The profiles from both CFDEM simulations were in good agreement with each other, indicating that the mesh did not strongly influence the model predictions and that the small cells obtained by the cut-cell method were not important. Since the small cells were located around the outside perimeter where the gas velocity was low, the effect of errors on the overall bed dynamics would be minimal.

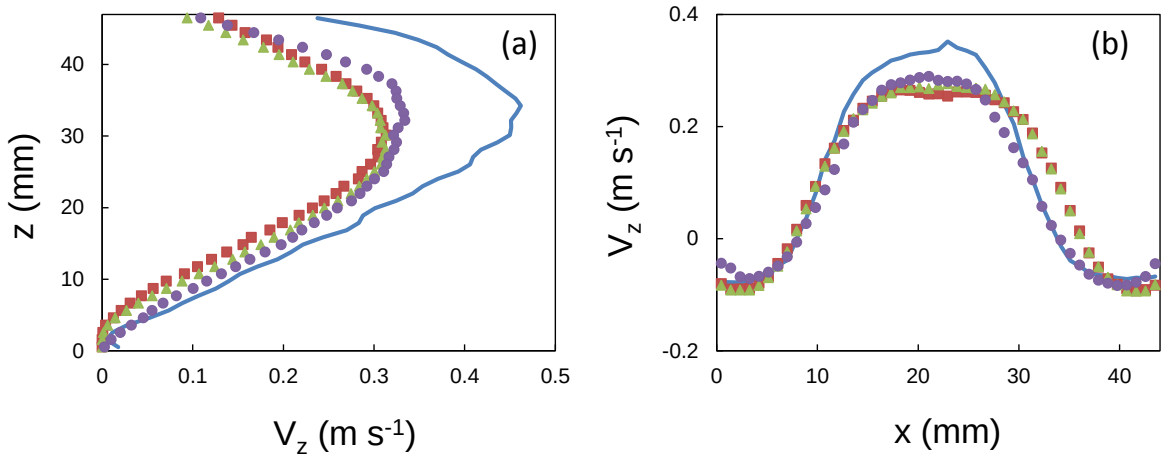

Figure 3.3. (a) Vertical profile of z velocity at $x = 22$ mm. (b). Horizontal profile of z velocity at $z = 22$ mm. MRI experiment: —, CFDEM with hybrid grid: ■, CFDEM with cut-cell grid: ▲, MFIX cut-cell grid: ●.

Unlike the CFDEM simulations, bubbles in the MFIX simulation were biased towards one side of the bed. Since the gas velocity inlet boundary condition was identical for all simulations, the lack of circular symmetry in the MFIX simulation may not be attributed to the inlet gas velocity boundary condition. Instead, this result suggested that the MFIX solution algorithm may have been responsible for the bias in the gas velocity away from the centre of the bed. It was not clear how the solution algorithm affected the gas velocity field. The MFIX validation study of Li et al. [16] tested a rectangular 3D spout-fluidised bed which found that the maximum particle phase velocity was located in the centre of the bed. Given that the simulations in this work are of a cylindrical fluidised bed, the cut-cell method may be the source of the observed asymmetry. However, by altering features such as the grid refinement and interphase coupling, it is possible to obtain circularly symmetric velocity maps with MFIX. There are two aspects of interphase coupling that may be adjusted: (1) the fluid phase time step, and (2) the interval at which the void fraction and the drag force are updated. Updating these variables between fluid time steps alters the drag forces that particles experience due to small changes in the void fraction and the interpolated value of the local fluid velocity, and changes in the particle velocity due to contacts. By default, the void fraction and drag forces are only updated at each fluid time step to reduce computational

expense. MFIX simulations of three modified cases were performed. (1) the grid refinement was increased to a resolution of 16 cells ×16 cells ×42 cells. (2) the fluid phase time step was reduced to 1×10^{-4} s. (3) the fluid phase time step was set at 1×10^{-3} s while the void fraction and drag force were updated at every DEM step (achieved by setting the "DES_EXPLICIT_COUPLING" variable to false in the MFIX input file). The velocity maps from these simulations are shown in Figure 3.4

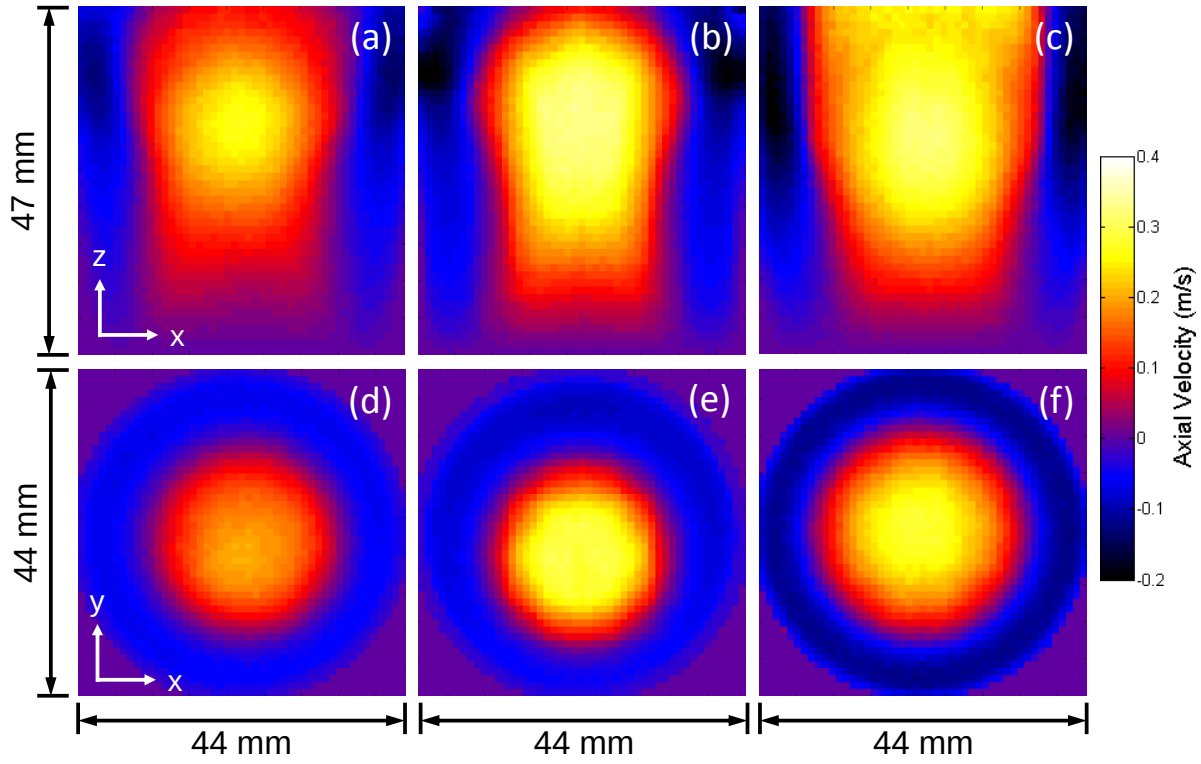

Figure 3.4. Particle-weighted time-averaged vertical velocity maps along the *x*-*z* plane for MFIX simulations: (a) grid resolution of 16 cells ×16 cells ×42 cells, (b) $\Delta t_f = 1\times10^{-4}$ s, (c) $\Delta t_f = 1\times10^{-3}$ s with the void fraction and drag forces updated at every DEM step. The maps along the *x*-*y* plane are: (d) $\Delta t_f = 5\times10^{-4}$ s, (e) $\Delta t_f = 1\times10^{-4}$ s, (f) $\Delta t_f = 1\times10^{-3}$ s with the void fraction and drag forces updated at every DEM step.

Considering the effect of grid refinement, the vertical velocity within the central bubbling region was reduced compared to the coarser grid in Figure 3.2, and bubble ascent was closer to the centre, although with a marginal offset. Reducing the fluid time step to 1×10^{-4} s had little noticeable effect, the maximum velocity was within 0.01 m s^{-1} of the 5×10^{-4} s case and the bubbling region remained offset. Updating the voidage and drag calculations at every DEM time step increased the expansion of the bed shown by the high velocity at the top of the image in Figure 3.4(c). The downward velocity of the particles in the dense phase of the bed was increased compared to the more weakly coupled simulations. The bubbling region was perfectly centred. The CFDEM simulations were able to produce central bubbling when

the drag was updated at every fluid time step. Hence both codes are capable of qualitatively replicating the experimental flow pattern. However, neither was capable of accurately predicting the velocity in the bubbling region. An attempt to improve quantitative accuracy by adjusting the gas-particle interaction term using the effective particle diameter method is covered in the following section.

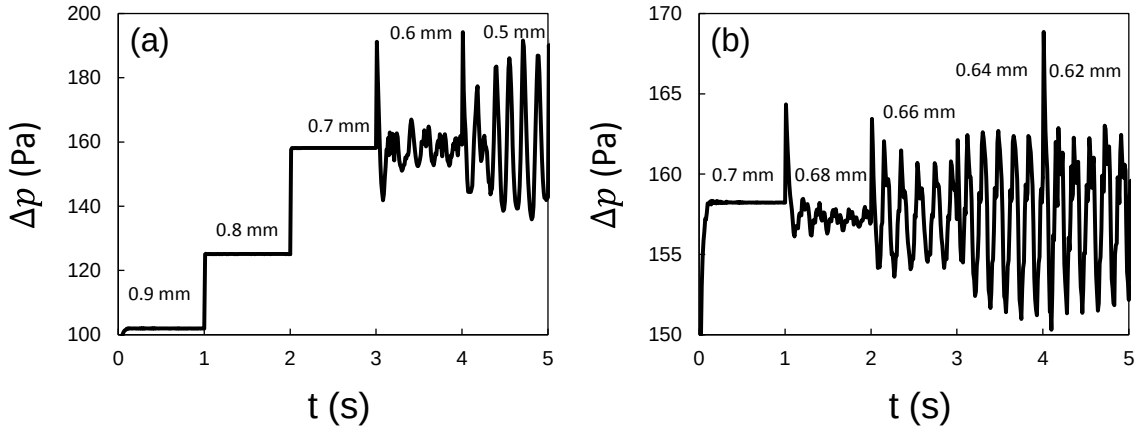

Figure 3.5. Pressure drop against time to estimate the effective drag diameter. The effective void fraction diameter was 1.00 mm, the contact diameter was 1.07 mm and the superficial gas velocity was equal to the experimental minimum fluidisation velocity of 0.3 m s^{-1}. The drag diameter is varied in increments of 0.1 mm in (a) and in 0.02 mm increments in (b).

3.3.2 Effective diameters

Compared to the experimental data, Figure 3.3 shows that the same drag diameter simulations underestimated the velocity of the particle phase in the central bubbling region. These results support previous work suggesting that the gas-solid interaction is not correctly estimated using standard drag models [5, 40, 41]. The Beetstra drag model was developed from flow around spheres and is not representative of the poppy seed particles used for the experiment. This system is a useful basis for evaluating the applicability of the effective diameter method. The void fraction at minimum fluidisation from experiments (0.51 in this case) defines the diameter used for the void fraction. Using Equation 3.1, where $\varepsilon_{mf,sim} = 0.37$ (representing random close packing for spheres), the void fraction diameter was found to be 1.00 mm. Figure 3.5(a) gives a time series of the pressure drop against time for five different values of $d_{p,d}$. When the effective drag diameter is 0.9 mm, the pressure drop was less than the weight of the particles, and hence $U_{mf,sim} > U_{mf,exp}$. For an effective drag diameter of 0.5 mm, the pressure drop fluctuated significantly about the mean pressure drop (which was equal to the weight of the bed). The pressure fluctuations were due to the formation of bubbles, thus $U_{mf,sim} < U_{mf,exp}$. For $d_{p,v} = 0.7$ mm, the pressure drop did not fluctuate and was equal to

the weight of the bed. Hence, the drag diameter for the system was 0.7 mm. This test was repeated over a smaller range of $d_{p,v}$ to attain a more accurate estimate, shown in Figure 3.5(b). The onset of pressure drop fluctuations at 0.68 mm indicates that 0.7 mm was a suitable choice for the drag diameter.

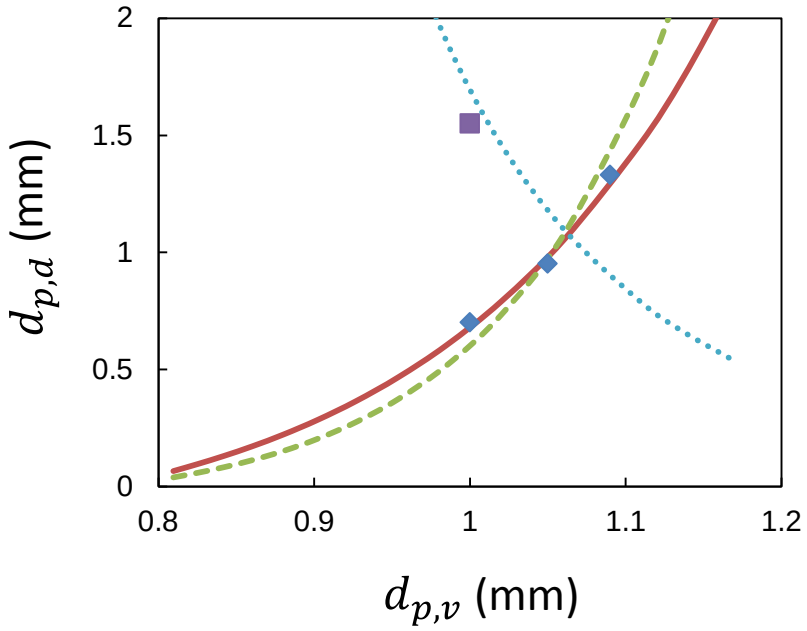

Figure 3.6. Effective drag diameter against effective void fraction diameter. Model estimate for humid air (U_{mf} = 0.3 m s^{-1}, ρ_g = 1.2 kg m^{-3}): — ; Model estimate for SF_6 (U_{mf} = 0.088 m s^{-1}, ρ_g = 52 kg m^{-3}): - - ; Model for SF_6 where $d_{p,d}$ is applied to Equation 3.2: · · · ; CFDEM results for humid air: ♦; data from [34]: ■.

The theoretical relationship between the void fraction and drag effective diameters is given in Figure 3.6. The results from drag diameter-varying CFD-DEM simulations at U_{mf} for three different void fraction diameters are overlaid. The agreement between the model and the simulations is excellent and demonstrates that simulation design can be enhanced by avoiding the need to run time-consuming exploratory CFD-DEM simulations. Applying the drag diameter found from Figure 3.5 to the cylindrical fluidised bed gives the vertical particle phase velocity data shown in Figure 3.7(a). For both solvers using the effective diameter method, the vertical velocity was in excellent agreement with the MRI experiment where $z < 20$ mm, indicating that this method is an effective analogue for describing the packing and drag for poppy seed particles. However, the effective diameter method simulations offered marginal to no increase in the maximum vertical velocity compared to the corresponding same diameter simulations. Therefore, the systematic underestimation of the

vertical particle velocity for $z > 20$ mm remained when incorporating the nonsphericity of the particles. It is possible that this discrepancy is due to the drag model not incorporating the effect of the motion of nearby granules [40, 41]. An offset in the bubbling region was apparent for the MFIX effective diameter simulation shown in Figure 3.7(b) and was not mitigated by updating the drag and void fraction at every DEM step.

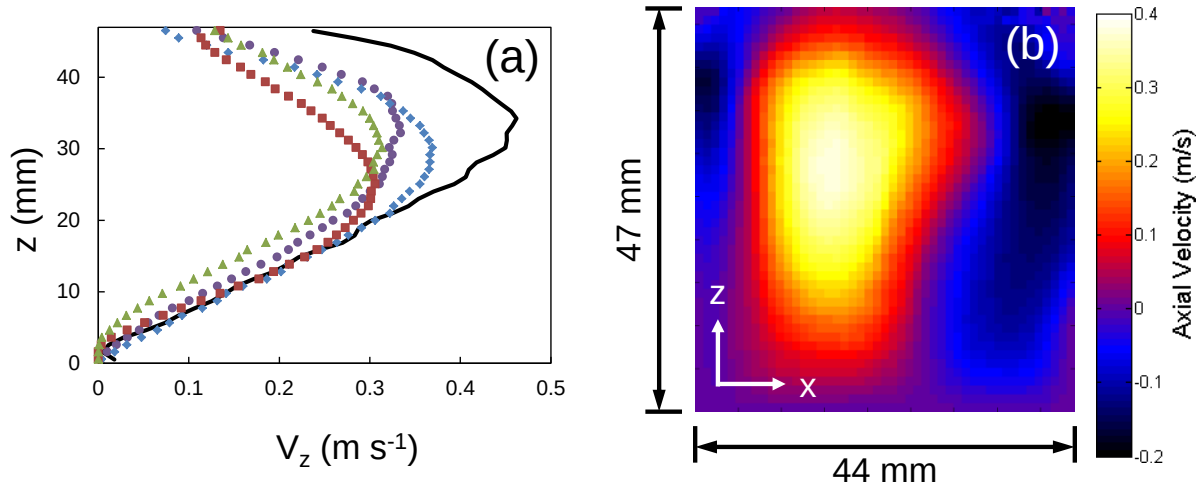

Figure 3.7. (a) Profile of z velocity for the particle phase at $x = 22$ mm. MRI experiment: —. MFIX with same diameters: ●. MFIX with effective diameters: ♦. CFDEM hybrid grid with same diameters: ▲. CFDEM hybrid grid with effective diameters: ■. (b) z velocity map along the x-z plane for MFIX with effective diameters.

It is interesting to note that the effective drag diameter of 0.7 mm obtained for the poppy seeds in this work differs from the value determined by Boyce et al. [34] of 1.55 mm. In that study, the drag diameter was found using CFD-DEM simulations of defluidisation experiments, where the inlet gas velocity was decreased over time. The drag diameter was selected from the simulation that best matched the physical experiment defluidisation curve. The maximum vertical particle velocity measured by MRI was twice that of the same diameter simulations, and three times that of the effective diameter simulations. In this regard, the effective diameter method did not offer an advantage over the same diameter method. It should be noted that the bed dimensions and fluidising gas (SF_6) used in their study were not the same as the system these simulations represent. A curve for the effective diameters including the physical properties of SF_6 is also shown in Figure 3.6. This curve does not collapse onto the curve for air, which indicates that different sets of effective diameters are required for different fluidising gases. However, accounting for the fluid properties does not address the disparity between the reported diameters and theory. A speculative explanation for this difference is that the application of the drag diameter in the

model equations was not consistent. For example, the particle volume in Equation 3.2 does not use the drag diameter, however it is possible that this volume was calculated with $d_{p,d}$ in [34]. A curve using the particle volume in terms of the drag diameter is in good agreement with the result of Boyce et al. [34]. It is noteworthy that the trend is inverted by this subtle alteration to the model. The exact form of the model likely affects the hydrodynamics of the bed above minimum fluidisation since the drag coefficient is a non-linear function of the Reynolds number.

3.4. Conclusions

A 3D cylindrical bubbling fluidised bed was simulated using the open-source CFD-DEM software programmes MFIX and CFDEM. Cut-cell meshes were implemented in both codes in addition to a cylindrical/Cartesian hybrid grid for CFDEM. The vertical particle velocity maps produced by CFDEM using the cut-cell and hybrid grids were in excellent agreement with each other, demonstrating that the small cells in the cut-cell grid did not negatively influence the solution to the gas phase mass and momentum conservation equations. Both codes correctly predicted the particle circulation pattern that was observed experimentally, although there was a slight offset in the bubbling region for the MFIX simulations. This offset was removed by increasing the frequency at which the void fraction and drag forces were calculated.

The quantitative accuracy of the simulations was improved by adjusting the calculation of drag on the particles. A simple method of using different effective diameters in the calculation of the void fraction and the drag was applied. These diameters were selected to match the void fraction and superficial gas velocity at the onset of fluidisation. CFD-DEM simulations of this process agreed well with the theoretical predictions. Applying the effective diameters to the fluidised bed simulations improved the prediction of the vertical velocity in the lower half of the bed. These results demonstrate that the effective diameters method is an efficacious approach towards modelling gas-particle flow, without the computational expense of more detailed nonspherical models.

3.5. References

1. Anderson, T.B. and R. Jackson, *A Fluid Mechanical Description of Fluidized Beds.* Industrial & Engineering Chemistry Fundamentals, 1967. **6**(4): p. 527-539
2. Peng, Z., et al., *Influence of void fraction calculation on fidelity of CFD-DEM simulation of gas-solid bubbling fluidized beds.* AIChE Journal, 2014. **60**(6): p. 2000-2018
3. Igci, Y., et al., *Filtered two-fluid models for fluidized gas-particle suspensions.* AIChE Journal, 2008. **54**(6): p. 1431-1448
4. Andrews, P.N. Loezos, and S. Sundaresan, *Coarse-Grid Simulation of Gas-Particle Flows in Vertical Risers.* Industrial & Engineering Chemistry Research, 2005. **44**(16): p. 6022-6037
5. Radl, S. and S. Sundaresan, *A drag model for filtered Euler–Lagrange simulations of clustered gas–particle suspensions.* Chemical Engineering Science, 2014. **117**(0): p. 416-425
6. Goldenberg, C., et al., *Scale separation in granular packings: Stress plateaus and fluctuations.* Physical Review Letters, 2006. **96**(16)
7. Labra, C., J.Y. Ooi, and J. Sun, *Spatial and temporal coarse-graining for DEM analysis.* AIP Conference Proceedings, 2013. **1542**(1): p. 1258-1261
8. Boyce, C.M., et al., *Limitations on Fluid Grid Sizing for Using Volume-Averaged Fluid Equations in Discrete Element Models of Fluidized Beds.* Industrial and Engineering Chemistry Research, 2015. **54**(43): p. 10684-10697
9. Bakshi, A., C. Altantzis, and A.F. Ghoniem, *Towards accurate three-dimensional simulation of dense multi-phase flows using cylindrical coordinates.* Powder Technology, 2014. **264**: p. 242-255
10. Lu, X. and D.J. Holland, *Investigation of drag models for the two fluid simulation of Geldart group A powders.* Powder Technology, 2016. **304**: p. 41-54
11. NETL, *MFIX 2015-1 User Guide*. 2015.
12. Dietiker, J., *MFIX: Cartesian Grid User Guide.* National Energy Technology Laboratory, Morgantown, 2009
13. Boyce, C.M., et al., *Novel fluid grid and voidage calculation techniques for a discrete element model of a 3D cylindrical fluidized bed.* Computers and Chemical Engineering, 2014. **65**: p. 18-27
14. Wu, C.L., et al., *Dense particulate flow model on unstructured mesh.* Chemical Engineering Science, 2006. **61**(17): p. 5726-5741
15. Syamlal, M.R., W; O'Brien, T, *MFIX Documentation: Theory Guide*. 1993.
16. Li, T., et al., *Open-source MFIX-DEM software for gas-solids flows: Part II — Validation studies.* Powder Technology, 2012. **220**: p. 138-150
17. Müller, C.R., et al., *Validation of a discrete element model using magnetic resonance measurements.* Particuology, 2009. **7**(4): p. 297-306
18. Link, J.M., et al., *PEPT and discrete particle simulation study of spout-fluid bed regimes.* AIChE Journal, 2008. **54**(5): p. 1189-1202
19. Gopalakrishnan, P. and D. Tafti, *Development of parallel DEM for the open source code MFIX.* Powder Technology, 2013. **235**: p. 33-41
20. Kloss, C., et al., *Models, algorithms and validation for opensource DEM and CFD-DEM.* Progress in Computational Fluid Dynamics, 2012. **12**(2-3): p. 140-152
21. Weller, H.G., et al., *A tensorial approach to computational continuum mechanics using object-oriented techniques.* Computers in physics, 1998. **12**(6): p. 620-631
22. Goniva, C., et al., *Influence of rolling friction on single spout fluidized bed simulation.* Particuology, 2012. **10**(5): p. 582-591

23. Link, J.M., et al., *Flow regimes in a spout-fluid bed: A combined experimental and simulation study.* Chemical Engineering Science, 2005. **60**(13): p. 3425-3442
24. Cundall, P.A., *Formulation of a three-dimensional distinct element model—Part I. A scheme to detect and represent contacts in a system composed of many polyhedral blocks.* International Journal of Rock Mechanics and Mining Sciences & Geomechanics Abstracts, 1988. **25**(3): p. 107-116
25. Nolan, G.T. and P.E. Kavanagh, *Random packing of nonspherical particles.* Powder Technology, 1995. **84**(3): p. 199-205
26. Wachs, A., et al., *Grains3D, a flexible DEM approach for particles of arbitrary convex shape - Part I: Numerical model and validations.* Powder Technology, 2012. **224**: p. 374-389
27. Podlozhnyuk, A., S. Pirker, and C. Kloss, *Efficient implementation of superquadric particles in Discrete Element Method within an open-source framework.* Computational Particle Mechanics, 2017. **4**(1): p. 101-118
28. Hilton, J.E., L.R. Mason, and P.W. Cleary, *Dynamics of gas-solid fluidised beds with non-spherical particle geometry.* Chemical Engineering Science, 2010. **65**(5): p. 1584-1596
29. Cleary, P.W., *Large scale industrial DEM modelling.* Engineering Computations (Swansea, Wales), 2004. **21**(2-4): p. 169-204
30. Haider, A. and O. Levenspiel, *Drag coefficient and terminal velocity of spherical and nonspherical particles.* Powder Technology, 1989. **58**(1): p. 63-70
31. Hölzer, A. and M. Sommerfeld, *Lattice boltzmann simulations to determine forces acting on non-spherical particles,* in *Fluid Mechanics and its Applications*. 2006. p. 99-108.
32. Rong, L.W., Z.Y. Zhou, and A.B. Yu, *Lattice-Boltzmann simulation of fluid flow through packed beds of uniform ellipsoids.* Powder Technology, 2015. **285**: p. 146-156
33. Chen, Y., J.R. Third, and C.R. Müller, *A drag force correlation for approximately cubic particles constructed from identical spheres.* Chemical Engineering Science, 2015. **123**: p. 146-154
34. Boyce, C.M., et al., *Effective particle diameters for simulating fluidization of non-spherical particles: CFD-DEM models vs. MRI measurements.* AIChE Journal, 2017. **63**(7): p. 2555-2568
35. Beetstra, R., M.A. Van Der Hoef, and J.A.M. Kuipers, *Drag force of intermediate reynolds number flow past mono- And bidisperse arrays of spheres.* AIChE Journal, 2007. **53**(2): p. 489-501
36. Verlet, L., *Computer "experiments" on classical fluids. I. Thermodynamical properties of Lennard-Jones molecules.* Physical review, 1967. **159**(1): p. 98-103
37. Radl, S., et al., *State of the Art in Mapping Schemes for Dilute and Dense Euler-Lagrange Simulations,* in *10th International Conference on CFD in Oil & Gas, Metallurgical and Process Industries*. 2014: Trondheim, Norway. p. 1 - 9.
38. Li, Y., Y. Xu, and C. Thornton, *A comparison of discrete element simulations and experiments for 'sandpiles' composed of spherical particles.* Powder Technology, 2005. **160**(3): p. 219-228
39. Garg, R., et al., *Documentation of open-source MFIX-DEM software for gas-solids flows*. 2012.
40. Kriebitzsch, S.H.L., M.A. Van Der Hoef, and J.A.M. Kuipers, *Fully resolved simulation of a gas-fluidized bed: A critical test of DEM models.* Chemical Engineering Science, 2013. **91**: p. 1-4

41. Tang, Y., E.A.J.F. Peters, and J.A.M. Kuipers, *Direct numerical simulations of dynamic gas-solid suspensions.* AIChE Journal, 2016

4. Investigation of void fraction schemes for use with CFD-DEM simulations of fluidised beds

The transfer of momentum between the fluid phase and discrete particles in unresolved CFD-DEM model requires knowledge of the local void fraction. Void fraction schemes that approximate the proportion of volume occupied by each phase are used in preference to exact methods for reasons of efficiency and generality. However, it is questionable whether these approximate schemes are sufficiently accurate over a range of grid sizes. In this chapter, seven void fraction schemes were applied to CFD-DEM simulations of a square fluidised bed with a drilled plate gas distributor. For fluid grids with cell sizes of 3.5 and 1.6 particle diameters (d_p) , the particle velocity was in qualitative agreement with MRI measurements. The $1.6d_p$ fluid grid simulations were in excellent quantitative agreement with the experiment in the lower half of the bed. This result was due to the realistic inlet boundary condition that is possible to model at this grid size. For the $1.6d_p$ grid the particle centred approach was unsuitable, the method of Khawaja et al. [1] had the best predictive accuracy, and the diffusive smoothing method had the fastest run time.

4.1. Introduction

The multiscale modelling philosophy introduced in Chapter 1 specifies that detailed, computationally expensive simulations of small scale systems are used to derive closure relations for less detailed simulations of large scale systems. For example, computational fluid dynamics coupled with the discrete element method (CFD-DEM) simulations are only viable for systems sized at the laboratory scale. Yet they can be used to develop a constitutive equation for the granular stress tensor used by the two-fluid model, which is suitable for simulating industrial length scales. These latter models are then used to aid process design [2]. CFD and DEM are coupled by calculating the localised proportion of volume occupied by the gas phase, referred to here as the void fraction, or voidage. This calculation is handled by a void fraction scheme. The void fraction within a fluid cell may be determined exactly [3]. However, such a calculation requires a complicated mathematical model and considerable computational expense, especially for complex geometries, non-spherical particles, and unstructured CFD grids. As a result, non-analytical approximations to the void

fraction have been used to simulate interacting fluid-particle flows. CFD-DEM models require careful balancing of the cell sizes used in the fluid model. If the cells are too coarse, key features of the fluid flow field will be missed. On the other hand if the cells are too fine, the volume averaging assumptions used to derive the fluid dynamic equations may break down [4-6]. The approximations made by void fraction schemes can alter the minimum acceptable cell size for the fluid dynamics model [5]. In this chapter, several of the most common void fraction schemes were used to simulate the fluidisation above a drilled plate distributor where a refined fluid grid was required.

The CFD-DEM approach is based on volume averaging of the gas and particulate phases [4]. In these equations an assumption is made that the length scale over which the fluid dynamics changes is large compared with the length scale of the particles. This so called "separation of scales" is what permits the use of a simple drag force correlation to describe the fluid-particle interaction. Many studies simply assume that a minimum cell size of ~3 particle diameters (d_p) is sufficient for the volume averaging equations to be valid. However, in a detailed study Peng et al. [5] demonstrated by analysis of bubble evolution and pressure fluctuations that cell sizes as small as about $1.6d_p$ may be sufficient for the assumption of a separation of scales to be valid. By contrast, Boyce et al. [6] found that a minimum cell size of ~$3d_p$ was required to accurately simulate the frequency of bubble eruptions and pressure fluctuations. Therefore, there is still some debate in the literature as to the minimum cell size that can be used in CFD-DEM simulations. In the work of Peng et al. [5], the method used to calculate the void fraction was critical in establishing the minimum feasible cell size. Here these methods are investigated further.

A void fraction scheme should (1) conserve the total mass of the solid phase, (2) predict a grid-independent velocity field, and (3) produce smooth void fraction fields within the densely packed particle phase [7]. If these conditions are not met, then the local void fraction may be unrealistic (i.e. below the close packing limit or greater than unity). It is then likely that the value of the local drag force would also be unrealistic. An unreasonably high (or low) local drag force may give an unstable solution to the fluid phase system of equations. The solution may also be unstable if the time derivative of the local void fraction were to become unrealistically large [5]. This result may occur if a small change in the positions of the particles results in a large change in the local void fraction in a cell. Several void fraction schemes have been devised to attempt to fulfil these three criteria.

The simplest void fraction scheme is the particle-centred method (PCM), which assumes that the entire particle volume is located at the centroid of the particle [8]. Void fraction fields in simulations using the PCM display large fluctuations with time due to particle centres crossing cell boundaries [9]. If the cell size to particle diameter ratio is greater than 3.8, then unrealistic spikes in the local gas pressure do not occur [5]. Thus, the PCM approach is likely satisfactory if fluid cells are large compared to the particle size. However, in order to capture the fluid flow field, especially near surfaces, it is often desirable to use cells that are not much larger than the diameter of the particles where the PCM approach is likely invalid.

Exact void fractions can be obtained analytically [3] and quickly, but this analytical approach is only practicable if using a simple cuboidal mesh. For more complex meshes, the intersecting volumes between each particle and the local mesh elements can be determined by decomposing the sphere into a collection of spherical caps, wedges and cones [10]. In theory, a typical system comprising ~10^5 particles would require ~10 seconds to calculate all the potential overlap volumes for all of the particles in all 27 neighboring cells (in a three-dimensional system), several orders of magnitude longer than the cuboidal exact method. Several methods have been proposed to strike a balance between computational efficiency and accuracy of voidage calculations.

The first methods considered are the so called “divided particle volume methods” (DPVMs) in which the shape of the particle is approximated by some simple geometric approach, such as a cube. Portions of the volume of the particle are then assigned to several nearby cells. One example of this approach is used in the MFIX software [1, 11, 12].

A second approach, the statistical kernel methods, determine the solid volume fraction by distributing the particle volume by a weighting function that decays away from the particle center [13]. The Gaussian distribution is often used as a weighting function and hence a particle may contribute a portion of its volume to distant cells. In order to execute the statistical kernel method with distributed memory parallel systems, a PDE for the diffusion of the void fraction may be solved over a series of pseudo-time steps [7]. With the correct initialisation, the diffusion method is equivalent to the statistical kernel method and is faster to implement.

Another approach that has been proposed is to sub-divide the particle into a collection of smaller entities. The volume fraction of the particle may then be determined by the amount of these entities within each cell. Here, such methods are denoted as “satellite point methods”

[14-17]. This method was used by Hobbs [18] to estimate the void fraction for non-rectangular cells in an unstructured grid without strenuous mathematical effort.

Two-grid methods consist of a dedicated particle grid and a dedicated fluid grid. The void fraction is calculated on the particle grid, which is usually taken to be a Cartesian grid. The void fraction on the Cartesian grid may be calculated using the PCM, or any other suitable scheme. This void fraction data is then mapped onto a fluid grid where the fluid phase conservation equations are solved. The two–grid method has been used to map void fraction data to unstructured or non-Cartesian grids where other void fraction calculations are more difficult to implement [19]. In this case, the volume fraction of each fluid cell in each particle cell only needs to be determined at the initialisation stage, reducing the computational expense [19].

The purpose of this chapter was to investigate the different void fraction schemes used with CFD-DEM when simulating a flow field with features that occur on a length scale comparable to the length scale of the particles. Seven different void fraction schemes were tested, with the specific methods used outlined in Section 4.2.3. Simulations were performed of a fluidised bed with a drilled plate distributor. The holes in the drilled plate were 1 mm diameter, while the particles simulated were 1.07 mm in diameter, thus some features of the fluid flow field will occur over a length scale comparable to the size of the particles. Here simulations of the fluidisation were performed with cell sizes of 3.7 mm, 1.8 mm, and 1.4 mm. Simulation results were validated by comparison with experimental measurements performed by Magnetic Resonance Imaging (MRI). This investigation builds upon the work in this field by comparing the non-analytical methods in order to ascertain the efficacy of these methods when simulating a high-resolution flow field.

4.2. Method

4.2.1 Experiment

The data were collected from a square fluidised bed, with cross-sectional dimensions of 37 mm × 37 mm and with a settled bed height of 30 mm. Humid air at a pressure of 1 barg was used as the fluidising gas. The gas distributor was a drilled plate with a 4 × 4 grid of 1 mm diameter holes, each spaced 7 mm apart. The pressure drop across the distributor exceeded the pressure drop across the bed at minimum fluidisation, thus ensuring even gas distribution. Air flow near the walls was restricted since the holes were all located inside a 23 mm wide square region at the center of the distributor. The time-averaged particle velocity

throughout the bed was measured using MRI. *Papaver rhoeas* (poppy) seeds were used as particles, since their nuclear spin relaxation properties were advantageous for imaging. The seeds were kidney shaped and had a mean projected area-equivalent diameter of 1.07 mm and a measured minimum fluidisation velocity of 0.3 m s^{-1} at STP. The superficial gas velocity was equal to 0.6 m s^{-1}.

The MRI experiments were conducted with a Bruker DMX 200 spectrometer operating in the vertical direction, for which the proton (^{1}H) frequency was 199.7 MHz. The seeds were excited and detected using a birdcage radio frequency coil surrounding the fluidised bed. A 3-axis shielded gradient system was used to establish spatial resolution, with a maximum magnetic field gradient strength of 0.139 T m^{-1}. A Cartesian coordinate system, with the *z*-axis pointing along the vertical direction was used. The velocity of the particles was measured using pulsed field gradient MRI as is described in detail elsewhere [20]. In brief, a pair of half sine-shaped motion encoding gradients were used to encode the velocity in the phase of the observed signal. The gradients were each applied for a half-period (δ) of 0.56 ms and the observation time between gradients (Δ) was 2 ms. The amplitude of the sine gradient (g) was adjusted in 10 steps about 0 T m^{-1}, with a maximum gradient strength of 0.11 T m^{-1}. A time-averaged image of the velocity was obtained by collecting 48 averages over a total time of 2 hours.

The local mean velocity was obtained by the gradient of the linear equation fitted to the plot of the angle of the complex signal against the inverse variable $\boldsymbol{p} = \gamma g \delta \Delta$. The uncertainty of the measurement was estimated from the error of the fitted line. In areas of low velocity, the uncertainty was ± 0.002 m s^{-1}. In regions of high velocity and low signal-to-noise, the error increased but was < 0.02 m s^{-1} for 95% of the voxels. For simplicity, a constant margin of ± 0.02 m s^{-1} was used to denote the uncertainty in the experimental velocity profiles.

4.2.2 Simulation setup

The open-source CFD-DEM package in MFIX was used to run the simulations in this work. The particle motions were modelled using the soft-sphere DEM, while the fluid flow was resolved by solving the volume-averaged mass and momentum conservation equations using an extension of the SIMPLE method. Full details of the computational model are provided by Syamlal et al. [21]. Verification [22-24] and validation [25, 26] of MFIX has been performed, demonstrating that the models have been correctly implemented and are physically meaningful. The MFIX source code was modified to add the void fraction schemes that were

not incorporated into the standard MFIX package. The simulated domain was a square fluidised bed, with dimensions of 37 mm × 37 mm × 120 mm. The square grid configuration avoids complications arising from curved boundaries and simplifies the implementation of the void fraction codes since they did not need to consider non-rectangular cells. Three grid resolutions were tested: 10 × 10 × 32 cells (cell length to particle diameter ratio = 3.5), 21 × 21 × 68 cells (cell length to particle diameter ratio = 1.6), and 26 × 26 × 84 cells (cell length to particle diameter ratio = 1.3). Here these grids are referred to as coarse, fine and very fine respectively. The cell length to particle diameter ratios were greater than the minimum recommended value of 1.63 [5] for the coarse and fine grids, but below this threshold for the very fine grid. The dimensions of the fluid domain and the settled particle bed are given by Figure 4.1(a).

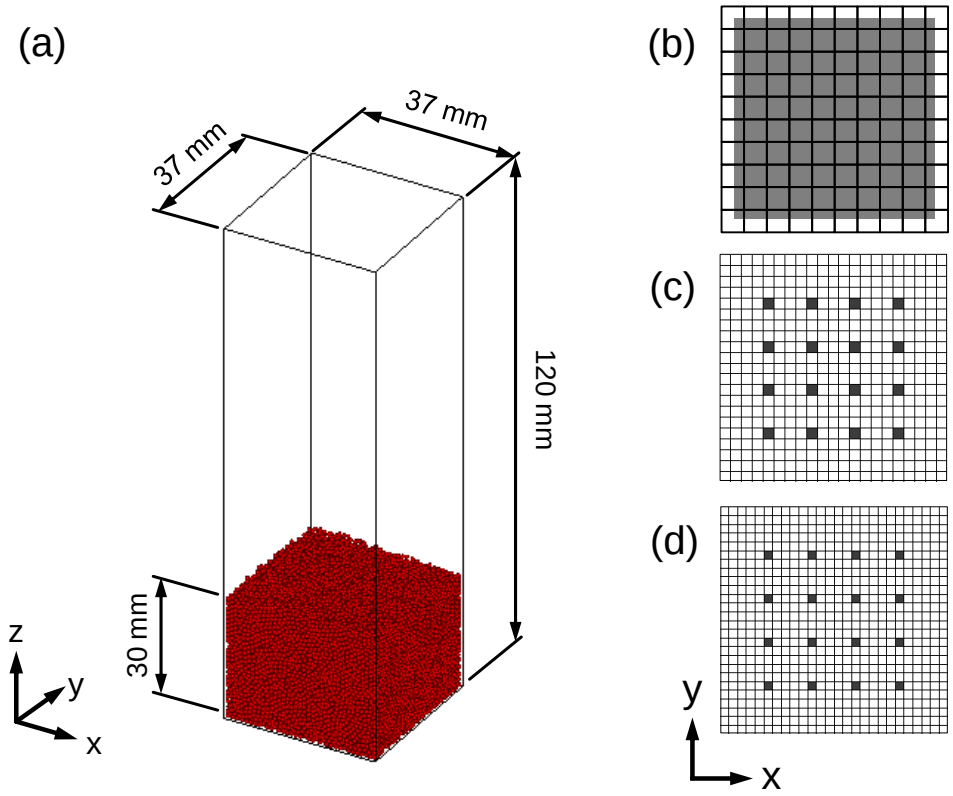

Figure 4.1. (a) Schematic diagram of the square fluidised bed used in the simulations. The domain boundaries are denoted by the black outlines. (b) Uniform inlet boundary condition and fluid grid used for the coarse grid simulation. (c) Drilled plate inlet boundary condition and fluid grid used for fine grid simulation. (d) Drilled plate inlet boundary condition and fluid grid used for very fine grid simulation. The gas flow regions are denoted by dark grey.

A constant-mass inflow boundary condition was applied at the inlet. The coarse grid was not able to resolve the gas flow through the holes since the hole diameter was about one quarter of the cell length. Thus, a uniform boundary was applied to the central 33 mm × 33 mm

region to provide the best approximation to the distributor geometry. The velocity in this region was set to 0.754 m s^{-1}, while the gas velocity in the outer perimeter was set to zero. This arrangement gave the same total mass flow rate of gas as in the experiments. For the fine grid, the gas velocity was set to 16.54 m s^{-1} in 16 cells, each representing a hole in the distributor. The air velocities into the remaining cells at the distributor were set to zero. This level of grid refinement was close to the minimum cell size to particle diameter ratio at which the separation of scales assumption was found to be valid [5]. For the very fine grid, the gas velocity was set to 25.35 m s^{-1} in 16 cells. This grid is below the recommended minimum cell size to particle diameter ratio. Figure 4.1 shows the configurations of the inlets. The outlet boundary condition was set to constant-pressure outflow.

A no-slip boundary condition was applied at the wall for the gas phase. Müller et al. [27] found that the choice of wall boundary condition did not affect the void fraction profile. Ye et al. [28] found that for Group A particles, the no-slip boundary condition predicted a minimum bubbling velocity that was considerably higher than the experimental value. In contrast, the full-slip boundary condition predicted a minimum bubbling velocity that was slightly lower than the value obtained experimentally. In our case, analysis of averaged particle phase velocity maps suggested that the choice of gas phase wall boundary condition did not have a discernible impact upon the particle trajectories. Thus, the selection of the no-slip boundary condition was arbitrary.

The linear-spring dashpot model was used to calculate the contact forces during particle-particle and particle-wall interactions. The Beetstra model [29] was used to calculate the drag force acting on the particles. The main parameters that were used in all the simulations are given in Table 4.1. The ratio between the tangential and normal spring constants was equal to 2/7 to equalise the periods of normal and tangential contact oscillations [30, 31]. The DEM time step was 1.15×10^{-6} s, or $1/50^{th}$ of the minimum collision time [32]. The local relative velocity distribution of colliding particles shown in Figure 4.2 showed that the relative velocity of all contacts was below 0.06 m s^{-1}. For the contact parameters used, the maximum overlap between particles for a collision with a relative velocity of 0.06 m s^{-1} was 0.1%, well below the threshold of 1% that is required to ensure that rigid particle contacts are well approximated [33]. The fluid time step was adaptive. If the solution to the fluid phase conservation equations did not converge at a particular time step, the time step value was reduced. The maximum time step that was allowed was 5×10^{-4} s. This time step was sufficient to achieve convergence in the coarse grid case. For the fine grid, the time step was

usually between 1×10^{-4} and 2×10^{-4} s owing to the reduction of the cell size. The simulations were weakly coupled and up to 400 steps of the DEM were run between each fluid phase time step. In coarse grid simulations using the PCM, it was found that reducing the fluid phase time step to as little as 5×10^{-6} s, or ~5 DEM steps, did not quantitatively influence the time-averaged particle velocity distribution. Thus, an upper limit of 5×10^{-4} s was used in subsequent simulations in order to reduce the total computation time.

Table 4.1. Parameters common to all simulations performed in this study.

Parameter	Value
Domain dimensions (m)	0.037 × 0.037 × 0.12
Number of particles	38415
Particle diameter (m)	0.00107
Particle density (kg m^{-3})	1050
Normal particle spring constant (N m^{-1})	1000
Coefficient of normal restitution	0.93
Coefficient of friction	0.1
Tangential particle spring constant (N m^{-1})	285.7
Normal viscous damping coefficient (kg s^{-1})	7.85×10^{-4}
Tangential viscous damping coefficient (kg s^{-1})	3.92×10^{-4}
Superficial gas velocity (m s^{-1})	0.6
Gas density (kg m^{-3})	1.17
Gas viscosity (Pa·s)	1.8×10^{-5}

Each simulation was run in serial mode, using an Amazon Web Services EC2 virtual computing instance. The instance consisted of one thread of an Intel Xeon E5-2670 v2 CPU, with 3.75 GB of memory and a clock frequency of 2.5 GHz. Each simulation was run to simulate 5 s of operation. A simulation of this length took approximately 36 hours to complete for the coarse grid and 150 hours for the fine grid. The profiles of the pressure drop against time shown in Figure 4.3 demonstrate that the pressure fluctuates steadily after 1 s of simulated time. The standard deviation of pressure fluctuations calculated over intervals of 1 s was constant between 2 s and 5 s. For these reasons, data collected beyond 2 s was used for averaging.

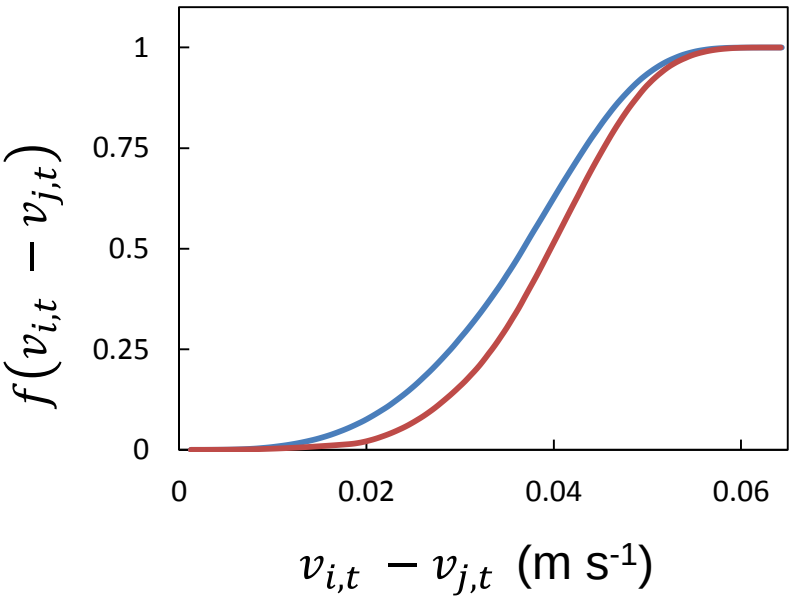

Figure 4.2. Cumulative frequency distribution function of the magnitude of the local relative velocity for all combinations of particles *i* and *j* that are within $1d_p$ of each other. Corrected cube method with coarse grid: blue line; corrected cube method with fine grid: red line.

The time required for the calculations associated with the void fraction schemes was an area of interest. If the void fraction code takes less time to execute, then the total simulation time may be reduced, thus minimising the computational resources required. However, it is also possible that temporal fluctuations in the void fraction may impede the convergence of the fluid phase solver. To assess these competing effects, the total CPU time for each coarse grid simulation was recorded from the output files. Additionally, the CPU time dedicated to calculating the void fraction itself was estimated by calculating the time taken to run the relevant subroutines. For the void fraction timing tests, the void fraction time was sampled for 0.01 s of operation (about 20 iterations for the coarse grid case) for each simulation.

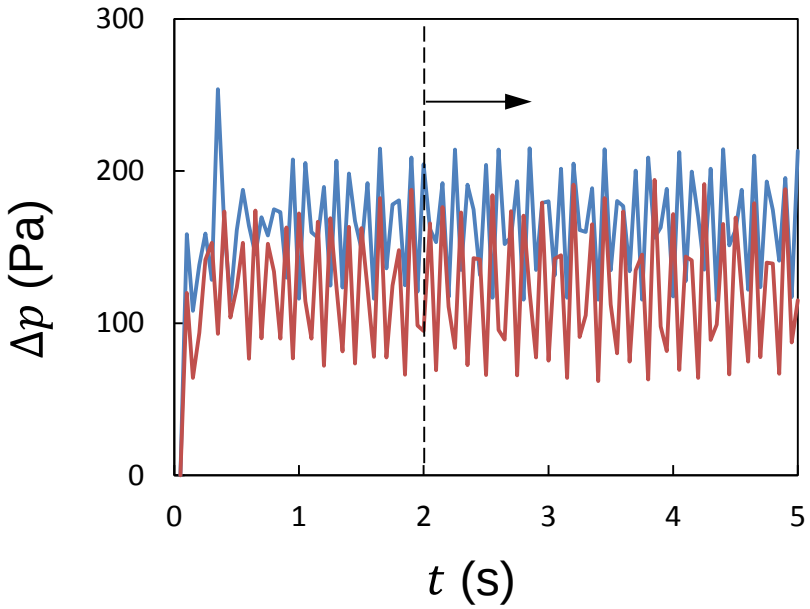

Figure 4.3. Profiles of pressure drop against simulated time. Beyond 2 s, the profiles fluctuate with a steady mean and frequency. Corrected cube method with coarse grid: blue line; corrected cube method with fine grid: red line. The dashed line and arrow indicate the start point from which the data were averaged.

4.2.3 Implementation of Void Fraction Schemes

Figure 4.4 gives visual illustrations of the analytical, PCM, MFIX DPVM, cube DPVM, corrected cube DPVM, statistical kernel and satellite point methods. Since the two-grid method is not completely distinct from the other void fraction models when used with regular Cartesian fluid cells, it will not be investigated in this study. The left-hand diagrams illustrate where the particle is positioned on the fluid grid. Visual representations of each void fraction scheme are included to illustrate how the particle volume fraction in each cell is calculated. The right-hand images describe the spatial distribution of the particle volume fraction, where high particle volume fraction is denoted with dark cells. The formulation of each void fraction scheme and the values of the relevant parameters are described in the following sections.

PCM

The void fraction of a fluid cell using the PCM is given by:

$$\varepsilon_g(\boldsymbol{x}) = 1 - \frac{\sum_{p=1}^{N_p} V_p}{V(\boldsymbol{x})} \tag{4.1}$$

where $\varepsilon_g(\boldsymbol{x})$ is the local gas phase volume fraction at position $\boldsymbol{x}$, V_p is the volume of particle p and $V(\boldsymbol{x})$ is the volume of the cell located at position $\boldsymbol{x}$. N_p is the number of particle centres located inside the cell.

MFIX DPVM

The MFIX DPVM estimated the void fraction in a cell by:

$$\varepsilon_g(\boldsymbol{x}) = 1 - \frac{\sum_{p=1}^{N_p} \phi_p(\boldsymbol{x}) V_p}{V(\boldsymbol{x})} \tag{4.2}$$

where ϕ_p is the volume fraction of particle p within the cell located at position $\boldsymbol{x}$. Particles with centres in the cell of interest, or in the 26 neighbouring cells can have a non-zero value of ϕ_p with respect to the cell at position $\boldsymbol{x}$. Therefore, N_p is the number of particles with centers located in the cell of interest and in its immediate neighbours.

Firstly, two weightings were calculated for each dimension, $\phi_{k,F-}$ located at the cell face before the central co-ordinate and $\phi_{k,F+}$ located at the cell face after the central co-ordinate. The values of these weightings in direction k were given by:

$$\phi_{k,F} = \begin{cases} \dfrac{h_w^2(3w - h_w)}{4w^3} & \text{, if } \delta x_{p,F} < w \\ 0 & \text{, if } \delta x_{p,F} \geq w \end{cases} \tag{4.3}$$

where w is the filter width, $\delta x_{p,F}$ is the distance between the particle centre and the face F and $h_w = w - \delta x_{p,F}$. The filter width used for this investigation was equal to the particle diameter, 1.07 mm. Using these two weightings, the weighting along direction k for the cell in which the particle is located was calculated from:

$$\phi_k = 1 - \phi_{k,F+} - \phi_{k,F-} \tag{4.4}$$

The weighting for neighbouring cells is given by $\phi_{k,F}$. For example, in the x-direction, $\phi_{x,F-}$ and $\phi_{x,F+}$ would be the weightings obtained using the overlap between the x-component of the particle centre and the western and eastern faces respectively. If $\delta x_{p,F}$ is greater than the

filter width, then $\phi_{k,F}$ is set to zero. Provided that *w* is smaller than the dimension of the cell, either, $\phi_{k,F-}$ or $\phi_{k,F+}$ will be zero. Subsequently, the volume fraction for particle *p* in a cell is the product of the weightings calculated in each dimension:

$$\phi_p(\boldsymbol{x}) = \phi_x(\boldsymbol{x})\phi_y(\boldsymbol{x})\phi_z(\boldsymbol{x}) \tag{4.5}$$

The overall void fraction in a cell is then calculated from Equation 4.2.

Cube DPVM

Like the MFIX DPVM, the cube DPVM determined the void fraction using Equation 4.2. However, the volume fraction of particle *p* was estimated differently. ϕ_p was determined by:

$$\phi_p(\boldsymbol{x}) = \frac{\delta x \delta y \delta z}{d_p^3} \tag{4.6}$$

where δx, δy, and δz are the lengths of the cuboid that contains the portion of the particle that lies within the cell. The cuboid length in direction *k* is calculated from:

$$\delta x_k = \min\left(x_{k,F+}, (x_{p,k} + R)\right) - \max\left(x_{k,F-}, \left(x_{p,k} - R\right)\right) \tag{4.7}$$

where $x_{p,k}$ is the position of particle *p* in direction *k*, $x_{k,F+}$ is the position of the eastern, northern or top face in direction *k*, $x_{k,F-}$ is the position of the western, southern or bottom face, and *R* is the particle radius.

Corrected Cube DPVM

The cube DPVM approach is attractive as it is simple to implement and computationally efficient. However, Khawaja et al. [1] found that the volume fraction estimated using the cube DPVM under-estimated the true volume fraction when there was only a small amount of the particle outside of the cell. In order to improve the approximation of the particle volume fractions, they developed an equation to convert the cube volume fractions to values that were in closer agreement with the volume fraction obtained for a sphere analytically. Their correlation is given by:

$$\phi_p(\boldsymbol{x}) = -0.8457\phi_{cube}(\boldsymbol{x})^3 + 1.6625\phi_{cube}(\boldsymbol{x})^2 + 0.1832\phi_{cube}(\boldsymbol{x}) \tag{4.8}$$

where ϕ_{cube} was determined by Equations 4.6 and 4.7. For each particle, it was unlikely that the values of ϕ_p over all the cells in which the particle resided would sum to unity. Thus to ensure conservation of mass, after ϕ_p was calculated, it was normalised such that $\sum \phi_p = 1$,

where the sum is performed over all cells in which the particle may reside. Equation 4.2 was then applied to determine the void fraction.

Statistical Kernel/Diffusion Method

The statistical kernel method determines the volume fraction of a particle in a cell by using a weighting function. Weighting functions that have been used in previous investigations include the Gaussian distribution [34] and the distribution function of Johnson [13, 35]. The region over which the volume of a particle is distributed may exceed the boundaries of the domain. The portion of the weighting function outside of the domain is discarded. In order to conserve the total solid volume, a ghost particle is placed outside the domain, mirroring the location of the original particle. The weighting functions of both particles are combined. The integral of the new weighting function within the domain is equal to unity, thus the particle volume is conserved.

Here the statistical kernel method was approximated using the diffusion approach [7]. The diffusion of the void fraction may be described by:

$$\frac{\partial \varepsilon_g}{\partial t_D} = \nabla^2 \varepsilon_g \tag{4.9}$$

where ε_g is the void fraction and t_D represents the pseudo-time domain over which the diffusion takes place. Equation 4.9 was discretised using the finite volume method with a central differencing scheme. The PCM solid volume fraction was used as the initial condition. The system of linear equations was solved to update the void fraction field at the next pseudo-time step. For each void fraction calculation, 5 pseudo-time steps were used. With 5 pseudo-time steps, the voidage distribution was approximately Gaussian but somewhat narrower than expected based on the specified diffusion time. Increasing the number of steps resulted in a distribution that was closer to Gaussian, but this was not felt to improve the results. The volume fraction of each particle in a cell using the statistical kernel method depends on the distance between the particle and cell centres. The particle volume fraction does not depend on this displacement for the diffusive method; hence it does not contain information about particle locations at the sub-grid scale. Therefore, the voidage calculated by the diffusive method is not, in general, identical to the statistical kernel method. However, if the diffusion length (or standard deviation) is sufficiently large the difference between the statistical kernel method and the diffusive method is negligible.

The analysis was performed using pseudo-time steps of 2.28×10^{-7} s and 9.16×10^{-7} s. The diffused voidage profiles for a single particle resembled a distribution where the standard deviation was equal to $1d_p$ and $2d_p$ respectively.

Satellite Point Method

The satellite point method approximates a particle as a cluster of smaller pseudo-particles. The pseudo-particles are distributed at different positions within the particle. The volume fraction of the particle within a particular cell is estimated by:

$$\phi_p(\boldsymbol{x}) = \frac{N_{SP}(\boldsymbol{x})}{N_{SP,total}} \tag{4.10}$$

where $N_{SP}(\boldsymbol{x})$ is the number of pseudo-particles located inside the cell located at position $\boldsymbol{x}$. $N_{SP,total}$ represents the total number of pseudo-particles that make up a real particle.

The code that was developed to use this scheme in MFIX distributed pseudo particles at the same locations as the CFDEM-Coupling scheme [36]. One pseudo-particle was at the centre of the real particle. Two rings, with elevation angles of $\frac{\pi}{4}$ and $\frac{3\pi}{4}$ and each with 4 pseudo-particles were distributed around the center of the real particle. The pseudo-particles in each of these rings had a radial coordinate of $0.62R$ and azimuth angles of $\frac{\pi}{4}, \frac{3\pi}{4}, \frac{5\pi}{4}$ and $\frac{7\pi}{4}$. There were a further 6 particles located $0.62R$ away from the center and positioned along the positive and negative directions of the *x*-, *y*- and *z*-axes. This arrangement was repeated for another 14 pseudo-particles at a radial coordinate of $0.92R$. In total, one particle was represented by 29 pseudo-particles. This arrangement of pseudo-particles means that each pseudo-particle represented approximately the same volume of the real particle. For the coarse grid, Peng et al. [15] recommend a minimum number of satellite points to be 5 and advise using at least five times this number for a realistic solution. Hence, the prediction accuracy of the satellite point method as implemented was deemed to be adequate.

The most simplistic approach for binning particles to the fluid grid was to search for each satellite point, which was computationally slow. Advanced search algorithms have been developed to improve the efficiency of this process [15, 37]. The gain in computation speed was marginal for the simulations in this study due to the weak coupling between the fluid and particle phases. Hence, the location of each satellite point was found individually.

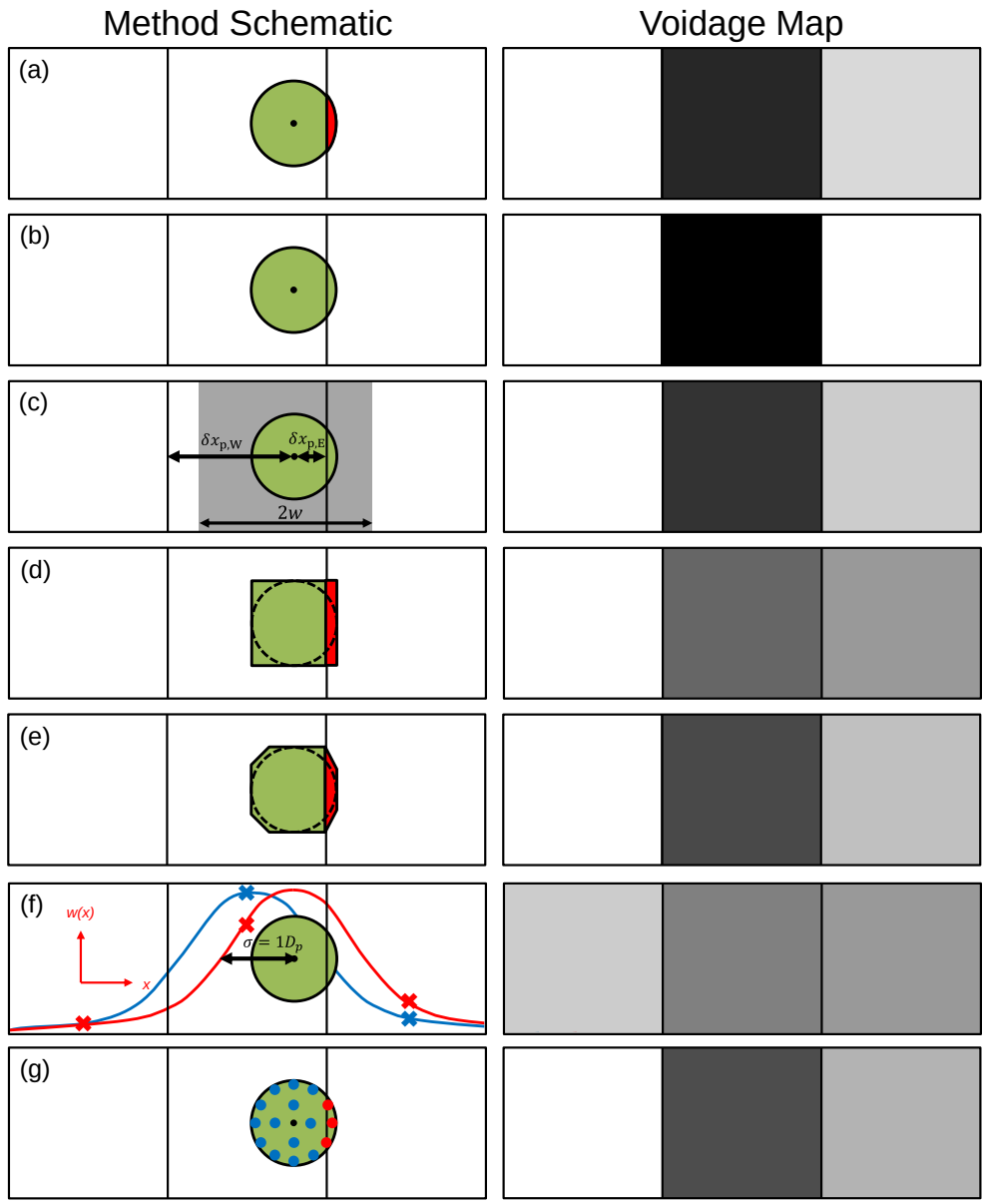

Figure 4.4. (Left) diagram illustrating how each void fraction scheme determines particle volume fractions and (right) representations of the particle volume fraction map for: (a) analytical method, (b) PCM, (c) MFIX DPVM, (d) cube DPVM, (e) corrected cube DPVM. (f) statistical kernel method using a Gaussian distribution with a standard deviation of $1d_p$ (red line). The equivalent PCM initialised diffusion method is shown by the blue line. (g) Satellite point method.

4.2.4 Post-processing and analysis

For the purpose of averaging, only the last 3 s of data was used to minimise any start-up effects that may have occurred. Averaging was necessary to facilitate a fair comparison between each set of results and the experimental data. The particle-weighted time-averaged

solid velocity was used since MR images correspond to a particle-based time average [34] and was calculated by:

$$\boldsymbol{v}_{s,\mathrm{avg}}(\boldsymbol{x}) = \frac{\sum_{t=1}^{N_s}\sum_{p=1}^{N_p}\boldsymbol{v}_{p,t}\phi_{p,t}(\boldsymbol{x})}{\sum_{t=1}^{N_s}\sum_{p=1}^{N_p}\phi_{p,t}(\boldsymbol{x})} \tag{4.11}$$

where $\boldsymbol{v}_{p,t}$ is the velocity of particle *p* at time *t* and $\phi_{p,t}(\boldsymbol{x})$ represents the volume fraction of particle *p* inside the voxel $\boldsymbol{x}$ at time *t*. The volume fraction was determined using the corrected cube DPVM of Khawaja et al. [1] irrespective of which void fraction scheme was used during the simulation itself. This method was used since it was able to give accurate estimations of the volume fractions, while still being efficient to implement computationally. The PCM was considered as well, however it was not able to give representative averages of the particle velocity for voxels near the domain boundary due to ordering of the particles near the walls.

The relative discrepancy between two fields was calculated using:

$$\Delta\zeta = \frac{\sum\left(\zeta^A(\boldsymbol{x}) - \zeta^B(\boldsymbol{x})\right)^2}{\sum\zeta^B(\boldsymbol{x})^2} \times 100\% \tag{4.12}$$

where ζ may be either the void fraction or the particle phase velocity. For comparisons with the experiments, the simulation data took the place of $\zeta^A(\boldsymbol{x})$ and the experimental particle velocity field took the place of $\zeta^B(\boldsymbol{x})$. Simulation data were also compared with other simulation data with the assignment to $\zeta^A(\boldsymbol{x})$ and $\zeta^B(\boldsymbol{x})$ detailed in the results.

4.3. Results and discussion

4.3.1 Evaluation of void fraction schemes

In order to identify and understand the differences in the void fraction schemes, each scheme was applied to a set of particles' positions selected from a simulation. Two points in time that were 0.01 s apart were used in order to identify any large temporal changes in the local void fraction. The coarse grid (10 × 10 × 32 cells) and the fine grid (21 × 21 × 68 cells) were used. The void fraction maps using the coarse grid are given in Figure 4.5 and the fine grid in Figure 4.6. The thickness of the sample region was equal to one fluid cell. Using the metrics of Peng et al. [5], the ratio between the effective domain length and the effective cell length, S_d/S_c for the coarse grid was equal to 14.7 and the fine grid 31.1. Thus, S_d/S_c was below the minimum recommended value of 19.3 for the coarse grid, which implied that the solution may be influenced by the resolution of the fluid grid. For each set of void fraction maps, the right-hand map was made using particle positions 0.01 s after those used to make the left-hand map. The exact void fraction was calculated using the method and code developed by Strobl et al. [10]. Using this method required a computation time of ~1 s, which was faster than estimated by Strobl et al. [10], and slower than the non-exact methods. With the exception of the fine grid PCM and $2d_p$ diffusive scheme, all of the void fraction schemes predicted void fraction fields that were visually similar to the exact void fraction field. The relative deviations obtained using each void fraction scheme and the exact void fraction field are shown in Table 4.2 and were consistently low. However, the relative discrepancy values differed over several orders of magnitude, ranging from ~10^{-5}% for the corrected cube DPVM, which was the most accurate technique, to ~10^{-1}% for the diffusive scheme which was the least accurate technique. The large deviation was due to the spatial smoothing which blurred out local features of the voidage maps.

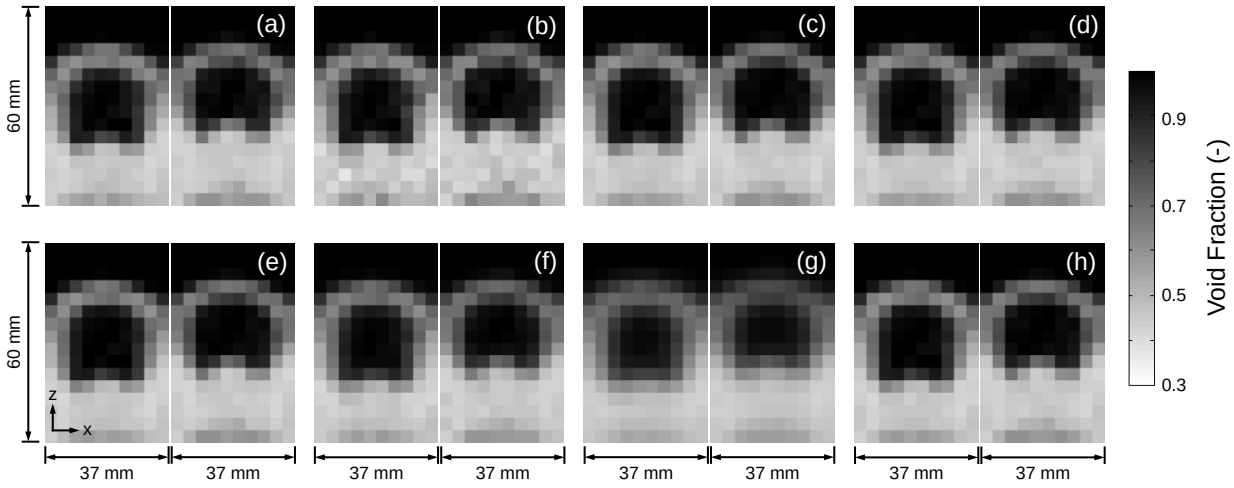

Figure 4.5. Instantaneous void fraction maps for two time steps 0.01 s apart obtained using the coarse fluid grid. The map was located in the *x*-*z* plane along a central slice in the *y*-direction for a snapshot of particles using: (a) exact, (b) PCM, (c) MFIX DPVM, (d) Cube DPVM, (e) Corrected cube DPVM, (f) diffusive scheme with $\sigma = 1d_p$, (g) diffusive scheme with $\sigma = 2d_p$, (h) satellite point method. Particle positions were the same for all void fraction images, only the method used to calculate the void fraction was changed. The grid dimensions were 10 cells × 10 cells × 32 cells.

The relative discrepancy was also affected by the resolution of the void fraction map. The PCM was found to be unsuitable for the fine grid since there were cells which had a negative void fraction due to too many particle centres being located within single cells. Increasing the grid refinement increased the relative discrepancy of all schemes by between a factor of 2 (diffusive) and a factor of 20 (PCM). The amplification in this total error was because more particles are located within several cells as the grid was refined; hence the errors introduced by each voidage scheme are more numerous. Furthermore, the relative error in the local volume fraction is increased by the reduction in the cell volume. Since the void fraction maps for all schemes were similar, fine grid simulations were only performed using the corrected cube and the diffusive ($\sigma = 1d_p$) schemes in further studies; coarse grid simulations were performed for all schemes.

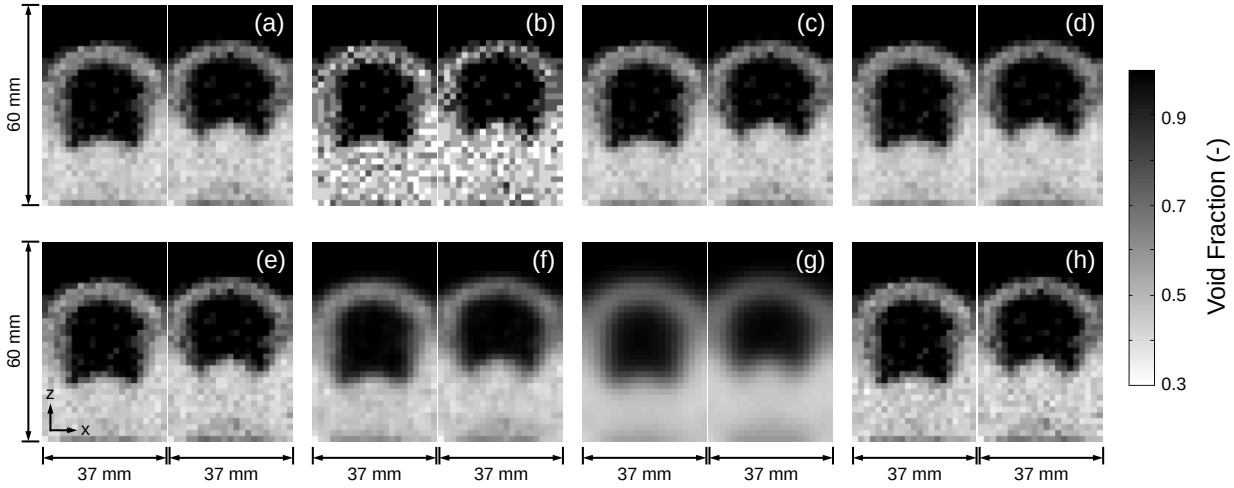

Figure 4.6. Instantaneous void fraction maps for two time steps 0.01 s apart obtained using the refined fluid grid. The map was located in the *x*-*z* plane along a central slice in the *y*-direction for a snapshot of particles using: (a) exact, (b) PCM, (c) MFIX DPVM, (d) Cube DPVM, (e) Corrected cube DPVM, (f) diffusive scheme with $\sigma = 1d_p$, (g) diffusive scheme with $\sigma = 2d_p$, (h) satellite point method. Particle positions were the same for all void fraction images, only the method used to calculate the void fraction was changed. The grid dimensions were 21 cells × 21 cells × 68 cells.

Table 4.2. The relative discrepancy between the exact void fraction map and the void fraction maps obtained using the void fraction schemes at each of the tested snapshots is shown for the coarse fluid grid (*CG*) in Figure 3 of the article, and fine fluid grid (*FG*) simulations shown in Figure 4 of the article. The subscript t_1 denotes left-hand void fraction maps; t_2 denotes right-hand void fraction maps. Relative discrepancies are calculated using Equation 4.12.

	PCM	MFIX DPVM	Cube DPVM	Corrected-cube DPVM	Diffusive $\sigma = 1d_p$	Diffusive $\sigma = 2d_p$	Satellite Point
$\Delta\varepsilon_{t_1,\mathrm{CG}}$	0.019%	0.000076%	0.00070%	0.000010%	0.018%	0.11%	0.0013%
$\Delta\varepsilon_{t_2,\mathrm{CG}}$	0.019%	0.00011%	0.00088%	0.000017%	0.019%	0.11%	0.0011%
$\Delta\varepsilon_{t_1,\mathrm{FG}}$	0.40%	0.0016%	0.015%	0.00032%	0.094%	0.26%	0.017%
$\Delta\varepsilon_{t_2,\mathrm{FG}}$	0.39%	0.0018%	0.016%	0.00038%	0.092%	0.25%	0.017%

4.3.2 Analysis of computation time

Details of the computation time of the void fraction schemes are provided in Table 4.3. $T_{sim,5\text{ s}}$ represents the total time required to run the simulation for 5 s of operation. $T_{\varepsilon_g,avg}$ gives the average time taken to calculate the void fraction. The ratio $T_{\varepsilon_g,tot}/T_{sim}$ indicates the relative amount of time spent calculating the void fraction during the period that the calculation time was sampled. For the coarse grid, there was no clear relation between the times required to

run the full simulations and the times required to calculate the void fraction. This result was not surprising since the simulations had weak gas-solid coupling. For the PCM, the total time spent calculating the void fraction was 0.02% of the total CPU time. Even for the satellite point method, the void fraction calculations accounted for only 1.21% of the total CPU time. In these simulations other processes would have had a larger influence on the total computational expense. For example, the contact forces between particles were another calculation that was computationally intensive. If there were a high number of particle pairs in contact, then the simulation would require more time to run than if there were a lower number of contacting pairs. When the bed was expanded, there were fewer contacts to resolve. The bed did not expand as much with the diffusive scheme ($\sigma = 2d_p$) compared to other void fraction schemes. Hence, the simulation using the diffusive scheme had to handle more particle contacts, leading to an increase in the simulation time overall, even though the time required to evaluate the void fraction calculation itself was short. Thus, the choice of void fraction scheme did not drastically increase the computational time, provided that the particle and fluid phases were weakly coupled and that all simulations use the same time step value.

For the fine grid simulations, the corrected cube DPVM required about the same amount of time to calculate the void fraction as for the coarse grid case. This was expected since the algorithm only considered the immediate neighbours of the cell in which the particles are centred, and hence scales with the number of particles and is not strongly influenced by the number of fluid grid cells. The diffusive method took considerably longer since the diffusion equation had to be solved for more cells compared to the coarse grid case. However, the diffusive method simulation had a much shorter run time overall, due to fewer fluid steps being performed (hence a longer mean time step) compared to the corrected cube simulation. The variance of the void fraction spatial gradients was around 1100 m^{-2} for the corrected cube method and 700 m^{-2} for the diffusive scheme. The means of the absolute normalised net gas mass flow rate were 0.84% for the corrected cube method and 0.58% for the diffusive scheme. These metrics suggested that the diffusive scheme offered superior mass conservation and spatial smoothing, allowing the solution to the system of equations to converge at a longer time step and hence reducing the overall computation time by about 15%. As an extreme case, the PCM was unstable using the fine grid. Thus, the choice of void fraction scheme had a noticeable effect upon the numerical stability for the fine grid simulations, but not for the coarse grid simulations.

Table 4.3. The time required to simulate 5 s of operation, T_{sim}, the number of fluid phase steps taken by the simulation, $N_{\mathrm{steps,g}}$, the average time to calculate the void fraction, $T_{\varepsilon_g,\mathrm{avg}}$, and the fraction of total simulation time spent calculating the void fraction, $T_{\varepsilon_g,\mathrm{tot}}/T_{\mathrm{sim}}$. The gas and particle phases were weakly coupled, i.e. void fraction was updated approximately every 400 DEM time steps.

Void Fraction Scheme	T_{sim} ($\times 10^3$ s)	$N_{\mathrm{steps,g}}$	$T_{\varepsilon_g,\mathrm{avg}}$ (ms)	$T_{\varepsilon_g,\mathrm{tot}}/T_{\mathrm{sim}}$
PCM	130	10000	2.8	0.02%
MFIX DPVM	130	10197	37.0	0.29%
Cube DPVM	123	10092	40.6	0.33%
Corrected-cube DPVM (coarse)	130	10198	76.0	0.60%
Diffusive $\sigma = 1d_p$ (coarse)	128	10000	23.4	0.18%
Diffusive $\sigma = 2d_p$	131	10002	22.0	0.17%
Satellite Point	124	10000	150	1.21%
Corrected-cube DPVM (fine)	581	26313	78.2	0.35%
Diffusive $\sigma = 1d_p$ (fine)	504	23273	161	0.74%

4.3.3 Comparison with experiment

The maps for the time-averaged vertical particle velocity along horizontal and vertical slices obtained using MRI were used as a reference against which the images produced from the simulation data were compared. For the coarse grid, the particle-weighted time-averaged vertical particle velocity maps parallel to the *x*-*z* plane are given in Figure 4.7, and for the *x*-*y* plane in Figure 4.8. The slice was 5 mm thick and located along the centre of the bed for the vertical images and at 22 mm above the distributor for the horizontal images. From visual observation, it was apparent that the velocity maps for each void fraction scheme were in qualitative agreement with the experimental data, with the bubbles ascending along the centre of the bed, regardless of which void fraction scheme was used. The experimental measurements show some asymmetry in the location and shape of the bubbling region, where the particles have high upward velocities. The cause of asymmetry of the bubbling region in the experiment was not clear but could arise from slight imperfections in the symmetry of the experimental apparatus. The simulations predicted that the central bubbling region was wider and more circular than what was recorded by the experiment. The simulations also showed higher particle velocities close to the distributor than was seen experimentally; no downwards particle velocities were observed near the distributor in the coarse grid simulations. A quantitative comparison of the experimental and simulated coarse grid velocity data is given

in Figure 4.9. Velocity profiles obtained from three separate experiments are shown in Figure 4.9(b) and indicate slight differences in the maximum velocity and width of the high-velocity region but confirm the reproducibility of the experimental measurements. The measurement uncertainty is indicated by the dashed lines in Figure 4.9(a) and is approximately 0.02 m s^{-1}. The simulation results in Figure 4.9(a) show the same trend as the experiments with high velocity in the centre of the bed that increases with height above the distributor. As seen in Figure 4.9(b), close to the vertical walls, the simulations were in good agreement with the experimental data. However, the central bubbling region in the simulations was wider when compared to the experiment, the simulations did not predict negative velocity near the base of the bed, and the velocity between $z = 20$ mm and $z = 30$ mm was higher than what was observed experimentally.

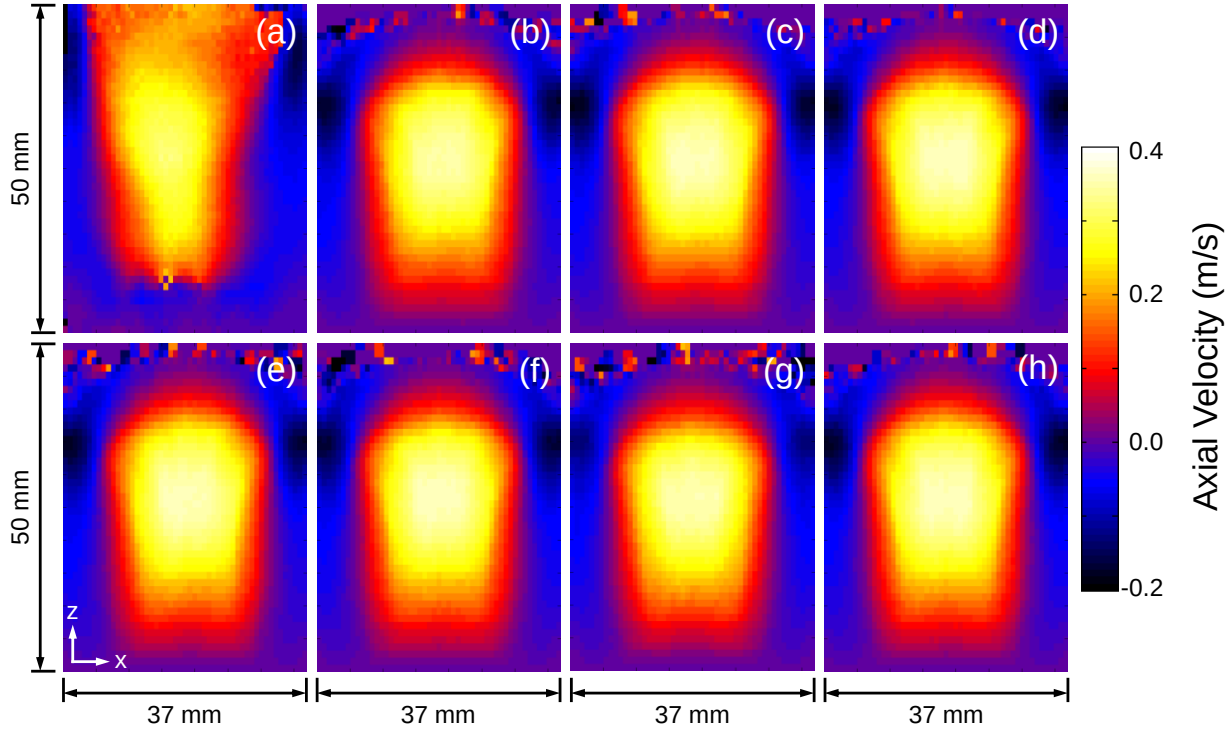

Figure 4.7. Particle-weighted time-averaged maps of the vertical component of the particle velocity along a central slice parallel to the *x*-*z* plane for: (a) experiment, (b) particle-centered method, (c) MFIX DPVM, (d) cube DPVM, (e) corrected cube DPVM, (f) diffusive scheme with $\sigma = 1d_p$, (g) diffusive scheme with $\sigma = 2d_p$, (h) satellite point method. Simulations were performed using the coarse fluid grid. The resolution of each image is 0.7 mm (*x*) × 1.09 mm (*z*).

The relative discrepancies between the horizontal particle velocity maps obtained using the void fraction schemes were found using Equation 4.12 shown in Table 4.4. The DPVM, diffusive and satellite point schemes all yield very similar time averaged particle velocity maps with discrepancies typically < 1%. However, the PCM void fraction scheme resulted in larger discrepancies of around 3% when compared with the other void fraction schemes. The higher discrepancy for the PCM scheme was due to the slight offset in the high-velocity bubbling region of the PCM velocity map compared to the other maps. These results indicate that there is little difference between the void fraction schemes when using a coarse grid, and suggest any of the methods are suitable for simulating the gas-solid flow in this fluidised bed qualitatively.

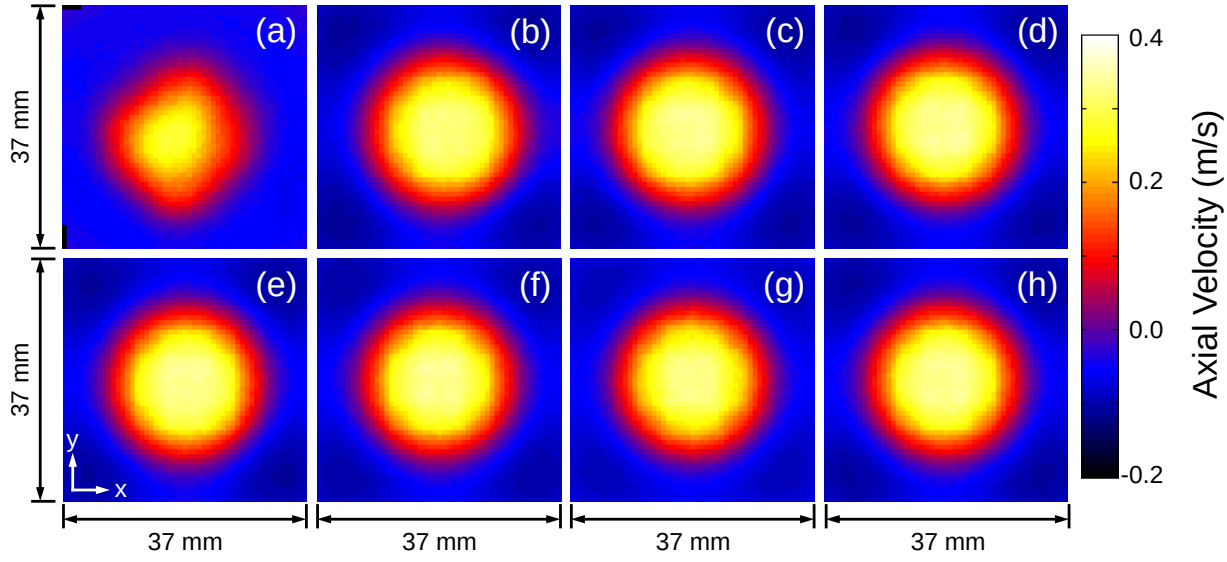

Figure 4.8. Particle-weighted time-averaged maps of the vertical component of the particle velocity along a horizontal slice centered at z = 22 mm for: (a) experiment, (b) particle-centered method, (c) MFIX DPVM, (d) cube DPVM, (e) corrected cube DPVM, (f) diffusive scheme with $\sigma = 1d_p$, (g) diffusive scheme with $\sigma = 2d_p$, (h) satellite point method. Simulations were performed using the coarse fluid grid. The resolution of each image is 0.7 mm (x) × 0.7 mm (y).

The discrepancies between the simulation and the experiments are shown in Table 4.5. For the vertical maps, the discrepancy was generally between 15% and 20%, and the discrepancies for the horizontal slice was between 30% and 45% for all void fraction schemes. It was of interest that the error in the PCM results was around the lowest of all of the schemes; this observation was attributed to the offset in the bubbling region of the PCM simulations coinciding with the offset bubbling region from the experiments. It is unlikely that these results would generalise to all conditions, owing to the error in the local void

fraction simulations seen in Figure 4.5. The large error in the horizontal slices arises from differences in the bed expansion and width of the central upward moving particle region. Other studies have found that the behaviour of bubbling fluidised beds was not sensitive to the choice of contact force scheme [38] or contact parameters [27]. Here, it was found that all void fraction schemes give similar results, indicating that this discrepancy is unlikely to be due to errors in the void fraction calculation either. Therefore, the effect of refining the fluid grid was investigated.

Table 4.4. Total relative discrepancy between the coarse grid particle-weighted time-averaged vertical particle velocity maps from Figure 4.8. The items along the top row took the place of $\zeta^{A}(x)$, the items along the left-hand column took the place of $\zeta^{B}(x)$.

	PCM	MFIX DPVM	Cube DPVM	Corrected-cube DPVM	Diffusive $\sigma = 1d_p$	Diffusive $\sigma = 2d_p$	Satellite Point
PCM		4.76%	4.08%	1.42%	3.17%	3.31%	3.54%
MFIX DPVM	4.93%		0.47%	1.14%	0.51%	1.48%	0.50%
Cube DPVM	4.29%	0.47%		1.09%	0.19%	0.80%	0.06%
Corrected-cube DPVM	1.47%	1.15%	1.08%		0.61%	1.21%	0.80%
Diffusive $\sigma = 1d_p$	3.20%	0.50%	0.18%	0.60%		0.42%	0.09%
Diffusive $\sigma = 2d_p$	3.09%	1.34%	0.71%	1.08%	0.39%		0.57%
Satellite Point	3.69%	0.51%	0.06%	0.80%	0.09%	0.64%	

The particle-weighted time averaged vertical velocities for the fine grid simulations are given in Figure 4.10. For both tested void fraction schemes, the fine grid simulations predict less regular bubbles and were able to predict the negative particle velocity at the base of the system and the magnitude of the velocity in the center of the bed. Jets due to the inlet holes were more prominent in the simulation than in the experiment, since a cuboidal cell with a side length of ~1.75 mm was not a perfect representation of a 1 mm diameter hole. Fine grid simulations were also performed using a uniform inlet shown by Figure 4.10. These

simulations exhibited similar features to the coarse grid simulations such as positive velocity at the base of the bed, while the horizontal profile 22 mm above the base was similar to the fine grid with the realistic inlet. Hence the large error in the coarse grid horizontal maps was reduced by increasing the grid resolution. At heights greater than 22 mm above the distributor, the fine grid simulation with the uniform inlet closely matches the fine grid simulation with the realistic inlet, while the coarse grid simulations differ significantly. These results suggest that the bubbles are not adequately represented when using the coarse grid. Therefore, it is necessary for the fluid grid to be sufficiently refined that it can capture the boundary conditions and flow features such as bubbles accurately, and that this may require cells as small as $1.6d_p$. The results also highlight the need for accurate void fraction schemes in these situations, where the PCM method was ineffective.

Table 4.5. Total relative discrepancy between the particle-weighted time-averaged particle-phase velocity maps of the simulations and the experiment. Only the bottom 40 mm of data was used for the vertical slice discrepancy since there were not enough particle samples to accurately calculate the average particle velocity in the uppermost pixels of the velocity maps.

Fluid Grid	Void Fraction Scheme	$\Delta v_{s,\text{avg},x-z}$	$\Delta v_{s,\text{avg},x-y}$
Coarse	PCM	13.2%	35.4%
	MFIX DPVM	15.1%	38.6%
	Cube DPVM	17.7%	43.6%
	Corrected-cube	15.1%	39.5%
	Diffusive σ = $1d_p$	16.8%	39.0%
	Diffusive σ = $2d_p$	16.4%	34.3%
	Satellite Point	17.8%	42.6%
Fine	Corrected-cube	10.9%	12.2%
	Corrected-cube (uniform inlet)	11.0%	16.4%
	Diffusive σ = $1d_p$	12.0%	12.6%
	Diffusive σ = $1d_p$ (uniform inlet)	15.6%	16.3%
Very Fine	Corrected-cube	16.1%	16.6%

Thus, it is likely that the discrepancy arises in part from insufficient resolution of the inlet geometry, even with the fine grid simulations. To test this theory further, a very fine grid was simulated, where the cell size was $1.3d_p$, however the quantitative agreement with the experiment was inferior to the fine grid simulations, shown in Figure 4.9(c) and (d). These results are consistent with the findings of Peng et al. [5] and Boyce et al. [6], who both identified problems in CFD-DEM simulations when the cell size becomes too small. These

errors were attributed to a breakdown of the volume averaging assumptions used to derive the fluid equations.

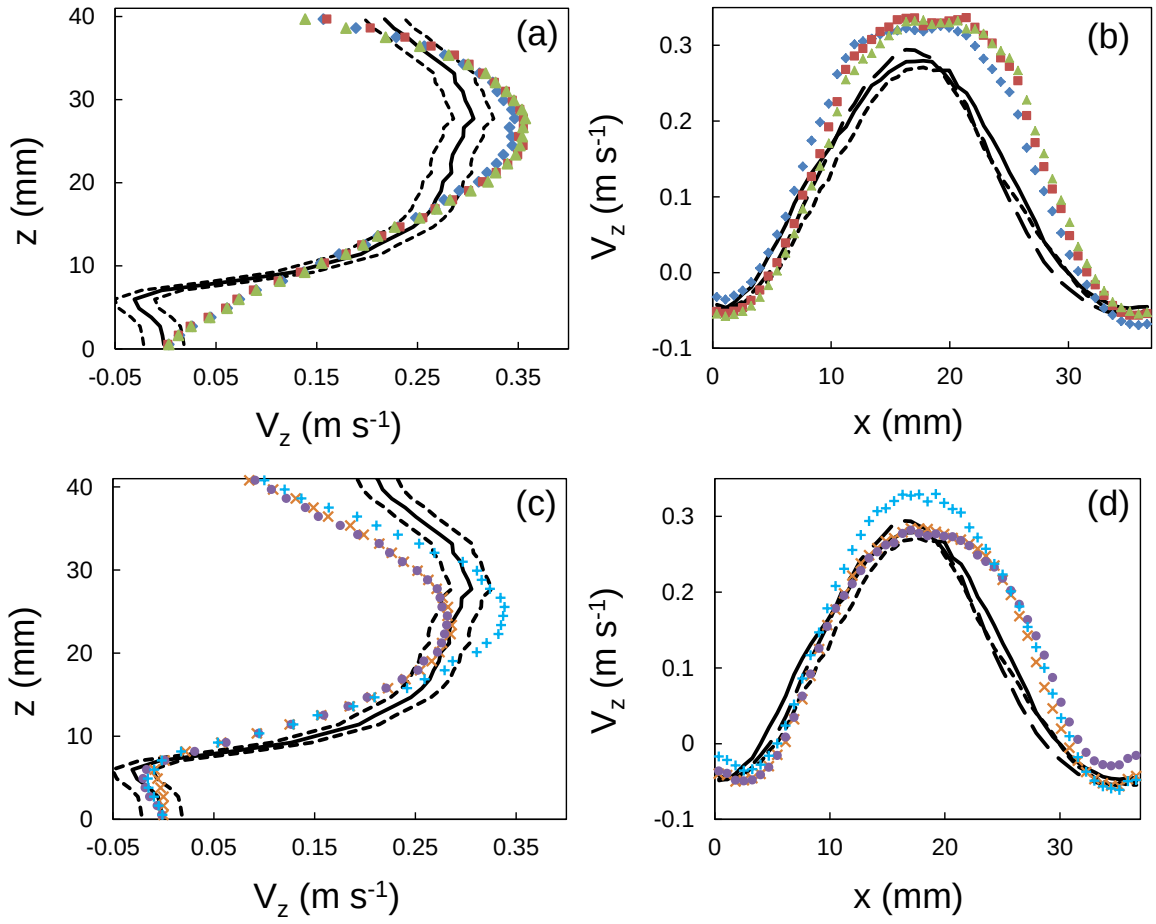

Figure 4.9.Comparison of the experimental measurement and coarse grid simulations for the particle-weighted time-averaged vertical component of the particle velocity. The profiles are shown along the: (a),(c) central axis in the *z*-direction at *x* = 18.5 mm, and *y* = 18.5 mm, (b),(d) *x*-direction at *y* = 18.5 mm and *z* = 22 mm. (Experiments: lines, coarse PCM: ♦, coarse corrected cube DPVM: ■, coarse diffusive with $\sigma = 1d_p$: ▲, fine grid with corrected cube DPVM: ●, fine diffusive with $\sigma = 1d_p$: ×, very fine grid with corrected cube DPVM: +.)

Figure 4.9(c) illustrates the effect that the enhanced inlet boundary condition had upon the vertical profile of the particle velocity. For $z < 25$ mm, the fine grid was in excellent agreement with the experiment. Compared to the equivalent coarse grid simulations, the fine grid simulations reduced the discrepancy with the experiment from ~15% to ~10% in the vertical images and from ~30% to ~10% in the horizontal images. Figure 4.9(d) shows that the fine grid predicted a narrower high velocity region near the centre, and the maximum velocity is closer to the experiment compared to the coarse grid. These simulations accurately represent the experimental measurements in the vicinity of the distributor, indicating that it is

essential to model the gas inlet with a sufficiently fine resolution to capture gas flow accurately.

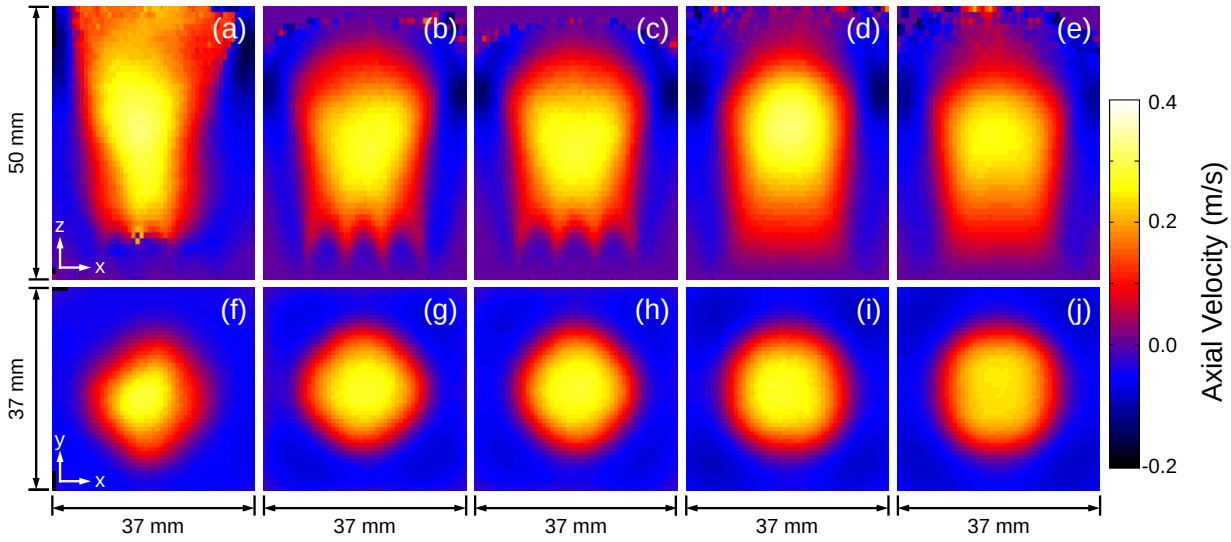

Figure 4.10. Particle-weighted time-averaged maps of the vertical component of the particle phase velocity along a central slice parallel to the *x*-*z* plane for: (a) experiment, (b) corrected cube DPVM with drilled plate inlet, (c) diffusive scheme ($\sigma = 1d_p$) with drilled plate inlet, (d) corrected cube DPVM with uniform inlet, (e) diffusive scheme ($\sigma = 1d_p$) with uniform inlet. The resolution of the images along the top row is 0.7 mm (*x*) × 1.09 mm (*z*). Velocity maps along a horizontal slice centered at *z* = 22 mm for: (f) experiment, (g) corrected cube DPVM with drilled plate inlet, (h) diffusive scheme ($\sigma = 1d_p$) with drilled plate inlet, (i) corrected cube DPVM with uniform inlet, (j) diffusive scheme ($\sigma = 1d_p$) with uniform inlet. Simulations used the refined fluid grid. The resolution of the images along the lower row is 0.7 mm (*x*) × 0.7 mm (*y*).

4.4. Conclusions

A square bubbling fluidised bed was modelled using the CFD-DEM multiphase flow simulation method with several different void fraction schemes at three levels of grid refinement. For the coarse grid, all void fraction schemes produced void fraction maps that were in good agreement with the exact void fraction. Under these conditions, the choice of void fraction scheme did not have an appreciable impact upon the results of the simulation, however there was an error of approximately 30% in the quantitative predictions of the particle velocity in these cases. The inlet geometry was able to be modelled more accurately by using a fine grid with a cell size of $1.6d_p$. The particle velocity maps obtained from the fine grid simulations were in good qualitative and quantitative agreement with the experiment, providing velocity maps with a relative error of only 10% for both void fraction schemes tested with the fine grid. It was also found that the PCM was unsuitable for

calculating the void fraction with such a refined fluid grid, in agreement with previous research [5, 6]. Furthermore, if the cell size was reduced below $1.6d_p$, the quantitative agreement of the simulations and the experiments worsened.

In conclusion, it was found that the PCM approach is only valid for large cell sizes, consistent with the recommendation of Peng et al. [5]. All other approximate void fraction schemes were able to produce similar void fraction fields and velocity fields in similar computational time, provided that the length scale over which the void fraction is distributed is approximately equal to the diameter of the particles. If run time is critical, the diffusive scheme is attractive, but in most cases the corrected cube method proposed by Khawaja et al. is likely preferable. Finally, it is important to consider the relevant dimensions of the fluid phase cells, if CFD-DEM is to become established as a design tool in engineering.

4.5. References

1. Khawaja, H., et al., *Quantitative analysis of accuracy of voidage computations in CFD-DEM simulations.* Journal of Computational Multiphase Flows, 2012. **4**(2): p. 183-192
2. van der Hoef, M.A., M. van Sint Annaland, and J.A.M. Kuipers, *Computational fluid dynamics for dense gas-solid fluidized beds: A multi-scale modeling strategy.* Chemical Engineering Science, 2004. **59**: p. 5157-5165
3. Freireich, B., M. Kodam, and C. Wassgren, *An exact method for determining local solid fractions in discrete element method simulations.* AIChE Journal, 2010. **56**(12): p. 3036-3048
4. Anderson, T.B. and R. Jackson, *A Fluid Mechanical Description of Fluidized Beds.* Industrial & Engineering Chemistry Fundamentals, 1967. **6**(4): p. 527-539
5. Peng, Z., et al., *Influence of void fraction calculation on fidelity of CFD-DEM simulation of gas-solid bubbling fluidized beds.* AIChE Journal, 2014. **60**(6): p. 2000-2018
6. Boyce, C.M., et al., *Limitations on Fluid Grid Sizing for Using Volume-Averaged Fluid Equations in Discrete Element Models of Fluidized Beds.* Industrial and Engineering Chemistry Research, 2015. **54**(43): p. 10684-10697
7. Sun, R. and H. Xiao, *Diffusion-based coarse graining in hybrid continuum–discrete solvers: Theoretical formulation and a priori tests.* International Journal of Multiphase Flow, 2015. **77**: p. 142-157
8. Tsuji, Y., T. Kawaguchi, and T. Tanaka, *Discrete particle simulation of two-dimensional fluidized bed.* Powder Technology, 1993. **77**(1): p. 79-87
9. Sun, R. and H. Xiao, *Diffusion-based coarse graining in hybrid continuum–discrete solvers: Applications in CFD–DEM.* International Journal of Multiphase Flow, 2015. **72**: p. 233-247
10. Strobl, S., A. Formella, and T. Pöschel, *Exact calculation of the overlap volume of spheres and mesh elements.* Journal of Computational Physics, 2016. **311**: p. 158-172
11. NETL, *MFIX 2015-1 User Guide*. 2015.
12. Link, J.M., et al., *Flow regimes in a spout-fluid bed: A combined experimental and simulation study.* Chemical Engineering Science, 2005. **60**(13): p. 3425-3442
13. Zhu, H.P. and A.B. Yu, *Averaging method of granular materials.* Physical Review E - Statistical, Nonlinear, and Soft Matter Physics, 2002. **66**(2): p. 021302/1-021302/10
14. Fries, L., et al., *DEM-CFD modeling of a fluidized bed spray granulator.* Chemical Engineering Science, 2011. **66**(11): p. 2340-2355
15. Peng, Z., B. Moghtaderi, and E. Doroodchi, *A modified direct method for void fraction calculation in CFD-DEM simulations.* Advanced Powder Technology, 2016. **27**(1): p. 19-32
16. Gui, N., J.R. Fan, and K. Luo, *DEM-LES study of 3-D bubbling fluidized bed with immersed tubes.* Chemical Engineering Science, 2008. **63**(14): p. 3654-3663
17. Radl, S., et al., *State of the Art in Mapping Schemes for Dilute and Dense Euler-Lagrange Simulations*, in *10th International Conference on CFD in Oil & Gas, Metallurgical and Process Industries*. 2014: Trondheim, Norway. p. 1 - 9.
18. Hobbs, A., *Simulation of an aggregate dryer using coupled CFD and DEM methods.* International Journal of Computational Fluid Dynamics, 2009. **23**(2): p. 199-207
19. Boyce, C.M., et al., *Novel fluid grid and voidage calculation techniques for a discrete element model of a 3D cylindrical fluidized bed.* Computers and Chemical Engineering, 2014. **65**: p. 18-27

20. Holland, D.J., et al., *Spatially resolved measurement of anisotropic granular temperature in gas-fluidized beds.* Powder Technology, 2008. **182**(2): p. 171-181
21. Syamlal, M., W. Rogers, and T.J. O'Brien, *MFIX documentation theory guide*. 1993.
22. Garg, R., et al., *Open-source MFIX-DEM software for gas-solids flows: Part I-Verification studies.* Powder Technology, 2012. **220**: p. 122-137
23. Musser, J. and A. Choudhary, *MFIX Documentation Volume 3: Verification and Validation Manual*. 2015.
24. Li, T., et al., *The NETL MFiX Suite of multiphase flow models: A brief review and recent applications of MFiX-TFM to fossil energy Technologies.* Chemical Engineering Science, 2017. **169**(Supplement C): p. 259-272
25. Li, T., et al., *Open-source MFIX-DEM software for gas-solids flows: Part II — Validation studies.* Powder Technology, 2012. **220**: p. 138-150
26. Gopalakrishnan, P. and D. Tafti, *Development of parallel DEM for the open source code MFIX*. Powder Technology, 2013. **235**: p. 33-41
27. Müller, C.R., et al., *Validation of a discrete element model using magnetic resonance measurements.* Particuology, 2009. **7**(4): p. 297-306
28. Ye, M., M.A. van der Hoef, and J.A.M. Kuipers, *From discrete particle model to a continuous model of Geldart a particles.* Chemical Engineering Research and Design, 2005. **83**(7 A): p. 833-843
29. Beetstra, R., M.A. Van Der Hoef, and J.A.M. Kuipers, *Drag force of intermediate reynolds number flow past mono- And bidisperse arrays of spheres.* AIChE Journal, 2007. **53**(2): p. 489-501
30. Shäfer, J., S. Dippel, and D. Wolf, *Force schemes in simulations of granular materials.* Journal de Physique I, 1996. **6**(1): p. 5-20
31. Silbert, L.E., et al., *Granular flow down an inclined plane: Bagnold scaling and rheology.* Physical Review E, 2001. **64**(5): p. 051302
32. Garg, R., et al., *Documentation of open-source MFIX-DEM software for gas-solids flows*. 2012.
33. Deen, N.G., et al., *Review of discrete particle modeling of fluidized beds.* Chemical Engineering Science, 2007. **62**: p. 28-44
34. Boyce, C.M., et al., *Adapting data processing to compare model and experiment accurately: A discrete element model and magnetic resonance measurements of a 3d cylindrical fluidized bed.* Industrial and Engineering Chemistry Research, 2013. **52**(50): p. 18085-18094
35. Johnson, N.L., *Systems of frequency curves generated by methods of translation.* Biometrika, 1949. **36**(Pt. 1-2): p. 149-176
36. Kloss, C., et al., *Models, algorithms and validation for opensource DEM and CFD-DEM.* Progress in Computational Fluid Dynamics, 2012. **12**(2-3): p. 140-152
37. Hilton, J.E., L.R. Mason, and P.W. Cleary, *Dynamics of gas-solid fluidised beds with non-spherical particle geometry.* Chemical Engineering Science, 2010. **65**(5): p. 1584-1596
38. Di Maio, F.P. and A. Di Renzo, *Modelling Particle Contacts in Distinct Element Simulations.* Chemical Engineering Research and Design, 2005. **83**(11): p. 1287-1297

5. Measurement of rotational granular dynamics with MRI

The velocity distribution is an important variable involved with continuum simulations of granular systems. The integrity of continuum models necessitates validation of simulation results by comparison with experimental data. Nuclear magnetic resonance imaging of granular flow relies on assumptions relating to sampling time, time averaging and particle rotation. In this study, these assumptions were tested by performing discrete element method (DEM) simulations of spherical particles inside a Couette shear cell. The data were processed according to several definitions of the granular temperature and by simulations of pulsed field gradient (PFG) MRI experiments. In order to match the simulated MRI results, direct averaging of the DEM data had to account for the effect of time averaging and sampling time. The simulated MRI experiments demonstrated that particle rotation amplified the granular temperature measurements. A model was proposed to relate the MR signal to the angular velocity distribution in a sample and was validated by MRI simulation results. The key advance of this chapter over previous approaches is that a model to describe the effects of particle rotation on the measured signal has been developed.

5.1. Introduction

Granular materials demonstrate complicated, scale dependent flow behaviour that is difficult to predict. Depending on the local flow conditions, granular material may behave analogously to solid, liquid and gaseous states of matter. It is desirable to predict the behaviour of granular material using a continuum description, as is used with liquids and gases. There has been some success in describing granular flows using local rheological models [1]. However, granular flows are also known to exhibit non-local [2, 3] flow characteristics, that arise from the finite size of the grains. The non-local rheology has been linked to the velocity fluctuations of individual granules [3-5] and/or rotational motion of particles [6, 7]. Detailed experimental measurements of the granular flow dynamics are required to aid the development of these non-local rheological models. However, optical measurements of the dynamics are challenging owing to the opacity of granular beds, even if individual granules

themselves are made from transparent material. Here a magnetic resonance imaging approach is investigated to measure the granular flow dynamics.

When considering continuum descriptions of granular flow, it is conventional to use a Reynolds decomposition of the particle velocity $\boldsymbol{v}_p$, that is $\boldsymbol{v}_p$ is expressed as the sum of the mean $\boldsymbol{v}$, and fluctuation $\boldsymbol{u}$, of the velocity:

$$\boldsymbol{v}_p = \boldsymbol{v} + \boldsymbol{u}. \tag{5.1}$$

Measurement techniques to probe the velocity distribution include using acoustic shot noise [8], particle image velocimetry [9], diffusing wave spectroscopy [10] and speckle visibility spectroscopy [11]. However, these techniques are limited to observations in the near wall region or surface of the particles. Particle tracking techniques are not restricted to surface observations; however observations are typically restricted to the use of a single tracer particle and thus do not directly probe the entire ensemble [12-14]. Furthermore, only magnetic particle tracking is able to measure rotational motion [15]. Magnetic Resonance Imaging (MRI) is a promising alternative technique that can measure the entire ensemble inside optically opaque systems. For granular flows, MRI has been used to image the diffusion coefficient, correlation time, voidage [16], particle phase velocity [17] and velocity variance [18] in systems such as: rotating drums, vibro-fluidised beds [19], gas fluidised beds [20] and Couette shear cells [21]. The effect of rotation of the particles in an MRI experiment has not previously been considered.

One challenge when developing a new MRI measurement is the validation of the measurement. The physics of MRI is well understood and can be applied to many problems. However, the effect of factors such as velocity, acceleration and encoding time can be difficult to predict. Simulations of the signal acquisition with MRI are sometimes used to assist with quantifying these higher-level effects. The discrete-time solution of the Bloch equations [22] gives the spin magnetisation which is used to obtain the complex signal from which the image is generated. Modelling the transport of magnetisation due to flow allows for the effect of flow on the image to be studied [23]. Here the discrete element method (DEM) is used to generate a simulated particle flow field that can be used to confirm the model of rotational motion developed in this paper.

In DEM, Newton's second law of motion is numerically integrated with respect to time for each particle individually [24]. DEM simulations have been used to characterise a variety of granular flows, including annular Couette shear cells [25], rotating kilns [26, 27], and

hoppers [28]. DEM simulations are used to explore the fundamentals of granular flow in different flow regimes [29, 30], to characterise the rheology of the bulk material [1, 31, 32], and to investigate fluid-particle interaction [33, 34]. MRI has previously been used to validate DEM models of granular flow by measuring the voidage, velocity, and velocity fluctuations [35, 36]. DEM has also been used to investigate MRI measurements by integrating the resulting particle position information with equations to describe the MRI signal. These simulations were able to confirm that the mean velocity obtained from experiments is equivalent to a particle-weighted time averaged velocity [37]. In these simulations, particles were approximated as point masses and so the effects of rotation could not be modelled; the measurement of fluctuations in the particles' velocities was not considered.

This chapter presents a detailed investigation of pulsed-field-gradient (PFG) MRI measurements of the fluctuating component of the particles motion, including the effect of rotation. DEM simulations of an assembly of particles in a Couette cell under annular shear are used to produce a set of particle velocities and positions. These are then used to simulate the effects of time averaging on the measurement of velocity and velocity fluctuations. A theoretical model is also developed to describe the effect of rotation of granules on PFG measurements. The model is validated with numerically simulated MRI measurements of DEM simulations. In this work, the particles are modelled as a collection of uniformly distributed sub-units (denoted as satellite points) to approximate the nuclei present within real particles. Thus, the DEM simulations are used to confirm the validity of the theoretical model of the effect of rotation on the signal. The theoretical model of a PFG experiment, including the effects of rotation is first described. DEM simulations are then used to confirm the effect of time averaging on the measurement of motion and to validate the model of rotation.

5.2. Theory

Conventional Analysis

PFG experiments can be used to measure the velocity distribution of fluids or particles [38]. The phase shift of a spin is the integral of the strength of the magnetic field gradient and the position of the spin, $\boldsymbol{x}$, with respect to time

$$\theta = \gamma \int \boldsymbol{g}(t) \cdot \boldsymbol{x}(t)\, dt \tag{5.2}$$

where the gyromagnetic ratio is represented by γ and the gradient is denoted by $\boldsymbol{g}(t)$. For granular systems, signal is detected from the spins in the particles. The particle position is

decomposed into an initial position, $\boldsymbol{x}_0$, local mean velocity $\boldsymbol{v}$ and spatial fluctuation about the mean velocity $\boldsymbol{u}$ giving:

$$\theta = \gamma \int t\boldsymbol{g}(t) \cdot (\boldsymbol{v} + \boldsymbol{u})\, dt + \gamma \boldsymbol{x}_0 \cdot \int \boldsymbol{g}(t)\, dt. \tag{5.3}$$

For PFG measurements, the integral $\int \boldsymbol{g}(t)\, dt = 0$, and the second term on the RHS is equal to zero. Analogous to the concept of *k*-space for spin density imaging, an inverse variable known as $\boldsymbol{p}$ is defined by $\boldsymbol{p} = \gamma \int \boldsymbol{g}(t) t\, dt$. If acceleration and higher derivatives of position are ignored, the signal within a finite volume element is then defined as:

$$S(\boldsymbol{p}) = \int \rho(\boldsymbol{x}) \exp\big(i\boldsymbol{p} \cdot (\boldsymbol{v} + \boldsymbol{u})\big)\, dV, \tag{5.4}$$

where $\rho(\boldsymbol{x})$ is the spin density at position $\boldsymbol{x}$. We define the motion encoding as along the *x*-axis. Since the measurement is along x, only the components v_x, u_x and p_x need to be considered. If we assume the particles are point sources for the MR signal, then by defining the velocity distribution within the volume element as $P(u_x)$, the integral may be expressed as:

$$S(p_x) = \int P(u_x) \exp(ip_{\boldsymbol{x}}(v_x + u_x) du_x. \tag{5.5}$$

Given that the mean velocity is constant and assuming that the velocity distribution along x is Gaussian allows Equation 5.5 to be integrated with respect to u_x.

$$S(p_x) = \frac{1}{\sqrt{\langle u_x^2 \rangle 2\pi}} \exp(ip_x v_x) \exp\left(-\frac{1}{2} p_x^2 \langle u_x^2 \rangle\right). \tag{5.6}$$

The signal for when the gradient (and hence p_x) is equal to zero is denoted as S_0, and is used to normalise the signal. Thus, the phase of the normalised signal provides information about the mean velocity v_x, whereas the absolute value of the normalised signal gives the variance of velocity:

$$\left|\frac{S}{S_0}\right| = \exp\left(-\frac{1}{2} p_x^2 \langle u_x^2 \rangle\right) \approx 1 - \frac{1}{2} p_x^2 \langle u_x^2 \rangle. \tag{5.7}$$

According to Equation 5.7, the natural logarithm of the absolute value of the normalised signal has a quadratic relationship with p_x. At low values of p_x, the approximation of a quadratic relationship between the normalised signal and p_x can be made. The velocity variance is given by the coefficient of p_x^2.

Signal from rotation

Particle rotation is not normally considered in MR. However, it also contributes to the signal since the spins on a rotating particle will travel with different velocities. We define a Cartesian coordinate system x, y, z; where the flow encoding axis is along the *x*-axis. Therefore, we consider only rotation along the *y* and *z* axes, the angular velocity about these axes are denoted by ω_y and ω_z. Rotation about *x* does not affect the signal. Assuming that $\omega\Delta$ is sufficiently small (< 0.5 rad [39]), it is reasonable to assume the projection of the linear velocity along the velocity encoding axis is constant during the period Δ. Thus, the signal has a general form given by:

$$S = \int f(\omega_y, \omega_z, u_x) \exp\left(ip_x\left(v_x + u_x + z\omega_y + y\omega_z\right)\right) dV \tag{5.8}$$

where $f(\omega_y, \omega_z, u_x)$ describes the probability that a particle has a linear fluctuating velocity u_x and angular velocities equal to ω_y and ω_z. It was assumed that the distributions of the linear and angular velocities were independent, i.e. $f(\omega_y, \omega_z, u_x) = P(\omega_y)P(\omega_z)P(u_x)$, where $P(\omega_y)$ and $P(\omega_z)$ are the angular velocity distributions about axes *y* and *z*, respectively. It was assumed that $P(\omega_y)$ and $P(\omega_z)$ are Gaussian distributed, with a mean of zero and the variance denoted by $\langle\omega_y^2\rangle$ and $\langle\omega_z^2\rangle$. The mean velocity term is taken outside the integral and the integration with respect to u_x is performed as described in the previous section. Thus, the signal takes the form:

$$S(p_x) = \frac{\exp(ip_x v_x)\exp\left(-\frac{p_x^2}{2}\langle u_x^2\rangle\right)}{\sqrt{\langle u_x^2\rangle 2\pi}} \times$$
$$\int P(\omega_y)\int P(\omega_z)\iiint_V \exp\left(i\mathrm{p}_x\left(z\omega_y + y\omega_z\right)\right) dV_p\, d\omega_y d\omega_z. \tag{5.9}$$

The integration is simplified by approximating the exponential terms as Taylor series expansions:

$$S(p_x) = \frac{\exp(ip_x v_x)\exp\left(-\frac{p_x^2}{2}\langle u_x^2\rangle\right)}{\sqrt{\langle u_x^2\rangle 2\pi}} \times$$
$$\int P(\omega_y)\int P(\omega_z)\iiint_V \sum_{n=0}^{\infty}\frac{i^n\left(p_x z\omega_y\right)^n}{n!}\sum_{n=0}^{\infty}\frac{i^n(p_x y\omega_z)^n}{n!}\, dV_p\, d\omega_y d\omega_z. \tag{5.10}$$

Expressing these series multiplications as Cauchy products gives:

$$S(p_x) = \frac{\exp(ip_x v_x)\exp\left(-\frac{p_x^2}{2}\langle u_x^2\rangle\right)}{\sqrt{\langle u_x^2\rangle 2\pi}} \times$$
$$\int P(\omega_y)\int P(\omega_z)\iiint_V \sum_{m=0}^{\infty}\sum_{l=0}^{m}\frac{i^m p_x^m z^l \omega_y^l y^{m-l}\omega_z^{m-l}}{l!\,(m-l)!}\,dV_p d\omega_y d\omega_z. \quad (5.11)$$

Taking the independent terms out of the volume integral gives:

$$S(p_x) = \frac{\exp(ip_x v_x)\exp\left(-\frac{p_x^2}{2}\langle u_x^2\rangle\right)}{\sqrt{\langle u_x^2\rangle 2\pi}} \times$$
$$\sum_{m=0}^{\infty}\sum_{l=0}^{m}\frac{i^m p_x^m}{l!\,(m-l)!}\int P(\omega_y)\omega_y^l \int P(\omega_z)\,\omega_z^{m-l}\iiint_V z^l y^{m-l}\,dV_p d\omega_y d\omega_z. \quad (5.12)$$

The triple integral over the spherical region was found by converting to spherical coordinates and performing iterated integrals using reduction formulae. Details about the calculation of this integral are included in Section 5.2.1. If either one or both exponents are odd, the integral is equal to zero. Hence the signal associated with particle rotation is real. If the exponents are even, then the result takes the form: $c_{l,m-l}R^{m+3}$, where R is the particle radius and $c_{l,m-l}$ is the coefficient obtained from the triple integral for a particular term in the series. Equation 5.12 is then integrated with respect to each of the angular velocity components, these integrals take the following form:

$$\int_{-\infty}^{+\infty}\frac{1}{\sqrt{2\pi\langle\omega_y^2\rangle}}\exp\left(-\frac{\omega_y^2}{2\langle\omega_y^2\rangle}\right)\omega_y^l\,d\omega_y = \frac{(l-1)!!\sqrt{\pi}\left(2\langle\omega_y^2\rangle\right)^{(l+1)/2}}{2^{l/2}\sqrt{2\pi\langle\omega_y^2\rangle}}$$
$$= (l-1)!!\,\langle\omega_y^2\rangle^{l/2}. \quad (5.13)$$

Applying the result given by Equation 5.13 for each of the angular velocity components, followed by normalisation of the signal at $p_x = 0$ gives:

$$\frac{S}{S_0} = \exp(ip_x v_x)\exp\left(-\frac{p_x^2}{2}\langle u_x^2\rangle\right) \times$$
$$\sum_{m=0}^{\infty}\sum_{l=0}^{m}\frac{i^m(l-1)!!\,(m-l-1)!!}{c_{0,0}\,l!\,(m-l)!}\,p_x^m c_{l,m-l}R^m\langle\omega_y^2\rangle^{l/2}\langle\omega_z^2\rangle^{(m-l)/2}. \quad (5.14)$$

It is of interest to obtain the angular velocity variance in terms of the signal, For this reason, the series is truncated at m = 2. For consistency, the exponential that represents the linear velocity variance term is also truncated. Without prior knowledge of $\langle\omega_y^2\rangle$, $\langle\omega_z^2\rangle$ cannot be

determined (and vice versa). Thus, it is assumed that the system is isotropic, i.e. $\langle\omega_y^2\rangle = \langle\omega_z^2\rangle = \langle\omega^2\rangle$. Rewriting Equation 5.14 with these changes yields:

$$\frac{S}{S_0} = \exp(ip_x v_x)\left(1 - \frac{p_x^2}{2}\langle u_x^2\rangle\right)\left(1 - \frac{1}{5}p_x^2 R^2\langle\omega^2\rangle\right). \tag{5.15}$$

Hence, granule rotation contributes towards signal attenuation, whereas signal attenuation has previously been solely attributed to linear fluctuations in the standard analysis method. The rotational component of the signal may be expressed in terms of an apparent linear velocity variance, analogous to Equation 5.7. This apparent linear velocity variance is related to the angular velocity variance by:

$$\langle u_x^2\rangle_\omega = \frac{2}{5}R^2\langle\omega^2\rangle. \tag{5.16}$$

Equation 5.16 provides a basis to compare the magnitude of angular velocity fluctuations relative to linear velocity fluctuations.

5.2.1 Evaluation of volume integral

The integral $\int x^a y^b\, dV$, where $a = m - l$ and $b = l$ are positive integers was converted into spherical coordinates:

$$\int_0^r \int_0^\pi \int_0^{2\pi} r^{a+b+2}\sin(\theta)^{a+b+1}\sin(\varphi)^a\cos(\varphi)^b\, d\varphi d\theta dr \tag{5.17}$$

The integral with respect to φ was found using the following reduction formula which was applied recursively:

$$I_{a,b} = \int \sin^{\mathrm{a}}(x)\cos^{\mathrm{b}}(x)\, dx = \frac{\sin^{\mathrm{a-1}}(x)\cos^{\mathrm{b+1}}(x)}{a+b} + \frac{a-1}{a+b}I_{a-2,b} \tag{5.18}$$

As the definite integral is evaluated over the limits 0 and 2π, the first term on the right-hand side of Equation 5.18 is zero for every recursion due to the presence of the sine function. If a is an even integer, then the final term in the series is $I_{0,b} = \int \cos^{\mathrm{b}}(x)$. If a is an odd integer, then the final recursion $I_{1,b}$ contains a sine term and hence is zero. From this point onwards, we let a be an even integer. The coefficient of $I_{0,b}$ is the product of the preceding recursions.

$$I_{a,b} = I_{0,b}\prod_{i=1}^{a/2}\frac{2i-1}{2i+b} \tag{5.19}$$

The following recursion formula is used to derive $I_{0,b}$:

$$I_b = \int \cos^{\mathrm{b}}(x)\,dx = \frac{\sin(x)\cos^{\mathrm{b}-1}(x) + (b-1)I_{b-2}}{b} \tag{5.20}$$

Taking the definite integral over 0 to 2π cancels out all the trigonometric terms. If b is an even integer, then the final recursion $I_0 = \int_0^{2\pi} dx = 2\pi$. Thus, we let b be an even integer. I_0 has a coefficient that is the product of the preceding recursions, thus:

$$I_{a,b} = 2\pi \prod_{j=1}^{b/2} \frac{2j-1}{2j} \prod_{i=1}^{a/2} \frac{2i-1}{2i+b} \tag{5.21}$$

The integral with respect to θ was obtained by the following reduction formula:

$$I_c = \int \sin^{c}(x)\,dx = \frac{\cos(x)\sin^{\mathrm{c}-1}(x) + (c-1)I_{c-2}}{c} \tag{5.22}$$

where $c = a + b + 1$. If *a* and *b* are even, then *c* is odd. For this integral, the limits are 0 and π, hence the first term in Equation 5.22 is zero due to the sine function. The final term in the recursion is $I_1 = \int_0^{\pi} \sin(x)\,dx = 2$. The coefficient of I_1 is the product of preceding coefficients, thus:

$$I_c = 2 \prod_{k=1}^{c/2-1} \frac{2k}{2k+1} \tag{5.23}$$

Integration with respect to *r* from 0 to *R* gives:

$$\int_0^R r^{a+b+2}\,dr = \frac{R^{a+b+3}}{a+b+3} \tag{5.24}$$

The product of Equations 5.21, 5.23, and 5.24 gives the spherical integral for Equation 5.17:

$$\int x^a y^b\,dV = \frac{4\pi R^{a+b+3}}{a+b+3} \prod_{k=1}^{c/2-1} \frac{2k}{2k+1} \prod_{j=1}^{b/2} \frac{2j-1}{2j} \prod_{i=1}^{a/2} \frac{2i-1}{2i+b} \tag{5.25}$$

This integral is expressed in Section 5.2 as $c_{a,b}R^{a+b+3}$, the product of the granule radius term and a coefficient $c_{a,b}$, which is equal to:

$$c_{a,b} = \frac{4\pi}{a+b+3} \prod_{k=1}^{c/2-1} \frac{2k}{2k+1} \prod_{j=1}^{b/2} \frac{2j-1}{2j} \prod_{i=1}^{a/2} \frac{2i-1}{2i+b}. \tag{5.26}$$

5.3. Method

5.3.1 MRI experiment

The experiments used in this work for validation of the model are those of Fabich et al. [40], performed on a concentric cylinder rheo-NMR device. A complete description of the experimental measurements is already published; here only a brief summary of the key parameters is included. The Couette cell consisted of a stationary outer cylinder with inner diameter of 47.3 mm and a rotating inner cylinder whose dimension could be changed to control the gap size between the inner and outer wall. Particles were placed in the gap between the inner and outer cylinder. The base of the outer cylinder was fixed and the top of the bed was free to expand or contract. Particles were fixed to the walls of the cylinder to minimise slip and prevent solid body rotation. Experiments were performed with particles of diameter 0.44 mm, 0.60 mm and 1.0 mm with corresponding gap sizes of 7.65 mm, 7.65 mm, and 8.55 mm, respectively. Experiments were performed with inner wall velocities of 17 mm s^{-1} and 41 mm s^{-1}. The velocity distribution was measured using a slice-selective, pulsed-field-gradient spin echo measurement. Flow encoding was spatially resolved in the *y*-direction across the Couette cell with a 65 mm field-of-view and a resolution of 127 μm per pixel. Velocity was encoded in the *x*-direction, i.e. perpendicular to the direction of spatial encoding. A narrow slice of 1 mm was used to ensure that the curvature of the sample does not have a significant effect on the motion measured, hence providing a mapping $v_x = v_\theta$ of the Cartesian to cylindrical velocity components [41]. The flow encoding gradients were applied for a duration δ = 1 ms, with an observation time Δ = 3 ms. The choice of observation time may affect the measured velocity distribution due to collisions between granules. If Δ is below the mean collision time, then the velocity variance is expected to be independent of Δ [42]. For the experimental system, the velocity variance was insensitive to values of Δ between 3 and 4 ms [40], hence data collected using an observation time within this range is suitable for comparison.

5.3.2 Simulation details

The DEM simulations were performed in the open-source software LIGGGHTS. The full details of this programme are given by Kloss et al. [43]. In brief, the equations of motion are numerically solved for each particle. Collisions between particles were resolved using the Hertzian soft-sphere contact force scheme. The Couette cell had an outer diameter of 47.3 mm and an inner diameter of 32 mm, corresponding to the experimental geometry. To

replicate the seeds being glued to the side walls of the cell in the experimental setup, single layers of particles were placed in an FCC arrangement next to each wall. For the inner wall, the particle velocity components were set to match the linear velocity of the rotating cylinder. At the outer wall, the particle velocity components were set to zero. The system was initialised by simulating 40000 particles being poured into the annular gap. The particles were 0.44 or 0.6 mm diameter spheres. The system was sheared for 3 s. The rotational velocity of the inner cylinder was set to 17 mm s^{-1} or 41 mm s^{-1}. Figure 5.1 gives a diagram of the simulation domain and denotes the region from which data were selected. The Poisson ratio ν was set to 0.33, and the restitution coefficient e_n was 0.9. The static friction coefficient μ_f was tested at values of 0.1 and 0.5. These friction coefficients were not selected to be physically representative of the particles. Instead they were selected to illustrate how changing the friction can influence the contribution from rotational motion relative to linear motion. The elastic modulus for the particles was set to 1×10^7 Pa in order to ensure that the computational time required was suitably low. The time step Δt was fixed at 1×10^{-6} s. Time steps are advised to be below 25% of the Rayleigh time for numerical stability [44]. For the 0.44 mm particles with the given contact parameters, this time step was 8% of the Rayleigh time and was deemed to be sufficiently low. The velocity Verlet scheme was used to solve the equations of motion for the particle positions and velocities over time.

To obtain the spatial averages, a slice positioned along the *y*-axis was used analogous to that measured experimentally. The slice was divided into a series of voxels. The particles were binned to the voxels in which their centroids were located at the end of the sample period. For particles located in multiple voxels, the velocity was binned to each voxel and weighted by the volume fraction of the particle in each voxel. The volume fractions were calculated using the method of Khawaja et al. [45], which has previously been found to give accurate volume fractions and a low computation time [46]. The time averaged profiles were then obtained by taking the average over 30 samples collected at 0.1 s time intervals. Both sides of the slice were averaged, producing profiles of velocity and granular temperature against distance from the inner wall.

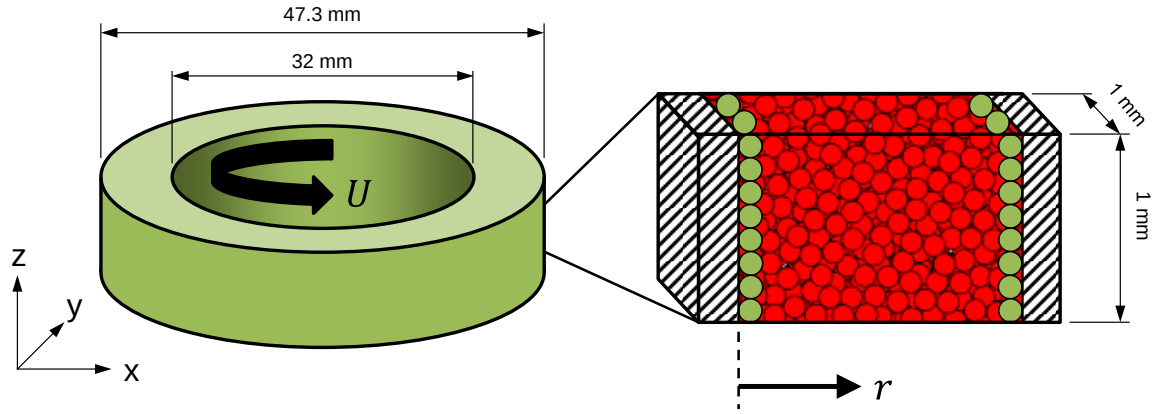

Figure 5.1. Diagram of the annular Couette flow system simulated by DEM. Data from the inset were used for post-processing.

5.3.3 MRI simulation algorithm

Simulating the MRI experiments enabled the contribution that particle rotation made to the signal to be determined. The signal was simulated using: (1) translational motion only, (2) rotational motion only, and (3) both translation and rotation. Differences in the mean and variance profiles of the velocity may be attributed to particle rotation. Each particle was represented as a collection of 3500 satellite points surrounding the centroid of the particle. The centre position of each particle was updated at each step by first-order numerical integration of the translational velocity obtained from the DEM simulation as a function of time. The difference between numerical integration of the velocity data and the DEM positions was negligible. The interval between steps was 0.1 ms. The angular velocity component of each particle was used to calculate the rotation matrix for each satellite point. The updated linear position $\boldsymbol{x}'$ due to rotation was calculated by generating a rotation matrix from the angular velocities, and multiplying this rotation matrix by the pre-rotation position $\boldsymbol{x}$ of the satellite point relative to the particle centre, as shown by:

$$\boldsymbol{x}' = \begin{bmatrix} 1 & 0 & 0 \\ 0 & \cos\theta_x & -\sin\theta_x \\ 0 & \sin\theta_x & \cos\theta_x \end{bmatrix} \begin{bmatrix} \cos\theta_y & 0 & \sin\theta_y \\ 0 & 1 & 0 \\ -\sin\theta_y & 0 & \cos\theta_y \end{bmatrix} \begin{bmatrix} \cos\theta_z & -\sin\theta_z & 0 \\ \sin\theta_z & \cos\theta_z & 0 \\ 0 & 0 & 1 \end{bmatrix} \boldsymbol{x} \quad (5.27)$$

where $\theta_i = \omega_i \Delta t$. This sequence was performed at 0.1 s intervals over 4.5 ms for 30 samples each containing approximately 1000 particles. The simulated MRI pulse sequence is shown in Figure 5.2.

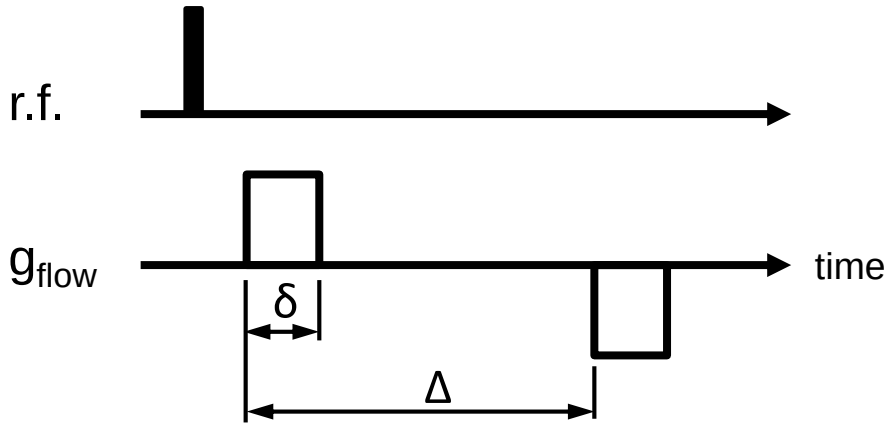

Figure 5.2. Diagram of the simulated MR sequence used to measure the mean velocity and the granular temperature in the DEM simulations of Couette flow.

A square-wave gradient was applied for a half-period (δ) of 1 ms. The observation time between gradients (Δ) was 3.5 ms. The amplitude of the gradient was adjusted in 64 steps about 0 T m^{-1}, with a maximum gradient strength equal to 0.34 T m^{-1}. The phase of each satellite point was calculated by first order numerical integration of $\gamma \boldsymbol{g}(t) \cdot \boldsymbol{x}(t)$ with respect to time. The phase of each satellite point was then converted into a complex signal. These signals were binned according to the position of the satellite points at the end of the sampling period ($\Delta + \delta$) using the particle-centred method. The signals were summed together to give the total signal within the voxel. The simulated signals are processed in the same manner as the experimental signals to extract the mean velocity and the variance of the velocity distribution. The mean velocity was calculated using:

$$v_x = \frac{\arg(S/S_0)}{p_x}. \tag{5.28}$$

According to Equation 5.7, the variance of the velocity is found by fitting a second-order polynomial to the linear motion component of normalised signal against p_x [42]. The variance is the second-order fitting coefficient. Considering rotation, the variances are found by fitting a second-order polynomial to the rotational component of the normalised signal against p_x as shown in Equation 5.15.

5.3.4 DEM averaging post-processing algorithm

MRI measurements of velocity variance differ from theoretical variance calculations by the following: (1) MRI measurements occur over a finite time, Δ; (2) MRI gives time averaged values of the mean and variance of the velocity; (3) the displacement of nuclear spins due to particle rotation is measured and contributes to the MRI signal. In general, DEM data would not be processed over short time intervals (i.e. 10^{-3} s) due to prohibitive storage requirements

and an increase in the computation time. Hence conventional analysis of DEM data overlooks the effect of the MRI measurement procedure when compared against experiments. In order to determine precisely the nature of the velocity information recovered by MRI, the mean and variance of the velocity were found by directly averaging the discrete particle velocities retrieved from the simulation.

To calculate the mean and variance of the velocity, five different averages were tested. The equations used to calculate the averages are given in Table 5.1. Methods 1 and 2 calculate the mean velocity using a particle-weighted time average of the entire instantaneous velocity data set. Method 1 is a time averaged variance of all these individual velocities, i.e. relative to the local instantaneous average velocity. This approach is consistent with the definition of particle granular temperature [47]. Method 2 is a time averaged semi-instantaneous variance. It is semi-instantaneous in the sense that it takes instantaneous velocity fluctuations about the time averaged mean velocity. Method 3 is a time averaged, instantaneous observation-average of the variance. Here, the mean velocity is found using particle velocities that are defined as the change in position during Δ divided by Δ. The particles' velocities may change over the time period Δ owing to collisions between particles. This approach is representative of how velocities are obtained in MRI where spins are dephased and rephased by the application of two gradient pulses separated by a time equal to Δ. However, variances are calculated about the local instantaneous mean velocity, as in Method 1. Method 4 is a time averaged, semi-instantaneous observation average where the same approach as Method 3 was used to find the individual particle velocities for each sample, and velocity fluctuations were taken about the time averaged mean velocity. This method is most representative of how the velocity variance is measured using MRI. Method 5 is the temporal variance of the mean velocity; referred to as bubble granular temperature in literature [47]. Granular temperature and velocity distributions obtained with each of these averaging methods are compared with those obtained from the MRI simulations.

Table 5.1. Equations used for each averaging method.

Method	Averaging Equations
1	$v_{x,i}(\boldsymbol{x}) = \frac{\sum_{p=1}^{N_p} v_{x,p,i}\phi_{p,i}(\boldsymbol{x})}{\sum_{p=1}^{N_p} \phi_{p,i}(\boldsymbol{x})}$ $v_x(\boldsymbol{x}) = \frac{\sum_{i=1}^{N_\mathrm{s}} \sum_{p=1}^{N_p} v_{x,p,i}\phi_{p,i}(\boldsymbol{x})}{\sum_{i=1}^{N_\mathrm{s}} \sum_{p=1}^{N_p} \phi_{p,i}(\boldsymbol{x})}$ $\langle u_x^2 \rangle(\boldsymbol{x}) = \frac{\sum_{i=1}^{N_\mathrm{s}} \sum_{p=1}^{N_\mathrm{part}} \left(v_{x,p,i} - v_{x,i}(\boldsymbol{x})\right)^2 \phi_{p,i}(\boldsymbol{x})}{\sum_{i=1}^{N_\mathrm{s}} \sum_{p=1}^{N_p} \phi_{p,i}\,(\boldsymbol{x})}$
2	$v_x(\boldsymbol{x}) = \frac{\sum_{i=1}^{N_s} \sum_{p=1}^{N_p} v_{x,p,i}\phi_{p,i}(\boldsymbol{x})}{\sum_{i=1}^{N_\mathrm{s}} \sum_{p=1}^{N_p} \phi_{p,i}\,(\boldsymbol{x})}$ $\langle u_x^2 \rangle(\boldsymbol{x}) = \frac{\sum_{i=1}^{N_\mathrm{s}} \sum_{p=1}^{N_p} \left(v_{x,p,i} - v_x(\boldsymbol{x})\right)^2 \phi_{p,i}(\boldsymbol{x})}{\sum_{i=1}^{N_\mathrm{s}} \sum_{p=1}^{N_p} \phi_{p,i}\,(\boldsymbol{x})}$
3	$v_{x,p,i} = \frac{x_p\big\vert_{t=\delta+\Delta} - x_p\big\vert_{t=0}}{\delta + \Delta}$ $v_{x,i}(\boldsymbol{x}) = \frac{\sum_{p=1}^{N_p} v_{x,p,i}\phi_{p,i}(\boldsymbol{x})}{\sum_{p=1}^{N_p} \phi_{p,i}\,(\boldsymbol{x})}$ $v_x(\boldsymbol{x}) = \frac{\sum_{i=1}^{N_\mathrm{s}} \sum_{p=1}^{N_p} v_{x,p,i}\phi_{p,i}(\boldsymbol{x})}{\sum_{t=1}^{N_\mathrm{s}} \sum_{p=1}^{N_p} \phi_{p,i}\,(\boldsymbol{x})}$ $\langle u_x^2 \rangle(\boldsymbol{x}) = \frac{\sum_{i=1}^{N_\mathrm{s}} \sum_{p=1}^{N_p} \left(v_{x,p,i} - v_{x,i}(\boldsymbol{x})\right)^2 \phi_{p,i}(\boldsymbol{x})}{\sum_{i=1}^{N_\mathrm{s}} \sum_{p=1}^{N_p} \phi_{p,i}\,(\boldsymbol{x})}$
4	$v_{x,p,i} = \frac{x_p\big\vert_{t=\delta+\Delta} - x_p\big\vert_{t=0}}{\delta + \Delta}$ $v_x(\boldsymbol{x}) = \frac{\sum_{i=1}^{N_\mathrm{s}} \sum_{p=1}^{N_p} v_{x,p,i}\phi_{p,i}(\boldsymbol{x})}{\sum_{t=1}^{N_\mathrm{s}} \sum_{p=1}^{N_p} \phi_{p,i}\,(\boldsymbol{x})}$ $\langle u_x^2 \rangle(\boldsymbol{x}) = \frac{\sum_{i=1}^{N_\mathrm{s}} \sum_{p=1}^{N_p} \left(v_{x,p,i} - v_x(\boldsymbol{x})\right)^2 \phi_{p,i}(\boldsymbol{x})}{\sum_{i=1}^{N_\mathrm{s}} \sum_{p=1}^{N_p} \phi_{p,i}\,(\boldsymbol{x})}$
5	$v_{x,i}(\boldsymbol{x}) = \frac{\sum_{p=1}^{N_p} v_{x,p,i}\phi_{p,i}(\boldsymbol{x})}{\sum_{p=1}^{N_p} \phi_{p,i}(\boldsymbol{x})}$ $v_x(\boldsymbol{x}) = \frac{\sum_{i=1}^{N_\mathrm{s}} \sum_{p=1}^{N_p} v_{x,p,t,i}\phi_{p,t,i}(\boldsymbol{x})}{\sum_{i=1}^{N_\mathrm{s}} \sum_{p=1}^{N_p} \phi_{p,t,i}(\boldsymbol{x})}$ $\langle u_x^2 \rangle(\boldsymbol{x}) = \frac{1}{N_\mathrm{s}} \sum_{i=1}^{N_\mathrm{s}} \left(v_{x,i}(\boldsymbol{x}) - v_x(\boldsymbol{x})\right)^2$

5.4. Results and discussion

In this section, we first compare the velocity mean and variance profiles obtained using the five spatial averaging methods for DEM results against the profiles obtained by MRI simulation of granular Couette flow. Next, the signal model including rotation is compared to MRI simulations of an idealised test case where the linear and angular velocities are independent. Finally, the signal model is validated for granular Couette flow.

5.4.1 DEM post-processing methods

MRI measures motion over an encoding time Δ, which is typically short (< 10 ms). However, the measurement itself may take minutes, or hours. Here, the effect of these averaging times is investigated. Figure 5.3 gives the profiles of the azimuthal component of the mean velocity and the variance of the velocity obtained using the MRI simulations without particle rotation and the DEM averaging methods. There was excellent agreement between the velocity profiles obtained using all 5 conventional post processing methods and the MRI simulation, as shown in Figure 5.3(a), suggesting that particle velocities did not change significantly during the observation over Δ. Thus, v_x is readily extracted from the MRI data; for this system, the method of time averaging is not important for the extraction of v_x. Figure 5.3(b) shows the velocity variance profiles obtained with each method. Under the investigated conditions, the temporal variance of the mean velocity was nearly an order of magnitude lower than the instantaneous variance, confirming that the bulk motion within the system was only weakly transient. Individual particle velocities for each sample were closer to the instantaneous mean velocity compared to the time averaged mean velocity. Consequently, the sum of the squares of the fluctuations were lower for the instantaneous variance compared to fluctuations about the time averaged velocity of the semi-instantaneous variance, hence the variance calculated by Method 1 was lower compared to Method 2. The difference between Methods 1 and 2 is due to the time scale over which the mean velocity is measured.

Incorporating the effect of acquiring the MR signal over Δ (Methods 3 and 4) decreases the sum of the squares of the fluctuations compared to the instantaneous velocity cases (Methods 1 and 2). Therefore, the variance obtained using the instantaneous observation average of Method 3 was smaller than those acquired with Methods 1 and 2. For similar reasons as discussed previously, the variance was higher when calculated for the semi-instantaneous observation average of Method 4 than for Method 3 due to Method 4 using the time averaged mean velocity. Method 4 was the closest match to the MRI simulations for most of the

simulated conditions. These results confirm that for the DEM velocity variance to match that of the MRI, it is important that: (1) The individual particle velocities should be averaged over the observation period $\Delta + \delta$, and (2) fluctuations must be taken about the time averaged mean velocity. Equivalently, when using MRI to probe granular rheology, one must be aware of the effect of changing observation time Δ and flow encoding time δ.

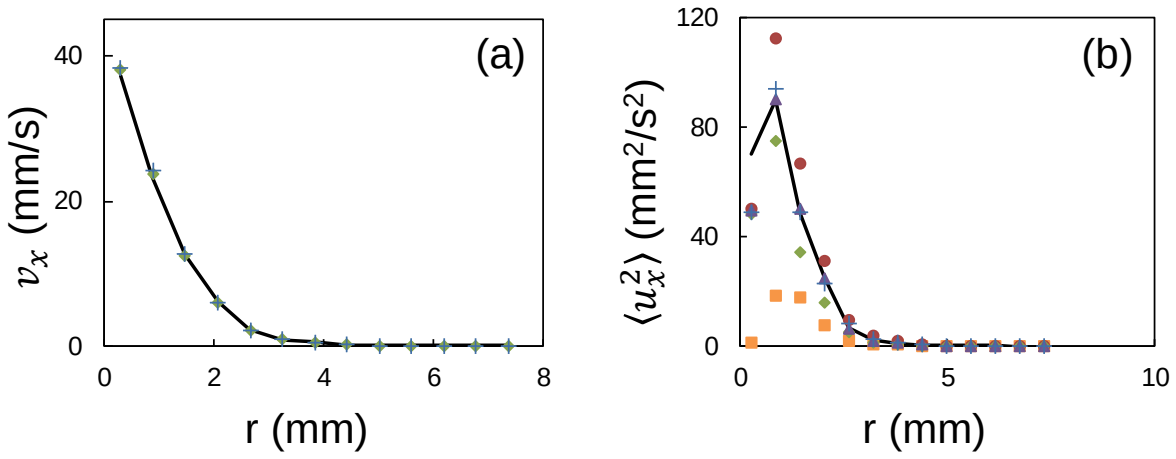

Figure 5.3. Radial profiles for (a) mean azimuthal velocity (b) variance of velocity demonstrating the effect of time averaging and observation over Δ where r is the distance from the inner wall. In these simulations d_p = 0.44 mm, e_n = 0.9, μ_f = 0.1, and U = 41 mm s^{-1}. (MRI method neglecting particle rotation: solid line; Method 1: +; Method 2: ●; Method 3: ◆; Method 4: ▲; Method 5: ■).

5.4.2 Verification of signal model for rotation

In this section, the signal model for rotation developed in Section 5.2 is verified. The prediction from Equation 5.14 was compared with simulations of the spatially unresolved signal for a collection of 10000 non-interacting particles. The motion encoding gradient was defined as being along the x-axis, and the gradient strength, observation time and encoding time were set as defined in Section 5.3.3. Gaussian linear and angular velocity distributions were imposed on the system. In all cases, the mean linear and angular velocities of the system were set to zero. In these simulations, the linear and both angular velocity components were uncorrelated and sampled from distributions with variances $\langle u_x^2 \rangle$, $\langle \omega_y^2 \rangle$ and $\langle \omega_z^2 \rangle$, respectively. The variance of the angular velocity about each axis was identical. Figure 5.4(a) shows the absolute value of the normalised signal against the angular velocity variance for several linear velocity variances. Irrespective of the linear velocity variance, excellent agreement between the simulations and model was observed, demonstrating that the model was able to describe linear and rotational motion, at least when these components were independent. Figure 5.4(b) demonstrates that the model predictions agree well with the MRI

simulation, even at the maximum values of $|p_x|$ that could be measured experimentally ($p_x = 400$ s mm^{-1}). An example of correlated rotational velocities is shown, where the agreement between simulations and model is poor since the assumption of independent velocity distributions was violated. These results confirm the validity of the model of rotational motion on the MRI signal.

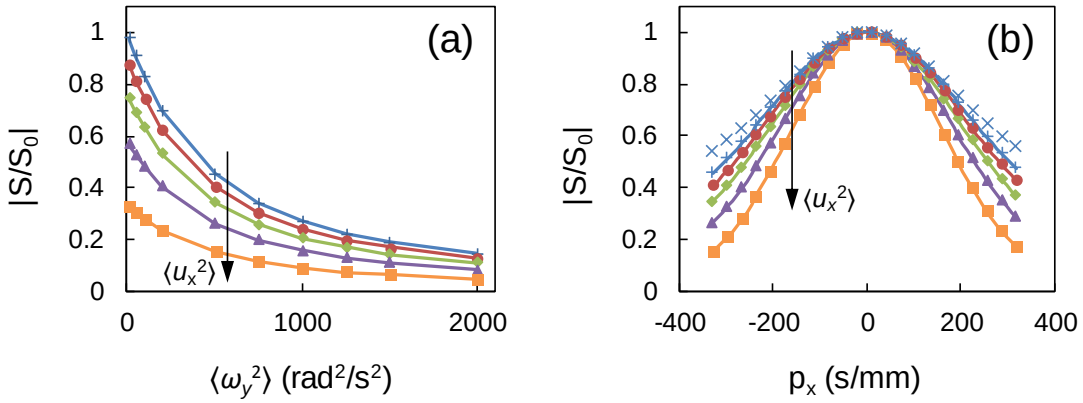

Figure 5.4. MRI simulations of a generated set of particles with Gaussian linear and angular velocity distributions. (a) Normalised signal against angular velocity variance where $p_x = -330$ s mm^{-1}, $\langle \omega_z^2 \rangle = \langle \omega_y^2 \rangle$. (b) Normalised signal against p where $\langle \omega_y^2 \rangle = \langle \omega_z^2 \rangle = 500$ rad^2/s^2. MRI simulation data are denoted by markers, Equation 5.14 is denoted by solid lines. $\langle u_x^2 \rangle = 0$ mm^2 s^{-2}: +, $\langle u_x^2 \rangle = 2$ mm^2 s^{-2}: ●, $\langle u_x^2 \rangle = 5$ mm^2 s^{-2}: ♦, $\langle u_x^2 \rangle = 10$ mm^2 s^{-2}: ▲, $\langle u_x^2 \rangle = 20$ mm^2 s^{-2}: ■. A special case where $\langle u_x^2 \rangle = 0$ and the angular velocity components of the granules are correlated (i.e. $\omega_y = \omega_z$) is shown by ×.

The simulation described in the preceding paragraph was repeated with anisotropic rotational components by sampling ω_y and ω_z from distributions with variances $\langle \omega_y^2 \rangle$, and $\langle \omega_z^2 \rangle$, respectively. Figure 5.5(a) gives the signal attenuation with respect to the velocity variances about the *y* and *z* axes for the MRI simulation and the signal model when the velocity variance was zero. Figure 5.5(b) shows the relationship between the signal and the inverse variable p_x for several combinations of the angular velocity variances. Agreement between the simulations and the model is excellent.

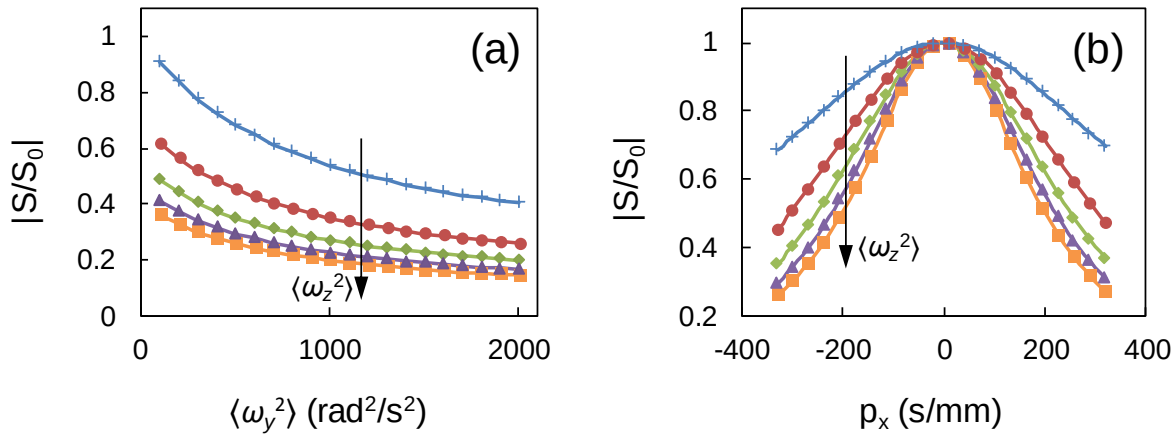

Figure 5.5. MRI simulations of a generated set of particles with Gaussian linear and angular velocity distributions. (a) Normalised signal against angular velocity variance about the *y*-axis for constant values of angular velocity about the *z*-axis for $\langle u_x^2 \rangle$ = 0 and p_x = −330 s mm^{-1}. (b) Normalised signal against p where $\langle u_x^2 \rangle$ = 0 and $\langle \omega_z^2 \rangle$ = 500 rad^2/s^2. MRI simulation data are denoted by markers, Equation 5.14 (*m* = 40) is denoted by solid lines. $\langle \omega_y^2 \rangle$ = 0 rad^2/s^2: +, $\langle \omega_y^2 \rangle$ = 500 rad^2 s^{-2}: ●, $\langle \omega_y^2 \rangle$ =1000 rad^2 s^{-2}: ♦, $\langle \omega_y^2 \rangle$ = 1500 rad^2 s^{-2}: ▲, $\langle \omega_y^2 \rangle$ = 2000 rad^2 s^{-2}: ■.

5.4.3 Couette flow verification and validation

To validate the signal model for use with granular Couette flow, Equation 5.14 was evaluated using Method 4 DEM averages of the mean velocity, and the variance of the linear velocity as inputs. The DEM averages of the angular velocity were calculated using a modified version of Method 4, where the local mean angular velocity was given by:

$$\bar{\omega}_y(\boldsymbol{x}) = \frac{\sum_{i=1}^{N_s} \sum_{p=1}^{N_p} \omega_{y,p,i} \phi_{p,i}(\boldsymbol{x})}{\sum_{t=1}^{N_s} \sum_{p=1}^{N_p} \phi_{p,i}(\boldsymbol{x})} \tag{5.29}$$

where the individual particle velocities were averaged over the imaging acquisition period consisting of N snapshots, i.e. $\omega_{y,p,i} = 1/N \sum_{t=0}^{N} \omega_{y,p,i,t}$. The angular velocity variance was calculated using:

$$\langle \omega_y^2 \rangle(\boldsymbol{x}) = \frac{\sum_{i=1}^{N_s} \sum_{p=1}^{N_p} \left(\omega_{y,p,i} - \bar{\omega}_y(\boldsymbol{x}) \right)^2 \phi_{p,i}(\boldsymbol{x})}{\sum_{i=1}^{N_s} \sum_{p=1}^{N_p} \phi_{p,i}(\boldsymbol{x})}. \tag{5.30}$$

The model signal was compared against the signal predicted using the MRI simulation of linear motion, shown by Figure 5.6 for the 0.44 mm particles. Similar profiles were found for the simulations involving 0.6 mm diameter particles (not shown here). At the inner moving wall i.e. $r < d_p$, the agreement is poor since the granules have identical velocities, which violated the assumption of normally distributed velocities. Beyond the moving wall, the

agreement between the model and the simulations was generally very good. However, in cases where the angular velocity variance is particularly high, for example Figure 5.6(d) where μ_f = 0.5 and U = 41 mm s^{-1}, significant deviations occur for greater values of p_x. These localised deviations suggest that obtaining the most accurate value for the variance requires fitting to a subset of the data at low p_x, analogous to the measurement of flow propagators in porous media [48].

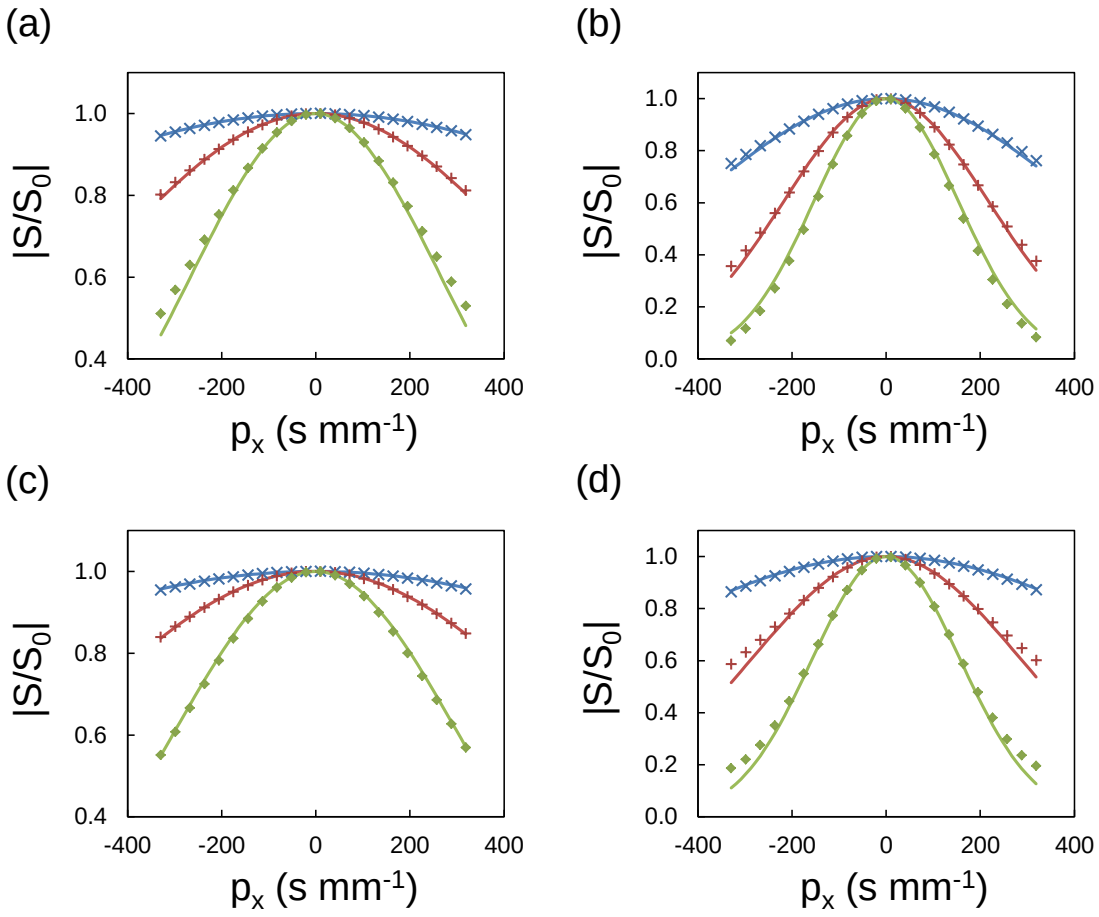

Figure 5.6. Profiles of the absolute normalised signal from linear motion against the inverse variable for granular Couette flow of 0.44 mm particles (a) U = 17 mm s^{-1}, μ_f = 0.1, (b) U = 41 mm s^{-1}, μ_f = 0.1, (c) U = 17 mm s^{-1}, μ_f = 0.5, (d) U = 41 mm s^{-1}, μ_f = 0.5. Simulation data are denoted by markers, the model results were calculated using DEM averages of the local velocity distributions and are denoted by solid lines. Profiles at r = 1.5 mm: ♦, r = 2.1 mm: +, and r = 2.6 mm: ×.

The variance is found by fitting over a range of p_x such that there are an equal number of points about $p_x = 0$. Figure 5.7 shows how the value of the fitted variance changes with the maximum value of p_x compared to the Method 4 DEM average. The standard error in the DEM average assuming that the velocity is normally distributed was calculated by [49]:

$$\Delta\langle u_x^2\rangle = \sqrt{\frac{2\langle u_x^2\rangle}{N_p - 1}}. \tag{5.31}$$

For these cases, the value of the variance is not sensitive to the fitting range over $p_x < 100$ s mm^{-1}. When fitted over the maximum p_x tested, a growing deviation from the low-p_x fit is observed. This deviation occurs due to the signal departing from the parabolic form assumed by Equation 5.7. The deviation is strongest at the highest variances tested (about 40 mm^2 s^{-2}). For these systems, the signal flattens out as it is nearly completely attenuated. The agreement between the variance fitted to the signal data and the DEM averages (shown by the solid lines) is very good, with deviations below 10%. Hence, if the fit to the signal is over a range of p_x where the fit is not sensitive to the maximum value of p_x then MRI is able to recover the time average of the observation-averaged linear velocity variance.

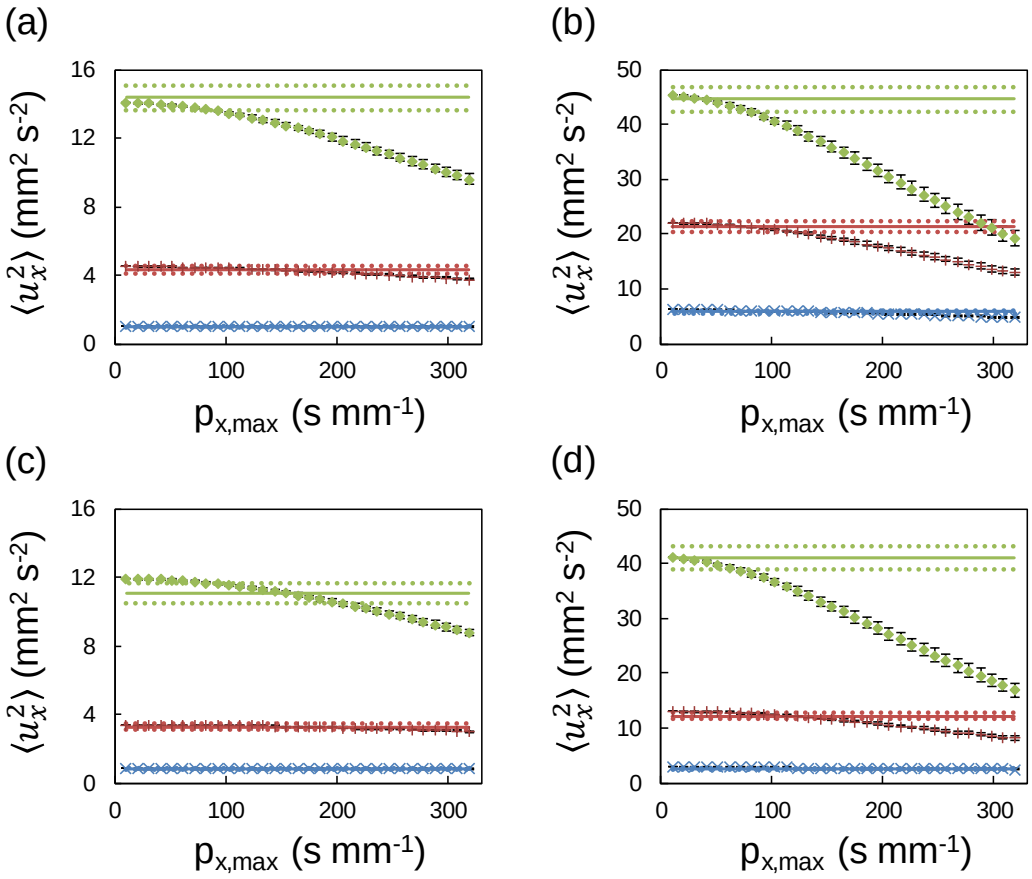

Figure 5.7. The linear velocity variance measured by fit to signal data as a function of the fitting range for granular Couette flow of 0.44 mm particles. (a) U = 17 mm s^{-1}, μ_f = 0.1, (b) U = 41 mm s^{-1}, μ_f = 0.1, (c) U = 17 mm s^{-1}, μ_f = 0.5, (d) U = 41 mm s^{-1}, μ_f = 0.5. DEM averages are shown by solid lines. The standard error in the DEM average is denoted by the dotted lines. Markers show the fits to the signals at r = 1.5 mm: ♦, r = 2.1 mm: +, and r = 2.6 mm: ×. The error bars represent the uncertainty in the fit to the signal data.

The suitability of PFG sequences for measuring the angular velocity variance was assessed using the same approach. Figure 5.8 compares the MR simulations and model predictions of the signal from angular motion against p_x. The model follows the simulated signal well, although deviations are apparent at the highest values of p_x tested for μ_f = 0.5 and U = 41 mm s^{-1} shown in Figure 5.8(d). The effect of fitting range on the recovered angular velocity variance is related to the DEM average in Figure 5.9. At small fitting ranges, the recovered angular velocity variance was approximately constant, however significant deviation was observed for the widest fitting ranges at high angular velocity variances, identical to the linear motion shown in Figure 5.7. The region of constant $\langle\omega^2\rangle$ was generally in good agreement with the DEM average angular velocity variance, to within 10%. As with the linear velocity variance, if the fit to the signal is limited to a narrow range of p_x then MRI is able to recover the time average of the observation averaged angular velocity variance.

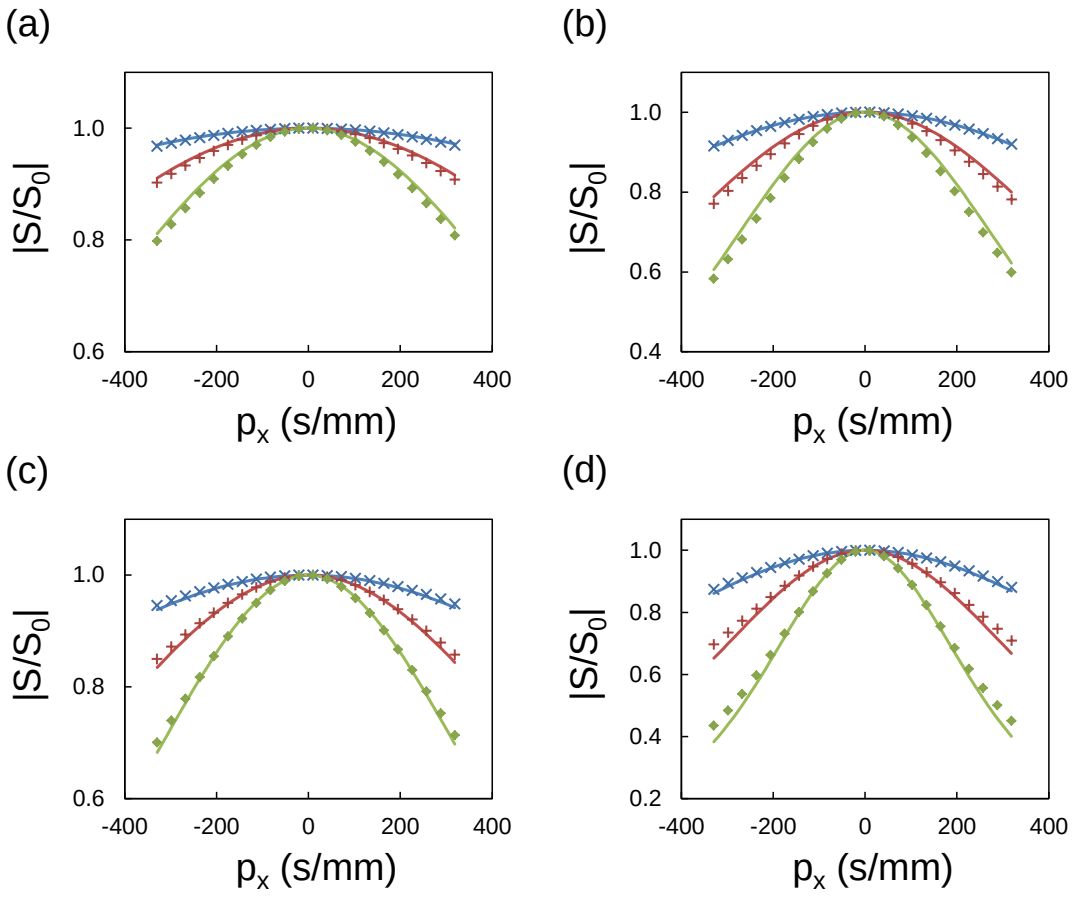

Figure 5.8. Profiles of the absolute normalised signal from angular motion against the inverse variable for granular Couette flow of 0.44 mm particles (a) U = 17 mm s^{-1}, μ_f = 0.1, (b) U = 41 mm s^{-1}, μ_f = 0.1, (c) U = 17 mm s^{-1}, μ_f = 0.5, (d) U = 41 mm s^{-1}, μ_f = 0.5. Simulation data are denoted by markers, the model results were calculated using DEM averages of the local velocity distributions and are denoted by solid lines. Profiles at r = 1.5 mm: ♦, r = 2.1 mm: +, and r = 2.6 mm: ×.

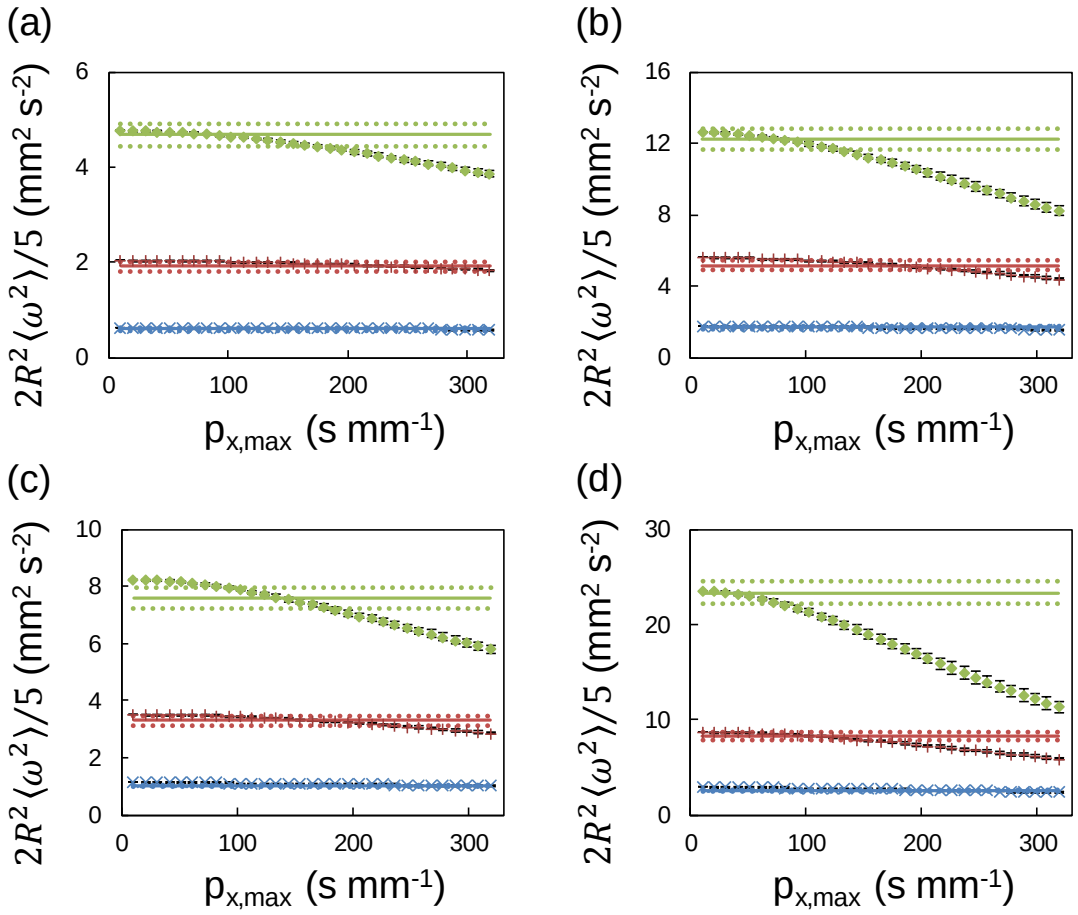

Figure 5.9. The angular velocity variance measured by fit to signal data as a function of the fitting range for granular Couette flow of 0.44 mm particles. (a) U = 17 mm s^{-1}, μ_f = 0.1, (b) U = 41 mm s^{-1}, μ_f = 0.1, (c) U = 17 mm s^{-1}, μ_f = 0.5, (d) U = 41 mm s^{-1}, μ_f = 0.5. DEM averages are shown by solid lines. The standard error is shown by the dotted lines Markers show the fits to the signals at r = 1.5 mm: ♦, r = 2.1 mm: +, and r = 2.6 mm: ×. The error bars represent the uncertainty in the fit to the signal data.

The velocity variance was fitted to Equation 5.7 using three versions of the simulated MR signal: (1) only linear motion of the granules contributed towards the signal, (2) only particle rotation contributed to the signal, and (3) both rotation and translation of granules contributed to the signal. For (2), the apparent linear velocity variance obtained from the fit is related to the angular velocity variance by Equation 5.16. Experimentally, the situation described in (3) occurs. MRI simulation has enabled us to produce variance profiles for (1) and (2), which are not currently possible to obtain from these experiments. Figure 5.10(a) shows the signal attenuation across the gap as measured by the MRI simulation for these three cases. At the inner wall, signal attenuation is low for all cases. Particles fixed to the wall have the same velocity and are not free to rotate. The signal reaches a local minimum about ~1d_p from the

inner wall. In this rapid flowing region, granules exhibit a distribution of velocities and rotate as a result of frictional contacts. Further away from the inner wall, the signal attenuation is reduced due to the narrowing of velocity distributions as kinetic energy is dissipated. Near the outer wall, there is negligible signal attenuation since the granules are static. The signal attenuation is greatest for case 3 where the effects of cases 1 and 2 occurred simultaneously. The relationship between the signal against $p_x$within the high-shear region (circled in black) is shown in Figure 5.10(b). The profiles exhibited the parabolic relationship predicted by Equation 5.7 for $|p_x| < 100$ s mm $^{-1}$. It is noteworthy that the product of the signals for cases 1 and 2 is equal to the signal from case 3, as was observed from the test cases in the preceding section. This relation confirms that the velocity distributions are independent.

Figure 5.10(c) shows the angle of the complex signal against p_x for the high shear region. The local mean velocity was found from the gradient of these data. The profiles from cases 1 and 3 were similar, while case 2 had a gradient close to zero. These data were consistent with the signal model prediction that the rotation component was real. Thus, rotation has no effect on measurement of mean translational velocity and the conventional analysis is suitable for mean velocity measurements.

The local variance of the velocity in the sample was found by fitting parabolas to the absolute value of the complex signals such as those shown in Figure 5.10(b). The resulting velocity variance across the gap is shown in Figure 5.10(d). The variance profile mirrors the signal profile, where regions with large velocity fluctuations corresponded to high signal attenuation. The variance obtained by only considering translational motion (case 2) was about 75% of the variance measured when including both modes of motion (case 3). This disparity demonstrates that the velocity variance measured by experiments is not a direct measurement of linear velocity fluctuations; instead it is amplified due to the additional signal attenuation induced by rotating granules.

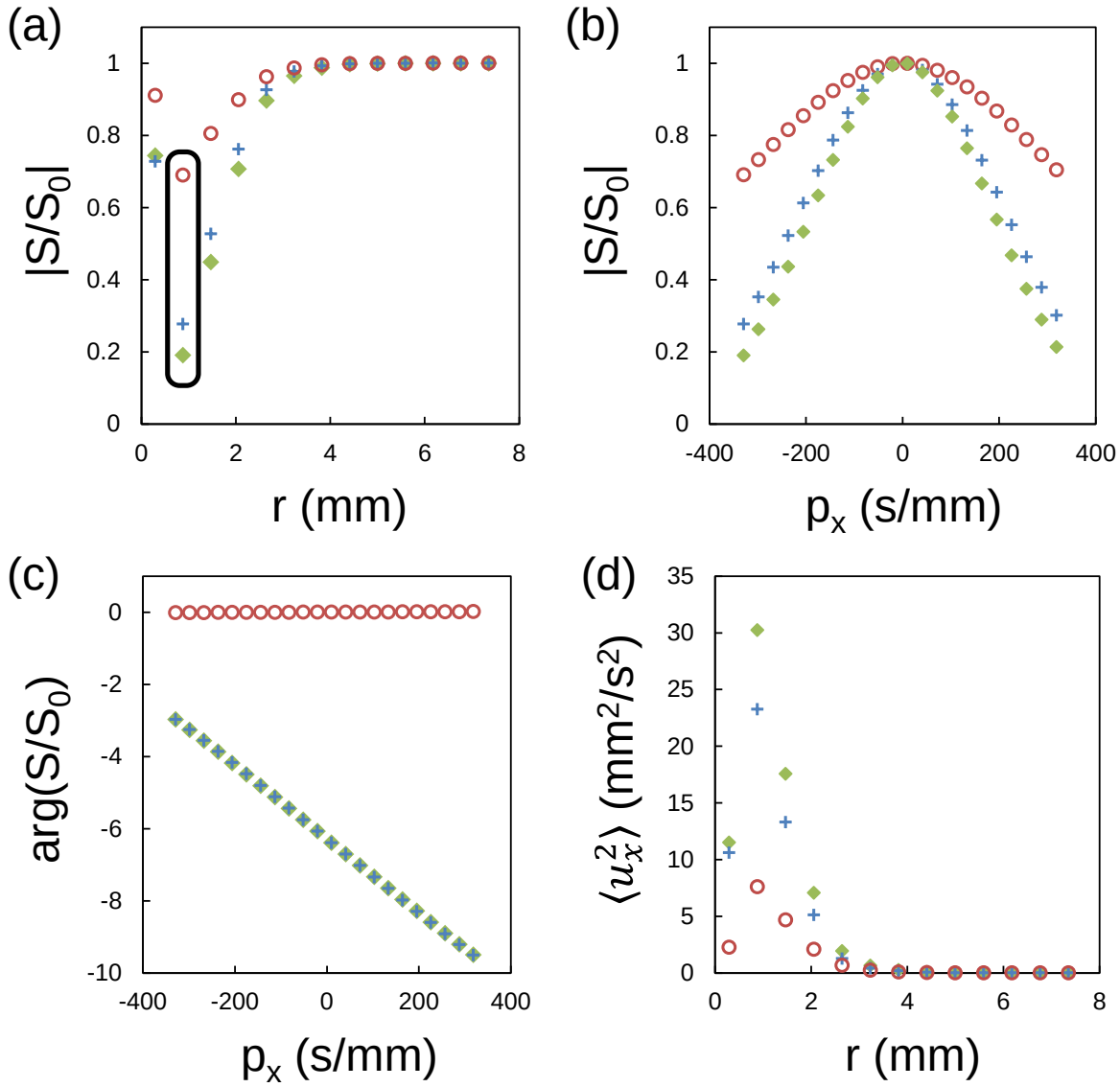

Figure 5.10. Analysis of granular Couette flow of 0.44 mm particles with e_n = 0.9, μ_f = 0.1, and U = 17 mm s^{-1} using MRI simulation method. (a) Normalised absolute signal across the gap (p_x = 330 s mm^{-1}). (b) Normalised absolute signal against p for the region circled in black on (a). (c) Angle of the complex signals against p, the local mean velocity is given by the gradient. (d) Velocity variance profile. Considering only particle translation (case 1): +; Considering only particle rotation (case 2): ○; Considering both rotation and translation (case 3): ♦.

Figure 5.11 and Figure 5.12 compare the three signal fitting cases to experimental data. For the 0.44 mm particles shown in Figure 5.11, linear motion alone was sufficient to account for the experimentally observed velocity variance for the 17 mm s^{-1} cases. Modelling the effect of rotation caused the simulation data to exceed the experiment by up to 50% at the peak value. These deviations may be due to the difference in shape between the spherical simulated particles and the ellipsoidal lobelia seeds of the experiment. Figure 5.12 gives the variance profiles for the 0.6 mm particles. Including the effect of granule rotation resulted in

good agreement between experiment and simulation for the 17 mm s^{-1} cases, particularly at the peak values. A coefficient of friction of 0.5 offered better agreement than 0.1; although it is unclear which value is more physically representative of the particles used in the experiments. Simulations where the inner wall speed was 41 mm s^{-1} showed that the simulated peak variance was less than half that of the experiment, although the decay beyond 1.5 mm was captured accurately. This disparity could be caused by wobbling of the inner cylinder which contributed to the velocity variance measured in experiments.

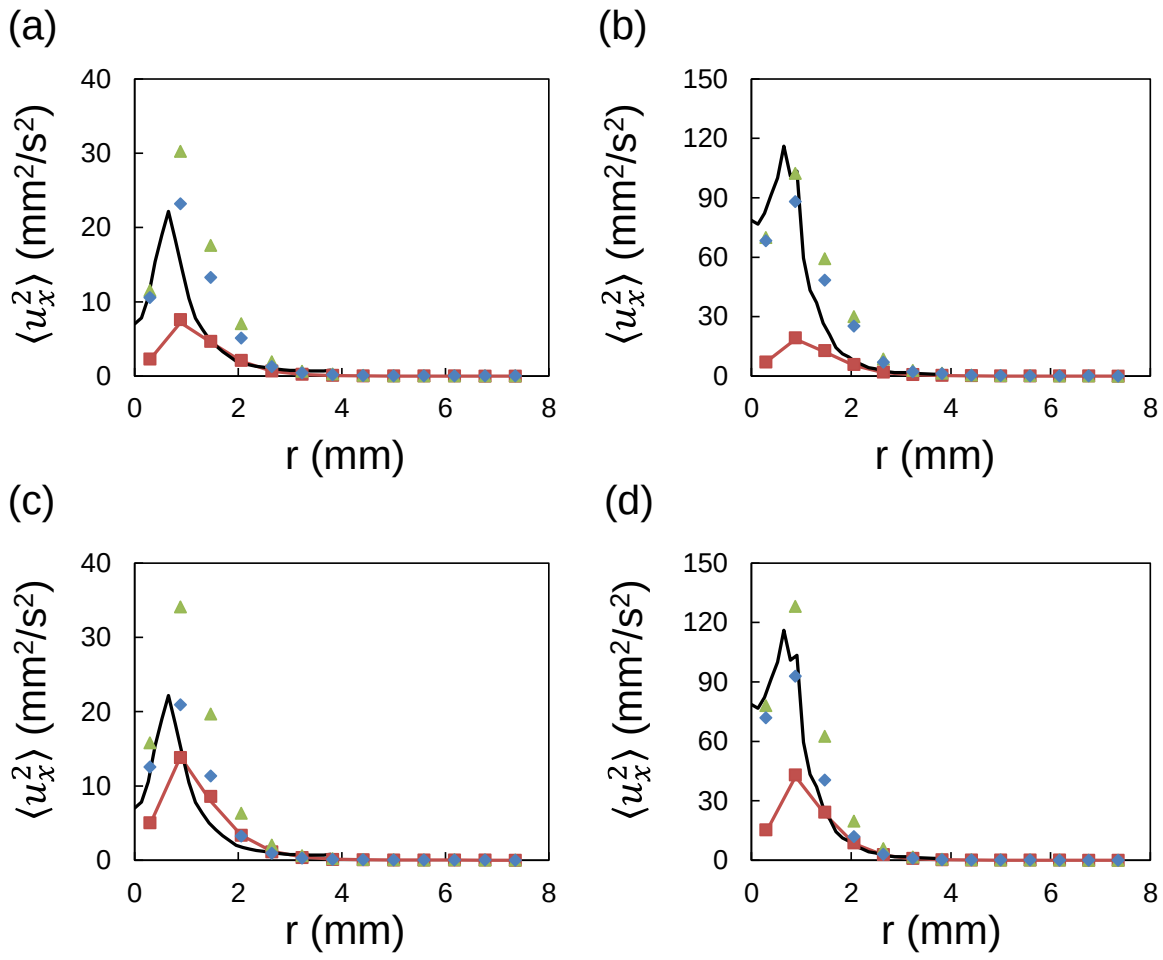

Figure 5.11. Velocity variance profiles for Couette shear with 0.44 mm d_p particles. (a) μ_f = 0.1, U = 17 mm s^{-1}, (b) μ_f = 0.1, U = 41 mm s^{-1}, (c) μ_f = 0.5, U = 17 mm s^{-1}, (d) μ_f = 0.5, U = 41 mm s^{-1}. MRI experiment: solid line; MRI simulation incorporating linear motion only (case 1): ♦; MRI simulation incorporating angular motion only (case 2): ■; DEM average (method 4) of angular velocity variance: —; MRI simulation incorporating both linear and angular motion (case 3): ▲.

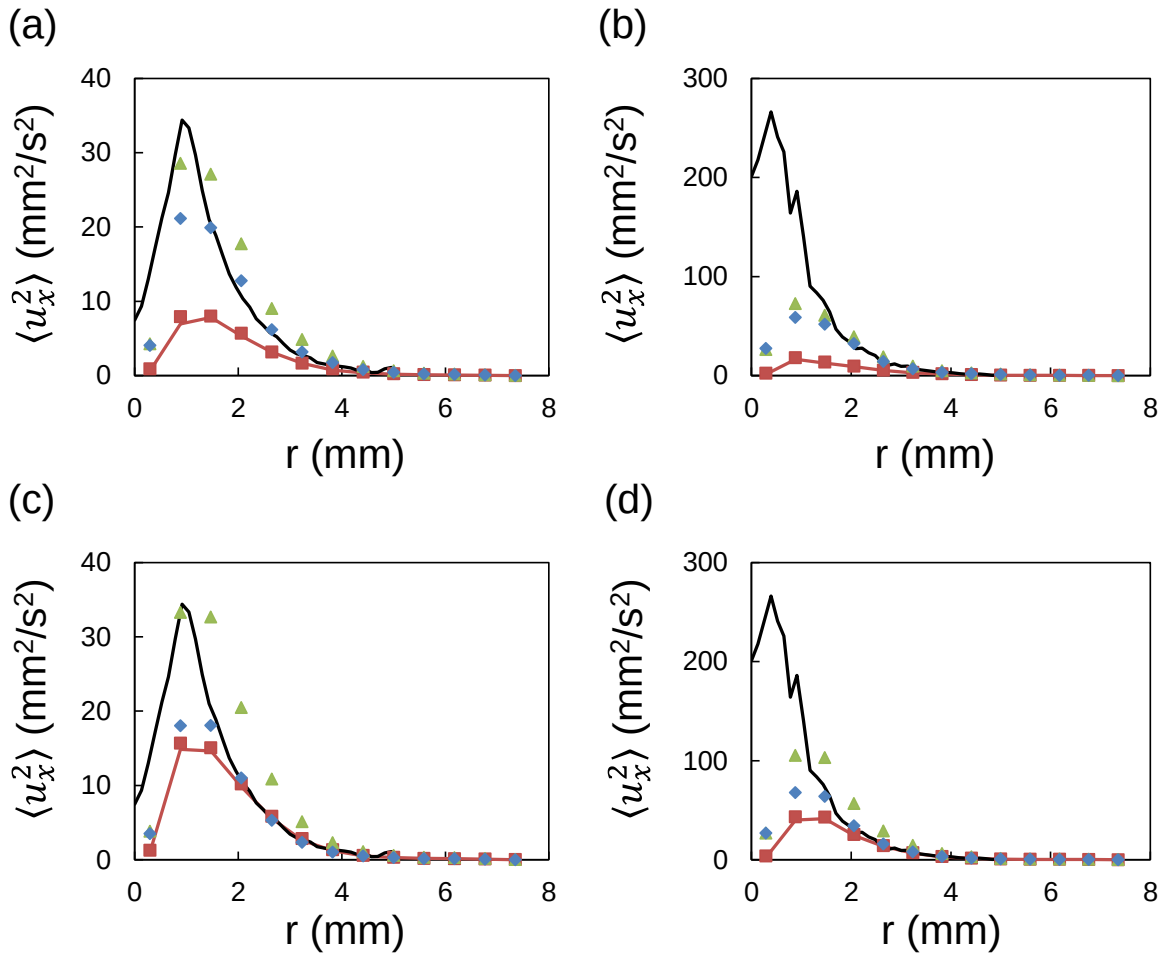

Figure 5.12. Velocity variance profiles for Couette shear with 0.6 mm d_p particles. (a) μ_f = 0.1, U = 17 mm s^{-1}, (b) μ_f = 0.1, U = 41 mm s^{-1}, (c) μ_f = 0.5, U = 17 mm s^{-1}, (d) μ_f = 0.5, U = 41 mm s^{-1}. MRI experiment: solid line; MRI simulation incorporating linear motion only (case 1): ♦; MRI simulation incorporating angular motion only (case 2): ■; DEM average (method 4) of angular velocity variance: —; MRI simulation incorporating both linear and angular motion (case 3): ▲.

The apparent velocity variance from granule rotation was a significant fraction of the total variance. In general, the angular motion was 20% of the total variance at the inner wall, this ratio increased with distance across the gap. For μ_f = 0.1, the maximum ratio was about 40% at the outer wall. For μ_f = 0.5, the maximum ratio increased to about 70%. If the friction coefficient is increased, then the torque on a particle increases, increasing its angular velocity. As a result, the sample may have a wider range of angular velocities, increasing the angular velocity variance. The granule radius did not affect the ratio significantly since the increase of the contribution to the signal associated with increasing the radius was counteracted by the 0.44 mm particles experiencing higher angular velocity variances. These results demonstrate

that the size of the effect of rotation on the signal is highly sensitive to the particle radius and friction coefficient.

Rotational motion between contacting granules is resisted by frictional torque. This frictional torque, commonly known as “rolling friction” is an important mode of kinetic energy dissipation and provides support to geometrically stable granular structures [50]. Rolling friction has been found to have a minimal effect on the linear velocity distribution of sheared granular flows in the intermediate regime [51]. However, the effect of rolling friction on the angular velocity distribution in sheared flows has not been studied. It is hypothesised that rolling friction would inhibit granule rotation, thus reducing the angular velocity variance. The effect of rolling friction is likely to be important but has not been considered in this work.

The significant contribution that rotation makes to the measured variance raises an important consideration when validating simulation velocity distributions against MRI experiments. Unlike particle tracking methods, which measure the linear velocity variance, the MRI velocity variance consists of both linear and angular variances. Thus, it is necessary to analyse the simulation data in accordance with the physics of signal acquisition. The results shown here confirm that in most cases the best agreement with MRI experiments is achieved by incorporating the effects of both linear and angular motion.

To ascertain how useful the rotation signal model is for measuring rotational motion, the DEM average apparent linear velocity variance is shown in Figure 5.11 and Figure 5.12. Compared to the apparent linear velocity variance fitted from the rotation-only signal (case 2), the agreement is excellent, demonstrating that MRI can accurately measure the angular velocity variance of granular flows. However, the analysis performed in this chapter relies on the ability to study the simulated translation and rotation signal components in isolation. This analysis is more complicated for physical granular flows, where the signal can only be separated into these components with additional information. An independent measure of the linear velocity variance could be obtained using a different gradient sequence or experimental technique. From this measurement the rotational component of the signal (and hence the angular velocity variance) could be obtained from the total signal.

5.5. Conclusions

A model describing the signal in terms of the linear and angular velocity distributions of granules was developed and validated against simulated MRI experiments. For an idealised test case of non-interacting particles, the model perfectly describes the behaviour of the signal for $p_x < 330$ mm s^{-1}. Soft-sphere DEM simulations were conducted for a collection of spherical particles under annular shear flow. The mean and variance of the linear velocity were calculated by simulating MRI experiments including and excluding the rotation of particles. The model shows that when using experimental MRI data collected to validate simulations, particle rotation must be considered when averaging simulation data for the validation to be a fair comparison.

Several averaging algorithms were applied to the data in order to verify that the rotation-exclusive MRI simulations were able to give a reasonable representation of the mean velocity and variance of velocity. With regard to the mean velocity, it was found that all of the DEM post-processing methods were in good agreement with the MRI simulations. For the velocity variance, it was found that a suitable method must: (1) take the individual particle velocities in each sample as constant over Δ and (2) take velocity fluctuations about the time-averaged mean velocity.

The model of granule rotation developed here has the potential to enable experimental measurements of the angular velocity distribution. Few other techniques are sensitive to granular rotation, at present it is not possible to separate these contributions to the signal. However, the model developed shows that the two contributions to the signal are multiplicative. Hence if an independent measure of translational motion is possible, the rotational motion can also be determined. This information would allow for valuable insights into the dynamics of flowing granular media.

5.6. References

1. Jop, P., Y. Forterre, and O. Pouliquen, *A constitutive law for dense granular flows.* Nature, 2006. **441**(7094): p. 727-730
2. Kamrin, K. and G. Koval, *Nonlocal constitutive relation for steady granular flow.* Physical Review Letters, 2012. **108**(17)
3. Lun, C.K.K., et al., *Kinetic theories for granular flow: inelastic particles in Couette flow and slightly inelastic particles in a general flowfield.* Journal of Fluid Mechanics, 1984. **140**: p. 223-223
4. Zhang, Q. and K. Kamrin, *Microscopic Description of the Granular Fluidity Field in Nonlocal Flow Modeling.* Physical Review Letters, 2017. **118**(5)
5. Artoni, R. and P. Richard, *Effective Wall Friction in Wall-Bounded 3D Dense Granular Flows.* Physical Review Letters, 2015. **115**(15)
6. Lun, C.K.K., *Kinetic theory for granular flow of dense, slightly inelastic, slightly rough spheres.* Journal of Fluid Mechanics, 1991. **233**(539): p. 539-559
7. Jenkins, J.T. and C. Zhang, *Kinetic theory for identical, frictional, nearly elastic spheres.* Physics of Fluids, 2002. **14**(3): p. 1228-1235
8. Cody, G.D., et al., *Particle granular temperature in gas fluidized beds.* Powder Technology, 1996. **87**(3): p. 211-232
9. Dijkhuizen, W., et al., *Extension of PIV for measuring granular temperature field in dense fluidized beds.* AIChE Journal, 2007. **53**(1): p. 108-118
10. Menon, N. and D.J. Durian, *Diffusing-Wave Spectroscopy of Dynamics in a Three-Dimensional Granular Flow.* Science, 1997. **275**(5308): p. 1920-1922
11. Dixon, P.K. and D.J. Durian, *Speckle visibility spectroscopy and variable granular fluidization.* Physical Review Letters, 2003. **90**(18): p. 184302/1-184302/4
12. Wildman, R.D., et al., *Experimental determination of temperature profiles in a sheared granular bed containing two and three sizes of particles.* Granular Matter, 2012. **14**(2): p. 215-220
13. Wildman, R.D., J.M. Huntley, and D.J. Parker, *Granular temperature profiles in three-dimensional vibrofluidized granular beds.* Physical Review E - Statistical, Nonlinear, and Soft Matter Physics, 2001. **63**(6 I): p. 061311/1-061311/10
14. Mohs, G., et al., *Magnetic monitoring of a single particle in a prismatic spouted bed.* Chemical Engineering Science, 2009. **64**(23): p. 4811-4825
15. Buist, K.A., et al., *Improved magnetic particle tracking technique in dense gas fluidized beds.* AIChE Journal, 2014. **60**(9): p. 3133-3142
16. Sederman, A.J., P. Alexander, and L.F. Gladden, *Structure of packed beds probed by Magnetic Resonance Imaging.* Powder Technology, 2001. **117**(3): p. 255-269
17. Nakagawa, M., et al., *Non-invasive measurements of granular flows by magnetic resonance imaging.* Experiments in Fluids, 1993. **16**(1): p. 54-60
18. Seymour, J.D., et al., *Pulsed Gradient Spin Echo Nuclear Magnetic Resonance Imaging of Diffusion in Granular Flow.* Physical Review Letters, 2000. **84**(2): p. 266-269
19. Yang, X., et al., *Measurements of grain motion in a dense, three-dimensional granular fluid.* Physical Review Letters, 2002. **88**(4): p. 443011-443014
20. Savelsberg, R., et al., *Particle motion in gas-fluidized granular systems by pulsed-field gradient nuclear magnetic resonance.* Physical Review E - Statistical, Nonlinear, and Soft Matter Physics, 2002. **65**(2): p. 020301/1-020301/4
21. Mueth, D.M., et al., *Signatures of granular microstructure in dense shear flows.* Nature, 2000. **406**(6794): p. 385-389

22. Bittoun, J., J. Taquin, and M. Sauzade, *A computer algorithm for the simulation of any Nuclear Magnetic Resonance (NMR) imaging method.* Magnetic Resonance Imaging, 1984. **2**(2): p. 113-120
23. Jurczuk, K., et al., *Computational modeling of MR flow imaging by the lattice Boltzmann method and Bloch equation.* Magnetic Resonance Imaging, 2013. **31**(7): p. 1163-1173
24. Cundall, P.A. and O.D.L. Strack, *A discrete numerical model for granular assemblies.* Géotechnique, 1979. **29**(1): p. 47-65
25. Schöllmann, S., *Simulation of a two-dimensional shear cell.* Physical Review E - Statistical Physics, Plasmas, Fluids, and Related Interdisciplinary Topics, 1999. **59**(1): p. 889-899
26. Finnie, G.J., et al., *Longitudinal and transverse mixing in rotary kilns: A discrete element method approach.* Chemical Engineering Science, 2005. **60**(15): p. 4083-4091
27. Komossa, H., et al., *Transversal bed motion in rotating drums using spherical particles: Comparison of experiments with DEM simulations.* Powder Technology, 2014. **264**: p. 96-104
28. Langston, P.A., U. Tüzün, and D.M. Heyes, *Discrete element simulation of granular flow in 2D and 3D hoppers: Dependence of discharge rate and wall stress on particle interactions.* Chemical Engineering Science, 1995. **50**(6): p. 967-987
29. Forterre, Y. and O. Pouliquen, *Flows of Dense Granular Media.* Annual Review of Fluid Mechanics, 2008. **40**(1): p. 1-24
30. Khain, E., *Hydrodynamics of fluid-solid coexistence in dense shear granular flow.* Physical Review E - Statistical, Nonlinear, and Soft Matter Physics, 2007. **75**(5)
31. Saitoh, K. and H. Hayakawa, *Rheology of a granular gas under a plane shear.* Physical Review E - Statistical, Nonlinear, and Soft Matter Physics, 2007. **75**(2)
32. Chialvo, S. and S. Sundaresan, *A modified kinetic theory for frictional granular flows in dense and dilute regimes.* Physics of Fluids, 2013. **25**(7)
33. Tsuji, Y., T. Kawaguchi, and T. Tanaka, *Discrete particle simulation of two-dimensional fluidized bed.* Powder Technology, 1993. **77**(1): p. 79-87
34. Deen, N.G., et al., *Review of discrete particle modeling of fluidized beds.* Chemical Engineering Science, 2007. **62**: p. 28-44
35. Müller, C.R., et al., *Granular temperature: Comparison of Magnetic Resonance measurements with Discrete Element Model simulations.* Powder Technology, 2008. **184**: p. 241-253
36. Müller, C.R., et al., *Validation of a discrete element model using magnetic resonance measurements.* Particuology, 2009. **7**(4): p. 297-306
37. Boyce, C.M., et al., *Adapting data processing to compare model and experiment accurately: A discrete element model and magnetic resonance measurements of a 3d cylindrical fluidized bed.* Industrial and Engineering Chemistry Research, 2013. **52**(50): p. 18085-18094
38. Fukushima, E., *Nuclear magnetic resonance as a tool to study flow.* Annual Review of Fluid Mechanics, 1999. **31**: p. 95-123
39. Wheeler-Kingshott, C.A., Y. Crémillieux, and S.J. Doran, *Burst Imaging: Rotation Artifacts and How to Correct Them.* Journal of Magnetic Resonance, 2000. **143**(1): p. 161-171
40. Fabich, H.T., et al., *Measurements of the velocity distribution for granular flow in a Couette cell.* Physical Review E, 2018. **98**(6)

41. Kuczera, S. and P. Galvosas, *Advances and artefact suppression in RARE-velocimetry for flow with curved streamlines.* Journal of Magnetic Resonance, 2015. **259**: p. 135-145
42. Holland, D.J., et al., *Spatially resolved measurement of anisotropic granular temperature in gas-fluidized beds.* Powder Technology, 2008. **182**(2): p. 171-181
43. Kloss, C., et al., *Models, algorithms and validation for opensource DEM and CFD-DEM.* Progress in Computational Fluid Dynamics, 2012. **12**(2-3): p. 140-152
44. Rackl, M. and K.J. Hanley, *A methodical calibration procedure for discrete element models.* Powder Technology, 2017. **307**: p. 73-83
45. Khawaja, H., et al., *Quantitative analysis of accuracy of voidage computations in CFD-DEM simulations.* Journal of Computational Multiphase Flows, 2012. **4**(2): p. 183-192
46. Clarke, D.A., et al., *Investigation of Void Fraction Schemes for Use with CFD-DEM Simulations of Fluidized Beds.* Industrial and Engineering Chemistry Research, 2018. **57**(8): p. 3002-3013
47. Jung, J., D. Gidaspow, and I.K. Gamwo, *Measurement of Two Kinds of Granular Temperatures, Stresses, and Dispersion in Bubbling Beds.* Industrial & Engineering Chemistry Research, 2005. **44**: p. 1329-1341
48. Scheven, U.M., et al., *A cumulant analysis for non-Gaussian displacement distributions in Newtonian and non-Newtonian flows through porous media.* Magnetic Resonance Imaging, 2007. **25**(4): p. 513-516
49. Rao, C.R., *Linear statistical inference and its applications.* Vol. 2. 1973: Wiley New York.
50. Ai, J., et al., *Assessment of rolling resistance models in discrete element simulations.* Powder Technology, 2011. **206**(3): p. 269-282
51. Wang, X., H.P. Zhu, and A.B. Yu, *Microdynamic analysis of solid flow in a shear cell.* Granular Matter, 2012. **14**(3): p. 411-421

6. Quantitative validation of MRI volume fraction measurements for granular flow

Experimental validation of discrete and continuum models for granular media requires accurate measurements of the local solid volume fraction within granular flows. Magnetic resonance imaging experiments are capable of measuring the local density of spin-active nuclei. However, there is potential for the images to be distorted, particularly due to spin motion, or by the reconstruction algorithm. The signal attenuation effects of spin motion can be minimised by use of velocity compensated phase encoding and slice selection gradient pulse sequences. To verify that the images are quantitative measures of the solid volume fraction, MRI simulations were performed on an annular shear cell of spheres and compared to the exact volume fraction. A model for the signal intensity was developed to reduce the computation time compared to the satellite point based method used in Chapter 5. Low resolution MR images were in poor quantitative agreement with the exact volume fraction due to the presence of Gibbs ringing associated with the implicit truncation of the signal in k-space. Images without ringing were generated by mapping high resolution images onto coarser spatial grids. Radial profiles of the signal intensity were in excellent agreement with the exact volume fraction. MRI experiments with several slice gradient strengths were performed and found to agree, demonstrating that the gradient sequence was able to compensate for velocity related artifacts. The results in this chapter confirm that with the use of velocity compensating gradient sequences and suitable image reconstruction, it is possible to obtain quantitative volume fraction measurements.

6.1. Introduction

Solid volume fraction is an important continuum mechanical variable used in the characterisation of granular flows. The void fraction is defined as the ratio of volume occupied by the fluid phase to the total volume. The rheology of granular media is strongly dependent upon the void fraction, which gives a measure of whether the material is like a solid, liquid or gas. Experimental measurement of the volume fraction is required for the purposes of model development and validation. For example, recent work towards a microscopic definition of the nonlocal granular fluidity postulates that the dimensionless

fluidity has a characteristic relationship with the void fraction common to several flow configurations [1]. Non-invasive techniques are advantageous as they do not interfere with the flow and can be applied to opaque systems. Radiation imaging techniques such as gamma radiation densitometry operate on the principle that radiation intensity is attenuated when passing through matter [2]. This attenuation is measured by placing a radiation source and detector outside of the system. Densitometry has been widely used to measure the void fraction in lab-scale bubbling fluidised beds [3, 4] and circulating fluidised beds [5]. Single measurements are limited by the lack of spatial resolution along the direction of the beam [6]. However, tomographic techniques enable maps of the cross-section to be produced [5, 7] by collecting beam attenuation data along several directions and creating the map with a reconstruction algorithm.

Particle tracking techniques such as positron emission particle tracking (PEPT) and magnetic particle tracking (MPT) consist of a single (or several) tracer particles whose position may be inferred (from emitted radiation or magnetic field, respectively) over time. For PEPT, the tracer is a positron producing nuclide, such as ^{18}F. A pair of gamma rays travelling in opposite directions is produced by positron-electron annihilation events. Detectors are placed in an array around the system and the tracer position is inferred from the intersection of detected rays [8]. For MPT, the magnetic field produced by a bar magnet embedded within the tracer particle is detected by an array of anisotropic magnetic resistive sensors. The position and orientation of the tracer is inferred by relating the magnetic field at the detectors to the theoretical magnetic field around the particle [9]. These position data are grouped into spatial bins to obtain a local occupancy fraction, which is used as a proxy for void fraction assuming that the system is ergodic. Particle tracking methods are limited by uncertainty in the position of the tracer and by long experiment times to gain a representative sample of the full system, which are not always possible.

Magnetic resonance imaging is another non-invasive measuring technique that can recover density information. In this case, the density of spin-active nuclei can be related to the signal intensity. The use of NMR for spatially unresolved phase concentration measurements was developed for a water-air mixture by Lynch and Segel [10]. In this system, only water contained spin-active nuclei, thus the signal intensity was proportional to the fraction of water in the system. The fraction of oil-water mixes was measured using continuous-wave NMR by Abouelwafa and Kendall [11]. Although both materials contained spin-active nuclei, this method exploited the difference in the relaxation times of the fluids. The fraction of each

fluid was a function of the optimal RF magnetic field that produced the maximum signal amplitude. Spatially resolved 2D density images were produced by Kose et al. [12] for single phase flow. The spins are dephased due to the flow and are rephased by the application of pulsed field gradients. This approach was extended to granular suspensions by Majors et al. [13] with a second-echo frequency encoding sequence along the direction of flow and phase encoding in the transverse plane. Void fraction measurements in granular Couette flow were performed by Graham et al. [14]. These measurements were able to resolve localised ordering of granules. The aforementioned studies measured the signal from an interstitial fluid due to the challenges of applying NMR to solids. Measurements of the particle phase can be achieved by using particles that contained mobile oil, such as the mustard seeds used in the experiments of Nakagawa et al. [15].

For systems with rapid granular motion, signal attenuation due to particle motion becomes more prominent. These artifacts can be reduced by conducting measurements over a time scale below that of particle motion. Density measurements have been applied to fluidised beds [16] and hopper flow [17] using single point imaging, where one point in k-space is acquired per excitation. For fluidised beds, other imaging sequences that have been applied include a tailored spin-echo sequence [18], and ultrashort echo time measurements [19]. For granular flow in the Couette shear cell geometry, volume fraction measurements were performed by de Cagny et al. [20], however, they did not specify the imaging sequence that was used. Moucheront et al. [21] measured the solid volume fraction when the system was stationary after it was sheared. It is not certain that static measurements following shearing are a suitable proxy for measurements while shearing. There has been limited validation of these methods to confirm that motion does not influence the signal intensity. Thus, it is still an open question whether MRI is capable of quantitative volume fraction measurements of granular flows.

Chapter 5 demonstrated that phase encoded MRI is an excellent method for velocimetry since the imperfect rephasing of moving spins is used to measure the mean velocity and the signal attenuation is used to measure the variance of velocity. Signal attenuation is undesirable for volume fraction measurements since regions with a large variance in velocity have reduced signal intensity and hence appear to be less densely packed. To mitigate this effect, the gradient sequence is changed to compensate for constant motion during the acquisition. If there are fluctuations in the velocity during the acquisition, then this imaging sequence is not able to completely remove motion related artifacts. Changes in the velocity of the spins can

be caused by collisions between granules, or by rotational motion. Thus, there is still uncertainty whether this velocity compensated imaging technique is able to accurately measure the volume fraction due to artifacts in image reconstruction, or motion variations in time. In this chapter, computer simulations were used to simulate the MRI experiments on DEM simulations of annular shear flow, which were validated against exact void fraction measurements.

6.1.1 Theory

Section 2.4 introduces the fundamental concepts behind MRI, which forms the starting point for the derivation for void fraction measurements. The signal over the system volume, V is given by:

$$S(\boldsymbol{k}) = \int \rho(\boldsymbol{x}) \exp(i\theta)\, dV \tag{6.1}$$

where $\rho(\boldsymbol{x})$ is the spin density, which is assumed to be uniform within a granule, $\boldsymbol{x}$ is the position vector for a spin, and θ is the phase which is defined by:

$$\theta = \gamma \int_0^t \boldsymbol{g}(t') \cdot \boldsymbol{x}(t')\, dt'. \tag{6.2}$$

The pulse time is denoted as δ, and it is assumed that the ramp time is zero. The gyromagnetic ratio is denoted by γ. A velocity compensated phase encoding gradient sequence is used, where the gradient of the first pulse is three times that of the second pulse and applied in the opposite direction. Therefore $\boldsymbol{g}(t')$ is expressed by:

$$\boldsymbol{g}(t') = \begin{cases} 3\boldsymbol{g}, & 0 \le t' < \delta \\ -\boldsymbol{g}, & \delta \le t' < 2\delta \\ 0, & \text{otherwise.} \end{cases} \tag{6.3}$$

If there is phase encoding along the x and y directions, then the dot product of $\boldsymbol{g}$ and $\boldsymbol{x}$ gives:

$$\theta = 3\gamma \int_0^{\delta} g_x x(t) + g_y y(t)\, dt - \gamma \int_{\delta}^{2\delta} g_x x(t) + g_y y(t)\, dt. \tag{6.4}$$

For a particle, the position $\big(x(t), y(t)\big)$ is decomposed into the sum of the position of the centre, $\big(x_c(t), y_c(t)\big)$ and the position relative to the centre, (x', y'). It is assumed that the particle does not rotate or deform, hence x' and y' were constant with time. The Fourier shift theorem states that a displacement in the spatial domain is equal to a linear phase term in the frequency domain. The Fourier shift theorem is applied here to split the phase into two components, $\theta = \theta_c + \theta'$. The term θ_c, which represents the phase of the centre is expressed as:

$$\theta_c = 3\gamma \int_0^{\delta} g_x x_c(t) + g_y y_c(t)\, dt - \gamma \int_{\delta}^{2\delta} g_x x_c(t) + g_y y_c(t)\, dt. \tag{6.5}$$

The phase from the granule relative to its centre is equal to:

$$\theta' = 3\gamma(g_x x' + g_y y') \int_0^{\delta} dt - \gamma(g_x x' + g_y y') \int_{\delta}^{2\delta} dt. \tag{6.6}$$

Integrating θ' with respect to time gives:

$$\theta' = 2\gamma\delta(g_x x' + g_y y') = 2\pi k_x x' + 2\pi k_y y' \tag{6.7}$$

where $\boldsymbol{k} = \frac{\gamma}{2\pi}\int_0^{2\delta} \boldsymbol{g}(t)\, dt$. For this gradient sequence, $k_x = \frac{\gamma\delta g_x}{\pi}$ and $k_y = \frac{\gamma\delta g_y}{\pi}$. The spin density is assumed to be uniform and arbitrarily set to unity. Equation 6.1 is expressed as:

$$S = \iiint \exp(i\theta_c) \exp(i2\pi k_x x') \exp\left(i2\pi k_y y'\right) dV. \tag{6.8}$$

For the integral of the terms involving x' and y', a change of variables is performed where V is replaced with the volume of a single particle, V_p. For granular systems, θ_c does not have a continuous functional form as centres are located at random, discrete positions. Thus, the integral of θ_c with respect to V is replaced with a summation over all particles, giving the following:

$$S = \sum_{p=1}^{N_p} \exp\left(i\theta_{c,p}\right) \iiint \exp(i2\pi k_x x') \exp\left(i2\pi k_y y'\right) dV_p. \tag{6.9}$$

To solve the volume integral, we let $\|\boldsymbol{k}\| = k_x$ to simplify the integration. Due to the spherical symmetry of the granule, the 2D signal in the frequency domain is constant for any given $\|\boldsymbol{k}\|$. From the geometry of the sphere, the area of the cross-section at x' is $\pi\left(R^2 - x'^2\right)$, thus the integral may be expressed in terms of a single variable:

$$S = \sum_{p=1}^{N_p} \exp\left(i\theta_{c,p}\right) \int_{-R}^{R} \pi\left(R^2 - x'^2\right) \exp(i2\pi k_x x')\, dx'. \tag{6.10}$$

This integral has an analytical solution, expressed in terms of trigonometric functions as follows:

$$S = \sum_{p=1}^{N_p} \exp\left(i\theta_{c,p}\right) \times \frac{\pi(-2\pi\|\boldsymbol{k}\|R\cos^2(\pi\|\boldsymbol{k}\|R) + \sin(\pi\|\boldsymbol{k}\|R)\cos(\pi\|\boldsymbol{k}\|R) + \pi\|\boldsymbol{k}\|R)}{\pi\|\boldsymbol{k}\|^3 R^3}. \tag{6.11}$$

Equation 6.11 suggests that the model can quantify the effect of translational particle motion on the signal as it does not make any assumptions about the granule trajectories. Equation 6.5 was numerically integrated with respect to time using DEM data for each particle. Since this method avoids the use of satellite points as used in Chapter 5, MRI experiments can be simulated more rapidly and without introducing discretisation of the particles. The method provides information about the effects that granule motion and image reconstruction have on the signal intensity. However, this approach is- not able to model the effect of rotation. If it is assumed that the angular displacement is low such that the projected velocity due to rotation is constant over the acquisition time, then this effect is removed by the gradient sequence. Thus, the effect of rotation can be considered to be negligible.

6.2. Method

6.2.1 Discrete element method

The system of interest is an annular Couette shear cell where granules are contained between two concentric cylindrical walls. Two different sizes were tested as shown in Figure 6.1: (1) the inner diameter was 16 mm, the outer diameter was 23.7 mm, and the inner cylinder was rotated at 0.5 Hz. (2) The inner diameter was 6 mm, the outer diameter was 9 mm, and the inner cylinder rotated at 1 Hz. The latter system had the same dimensions and velocity as the experiment. In both cases the outer wall was stationary. The open-source LIGGGHTS software [22] was used to run the simulations. The simulations in system (1) contained 100,000 spheres, while system (2) contained 50,000 spheres. The particle diameter was normally distributed with a mean of 0.44 mm with a standard deviation of 0.02 mm. System (2) was also run with multisphere particles to approximate monodisperse prolate ellipsoids. The semi-major axis was 0.53 mm and the semi-minor axis was 0.36 mm. Each particle was made from five spheres, as shown by Figure 6.1(d). The elastic modulus was set to 1×10^7 Pa to keep computation time to a minimum. The coefficient of restitution was set to 0.9, and the surface friction coefficient was set to 0.1. The selection of these values was arbitrary since the DEM trajectory data was used to test the imaging sequence. For spherical particle simulations, rough walls were modelled by a cylindrical layer of particles in a face-centred cubic arrangement. The remaining particles were randomly dropped into the annular gap. For the ellipsoid simulation, all the particles were dropped into the gap and the rough walls were defined by selecting the particles within $1d_p$ of either wall. Once the particles had settled, the inner rough wall was rotated about its central *z*-axis. A solid wall was imposed on the top of

system (1) to apply a load of 2000 Pa. No confining pressure was added to system (2) for consistency with experiments. The simulations were run with a time step of 1×10^{-6} s which was deemed to be sufficiently low as this step size was 8% of the Rayleigh time, below a recommendation of 25% [23]. The void fraction map was calculated using the same spatial grid obtained from MRI simulations. For each pixel, the void fraction was given by:

$$\varepsilon_s = \frac{\sum_{i=1}^{N_s}\sum_{p=1}^{N_p}\phi_{p,i}}{N_s V_{cell}} \tag{6.12}$$

where $\phi_{p,i}$ is the volume fraction of particle p of sample i in the cell of interest, N_s is the number of samples taken, and V_{cell} is the volume of the cell. Since high resolution void fraction maps are required for comparison with simulated MR images, the exact method of Strobl et al. [24] was used to produce accurate void fraction maps, even where the cells were below the scale of the particle diameter.

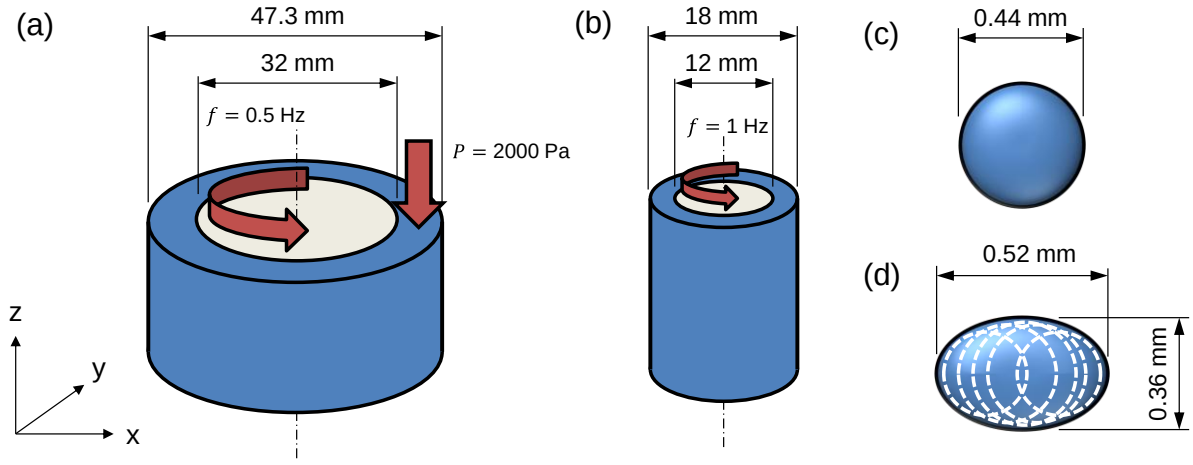

Figure 6.1. Schematics of annular Couette geometries simulated in this chapter. (a) MRI simulated cell, with an inner diameter of 32 mm and an outer diameter of 47.3 mm. The inner cylinder was rotated at 0.5 Hz and a confining pressure of 2000 Pa was applied. (b) Cell to compare to MRI experiments, with an inner diameter of 12 mm, an outer diameter of 18 mm, rotated at 1 Hz, and no confining pressure. (c) Spherical particles (d_p = 0.44 mm) were simulated in both geometries. (d) Multisphere ellipsoids were modelled in the smaller geometry shown in (b). The spheres that constituted the granule are denoted by the dashed lines.

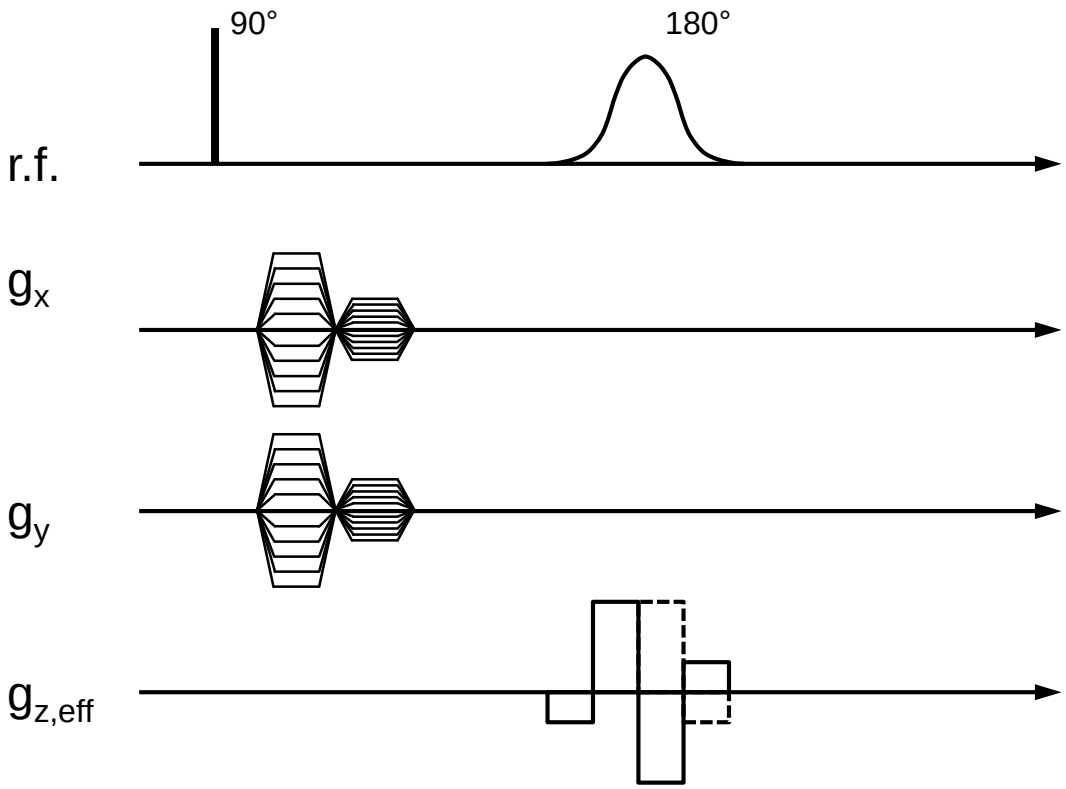

Figure 6.2. Imaging sequence used for the simulations and experiments. Phase encoding is done with two velocity compensating gradient pulses along the x-y plane. Slice selection is performed with a velocity compensating gradient sequence and a 180° soft RF pulse. The effective gradient is denoted by the solid line.

6.2.2 MRI simulations

The underlying theory for the acquisition of the signal was outlined in 6.1.1. The imaging sequence used in simulations and experiments is given in Figure 6.2. The sample is excited by a 90° RF pulse. Velocity compensated phase encoding is performed along the x and y directions. The strength of the first gradient pulse is three times the strength of the second, such that the reciprocal velocity vector is equal to zero. The time of each pulse was set to 300 μs. In simulations, the gradients were applied at full strength immediately, thus the effect of ramping in experiments was assumed to be minimal. Image resolutions of 32 × 32 px, 64 × 64 px, 128 × 128 px, 256 × 256 px, 512 × 512 px, and 1024 × 1024 px were computed. The field of view (FOV) and the image resolution depend upon the maximum magnetic field gradient and the number of gradient steps taken. The FOV is calculated from:

$$\mathrm{FOV} = \frac{1}{\Delta k}. \tag{6.13}$$

The increment between magnetic field gradients was 6.25×10^{-4} T m^{-1}, thus $\Delta k = 16$ m^{-1}, and the FOV is 63 mm. Since the FOV and hence the gradient increment is fixed, the image resolution is controlled by the number of gradient steps. The signal in k-space is calculated by

evaluating Equation 6.11 for every combination of k_x and k_y. A 2D discrete Fourier transform of the signal recovers the spatially resolved signal intensity. The solid volume fraction was determined by scaling the intensity of the image against a known void fraction. Here, the mean volume fraction at the inner rotating layer of fixed particles was used because of the uniformity of the image in this area. To isolate a vertical region, a velocity compensated slice selecting gradient was applied 500 μs after the end of the second phase encoding pulse. This gradient consisted of two pulses with duration of 256 μs during the soft RF pulse. The slice width Δz is controlled by the range of frequencies $\Delta\omega_s$ and the slice gradient g_z according to:

$$\Delta z = \frac{\Delta\omega_s}{\gamma g_z}. \tag{6.14}$$

Equation 6.14 shows that a narrower slice is obtained by increasing the slice gradient strength while keeping the time of the RF pulse fixed. Velocity encoding from the slice gradient is proportional to the strength of the slice gradient, thus the signal is more strongly attenuated by motion when imaging thin slices. For this reason, it is important to compensate for motion along the direction of the slice gradient. The slice gradient sequence is shown in Figure 6.2, and is designed such that $k_z = p_z = 0$. To confirm that motion parallel to slice selection did not affect the images, the z contribution to θ_c was calculated for a series of slice gradients. In reality, the slice width is inversely proportional to the slice gradient strength; however it is not of interest to model the changing slice thickness. Instead, the slice region where particles were sampled was fixed such that any changes to the image could be attributed to the slice gradient.

When reconstructing the image by Fourier transform, it is implicitly assumed that for values of $\|\boldsymbol{k}\|$ outside of the sampled region that the signal is zero. This truncation introduces an artifact known as Gibbs ringing. At sharp gradients in image intensity, the signal at large values of $\|\boldsymbol{k}\|$ are required to correctly resolve edges. For higher resolutions, the range of k-space is wider and information about the signal at high frequencies is captured, thus the effect of Gibbs ringing is reduced with increasing image resolution. Several approaches have been proposed to remove Gibbs ringing. Image filtering (such as Gaussian or sine filters) smooths the ringing by introducing a bias in favour of low frequencies, however blurring is introduced which makes filtered images unsuited for quantitative measurements of the volume fraction. More advanced methods extrapolate the signal in k-space. The form of this extrapolated signal may be controlled by total variation (TV) regularisation [25, 26]. As the ringing effect

is equivalent to the convolution of the true image with a sinc function, Kellner et al. [27] propose that the amplitude of these oscillations is related to the position of an edge relative to the sampling points. Their algorithm identifies the pixel shift that minimises the local intensity oscillation between pixels and interpolates the image intensity onto the original grid. In principle, it is possible to de-ring images by a least squares fit to the signal data, with the constraint that the signal intensity in the spatial domain outside of the shear cell was zero. This aspect of image reconstruction is not considered in this chapter, instead low-resolution images are produced by mapping a high-resolution image onto a coarse spatial grid. Since the pixels at different resolutions overlap each other, a weighted average was used to allocate signal intensity to the low-resolution map. The divided cube method [28], used in Chapter 4 to approximate the volume fraction of a sphere in a fluid phase computational cell was used to calculate the exact intersecting area between the image pixels and low resolution grid pixels.

6.2.3 MRI experiments

Couette shear experiments were performed at Victoria University of Wellington. The concentric cylinder shear cell consisted of a rotating inner cylinder of radius 6 mm, and a fixed outer cylinder with a radius of 9 mm. The granular material sheared were lobelia seeds, with a mean diameter of 0.44 mm. The particle size distribution was log-normal with a standard deviation of 0.027 mm. The seeds were approximately ellipsoidal, with a mean aspect ratio of 0.7. The standard deviation in the aspect ratio was 0.065. The walls were roughened by affixing seeds to the cylinders with adhesive tape. The imaging device consisted of a Bruker wide bore superconducting magnet, an Avance II spectrometer, a Micro2.5 three-axis imaging gradient coil system that generated a maximum gradient of 1.5 T m^{-1}, and a 25 mm birdcage RF coil. The phase encoding gradients were stepped about zero with a maximum strength of 0.0612 T m^{-1} in increments of 0.002 T m^{-1}, which corresponded to images with a resolution of 64 × 64 px. The phase encoding gradient pulses were ramped over 180 μs, and held at the specified strength for 120 μs. Assuming linear ramping, these pulses are equivalent (in terms of $\boldsymbol{k}$) to a square pulse where $\delta = 300$ μs. Images with slice thicknesses of 10 mm, 5 mm, 2.5 mm, and 1 mm were acquired. The corresponding slice gradients were: 0.0075 T m^{-1}, 0.015 T m^{-1}, 0.03 T m^{-1}, and 0.075 T m^{-1}.

6.3. Results and discussion

6.3.1 Validation of MRI

Figure 6.3 shows maps of the scaled image intensity found using the MRI simulations at several resolutions. Gibbs ringing is present at the lowest resolutions in Figure 6.3(a) and (b) as shown by the pattern of high-intensity voxels around the edges of the annulus. These rings are an artifact of the truncation of the signal to the sampled region in k-space. Increasing the span of the sampled region in k-space reduces the relative magnitude of the Gibbs ringing effect, at the expense of more time-consuming experiments which may prove to be infeasible in practice. For smaller voxels, the range of signal intensities widens as a voxel may either fully contain granules or the voids between granules, unlike in larger voxels which all contained many granules. Thus, the chequered pattern in the outer region of Figure 6.3(d) forms. Further refinement resolves individual particles as shown in Figure 6.3(e) and (f). In both cases, granules further away from the inner wall are resolved, but not particles near the inner moving wall. The simulated images were time averaged over a second, a time scale where granules near the inner wall were displaced, while particles near the outer wall were stationary. As a result, the signal intensity is smoothed at the inner wall. Since physical measurements are obtained over a period of minutes or hours, such smoothing would also likely occur near the outer wall in experiments. The local ordering of particles near the wall was visible by the dark circular fringes near the inner wall. This pattern forms due to the narrow size distribution of the spheres, and has been observed in physical experiments of dry granular flows [29].

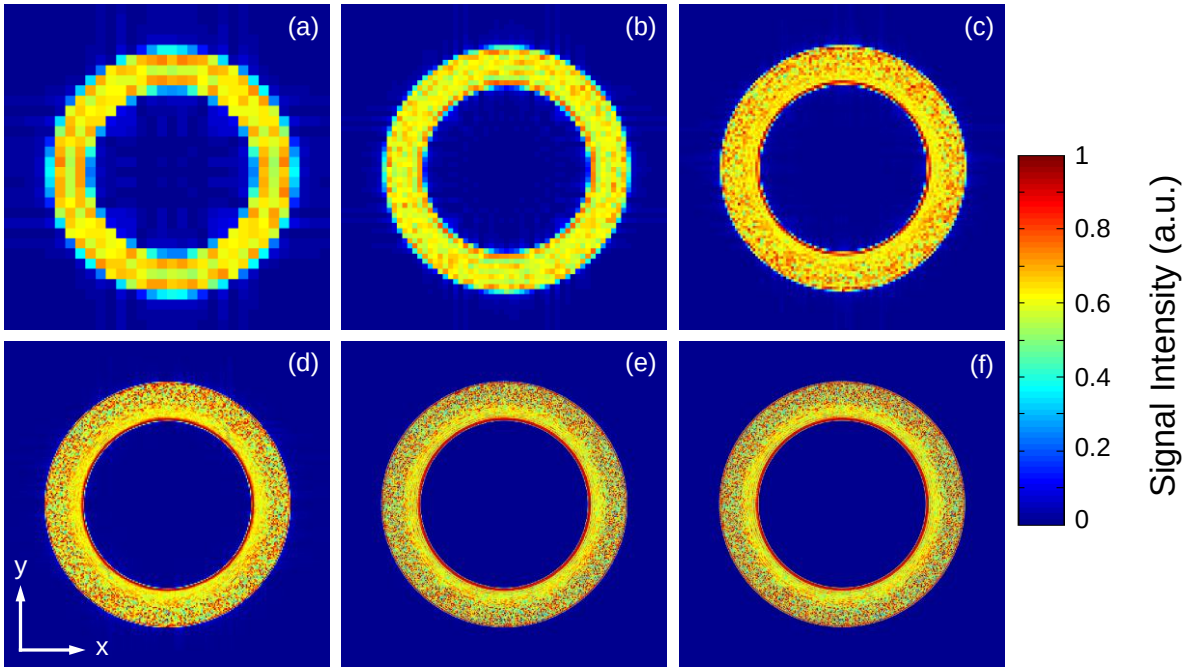

Figure 6.3. Scaled signal intensity (in arbitrary units) for annular Couette flow of 0.44 mm spheres. The FOV is 63 mm, the OD of the cell is 47.3 mm and the ID is 32 mm. The slice in the z direction is 1 mm thick. The image resolutions are: (a) 32 px × 32 px, (b) 64 px × 64 px, (c) 128 px × 128 px, (d) 256 px × 256 px, (e) 512 px × 512 px, (f) 1024 px × 1024 px.

Figure 6.4 shows the void fraction maps obtained using the exact method [24] where the bin positions were defined to correspond to the MR images in Figure 6.3. For the lowest resolution images, the solid volume fraction is generally uniform with a value of about 0.6. The high intensity rings of voxels in Figure 6.3(a) are absent in Figure 6.4(a), confirming that Gibbs ringing is significant at low resolutions. For resolutions of 256 × 256 px and above, the maps from the MRI simulations and the exact void fraction scheme appear visually similar, however they are not identical. Gibbs ringing is still present but is less perceptible.

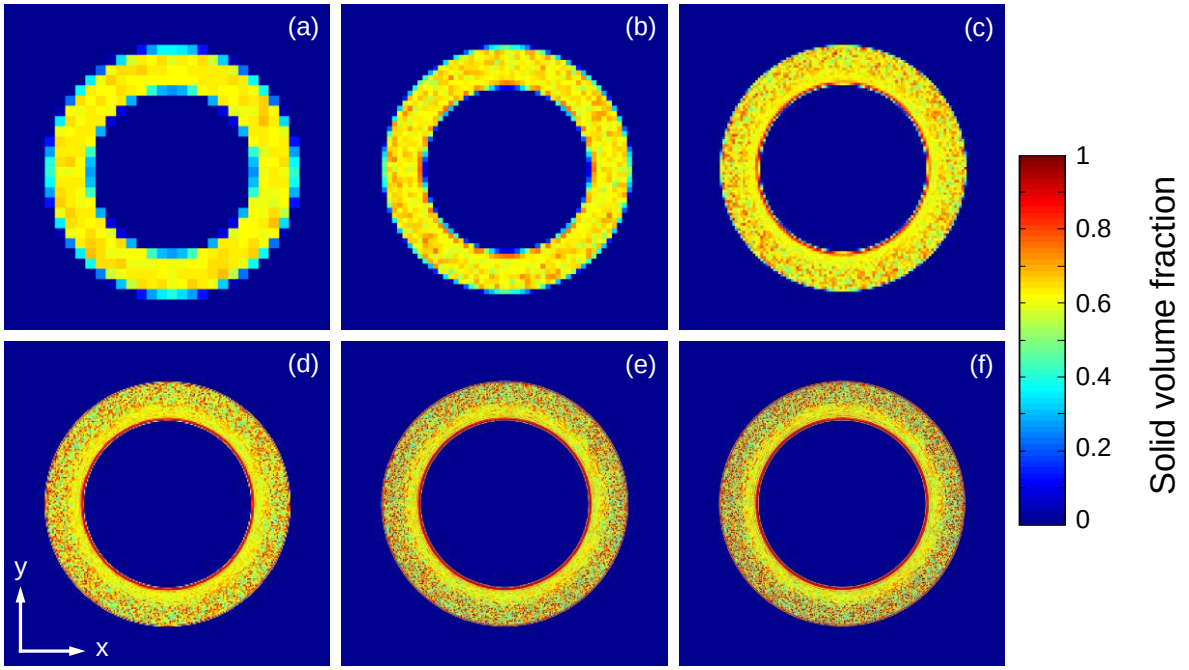

Figure 6.4. Void fraction for annular Couette flow of 0.44 mm spheres. The FOV is 63 mm, the OD of the cell is 47.3 mm and the ID is 32 mm. The slice in the z direction is 1 mm thick. The image resolutions are: (a) 32 px × 32 px, (b) 64 px × 64 px, (c) 128 px × 128 px, (d) 256 px × 256 px, (e) 512 px × 512 px, (f) 1024 px × 1024 px.

Since MRI is to be used to measure the solid volume fraction, the quantitative agreement between the signal intensity and void fraction was analysed. The scaled signal intensity within the gap was plotted against the exact void fraction in Figure 6.5. A measure of the density of the points was indicated by the standard deviation orthogonal to the direction of greatest variance. This standard deviation was calculated from the relevant eigenvalue of the covariance matrix. This standard deviation should be sufficiently small (< 0.01 units) such that the image intensity reliably corresponds to a particular volume fraction. For the 32 × 32 px images where the local solid volume fraction is close to the random packing limit as evidenced by the low standard deviation, the normalised intensity of the MR image varies between 0.7 and 1. The direction of greatest variance was not along the diagonal due to the insensitivity of the void fraction relative to the image intensity. This insensitivity and the prominence of Gibbs ringing mean that an image resolution of 32 × 32 px is inadequate for quantitative measurements. For the more resolved images, the direction of maximum variance was more closely aligned with the diagonal, indicating that Gibbs ringing was diminished. The error was around 0.03, which is too large to distinguish between the ordered shear band and the randomly packed slow region further away from the inner wall. However, as the image resolution increased, the standard deviation reduced to within a more acceptable level. For the 1024 × 1024 px image, the orthogonal error was 0.01. This variation is

acceptably low and lends confidence that MRI offers a quantitative relationship with the void fraction. The 64 × 64 px images obtained by experiment took place over about 30 minutes. A similar experiment for a 1024 × 1024 px image would take several days. Therefore, it is not practical to conduct experiments at the highest resolution simulated in this chapter.

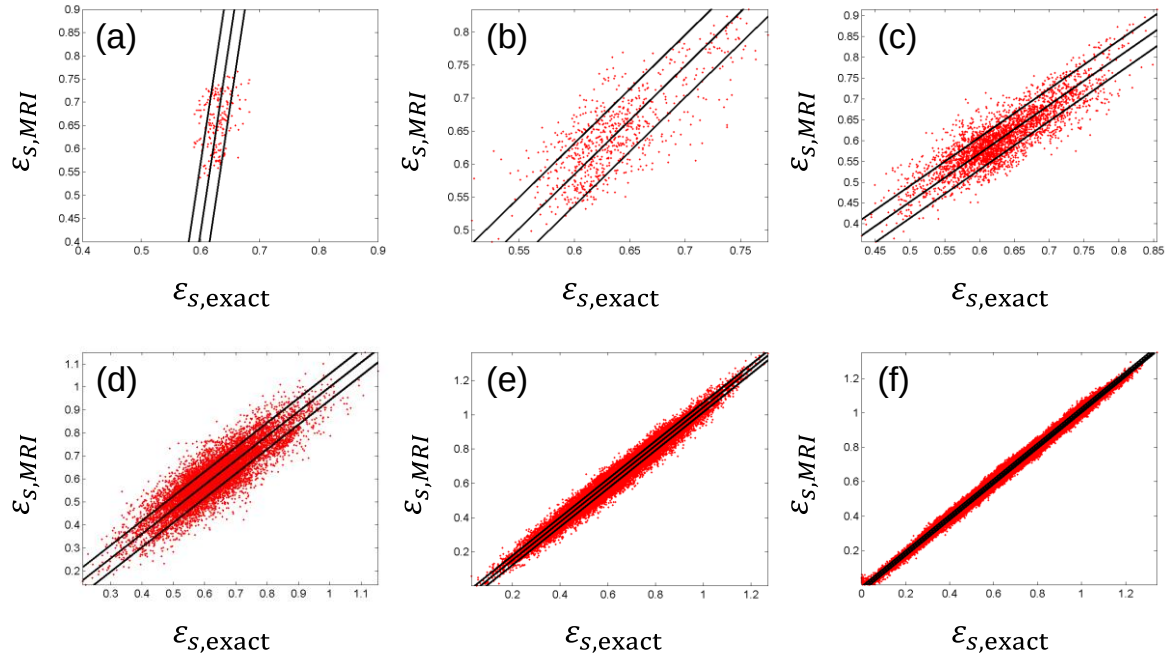

Figure 6.5. Scatter plot of scaled MRI image intensity against the exact solid volume fraction within the gap of the annular Couette shear cell. The images resolutions were: (a) 32 px × 32 px, (b) 64 px × 64 px, (c) 128 px × 128 px, (d) 256 px × 256 px, (e) 512 px × 512 px, (f) 1024 px × 1024 px. The direction of largest variance passing through the centroid of the data and the standard deviation orthogonal to this direction is indicated by the solid lines.

The effect of the slice gradient was assessed by correlating the signal intensities of an image obtained with simulated slice selection against a reference image without slice selection ($G_s = 0$). The relative discrepancy is shown by Table 6.1. In all cases, the discrepancy is sufficiently low that the effect of the slice selecting gradient can be considered negligible for slice thicknesses of 0.5 mm or more.

Table 6.1. Relative discrepancy between image with simulated slice gradient sequence and image without slice gradient.

G_s (T m^{-1})	32×32 px	64×64 px	128×128 px	256×256 px
0.00722	1.92×10^{-11}	1.88×10^{-11}	1.72×10^{-11}	6.34×10^{-12}
0.0144	7.79×10^{-11}	7.65×10^{-11}	7.02×10^{-11}	2.76×10^{-11}
0.144	1.92×10^{-8}	2.23×10^{-8}	2.67×10^{-8}	2.94×10^{-8}

6.3.2 Correcting for Gibbs ringing

In the preceding section, it was identified that low resolution images were susceptible to Gibbs ringing and that high-resolution images are not feasible for physical experiments. For these reasons, it is important to improve the quality of low resolution images by removing Gibbs ringing. As the Gibbs ringing for the 1024 × 1024 px image is low, the effect of removing Gibbs ringing can be tested in principle by mapping this image to a lower resolution grid. The coarse mapped images and correlations to the exact volume fraction are given in Figure 6.6. Coarse-mapping has less influence when mapping to 256 × 256 px and 512 × 512 px since these images had relatively little Gibbs ringing to begin with, hence are not shown here.

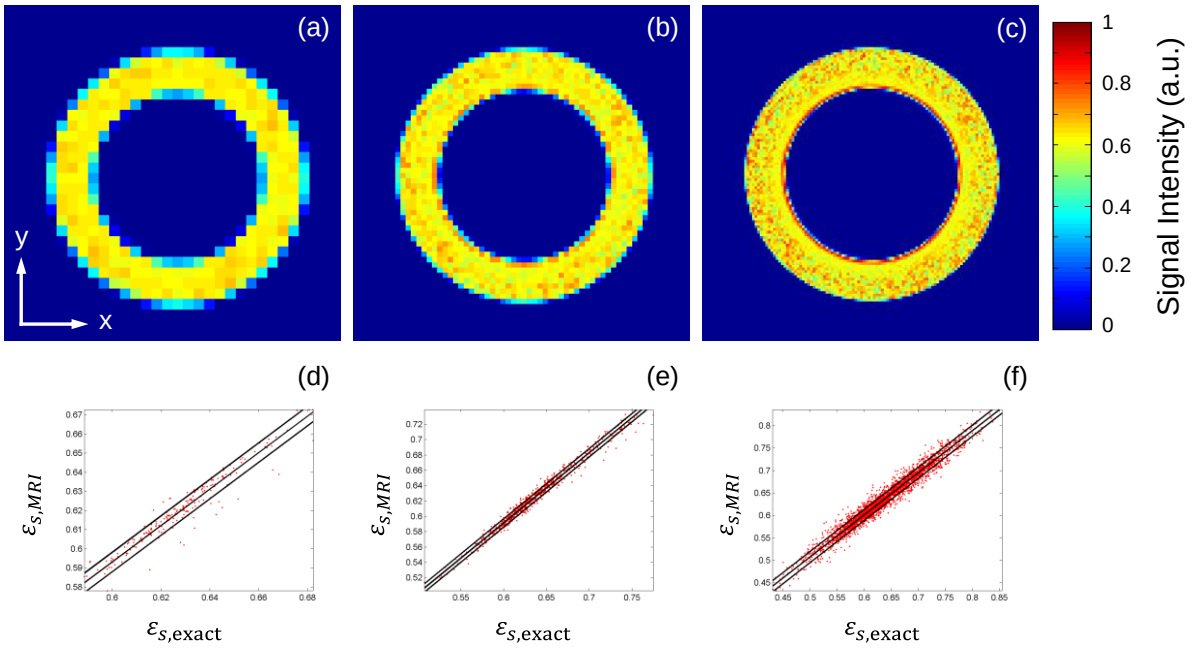

Figure 6.6. Top row: Images of MRI signal intensity of 1024 × 1024 px image mapped to lower resolutions. Bottom row: scatter plots of mapped signal intensities against exact void fraction. (a),(d): 32 × 32 px; (b),(e): 64 × 64 px; (c),(f): 128 × 128 px.

By almost entirely removing Gibbs ringing, the 32 × 32 px MR image was in excellent agreement with the exact void fraction. Comparing the scatter plot in Figure 6.5(a) to Figure 6.6(d), the direction of largest variance is now along the diagonal once Gibbs ringing has been removed, indicating that the MR signal intensity was sensitive to changes in the volume fraction and not motion. Removing Gibbs ringing also reduces the orthogonal spread of the data to less than 0.01 units for these low-resolution images. This level of accuracy is sufficient for studying dense granular flows such as annular shear. While this method is effective for removing Gibbs ringing, it is not suitable to perform in physical experiments since it requires knowledge about the very high-resolution image. The small deviations

between the MRI and the exact void fraction are the result of small differences in the position of granules. For MRI, the apparent position of the granules is an average of the positions traversed over the acquisition. For the exact void fraction, the particles positions corresponded to the end of the acquisition. Thus, it is sensible to correct for this effect by averaging the data over the azimuth to produce radial profiles of the signal intensity and volume fraction. These profiles are shown in Figure 6.7. The signal intensity is in excellent agreement with the solid volume fraction at all resolutions. Features such as the densely packed particle walls and local ordering were also captured at the 256×256 px resolution. The level of agreement was quantified by calculating the relative squared deviation, shown in Table 6.2. The discrepancy is remarkably low for all the tested resolutions. Hence MRI is able to quantitatively measure the solid volume fraction for granular flows to within the acceptable tolerance of 0.01 units.

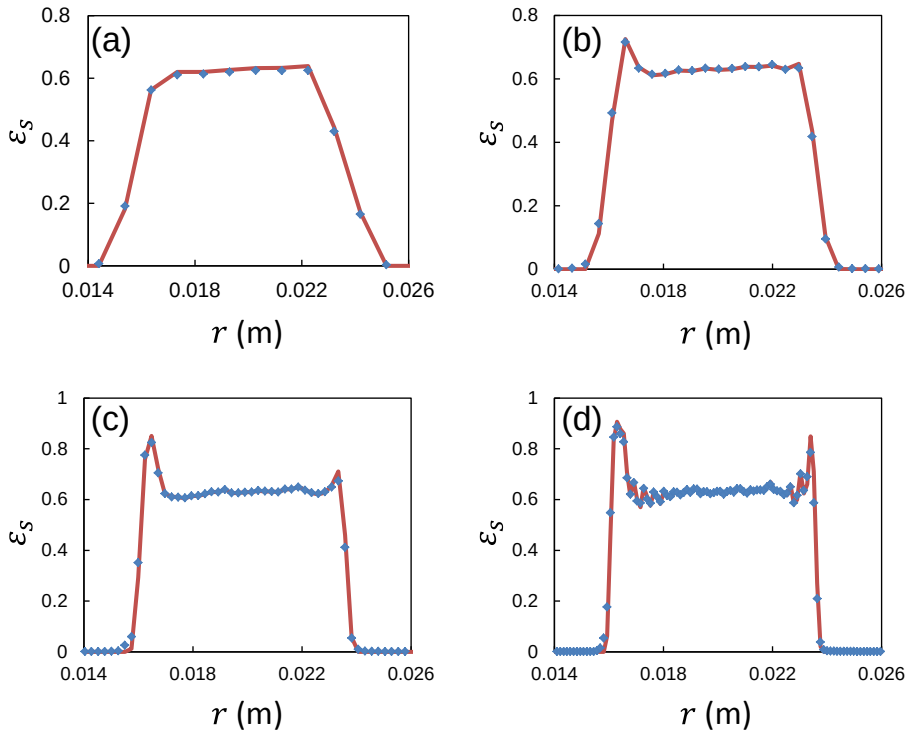

Figure 6.7. Radial profiles of scaled de-ringed signal intensity or solid volume fraction against radial coordinate for resolutions (a) 32×32 px, (b) 64×64 px, (c) 128×128 px, (d) 256×256 px. MRI simulation: ♦, exact solid volume fraction: (—).

Table 6.2. Relative squared deviation between radially averaged simulation MR image and exact volume fraction.

Image Resolution (px)	32 × 32	64 × 64	128 × 128	256 × 256
Relative squared deviation	0.02%	0.04%	0.09%	0.21%

6.3.3 Comparison with experiment

Signal intensity maps for the experiment are shown in Figure 6.8 for slice thicknesses of 10 mm, 5 mm and 1 mm. The Gibbs ringing artifact is apparent for the two largest slices shown and is masked by noise in the 1 mm slice, thus it is unclear if the signal intensity is an adequate representation of the volume fraction without further correction. However, these data are still useful from the perspective of assessing whether the slice gradient introduces motion-related signal attenuation. If these images quantitatively agree with each other, then it is inferred that slice selection does not affect the measured signal. To remove the effect of an inhomogeneous RF magnetic field, the images were scaled by an image obtained with the sample at rest. For this scaling to be sensible, the material must be in a similar state for the images obtained under flow and at rest. For example, a voxel containing voids in one image is not a suitable point for comparison against a voxel containing granules. This requirement places a restriction on the practical resolution of the image. If the resolution is on the order of the granule diameter, then the voxels will likely contain a combination of granules and voids such that the signal intensity is time invariant. The voxels in these experiments were $0.8d_p$ in length, thus local ordering effects were not resolved. Hence, it is suitable to rescale the images by a static reference. Radial profiles of the rescaled signal intensity were obtained by dividing the images by an image of the static system, averaged over the azimuth and rescaled by the maximum signal in the 10 mm slice. These profiles are shown in Figure 6.9(a) and are in excellent agreement with each other, suggesting that the velocity compensating slice selection gradient pulse sequence was effective for removing motion induced artifacts. From these experiments, it is concluded that the signal intensity is a real measure of the spin density and hence the solid volume fraction.

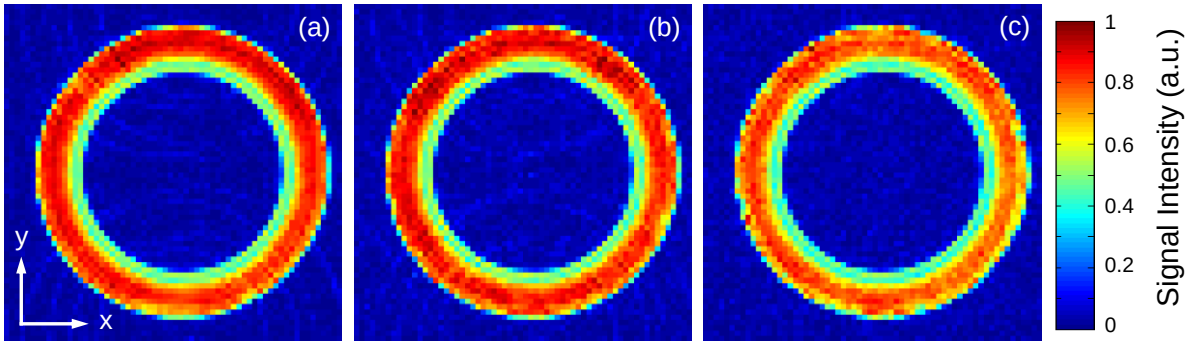

Figure 6.8. Signal intensity maps obtained by MRI experiments for slice thicknesses of (a) 10 mm, (b) 5 mm, (c) 1 mm.

DEM simulations were performed using the same geometry as the experiments using spherical and ellipsoidal particles. Radial volume fraction profiles are shown in Figure 6.9(b). For the simulations of spheres, radial ordering is apparent at the tested resolution. No ordering is apparent for the ellipsoids. This disparity indicates that it is important to model the nonsphericity of the experimental particles for DEM simulations to replicate the packing of granules accurately. It is also noteworthy that the ellipsoids pack more densely than the spheres, which is consistent with findings from literature [30]. Thus, knowledge of the packing of the real particles is required to quantitatively relate the image intensity to the volume fraction.

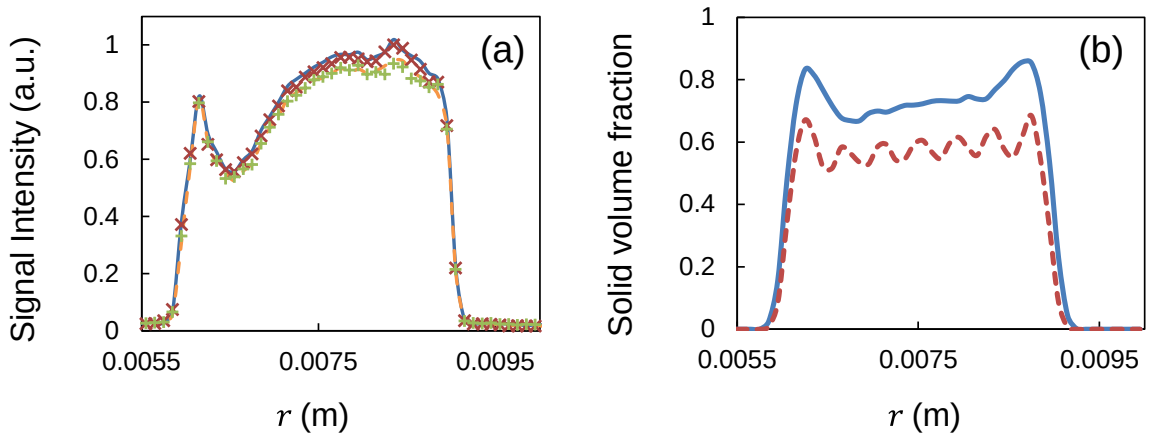

Figure 6.9. (a) Radial profile of the rescaled MR signal intensity for Couette flow physical experiments. The dotted lines indicate the expected positions of the inner and outer cylinders of the Couette shear device. The results obtained are for slice thicknesses of 10 mm (×) , 5 mm (—), 2.5 mm (- -), 1 mm (+). (b) Radial profile of Couette shear flow volume fraction in DEM simulations of the experimental device for ellipsoids (—) and spheres (- -).

The experimental signal intensity profiles differ from the DEM simulations in two regards. First, peaks at the walls in the simulation were higher than the volume fraction in the gap. The peaks in the experiment were similar to the gap material. This difference is the result of the packing at the rough walls. The simulation walls were created by isolating the first layers of particles poured into the gap, while the experiments applied particles to adhesive tape. These methods likely result in different packing fractions. Second, the material close to the inner moving wall was more dilute in the experiments than the simulations. In the experiments, the local minimum in the image intensity is about 60% of the intensity at the outer part of the gap. For the ellipsoid simulation, this ratio is about 90%. The exact reason for this dilation in the experiment is unclear. In bidisperse suspensions, shear-induced size segregation occurs [14, 31] where larger granules migrate to the outer wall. It is unlikely that this phenomenon occurred in the system studied in this chapter since the granules were not

bidisperse. The packing of the wall also had an influence in the form of the effective roughness since wall roughness is proportional to the spacing between granules. Couette shear experiments with variable granule spacing found that increasing wall roughness decreased the local volume fraction near the inner wall [32]. As the walls in the experiment were less densely packed than the simulations, the effective roughness was higher for the experiment than for the simulations. Rougher walls may account for the lower volume fraction observed near the inner wall by the experiments.

6.4. Conclusions

DEM simulations of granules under annular shear were used to generate MR images. The speed of the image generation process was improved by the analytical expression for the signal from a spherical object and by application of the Fourier shift theorem. The intensity of the MR images was compared to the exact local solid volume fraction. For the lowest resolution, the MR image intensity was insensitive to the local solid volume fraction due to the prominence of Gibbs ringing. High resolution images were in good quantitative agreement yet remain impractical due to long experiment times. It was demonstrated by mapping the highest resolution image to coarse grids that it is possible in principle to attain excellent quantitative agreement with the exact volume fraction, even at low image resolutions. Due to the motion of granules during acquisition, the signal intensity associated with each granule was in a different position relative to the exact volume fraction map. The images were azimuthally averaged to remove this effect. The radial profiles obtained from MRI simulations were in excellent agreement with the exact volume fraction. Experiments performed with different slice gradient strengths returned similar signal intensity profiles, confirming that the velocity compensating slice selection gradient pulse sequence did not cause granule motion to attenuate the signal. A DEM simulation of ellipsoids was not able to reproduce the volume fraction profile of the experiments. However, this disparity is likely due to the simulations not accurately representing the real particle size and shape distributions and not due to errors in the MRI measurement technique. Through careful design of the gradient pulse sequence and image reconstruction, non-invasive, quantitative measurements of the solid volume fraction can be achieved with MRI.

6.5. References

1. Zhang, Q. and K. Kamrin, *Microscopic Description of the Granular Fluidity Field in Nonlocal Flow Modeling.* Physical Review Letters, 2017. **118**(5)
2. Bartholomew, R.N. and R.M. Casagrande, *Measuring Solids Concentration in Fluidized Systems by Gamma-Ray Absorption.* Industrial and Engineering Chemistry, 1957. **49**(3): p. 428-431
3. Gidaspow, D., C. Lin, and Y.C. Seo, *Fluidization in Two-Dimensional Beds with a Jet. 1. Experimental Porosity Distributions.* Industrial and Engineering Chemistry Fundamentals, 1983. **22**(2): p. 187-193
4. Weimer, A.W., D.C. Gyure, and D.E. Clough, *Application of a gamma-radiation density gauge for determining hydrodynamic properties of fluidized beds.* Powder Technology, 1985. **44**(2): p. 179-194
5. Azzi, M., et al., *Mapping solid concentration in a circulating fluid bed using gammametry.* Powder Technology, 1991. **67**(1): p. 27-36
6. Mudde, R.F., et al., *Gamma radiation densitometry for studying the dynamics of fluidized beds.* Chemical Engineering Science, 1999. **54**(13-14): p. 2047-2054
7. Maccuaig, N., et al., *Application of gamma-ray tomography to gas fluidized beds.* Applied Optics, 1985. **24**(23): p. 4083-4085
8. Leadbeater, T.W., D.J. Parker, and J. Gargiuli, *Positron imaging systems for studying particulate, granular and multiphase flows.* Particuology, 2012. **10**(2): p. 146-153
9. Mohs, G., et al., *Magnetic monitoring of a single particle in a prismatic spouted bed.* Chemical Engineering Science, 2009. **64**(23): p. 4811-4825
10. Lynch, G.F. and S.L. Segel, *Direct measurement of the void fraction of a two-phase fluid by nuclear magnetic resonance.* International Journal of Heat and Mass Transfer, 1977. **20**(1): p. 7-14
11. Abouelwafa, M.S.A. and E.J.M. Kendall, *Optimization of continuous wave nuclear magnetic resonance to determine in situ volume fractions and individual flow rates in two component mixtures.* Review of Scientific Instruments, 1979. **50**(12): p. 1545-1549
12. Kose, K., K. Satoh, and T. Inouye, *NMR Flow Imaging.* Journal of the Physical Society of Japan, 1985. **54**(1): p. 81-92
13. Majors, P.D., R.C. Givler, and E. Fukushima, *Velocity and concentration measurements in multiphase flows by NMR.* Journal of Magnetic Resonance, 1989. **85**(2): p. 235-243
14. Graham, A.L. and E. Fukushima, *Note: NMR imaging of shear-induced diffusion and structure in concentrated suspensions undergoing Couette flow.* Journal of Rheology, 1991. **35**(1): p. 191-201
15. Nakagawa, M., et al., *Non-invasive measurements of granular flows by magnetic resonance imaging.* Experiments in Fluids, 1993. **16**(1): p. 54-60
16. Savelsberg, R., et al., *Particle motion in gas-fluidized granular systems by pulsed-field gradient nuclear magnetic resonance.* Physical Review E - Statistical, Nonlinear, and Soft Matter Physics, 2002. **65**(2): p. 020301/1-020301/4
17. Gentzler, M. and G.I. Tardos, *Measurement of velocity and density profiles in discharging conical hoppers by NMR imaging.* Chemical Engineering Science, 2009. **64**(22): p. 4463-4469
18. Müller, C.R., et al., *Validation of a discrete element model using magnetic resonance measurements.* Particuology, 2009. **7**(4): p. 297-306
19. Fabich, H.T., A.J. Sederman, and D.J. Holland, *Development of ultrafast UTE imaging for granular systems.* Journal of Magnetic Resonance, 2016. **273**: p. 113-123

20. de Cagny, H., et al., *Local rheology of suspensions and dry granular materials.* Journal of Rheology, 2015. **59**(4): p. 957-969
21. Moucheront, P., et al., *MRI investigation of granular interface rheology using a new cylinder shear apparatus.* Magnetic Resonance Imaging, 2010. **28**(6): p. 910-918
22. Kloss, C., et al., *Models, algorithms and validation for opensource DEM and CFD-DEM.* Progress in Computational Fluid Dynamics, 2012. **12**(2-3): p. 140-152
23. Rackl, M. and K.J. Hanley, *A methodical calibration procedure for discrete element models.* Powder Technology, 2017. **307**: p. 73-83
24. Strobl, S., A. Formella, and T. Pöschel, *Exact calculation of the overlap volume of spheres and mesh elements.* Journal of Computational Physics, 2016. **311**: p. 158-172
25. Block, K.T., M. Uecker, and J. Frahm, *Suppression of MRI truncation artifacts using total variation constrained data extrapolation.* International Journal of Biomedical Imaging, 2008. **2008**(1)
26. Veraart, J., et al., *Gibbs ringing in diffusion MRI.* Magnetic Resonance in Medicine, 2016. **76**(1): p. 301-314
27. Kellner, E., et al., *Gibbs-ringing artifact removal based on local subvoxel-shifts.* Magnetic Resonance in Medicine, 2016. **76**(5): p. 1574-1581
28. Link, J.M., et al., *Flow regimes in a spout-fluid bed: A combined experimental and simulation study.* Chemical Engineering Science, 2005. **60**(13): p. 3425-3442
29. Mueth, D.M., et al., *Signatures of granular microstructure in dense shear flows.* Nature, 2000. **406**(6794): p. 385-389
30. Rong, L.W., Z.Y. Zhou, and A.B. Yu, *Lattice-Boltzmann simulation of fluid flow through packed beds of uniform ellipsoids.* Powder Technology, 2015. **285**: p. 146-156
31. May, L.B.H., et al., *Shear-driven size segregation of granular materials: Modeling and experiment.* Physical Review E - Statistical, Nonlinear, and Soft Matter Physics, 2010. **81**(5)
32. Jasti, V. and C.F. Higgs III, *Experimental study of granular flows in a rough annular shear cell.* Physical Review E, 2008. **78**(4): p. 041306

7. Validation of nonlocal granular rheology using the discrete element method

Nonlocal rheology models have become an active area of research due to their ability to describe features in granular flows that are not captured by local rheological models, such as scale dependence and flow below the yield point. These features have been described with success by nonlocal rheological models. In this chapter, nonlocal granular fluidity models were validated against coarse-grained 3D discrete element method (DEM) simulations of an annular shear cell developed for use in MRI velocimetry. The effects of system size and wall friction were considered and were found to influence the stress distribution. For the stress distribution to be consistent with theory, it was necessary to remove friction between granules and the confining walls. The tested rheology models were in good agreement with simulations. To connect the fluidity to particle-scale features such as velocity fluctuations, the coarse-grained DEM data was compared to a fluidity equation of state. The dimensionless fluidity qualitatively agreed with the proposed model, however, there was a systematic bias towards higher volume fractions, indicating that a more detailed equation of state is likely required to fully characterise granular fluidity.

7.1. Introduction

Granular materials exhibit a wide variety of behaviour that is analogous to solid, liquid and gaseous states of matter. It is challenging to appropriately describe the rheological characteristics of granular media for industrial processes, such as gas-solid fluidised beds where the granular phase is simultaneously dense and dilute within different regions of the system. An early development in granular rheology was the kinetic theory of granular flow (KTGF) [1, 2]. This method was developed as an analogue of kinetic theory for dense gases, and was extended to include the effects of particle friction [3, 4], collisional elasticity [5], and enduring contacts [6]. This method was validated for dilute flows where contacts between particles primarily consisted of binary collisions [7]. Bocquet et al. [8] used the KTGF to derive equations for the velocity and granular temperature profiles of a system under planar shear. The KTGF is problematic for dense flows where frictional and enduring contacts dominate. To approximate the behaviour of dense granular flows, *ad-hoc* frictional stress

models [9, 10] were developed. Frictional stress models are often in poor agreement with experiments due to the strong sensitivity of flow features such as bubble size distribution in a fluidised bed to empirical parameters [11]. Thus, more advanced rheology models have been developed that attempt to describe the underlying physics of dense granular flows.

The viscoplastic $\mu(I)$ rheology was introduced by GDR MiDi [12]. The $\mu(I)$ model is classified as a local rheology model where the ratio of shear to normal stresses depends only on the local pressure and shear rate. The $\mu(I)$ rheology has demonstrated good predictive ability for simple flow configurations, for example it is able to recover the Bagnold velocity profile for inclined flows [13]. However, the local rheology model is not able to account for experimental observations such as increasing angle of repose for decreasing layer thickness. Similarly, regions below the yield criteria may flow if neighbouring regions are flowing, indicating that there is spatial cooperativity of granule motion that the local rheology cannot capture. From a practical perspective, the $\mu(I)$ model is well-posed for $\sim 10^{-1} < I/I_0 < \sim 10^{1}$ and is ill-posed outside of this range [14], which makes it challenging to implement for systems where part of the material is below yielding. However, regularisation can be used to attain a well-posed approximate solution [15].

A local approach is insufficient to describe cooperative effects between granules. Granular cooperativity allows for flow in regions below the yield condition and scale dependent flow behaviour. To account for these features of granular materials, one approach has been to extend to a nonlocal rheology, where nonlocality is described by the transport of a parameter known as the granular fluidity [16]. The exact definition of the granular fluidity is still the subject of debate. Here, two proposed descriptions are considered that are described in 7.1.1. Current research is exploring a microscale definition for fluidity that describes the relation between fluidity, particle packing and velocity fluctuations [17]. The nonlocal granular fluidity models have been validated by using discrete element method (DEM) simulations for several different flow configurations, such as 2D annular shear [18], unconfined chute flow [19], confined chute flow [17], and hoppers [20]. DEM simulations offer useful insights into systems that are not easily obtained using experiments, such as local stress measurements and measurements in opaque regions. Experimental validation of nonlocal models so far includes optical measurements of velocity of a split-bottom shear cell [21]. While such results may be used to infer the veracity of the nonlocal models, experimental measurements of the granular fluidity are necessary to fully validate the model and to relate the fluidity to microscale parameters in real systems. Experimentally determining the granular fluidity requires

knowledge of the local velocity and stress. Measuring the local velocity is possible using many established experimental techniques, however stress measurements are more difficult. For simple flow configurations, the local stress profile may be estimated using a force balance, meaning that a spatially unresolved measurement, for example, motor torque may be used as a proxy for local stress. For a pseudo-2D annular shear cell, Tang et al. [22] used inner wall motor torque and outer wall pressure to infer the local stress profile and optical measurements of the local mean velocity to obtain the first known experimental measurement of granular fluidity. However, these methods are limited for use in optically accessible systems. As covered in preceding chapters, magnetic resonance imaging is capable of measuring the spatially resolved velocity distribution of granular flows, thus it is possible to validate the non-local rheology and microscale models of fluidity for three-dimensional annular shear systems using only MRI and motor torque data. MRI is limited to small systems that can fit into the bore of the magnet. To confirm that annular shear experiments with a gap of ~15 grain diameters exhibit non-local behaviour, this chapter performed discrete element simulations of an annular shear cell sized for MRI experiments at a series of typical inner wall velocities. Measurements of the fluidity were obtained using coarse-graining and related to nonlocal rheological models.

7.1.1 Theory

The kinetic theory rheology model of Bocquet et al. [8] describes the transport of momentum and fluctuating kinetic energy according to:

$$\rho_s \varepsilon_s \left(\frac{\partial \boldsymbol{v}_s}{\partial t} + \boldsymbol{v}_s \cdot \nabla \boldsymbol{v}_s \right) = -\nabla \cdot \sigma^s \tag{7.1}$$

$$\rho_s \varepsilon_s \left(\frac{\partial T}{\partial t} + \boldsymbol{v}_s \cdot \nabla T \right) = -\nabla \cdot \boldsymbol{q} - \sigma^s : D - \epsilon T \tag{7.2}$$

where, $\boldsymbol{q}$ is the flux of fluctuating energy and is described by the Fourier law $\boldsymbol{q} = -\lambda \nabla T$, where λ is the pseudo-thermal conductivity and ϵ is the granular temperature loss rate. The velocity gradient tensor is denoted by $D = 0.5[\nabla v_s + (\nabla v_s)^T]$. The granular stress tensor is assumed to be Newtonian and takes the form:

$$\sigma^s = p_s \mathbf{I} - 2\eta_s (D - \nabla \cdot v_s \mathbf{I}) \tag{7.3}$$

where p_s is the pressure, and $\mathbf{I}$ is the identity tensor. The pressure is a function of the density and the granular temperature according to:

$$p_s = \frac{\rho_0 T}{\left(1 - \varepsilon_s / \varepsilon_{s,c}\right)} \tag{7.4}$$

Where e_n is the coefficient of restitution, $\rho_0 = 2(1+e_n)\varepsilon_s^2\rho_s$ and $\varepsilon_{s,c}$ is the volume fraction at random close packing. The shear viscosity is denoted by η_s and is equal to:

$$\eta_s = \frac{\eta_0 m_p \sqrt{T}}{d_p^2\left(1-\varepsilon_s/\varepsilon_{s,c}\right)^{\beta}} \tag{7.5}$$

The pseudo-thermal conductivity is calculated by:

$$\lambda = \frac{\lambda_0 p_s m_p}{d_p^2 \rho_0 \sqrt{T}} \tag{7.6}$$

The granular temperature loss rate is calculated by:

$$\epsilon = \frac{\epsilon_0 p_s}{d_p \sqrt{T}} \tag{7.7}$$

The conservation equations are solved by assuming that Couette flow has two distinct regions. (1) Close to the moving wall ($r < r_w$), the granular temperature is assumed to be constant, due to a balance between fluctuating energy production by shear, transport by diffusion and dissipation by inelastic collisions. (2) Several diameters away from the boundary, the dissipation of fluctuation energy is greater than the nonlinear heating term $\sigma^s : D$. The annular Couette system is approximated by planar Couette flow where two parallel walls along the azimuthal direction and separated by H in the r direction confine the granular material. The lower wall moves at fixed velocity U along the azimuth. This setup is shown in Figure 7.1. For this system Equation 7.2 is simplified to give:

$$\frac{d^2\sqrt{T}}{dr^2} - \frac{1}{\delta_B^2}\sqrt{T} = 0 \quad \text{for } r > r_w \tag{7.8}$$

where $\delta_B = \frac{2\lambda_0 m_p}{\epsilon_0 \rho_0 d_p}$. The boundary condition at r_w is denoted by T_0, while the boundary condition at the outer wall is set to zero flux of T. The solution to this equation is:

$$\sqrt{T} = \sqrt{T_0}\cosh\left(H - \frac{r}{\delta_B}\right)\Big/\left(H - \frac{r_w}{\delta_B}\right). \tag{7.9}$$

The simplified momentum balance in one dimension is given by:

$$\sigma_{r\theta}^s = \eta_s \frac{dv_\theta}{dr} = \text{const.} \tag{7.10}$$

Using the definition of the viscosity in Equation 7.5, the following relation between the shear rate, $\dot{\gamma}$ and the granular temperature appears:

$$\dot{\gamma} = \frac{\sigma_{r\theta}^{s}}{\eta_0 \, m_p / d_p^2 \, (p_s/\rho_0)^{\beta}} T^{0.5(2\beta-1)}. \tag{7.11}$$

This equation predicts a logarithmic relationship between the shear rate and granular temperature where the gradient is given by $0.5(2\beta - 1)$. The integral of the shear rate profile yields the velocity profile, which consists of a constant shear region below r_w and a decay above r_w

$$v_\theta(r) = U\left(1 - \int_0^r \psi(r')dr' \Big/ \int_0^H \psi(r')dr'\right) \tag{7.12}$$

where:

$$\psi(r) = 1 \quad \text{for } r < r_w \tag{7.13}$$

$$\psi(r) = \left[\cosh\left(\frac{H-r}{\delta_B}\right) \Big/ \cosh\left(\frac{H-r_w}{\delta_B}\right)\right]^{2\beta-1}.$$

Experiments have confirmed that the power law relationship between the shear rate and granular temperature holds for annular Couette shear flows. Bocquet et al. [8] found that the exponent β was 1.75 for glass beads and 1.5 for photoelastic discs. A value of 2.58 was found for simulated hard spheres [23]. Experiments on plant seeds by Fabich et al. [24] returned values between 1.3 and 1.5. Thus, there is some debate as to the value of β and it is likely that β depends on the material properties of the granules and may incorporate nonspherical contact effects.

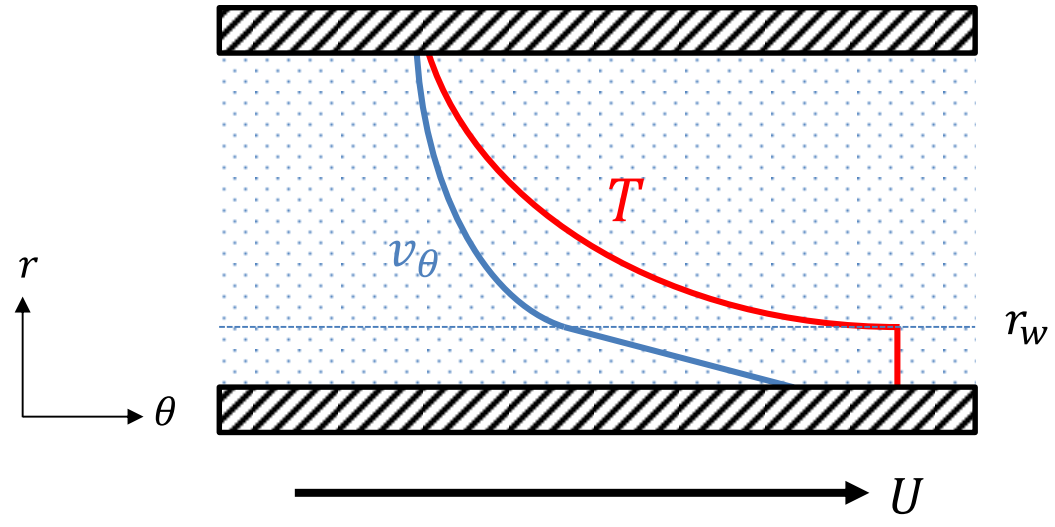

Figure 7.1. Schematic of Couette flow used to derive the Bocquet rheology model. The lower wall moves at velocity U, the delineation between the two regions locate at r_w is given by the dashed line. Typical profiles for the mean velocity and granular temperature are shown across the gap.

For the $\mu(I)$ rheology, the shear stress is defined as $\tau = \mu p_s$, where p_s is the pressure (i.e. the trace of the stress tensor) and μ is the local stress ratio. The stress ratio $\mu(I)$ is calculated using the following relations [25]:

$$\mu(I) = \mu_s + \frac{\Delta\mu}{I_0} I \tag{7.14}$$

$$\mu(I) = \mu_s + \frac{\Delta\mu}{I_0/I + 1} \tag{7.15}$$

where μ_s, $\Delta\mu$, and I_0 are dimensionless parameters. I is the inertial number that represents the ratio of a characteristic time for macroscopic deformations and a characteristic time for inertial regime flow. I is defined as:

$$I = \dot{\gamma} d_p \sqrt{\rho_s / p_s} \tag{7.16}$$

where $\dot{\gamma}$ is the shear rate, d_p is the particle diameter, and ρ_s is the granule density. For simplicity, the $\mu(I)$ law is sometimes approximated in the low inertial number limit by the linear form shown in Equation 7.14 [26], while the nonlinear form of Equation 7.15 models the observed asymptotic behaviour observed at $I > 10^{-1}$.

Nonlocal rheology models represent an extension of the local rheology. The "cooperative" model defines the fluidity as $g = \dot{\gamma}/\mu$ [18]. The steady state transport of granular fluidity is described by the following screened Poisson equation:

$$\nabla^2 g = \frac{1}{\xi^2}(g - g_{loc}) \tag{7.17}$$

where the parameter ξ is known as a cooperativity length that influences the transport of fluidity. The cooperativity length is calculated using:

$$\xi = \frac{A d_p}{\sqrt{|\mu - \mu_s|}} \tag{7.18}$$

where A is a dimensionless parameter that may be determined from experiments [21] or discrete element simulations [27]. The local rheology equivalent granular fluidity is denoted by g_{loc} and is found either by running a simulation using the local rheology, or by using an inverse function of $\mu(I)$. Given the ill-posed nature of the local rheology, the latter approach is preferable which involves rewriting either Equation 7.14 or 7.15 to make I the subject. Since there is no flow below the yield criterion for the local rheology, if $\mu \leq \mu_s$, then $g_{loc} = 0$. Hence the local granular fluidity is a piecewise function as follows:

$$g_{loc} = \begin{cases} \dfrac{I_0\sqrt{p_s/\rho_s d_p^2}\,(\mu - \mu_s)}{\Delta\mu\mu} & \text{if } \mu > \mu_s \\ 0 & \text{if } \mu \leq \mu_s \end{cases} \tag{7.19}$$

$$g_{loc} = \begin{cases} \dfrac{I_0\sqrt{p_s/\rho_s d_p^2}}{\mu \cdot \left(\dfrac{\Delta\mu}{\mu - \mu_s} - 1\right)} & \text{if } \mu > \mu_s \\ 0 & \text{if } \mu \leq \mu_s. \end{cases} \tag{7.20}$$

Equation 7.19 uses the inverse function of the linear $\mu(I)$ law, while Equation 7.20 uses the inverse function of the asymptotic $\mu(I)$ law. Using Equations 7.18 and 7.20, Equation 7.17 can be solved to find the fluidity of the system. The nonlocal rheology introduces an additional PDE which is coupled to the Navier-Stokes equations. This system of equations can be solved numerically [28] to obtain the flow field within the material.

Bouzid et al. [16] question the suitability of the definition used for g in the cooperative model as the relation between the fluidity and the shear rate requires experimental validation. Furthermore, g cannot be a state variable when it depends on the stress tensor. Instead, they argue that the fluidity should have a different definition, such as the inertial number for simplicity. On the basis of this assumption, Bouzid et al. [29] developed a "gradient expansion" model that assumes the constitutive model is a product of the linear $\mu(I)$ law and another function of the fluidity $\chi(I)$. Expanding $\chi(I)$ gives $1 - \kappa + O(\kappa^2)$ where $\kappa = d_p^2\nabla^2 I/I$. Truncating $\chi(I)$ to the first order term yields:

$$Y = \frac{\mu(I)}{\mu_s}(1 - \nu_l\kappa) \tag{7.21}$$

where $Y = \tau/(\mu_s P)$ is the yield parameter. The parameter ν_l influences the size of the non-local contribution and can be viewed as an analogue to ξ in the cooperative model. Substituting the definition of κ into Equation 7.21 and rearranging gives:

$$\nabla^2 I = \frac{I}{\nu_l d_p^2} - \frac{YI\mu_s}{\nu_l d_p^2 \mu(I)}. \tag{7.22}$$

In this form, the similarity to the cooperative model is apparent, that is the Laplacian of the fluidity is equal to the difference between a fluidity term and a local equivalent fluidity. As such, these models are both in excellent quantitative agreement with pseudo-2D annular shear flow experiments [22].

Recently, work has been done to determine a microscale description of the granular fluidity in terms of the solid volume fraction and velocity fluctuations. It has been postulated that the

granular fluidity may be related to the solid volume fraction and granular temperature by the following relation:

$$g = \frac{F(\varepsilon_s)\sqrt{T}}{d_p} \tag{7.23}$$

where ε_s is the solid volume fraction, and $F(\varepsilon_s)$ is a function that describes the relation between the normalised fluidity, $\frac{gd_p}{\sqrt{T}}$ and the solid volume fraction. Zhang and Kamrin [17] found that for DEM simulations of planar shear, gravity shear and confined chute flows, the normalised fluidity and solid volume fraction data collapsed onto a common curve where:

$$F(\varepsilon_s) = \frac{-(\varepsilon_s - 0.58) + \sqrt{(\varepsilon_s - 0.58)^2 + 1.54 \times 10^{-4}}}{0.048}. \tag{7.24}$$

These latest developments in the nonlocal fluidity model represent an important step in developing an accurate rheological description for dense granular flows with a basis in microscale flow phenomena.

7.2. Method

7.2.1 Discrete element method simulations

The system of interest is an annular Couette shear cell where granules are contained between two concentric cylindrical walls. The inner radius, r_i was 16 mm, and the outer diameter was 23.7 mm. The inner wall was rotated at a steady angular velocity, the outer wall was stationary. This configuration is axisymmetric and depth-dependent effects were assumed to be negligible. The open-source LIGGGHTS software [30] was used to run the simulations. Each simulation contained up to 100,000 spheres, each with a diameter of 0.44 mm. Simulations were performed using a Hookean contact model to match the conditions of Zhang and Kamrin [17]. Their work assumed that particles were hard such that the dimensionless ratio $k_n/(p_s d_p)$ was greater than 10^4. For the system studied in this chapter, a normal spring constant of 10^4 N m^{-1} met this criterion. The coefficient of restitution was set to 0.9, and the surface friction coefficient was set to 0.1. Rough walls were modelled by a cylindrical layer of particles in a hexagonal close packed arrangement. The remaining particles were randomly dropped into the annular gap. Once the particles had settled, the inner rough wall was rotated about its central *z*-axis. A solid wall was imposed on the top of the system to apply a load of 2000 Pa to minimise effects at the free surface. This pressure was equivalent to a weight force exerted by a ~35 cm column of grains. Each simulation was run to simulate 1.5 s of operation, the time interval between steps was 1×10^{-6} s which was

deemed to be sufficiently low given that this step size was 20% of the collision time. The momentum conservation equation for this system simplifies to a constant value of $r^2\tau$, where r is the radial coordinate. At the inner wall, this quantity is defined as $r_i^2\mu_i P$. Since the pressure is uniform and if the torque on the wall is known, then the stress profile across the gap is:

$$\mu(r) = \frac{\tau}{p_s} = \frac{r_i^2\mu_i}{r^2}. \tag{7.25}$$

This relation assumes that there are no additional forces acting on the system besides the motor torque. In practice, frictional forces exist between the particles and the base of the cell, or a confining top plate, and requires an additional contribution to the stress for small-depth 3D and pseudo-2D flows [22]. Basal friction was removed from the DEM simulations by setting the friction coefficient between the base material and the particles to zero. Ordering of particles exists near smooth walls, hence it is also necessary to set the domain depth such that there is a region in the centre where the particles are randomly packed. Two different depths of $7d_p$ and $20d_p$ were simulated to ascertain how deep the domain had to be to attain a randomly packed state in the middle of the flow.

7.2.2 Coarse-graining

Coarse-graining is used to produce continuous fields from discrete data. In general, coarse-graining involves the weighted sum of discrete particle data. The weighting is a function of the distance between particles and a chosen position. In previous chapters, weighted averages have been used [31]. Here, a coarse-graining approach described by Weinhart et al. [32] was used. Continuum variables at a position in space, $\boldsymbol{x}$ are determined by weighting the contributions from particles according to the particle position relative to $\boldsymbol{x}$. The local volume fraction at $\boldsymbol{x}$ is determined by:

$$\varepsilon_s(\boldsymbol{x}) = \frac{1}{\rho_s}\sum_{p=1}^{N_p} m_p W(\boldsymbol{x} - \boldsymbol{x}_p) \tag{7.26}$$

where m_p is the particle mass, and $W(\boldsymbol{x} - \boldsymbol{x_p})$ is the weighting function, given by:

$$W(\boldsymbol{x} - \boldsymbol{x_p}) = \begin{cases} \frac{1}{V_W}\exp\left(\frac{\|\boldsymbol{x} - \boldsymbol{x_p}\|^2}{2w^2}\right), & \text{if } \|\boldsymbol{x} - \boldsymbol{x_p}\| < c \\ 0, & \text{otherwise.} \end{cases} \tag{7.27}$$

As illustrated in Figure 7.2(a), this weighting function means that particles close to $\boldsymbol{r}$ have a strong influence on coarse graining, and that the influence decreases for particles that are

further away from $\boldsymbol{x}$. The coarse graining width, w controls how the weighting decreases with distance. Increasing w increases the influence of particles further away from $\boldsymbol{x}$, thus adding spatial smoothing to the continuum variables. Here $w = d_p$ was used. The cut-off distance $c = 3w$ represents the spacing between a granule and $\boldsymbol{x}$ at which the particle has no influence on the value of the continuum variables at $\boldsymbol{x}$. V_w ensures that mass is conserved and is given by:

$$V_w = (2\pi)^{\frac{3}{2}} w^3 \operatorname{erf}^3\left(\frac{\sqrt{2}c}{2w}\right). \tag{7.28}$$

The local mean velocity is determined by:

$$\boldsymbol{v}(\boldsymbol{x}) = \frac{\sum_{p=1}^{N_p} \boldsymbol{v}_p m_p W(\boldsymbol{x} - \boldsymbol{x_p})}{\sum_{p=1}^{N_p} m_p W(\boldsymbol{x} - \boldsymbol{x_p})}. \tag{7.29}$$

The kinetic components of the granular stress tensor $\sigma_{ij}^{s,k}$ is the outer product of the velocity fluctuation vectors, $\boldsymbol{u} = \boldsymbol{v}_p - \boldsymbol{v}(\boldsymbol{x})$:

$$\sigma^{s,k}(\boldsymbol{x}) = \sum_{p=1}^{N_p} \boldsymbol{u} \otimes \boldsymbol{u}\, m_p W(\boldsymbol{x} - \boldsymbol{x_p}). \tag{7.30}$$

The granular temperature is found from the kinetic stress tensor in a way similar to how the mean velocity is found from the momentum, that is, the kinetic stress tensor is divided by the bulk density of the flow. Only the normal (diagonal) components of the kinetic stress tensor contribute to the granular temperature, according to: $T = \sum\langle u_{ii}^2 \rangle$, where i denotes the directions of the coordinate system, and δv_{ii}^2 is determined by:

$$\langle u_{ii}^2 \rangle(\boldsymbol{x}) = \frac{\sum_{p=1}^{N_p} u_i u_i m_p W(\boldsymbol{x} - \boldsymbol{x_p})}{\sum_{p=1}^{N_p} m_p W(\boldsymbol{x} - \boldsymbol{x_p})}. \tag{7.31}$$

The contact component of the stress tensor is determined according to [33]:

$$\sigma^{s,c}(\boldsymbol{x}) = -\frac{1}{2} \sum_{p=1}^{N_p} \sum_{q=1}^{N_c} \boldsymbol{f}_{pq} \otimes \boldsymbol{x}_{pq} \int_0^1 W(\boldsymbol{x} - \boldsymbol{x_p} + s\boldsymbol{x}_{pq})\, ds \tag{7.32}$$

where N_c is the total number of contacts involving particle p, $\boldsymbol{f}_{pq}$ is the force acting on particle p exerted by particle q, and $\boldsymbol{x}_{pq} = \boldsymbol{x}_p - \boldsymbol{x}_q$. The built-in per-granule stress computation in LIGGGHTS assumes that the per-granule stress tensor, $\sum_{q=1}^{N_c} \boldsymbol{f}_{pq} \otimes \boldsymbol{x}_{pq}$ is symmetric, that is, the force acts parallel to the branch vector connecting the centres of contacting granules. In reality the contact force vector between granules is not perfectly

aligned with $\boldsymbol{x}_{pq}$ due to the tangential component of the contact force. The dependence of the weighting on *s* was also ignored, thus Equation 7.32 was simplified to give:

$$\sigma^{s,c}(\boldsymbol{x}) = -\frac{1}{2}\sum_{p=1}^{N_p}\sum_{q=1}^{N_c}\frac{|\boldsymbol{f}_{pq}|}{|\boldsymbol{x}_{pq}|}\boldsymbol{x}_{pq}\otimes\boldsymbol{x}_{pq}W(\boldsymbol{x}-\boldsymbol{x}_{\boldsymbol{p}}). \tag{7.33}$$

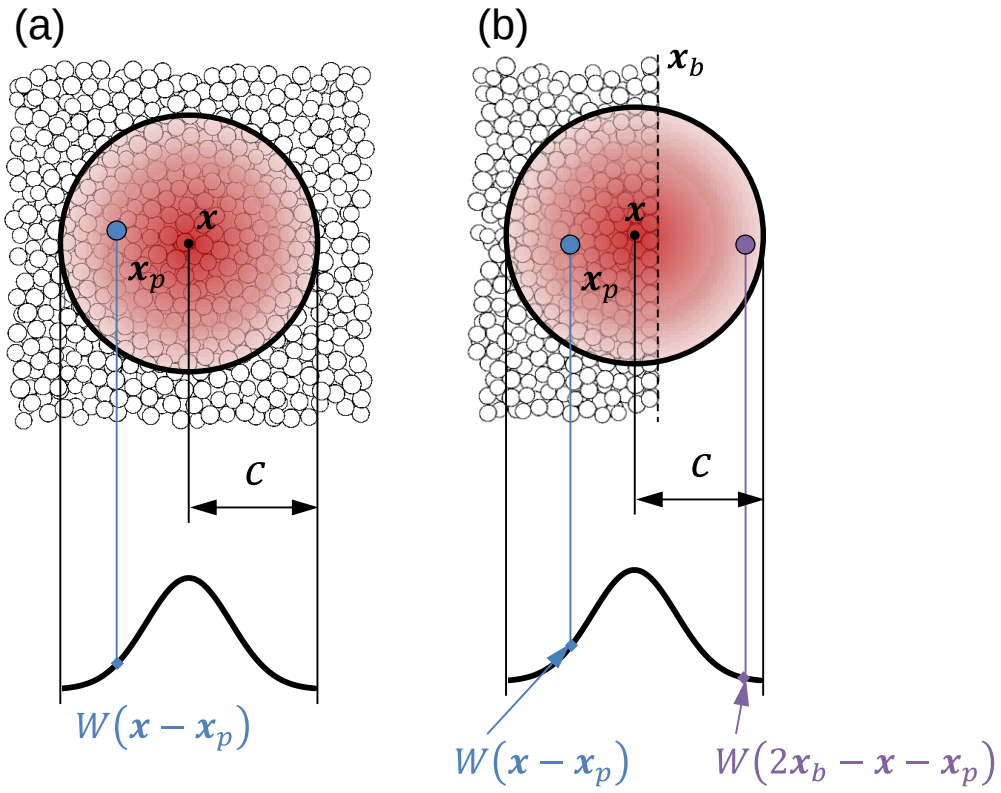

Figure 7.2. Schematic of coarse-graining method (a) where the probe point at $\boldsymbol{x}$ is more than distance $\boldsymbol{c}$ away from a boundary. (b) Where the averaging region crosses a boundary. The averaging region is denoted by the red circle, where the colour intensity is related to the value of the weighting function.

To confirm that these simplifications were valid, snapshots of the DEM data were coarse-grained according to Equation 7.33 and compared to the result obtained by Equation7.32. It was found that the effect on the value of the coarse-grained stress tensor was negligible, therefore coarse-graining of the stress tensor was performed using Equation 7.33 to minimise data storage and computation time. The total stress tensor σ^s is the sum of the kinetic and contact components. The pressure is determined from the trace of the stress tensor:

$$p_s = -\mathrm{tr}(\sigma^s) = -\frac{1}{3}\sigma_{ii}^s. \tag{7.34}$$

The shear stress is found from the off-diagonal components of the stress tensor by:

$$\tau = \sqrt{\frac{\sigma'_{ij}\sigma'_{ij}}{2}} \tag{7.35}$$

where $\sigma'_{ij} = \sigma^s_{ij} - p_s\delta_{ij}$ and δ_{ij} is the Kronecker delta. For Couette shear flow, shear occurs along the azimuthal direction, thus $\tau \sim |\sigma^s_{r\theta}|$. The velocity gradient along the radial coordinate $\dot{\gamma}(r)$ was found by the following numerical approximation:

$$\dot{\gamma}(r) = \frac{u_\theta(r + \Delta r) - u_\theta(r - \Delta r)}{2\Delta r} \tag{7.36}$$

where u_θ is the azimuthal velocity and Δr is the increment between the coordinates of sampled data, which was set to $0.5d_p$. Near boundaries, coarse-graining does not conserve mass since part of the averaging region is devoid of granules. Since it is challenging to calculate V_w for a partially occupied averaging region, the empty region is populated with fictitious particles whose positions are generated by reflecting the real particles in a plane along the location of the boundary, $\boldsymbol{x}_b$. This approach is illustrated by Figure 7.2(b). The weighting within the cut-off distance of the boundary, W_b is calculated by [34]:

$$W_b = W(\boldsymbol{x} - \boldsymbol{x}_p) + W(2\boldsymbol{x}_b - \boldsymbol{x} - \boldsymbol{x}_p). \tag{7.37}$$

7.2.3 Continuum model parameters

The tuneable parameters for the Bocquet model are the position of the interface between the two regions, r_w, and the parameter δ_B. Each of these parameters is expected to be on the order of the particle diameter. The Levenberg-Marquardt algorithm in Matlab was used to fit r_w and δ_B where the objective function was the sum of squared differences between the granular temperature predicted by the model and the DEM data.

The yield stress ratio μ_s can be estimated by calculating the cooperativity length from the DEM data according to Equation 7.17 and plotting the cooperativity length against the stress ratio. Equation 7.18 predicts that the cooperativity length diverges at μ_s. The Laplacian of the fluidity was found using numerical differentiation. For $\mu > \mu_s$, the local fluidity is not known due to its dependence on μ_s. However, it is not necessary to obtain an accurate estimate of ξ, instead we are interested in finding where the divergence occurs. The cooperativity length against the stress ratio is shown by Figure 7.3. While the peaks for each inner wall speed occur at different μ, these data indicate that setting μ_s to 0.26 is reasonable.

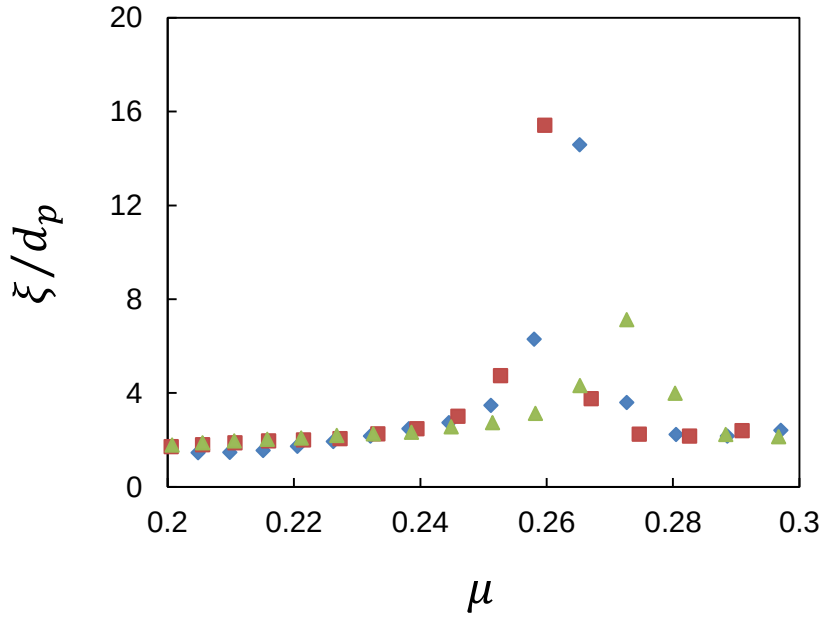

Figure 7.3. Cooperativity length versus the stress ratio. Three inner wall speeds are shown: $U = 17$ mm s^{-1}: ♦, $U = 54$ mm s^{-1}: ■, $U = 170$ mm s^{-1}: ▲.

The fluidity transport equations were solved along one dimension in both Cartesian and polar cylindrical coordinates. For the shear cell tested, the difference between the coordinate systems was small, however cylindrical coordinates were used to remain consistent with the system geometry. For the cooperative model, the fluidity profile was obtained by solving Equation 7.15 using the bvp4c function in Matlab. Fluidity boundary conditions were set to zero at the walls of the system. Here, the wall is defined as the interior surface of the wall granules. Zero fluidity is justified since particles affixed to the wall have coherent motion and thus can be considered to behave like a solid. The stress ratio was assumed to follow Equation 7.25. The Levenberg-Marquardt algorithm in Matlab was used to fit the parameters A, b and μ_i to minimise the objective function, which in this case was the sum of squared differences between the solution to Equation 7.17 and the fluidity from DEM simulations. The velocity profile predicted by the model was obtained by setting the velocity at the outer wall to zero and numerically integrating the shear rate (the product of the fluidity and the stress ratio) with respect to the radial coordinate. The gradient expansion model was approached in a similar fashion, the inertial number profile was obtained by solving Equation 7.22 using the bvp4c function, the parameters b, ν_l and μ_i were fitted using the Levenberg-Marquardt algorithm. The boundary conditions were obtained from the coarse-grained DEM data. The objective function was the sum of the squared differences between the model and DEM inertial number profiles.

7.3. Results and discussion

7.3.1 DEM simulations

To ensure that the simulation is reliable, we must first validate the assumption that the stress ratio follows the inverse-square relationship given by Equation 7.25. Figure 7.4 shows the stress ratio $\mu = \tau/p_s$ against the inverse of the squared radial coordinate. In the cases where the domain was $7d_p$ and $20d_p$ in depth and friction existed between the granules and the top and bottom walls, the gradient of the DEM data exceeded unity. In the experiments by Tang et al. [22], it was necessary to incorporate the contribution of friction between the particles and the base into their shear stress model. In DEM simulations, basal friction was eliminated by setting the friction coefficient between the particles and the flat top and bottom walls to zero. The simulation data showed improved agreement with the model, although there was plateau at low $1/r^2$. The frequency distribution of the vertical coordinate as shown by Figure 7.5(a) reveals that there was radial ordering within ~$5d_p$ from the wall. Figure 7.5(b) shows that this ordering pattern forms near the base and the confining top plate. As the domain is only ~$7d_p$ in depth, the system is ordered along the entire vertical coordinate. Another simulation containing ~10^5 particles was run, giving a system depth of $20d_p$. The frequency distribution along the radial coordinate shown by Figure 7.5(c) shows the same radial ordering as the shallower system, which was expected since the geometries were identical except for depth. The frequency distribution of the vertical coordinate given by Figure 7.5(d) shows that there is a uniformly dispersed random packing within the centre of the system, the spikes in the central region form due to radial ordering near the cylindrical rough walls. The stress ratio from this system agrees well with the model for all r. If the system is ordered in the vertical direction then the stress ratio decreases due to the formation of layers that reduce the flow resistance compared to random packing [35]. These results suggest that basal friction is more important than ordering, and that a ~$20d_p$ deep system with no basal friction is in the best agreement with the theoretical stress ratio. Hence, the assumed inverse-square stress ratio model is valid. From this point onwards, all simulations were ~$20d_p$ in depth and had no basal friction. In practice, MRI experiments of granular Couette flow have a depth of ~0.1 m (~$230d_p$) [36]. At the midpoint of this system, the grains are far away from the base such that there is no vertical ordering and the effect of basal friction is negligible. The polydispersity and nonsphericity of experimental particles further breaks up the radial

ordering that was observed in these simulations which used spheres with a narrow size distribution.

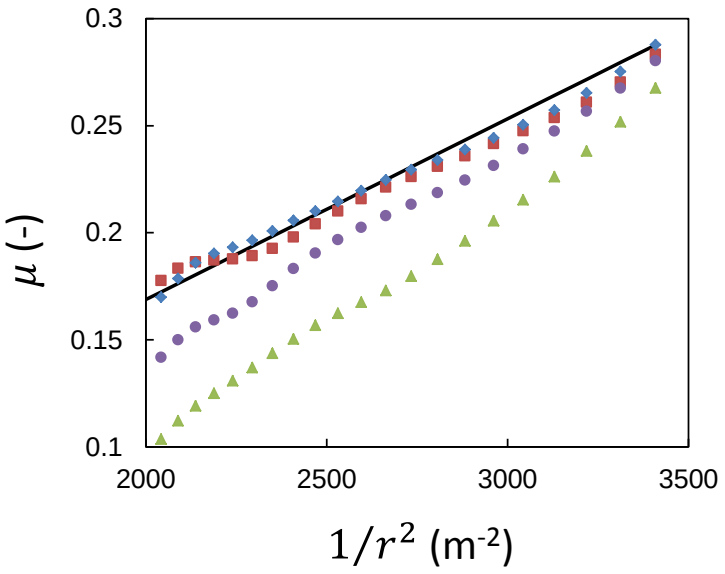

Figure 7.4. Stress ratio μ against the inverse square of the radial coordinate. The assumed continuum profile is denoted by the solid line, DEM simulation where z/d_p = 20 and without basal friction: ♦, DEM simulation where z/d_p = 7 and without basal friction: ■, DEM simulation where z/d_p = 20 with basal friction: ●, DEM simulation where z/d_p = 7 with basal friction: ▲.

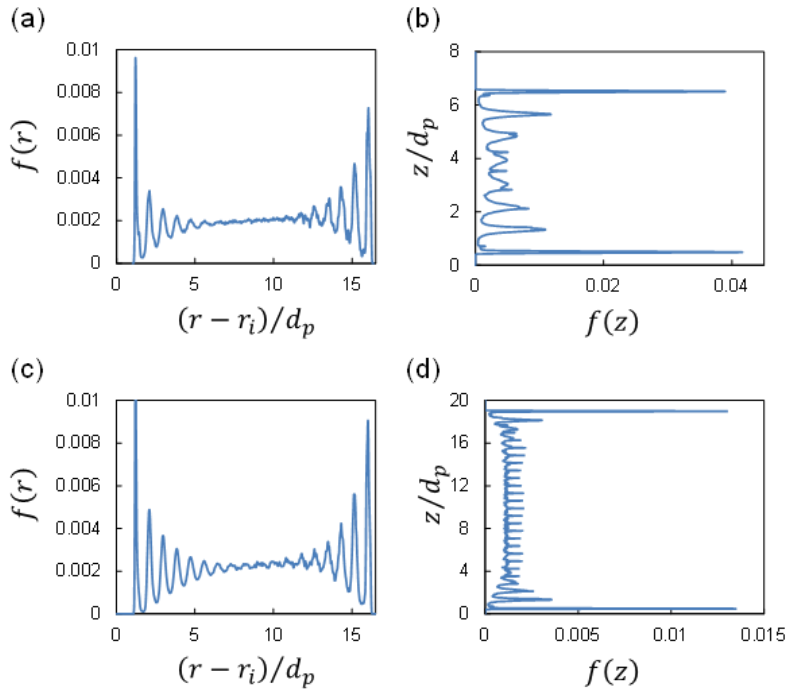

Figure 7.5. Frequency distribution of particle centroid positions for (a) radial position where the domain was $7d_p$ in depth, (b) vertical position where the domain was $7d_p$ in depth, (c) radial position where the domain was $20d_p$ in depth, (d) vertical position where the domain was $20d_p$ in depth.

7.3.2 Coarse-graining

The coarse-grained solid volume fraction profiles across the annular gap for the different wall speeds are shown in Figure 7.6(a). The profiles are in qualitative agreement, where the volume fraction near the inner wall reaches a plateau ~$2d_p$ in width. The volume fraction then increases to reach another plateau approximately halfway across the gap, followed by a peak near the outer wall. The inner plateau is approximately 95% of the outer plateau. It is noteworthy to compare coarse-graining to the MRI simulations from Chapter 6. For high-resolution MR images, features such as radial ordering and densely packed particle walls were apparent as the voxel size is below the size of the particles. Conversely, low-resolution MR images exhibit blurring as features below the size of the voxel are obscured. With coarse-graining, the level of detail captured depends on the averaging width while the resolution at which the coarse graining is evaluated has no effect on the profile. For a fair comparison between MR images and coarse-grained DEM data, the size of the MR voxels should be similar to the size of the averaging region used in coarse-graining. Here the coarse-graining width was $1d_p$, which is equivalent to a spatial resolution in MRI of $1d_p$.

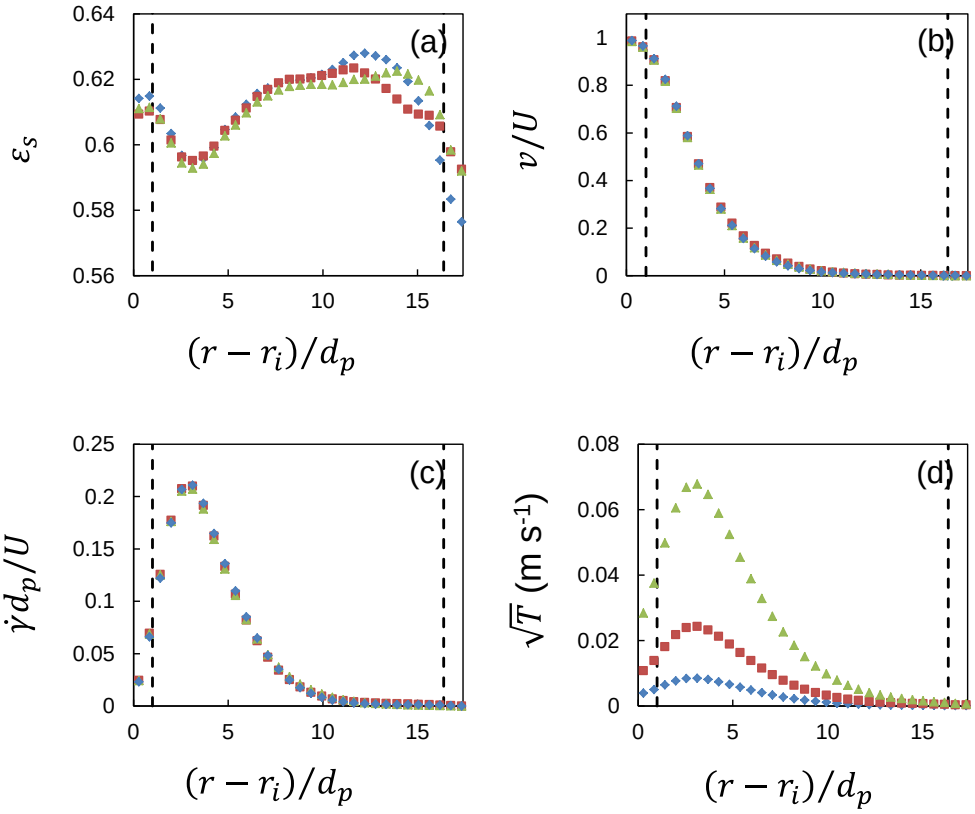

Figure 7.6. (a) solid volume fraction profile across the annular gap (b) velocity profile scaled by the inner wall velocity. (c) dimensionless shear rate profile (d) square root of the granular temperature. Three inner wall speeds are shown: U = 17 mm s^{-1}: ♦, U = 54 mm s^{-1}: ■, U = 170 mm s^{-1}: ▲. The dashed lines indicate the edges of the particles affixed to the walls.

The dimensionless velocity profiles are shown in Figure 7.6(b). The profiles at each inner wall speed were self-similar. No slip was observed at the inner moving wall, the velocity decays rapidly near the inner moving wall, while the material near the outer wall is close to static. The increase in the volume fraction corresponds to the onset of the non-linear velocity decay after the shear band. The dimensionless shear rate is shown in Figure 7.6(c). The shear rate rises next to the moving inner wall, followed by decay with increasing radial coordinate, confirming that shear is localised near the inner moving wall. The low volume fraction plateau near the inner wall corresponded to the shear band where the shear rate was approximately constant and at the maximum value across the gap. Profiles of the root mean square of the velocity fluctuations $\left(\sqrt{T}\right)$ are shown in Figure 7.6(d). The peak in fluctuating energy corresponds to the peak in the shear rate. Fluctuating energy is generated by shear and is dissipated by collisions. Outside of the shear band (~$4d_p$), the shear heating is negligible and the dissipation mechanism dominates.

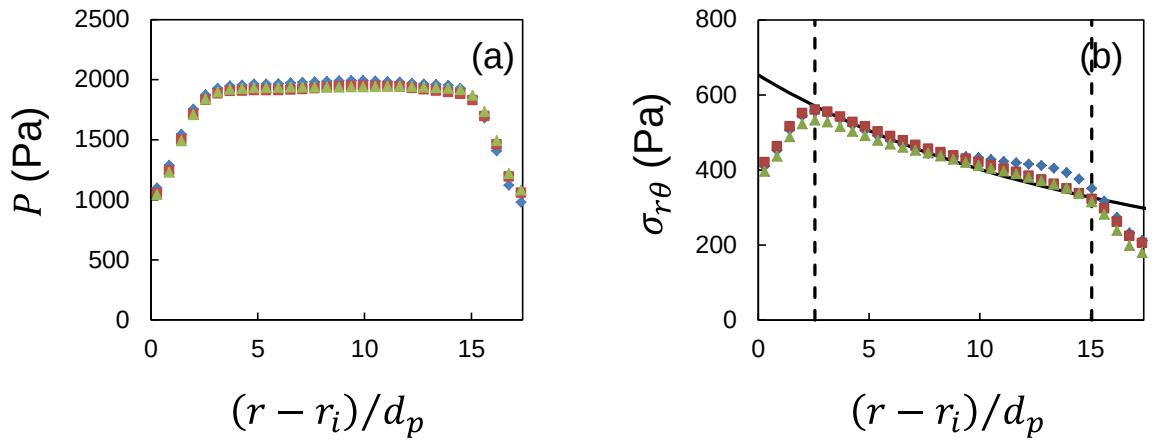

Figure 7.7. (a) Pressure across the gap. (b) Shear stress across the gap. DEM simulations were performed at inner wall velocities of 17 mm s^{-1}: ♦, 53 mm s^{-1}: ■, 170 mm s^{-1}: ▲. Equation 7.22: solid line. The dashed lines indicate the region where $r^2\tau$ was constant.

The pressure and the shear stress profiles are shown in Figure 7.7. The pressure is approximately uniform across the gap, which was consistent with theory and the applied load from the top wall. The stress was low for the wall granules since they were not subjected to the pressure from the confining top plate, and it is questionable whether the coarse-grained stress is accurate at the walls due to the reduced sample size. Therefore, the wall stress for the continuum models is estimated by least-squares fitting. As shown by the theoretical solid line in Figure 7.7(b), there was a region where the constant shear stress relation $r^2\tau$ held. Data from this part of the profile can be used to assess the continuum models in the following sections.

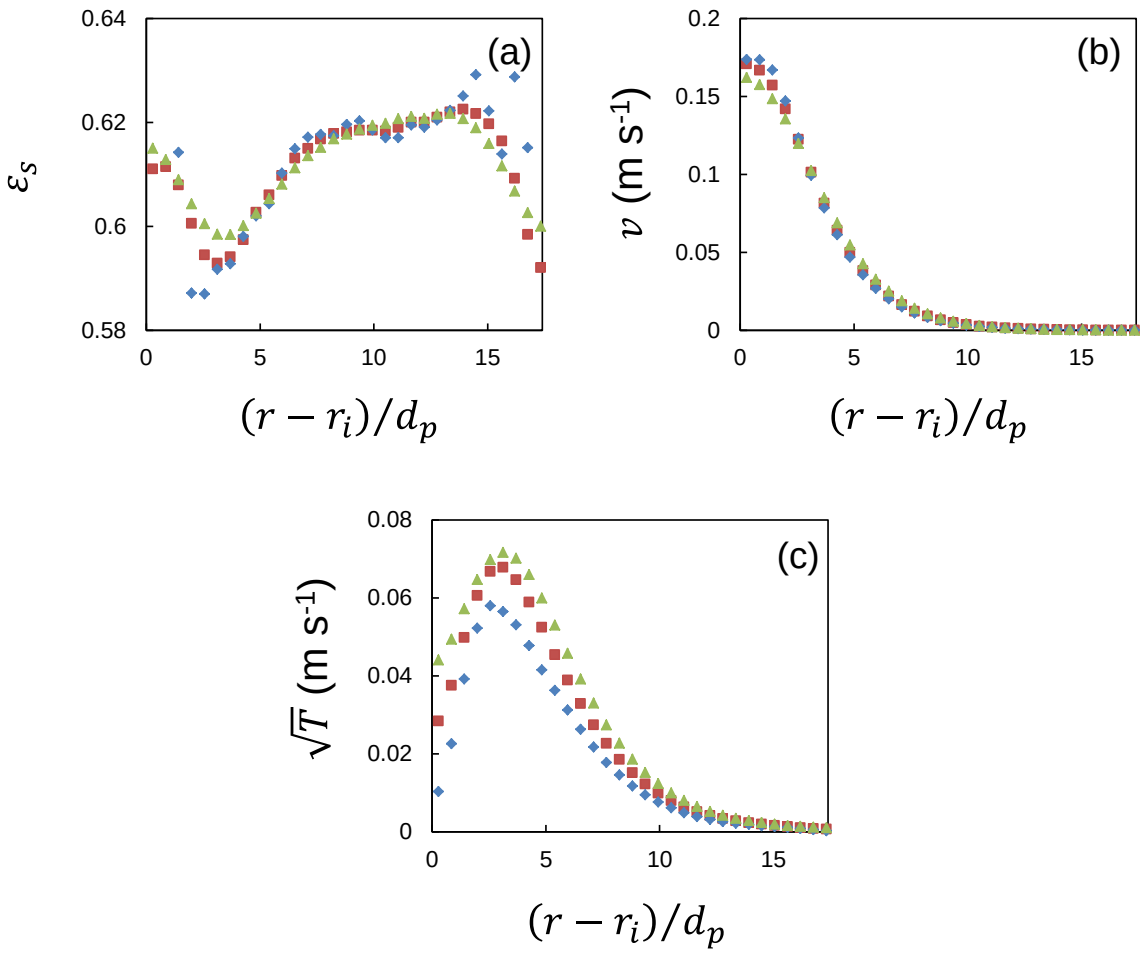

Figure 7.8. Effect of coarse-graining width on coarse grained radial profiles of (a) solid volume fraction (b) mean velocity and (c) square root of the granular temperature. w =0.5d_p: ♦; w = 1d_p: ■; w =1.5d_p: ▲.

The effect of the coarse-graining width is studied in Figure 7.8 for the U = 170 mm s^{-1} case. The solid volume fraction is similar in the densely packed region for all coarse graining widths tested. The uniformity of this region means that the volume fraction does not change as particles further away from the point of interest are sampled. The value of the local minimum volume fraction located near the inner moving wall increases with increasing w due to the inclusion of more densely packed granules in the average. The local mean velocity profiles are in good agreement, except at the inner moving wall where the velocity is reduced for 1.5d_p. This effect is caused by slower moving granules further away from the wall contributing to the local mean. The granular temperature increased with w due to the local averages incorporating particle data further away from the point of interest, thus increasing the variance. The coarse-graining width was limited to a maximum of 1.5d_p due to the size of the region where data was recorded. For subsequent analysis, $w = 1d_p$ was used since the continuum variables appear to be insensitive to the length scale around 1d_p. That is, the 1d_p

void fraction data collapses onto the $0.5d_p$ data and the $1d_p$ granular temperature data is close to the $1.5d_p$ data.

Table 7.1. Model parameters fitted to coarse-grained DEM simulations of annular shear flow.

	Bocquet			Gradient Expansion		Cooperative	
U (mm s^{-1})	r_w (m)	δ_B (m)	β	b	ν_l	b	A
17	0.00193	0.00126	1.29	2.66	0.244	2.68	0.495
54	0.00191	0.00128	1.24	0.956	0.243	1.38	0.401
170	0.00189	0.00134	1.23	1.654	0.139	1.18	0.321

7.3.3 Bocquet model

A log-log plot of the square root of granular temperature against the dimensionless shear rate is shown in Figure 7.9 for inner wall speeds of 17, 53, and 170 mm s^{-1}. The linear relationship between these parameters was very good between dimensionless shear rates of $10^{-0.5}$ and 10^{-2}. The values for β from these simulations are given in Table 7.1 and were between 1.2 and 1.3. The optical particle tracking experiments of Bocquet et al [8] found that $\beta = 1.75$ for glass spheres, while the MRI experiments of Fabich et al. [24] found that β was between 1.3 and 1.5 for plant seeds. These experimental works showed that a linear relationship held for the entire sampled data sets, yet these simulations predict a deviation from linearity for dimensionless shear rates below 10^{-2}, located close to the outer wall. Experimental measurement techniques are limited in sensitivity; hence it is likely that this feature is below the sensitivity of current experimental techniques. The fits for r_w were all within 2% of each other and the fits for δ_B were within 6% of each other, hence these parameters are a property of the granular material or geometry and not dependent on the shear rate and velocity fluctuations.

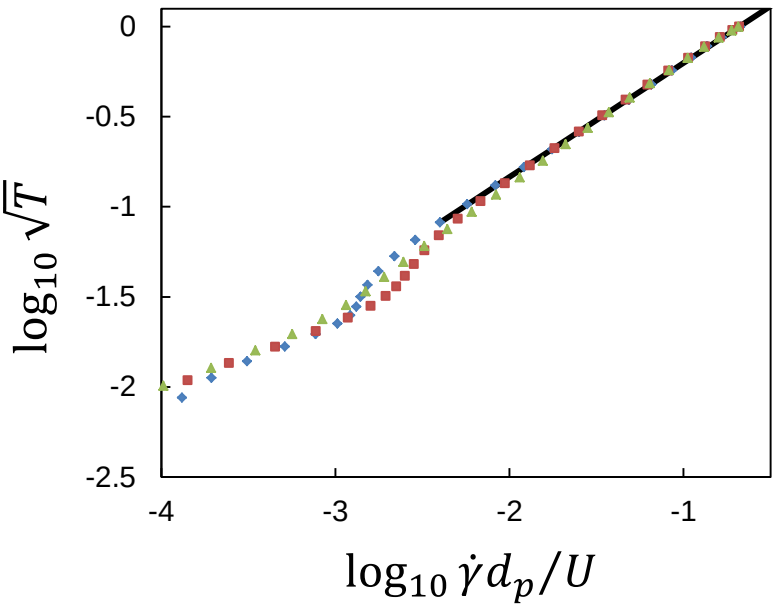

Figure 7.9. Square root of granular temperature against dimensionless shear rate for inner wall velocities of 17 mm s^{-1}: ♦, 53 mm s^{-1}: ■, 170 mm s^{-1}: ▲. At dimensionless shear rates above 10^{-2}, the data are well described by a power law (solid line).

Profiles of the mean velocity and the granular temperature are shown in Figure 7.10. using the Bocquet model and the coarse-grained DEM. In terms of the mean velocity, the model results are in excellent agreement with the DEM simulations. Regarding the granular temperature, the model can accurately capture the decay profile where $r > r_w$. However, the simplifying assumption of uniform granular temperature in the boundary layer region is not reflected in the DEM results. Of interest is that r_w is wider than the distance between the inner wall and the peak of the granular temperature. In the region immediately beyond the peak, the dissipative term exceeds shear heating, however shear heating is not negligible as assumed in the outer region. The concavity of the granular temperature profile in the inner region indicates a more complicated mechanism for fluctuating energy generation and transport than zero net fluctuating energy generation at every location within the inner region as assumed by the Bocquet model.

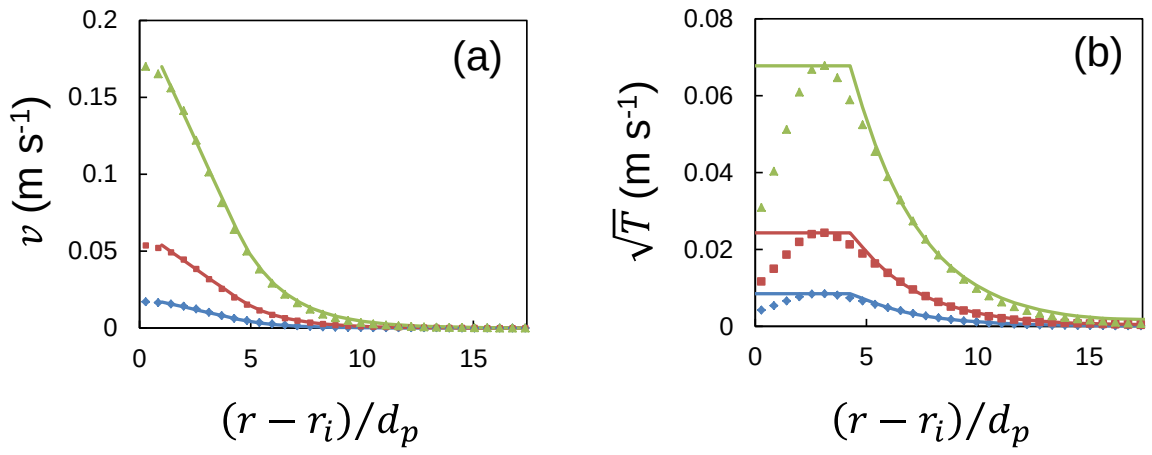

Figure 7.10. (a) profile of mean velocity across the annular gap. (b) normalised granular temperature profile. Coarse-grained DEM data for U = 17 mm s-1: ♦, 53 mm s^{-1}: ■, 170 mm s^{-1}: ▲. The predictions of the Bocquet model are given by the solid lines.

7.3.4 Gradient expansion model

The inertial number across the gap of the coarse-grained DEM data and the fit of Equation 7.22 to these data are shown in Figure 7.11(a). The model is able to capture the full peak in the profile in addition to the decaying region. The fitted parameters are given in Table 7.1 and show that for each wall speed, the fitted values for the nonlocal parameter ν_l are in reasonable agreement. The fitted values for b differ by a considerable margin. Since most of the flow is below the local yield condition, b was found from a small number of samples. Hence, there is considerable uncertainty in the fitted values. Running simulations at higher inertial numbers than studied here would allow for more accurate estimates of b to be obtained. Plotting these data on a log scale shown by Figure 7.11(b) illustrates that there is considerable deviation between the model and the simulations. The coarse-grained DEM velocity profiles and gradient expansion model fits are shown in Figure 7.11(c). The agreement is good near the moving inner wall, however, the model exaggerates the velocity decay when shown as the log-scaled velocity as in Figure 7.11(d). The deviation in the velocity profile is related to the deviation in the inertial number, indicating that improving the prediction of the inertial number should be a priority. The disparity shown in Figure 7.11(b) suggests that the rate of transport of fluidity to the outer region of the shear cell is underestimated by the model. It is likely that the model agreement could be improved by describing ν_l as a function of μ such that variable length scale cooperative effects can be captured.

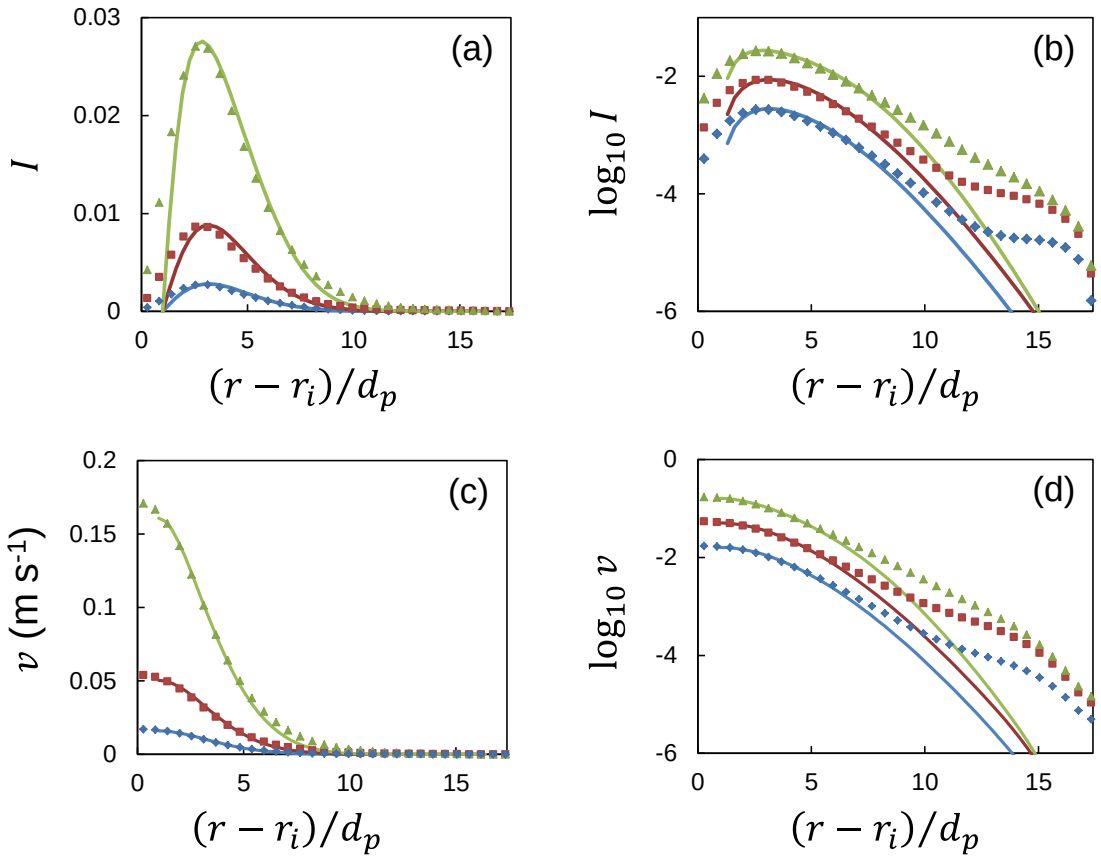

Figure 7.11. (a) Inertial number across the gap. (b) Logarithm of the inertial number across the gap (c) Velocity profile across the gap. (d) Logarithm of the velocity across the gap. Coarse-grained DEM data for U = 17 mm s-1: ♦, 53 mm s^{-1}: ■, 170 mm s^{-1}: ▲. The predictions of the gradient expansion model are given by the solid lines.

7.3.5 Cooperative model

Figure 7.12(a) plots the granular fluidity against the radial coordinate. The cooperative model was able to qualitatively replicate the coarse-grained fluidity profile across the annular gap. Near the inner moving wall, the fluidity increases from zero, reaches a peak ~$3d_p$ away from the inner wall, followed by decay towards the outer wall. The peak in the fluidity forms due to the balance between generation by shear near the inner wall (where $g_{loc} > 0$) and transportation by diffusion to the outer region of the shear cell. The model parameters are shown in Table 7.1. The fitted values for the nonlocal parameter A obtained at each wall speed vary by a considerable margin, however the values are typical of those reported in literature, which vary between 0.31 [18] and 1.05 [27] The local parameter, b varies widely for the wall speeds for the same reason as discussed for the gradient expansion model. The relationship between the inertial number and stress ratio is given in Figure 7.12(b). The stress ratio increases with increasing inertial number as has been observed for experimental and simulated pseudo 2D annular shear systems. The model agreement is good for several orders

of magnitude in I, however, deviations exist near the outer wall. The shear peak near the inner wall is responsible for the increase in the stress ratio for decreasing inertial number shown in the DEM data. The velocity across the gap is shown in Figure 7.12(c) and demonstrates that the agreement with the model was excellent over the range of sampled data. The log-scaled velocity profile is shown in Figure 7.12(d) and shows that the model does not capture the inflection observed near the outer wall. Considering the similarity of the fluidity transport equations of both models, the similarity of the model predictions was expected and is confirmed by experimental study [22]. It is notable however that the velocity decay is captured well by this model for $(r - r_i)/d_p < 10$, better than the gradient expansion model. This difference may be explained by the spatial variation in ξ arising from changes in μ compared to the assumption of constant ν_l. However, there is still a notable amount of deviation near the outer wall, which suggests that ξ is not accurately estimated in the outer region of the shear cell.

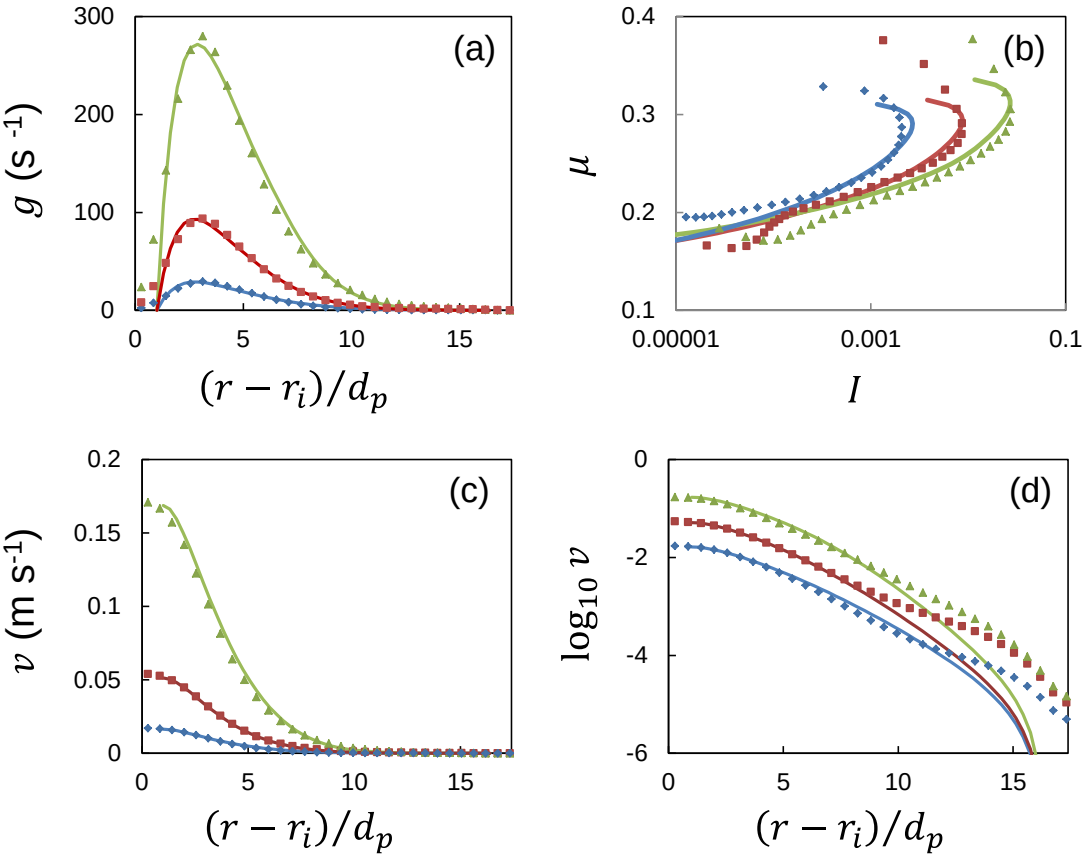

Figure 7.12. (a) Granular fluidity across the annular gap. (b) Stress ratio against the inertial number. (c) Velocity profile across the gap. (d) logarithm of the velocity profile. DEM data for U = 17 mm s^{-1}: ♦, 54 mm s^{-1}: ■, 170 mm s^{-1}: ▲. The predictions of the cooperative model are given by the solid lines.

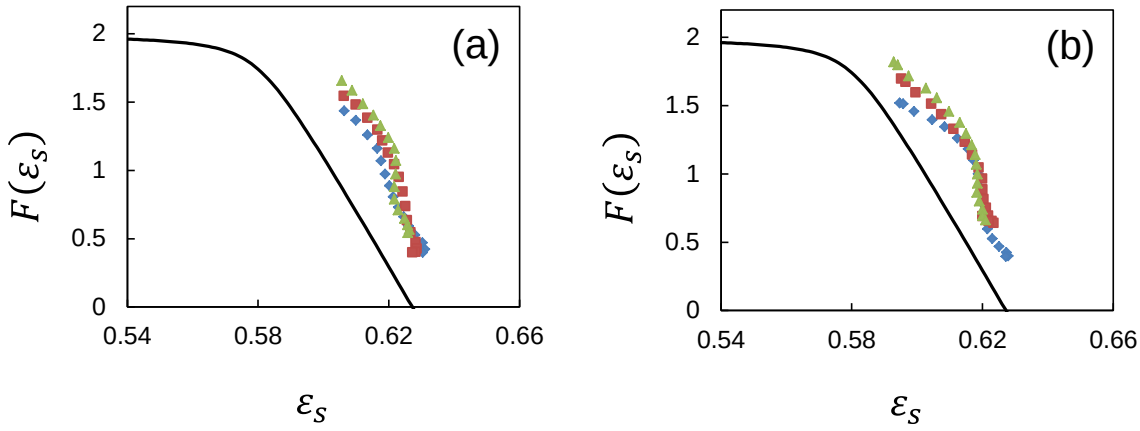

Figure 7.13. Profile of the dimensionless granular fluidity against the solid volume fraction for annular shear flow. (a) k_n =10^3 N m^{-1}, and (b) k_n =10^4 N m^{-1}. U = 17 mm s^{-1}: ♦, U = 53 mm s^{-1}: ■, U = 170 mm s^{-1}: ▲, Equation 7.24: solid line.

7.3.6 Microscale definition for fluidity

The dimensionless fluidity of each of the annular shear cases is related to the volume fraction in Figure 7.13. The effect of granule stiffness was investigated by running annular shear simulations for a normal spring constant of 10^3 N m^{-1} (which corresponds to $k_n/(p_s d_p) \sim 10^3$, below the criterion specified in [17]), shown in Figure 7.13(a). The annular shear simulations where $k_n = 10^4$ N m^{-1} are shown in Figure 7.13(b). For reference, the planar shear with gravity case from [17] was also performed and coarse-grained (the $F(\varepsilon_s)$ profile is shown in Section 9.6). It should be noted that the coarse-graining method utilised here is different to the method used in [17], however, the planar shear with gravity case is in reasonable agreement with Equation 7.24, demonstrating that the effect of the coarse-graining method on the results is small. The simulations where $k_n = 10^4$ N m^{-1} displayed marginally lower solid volume fractions than for $k_n = 10^3$ N m^{-1} due to the reduced overlap between granules. For both normal spring constants that were tested, the data collected for each of the inner rotating wall speeds collapsed well relative to each other, however they did not collapse onto Equation 7.24. The dimensionless fluidity for annular shear demonstrates the same decreasing trend with increasing volume fraction as the model, however it has a distinct curvature in contrast to the linear decay of the model. Hence, it appears that the postulated $F(\varepsilon_s)$ relation is not universal for all flow configurations and the microscopic definition for fluidity is more complicated than described by Equation 7.24, depending on additional factors besides packing and velocity fluctuations. For example, DEM simulations showed that $F(\varepsilon_s)$ varies with the orifice diameter in hopper flows [20]. If the system size or curvature is responsible for the observed deviation, then it could be investigated with a parametric study

where $F(\varepsilon_s)$ curves are retrieved for a variety of inner radii and gap widths. As the inner radius increases, $F(\varepsilon_s)$ would be expected to converge to the planar shear case, which has been shown to follow Equation 7.24.

7.4. Conclusions

Discrete element simulations of spherical granules in an annular shear cell were coarse-grained to obtain locally averaged flow parameters for comparison with kinetic theory and nonlocal rheology models. For the assumption of the inverse square relationship between the stress ratio and the radial coordinate to hold, the shear cell had to be $20d_p$ in depth with no friction between the granules and the horizontal confining walls. The "two regions" kinetic theory model of Bocquet et al. [8] was in good agreement with the mean velocity of DEM simulations. The granular temperature profile in the inner region was in poor agreement with simulations, thus the assumption of zero net fluctuating energy generation at every position in the inner region was not valid. The assumption of energy dissipation dominating over shear heating in the outer region was valid as demonstrated by the good agreement between the model prediction and the DEM data. The nonlocal gradient expansion model agreed well with the DEM data; however it was unable to describe the increase in shear rate next to the inner wall. The cooperative model predicted similar results, owing to the similarity of the fluidity transport equations of both models. These models did not accurately describe the transport of fluidity in the outer region of the shear cell, likely due to the assumed forms of the cooperativity length scales. The microscopic definition of the fluidity proposed by Kamrin and Zhang [17] represents the first attempt at understanding the physical meaning of granular fluidity, however it was found to not hold for annular shear, indicating that additional factors likely influence the fluidity. The results were not particularly sensitive to the coarse-graining method or the granule stiffness. It is postulated that domain size and curvature have an effect which should be the subject of future study.

7.5. References

1. Ogawa, S., A. Umemura, and N. Oshima, *On the equations of fully fluidized granular materials.* Zeitschrift für angewandte Mathematik und Physik ZAMP, 1980. **31**(4): p. 483-493
2. Lun, C.K.K., et al., *Kinetic theories for granular flow: inelastic particles in Couette flow and slightly inelastic particles in a general flowfield.* Journal of Fluid Mechanics, 1984. **140**: p. 223-223
3. Jenkins, J.T. and M.W. Richman, *Kinetic theory for plane flows of a dense gas of identical, rough, inelastic, circular disks.* Physics of Fluids, 1985. **28**(12): p. 3485-3494
4. Lun, C.K.K., *Kinetic theory for granular flow of dense, slightly inelastic, slightly rough spheres.* Journal of Fluid Mechanics, 1991. **233**(539): p. 539-559
5. Jenkins, J.T. and C. Zhang, *Kinetic theory for identical, frictional, nearly elastic spheres.* Physics of Fluids, 2002. **14**(3): p. 1228-1235
6. Jenkins, J.T., *Dense shearing flows of inelastic disks.* Physics of Fluids, 2006. **18**(10)
7. Saitoh, K. and H. Hayakawa, *Rheology of a granular gas under a plane shear.* Physical Review E - Statistical, Nonlinear, and Soft Matter Physics, 2007. **75**(2)
8. Bocquet, L., et al., *Granular shear flow dynamics and forces: Experiment and continuum theory.* Physical Review E, 2001. **65**(1)
9. Johnson, P.C. and R. Jackson, *Frictional-collisional constitutive relations for granular materials, with application to plane shearing.* Journal of Fluid Mechanics, 1987. **176**: p. 67-93
10. Srivastava, A. and S. Sundaresan, *Analysis of a frictional–kinetic model for gas–particle flow.* Powder Technology, 2003. **129**(1–3): p. 72-85
11. Passalacqua, A. and L. Marmo, *A critical comparison of frictional stress models applied to the simulation of bubbling fluidized beds.* Chemical Engineering Science, 2009. **64**(12): p. 2795-2806
12. GDR MiDi, *On dense granular flows.* The European Physical Journal E, 2004. **14**(4): p. 341-365
13. Lagrée, P.Y., L. Staron, and S. Popinet, *The granular column collapse as a continuum: Validity of a two-dimensional Navier-Stokes model with a Î(I)-rheology.* Journal of Fluid Mechanics, 2011. **686**: p. 378-408
14. Barker, T., et al., *Well-posed and ill-posed behaviour of the μ-rheology for granular flow.* Journal of Fluid Mechanics, 2015. **779**: p. 794-818
15. Saramito, P. and A. Wachs, *Progress in numerical simulation of yield stress fluid flows.* Rheologica Acta, 2017. **56**(3): p. 211-230
16. Bouzid, M., et al., *Non-local rheology in dense granular flows: Revisiting the concept of fluidity.* European Physical Journal E, 2015. **38**(11): p. 1-15
17. Zhang, Q. and K. Kamrin, *Microscopic Description of the Granular Fluidity Field in Nonlocal Flow Modeling.* Physical Review Letters, 2017. **118**(5)
18. Kamrin, K. and G. Koval, *Nonlocal constitutive relation for steady granular flow.* Physical Review Letters, 2012. **108**(17)
19. Kamrin, K. and D.L. Henann, *Nonlocal modeling of granular flows down inclines.* Soft Matter, 2015. **11**(1): p. 179-185
20. Bhateja, A. and D.V. Khakhar, *Rheology of dense granular flows in two dimensions: Comparison of fully two-dimensional flows to unidirectional shear flow.* Physical Review Fluids, 2018. **3**(6)

21. Henann, D.L. and K. Kamrin, *A predictive, size-dependent continuum model for dense granular flows.* Proceedings of the National Academy of Sciences of the United States of America, 2013. **110**(17): p. 6730-6735
22. Tang, Z., et al., *Nonlocal rheology of dense granular flow in annular shear experiments.* Soft Matter, 2018. **14**(16): p. 3040-3048
23. Barrat, J.L., W. Gotze, and A. Latz, *The liquid-glass transition of the hard-sphere system.* Journal of Physics: Condensed Matter, 1989. **1**(39): p. 7163
24. Fabich, H.T., et al., *Measurements of the velocity distribution for granular flow in a Couette cell.* Physical Review E, 2018. **98**(6)
25. Jop, P., Y. Forterre, and O. Pouliquen, *A constitutive law for dense granular flows.* Nature, 2006. **441**(7094): p. 727-730
26. Da Cruz, F., et al., *Rheophysics of dense granular materials: Discrete simulation of plane shear flows.* Physical Review E - Statistical, Nonlinear, and Soft Matter Physics, 2005. **72**(2)
27. Kamrin, K. and G. Koval, *Effect of particle surface friction on nonlocal constitutive behavior of flowing granular media.* Computational Particle Mechanics, 2014. **1**(2): p. 169-176
28. Henann, D.L. and K. Kamrin, *A finite element implementation of the nonlocal granular rheology.* International Journal for Numerical Methods in Engineering, 2016. **108**(4): p. 273-302
29. Bouzid, M., et al., *Nonlocal rheology of granular flows across yield conditions.* Physical Review Letters, 2013. **111**(23)
30. Kloss, C., et al., *Models, algorithms and validation for opensource DEM and CFD-DEM.* Progress in Computational Fluid Dynamics, 2012. **12**(2-3): p. 140-152
31. Khawaja, H., et al., *Quantitative analysis of accuracy of voidage computations in CFD-DEM simulations.* Journal of Computational Multiphase Flows, 2012. **4**(2): p. 183-192
32. Weinhart, T., et al., *Influence of coarse-graining parameters on the analysis of DEM simulations of silo flow.* Powder Technology, 2015. **293**: p. 138-148
33. Goldhirsch, I., *Stress, stress asymmetry and couple stress: From discrete particles to continuous fields.* Granular Matter, 2010. **12**(3): p. 239-252
34. Zhu, H.P. and A.B. Yu, *Averaging method of granular materials.* Physical Review E - Statistical, Nonlinear, and Soft Matter Physics, 2002. **66**(2): p. 021302/1-021302/10
35. Grebenkov, D.S., et al., *Flow, ordering, and jamming of sheared granular suspensions.* Physical Review Letters, 2008. **100**(7)
36. Brox, T.I., *New Methods for Studying Materials Under Shear with Nuclear Magnetic Resonance*, P. Galvosas and M. Hunter, Editors. 2016, Victoria University of Wellington.

8. Conclusions and future work

Characterisation of granular materials is an area of research interest due to the widespread applications in nature and industry. Computational methods have allowed for insights into granular flows that cannot be obtained using physical experiments. However, simulation techniques require simplification to be feasible for use at laboratory and industrial length scales. At the laboratory scale, fully resolved gas-particle interactions are prohibitive due to computational expense. Thus these interactions are simplified by use of a drag model. At the industrial scale, it is unfeasible to resolve the contacts between individual particles, thus a continuum description is adopted. Experimentation is necessary to validate these simplifying assumptions. Contributions to the body of knowledge made by this thesis in the areas of granular flow modelling and MRI of granular flows are presented in Section 8.1. Additional avenues of inquiry that were identified by this work are detailed in Section 8.2.

8.1. Summary of findings

In this work, unresolved computational fluid dynamics-discrete element method (CFD-DEM) simulations were performed to investigate the validity of the simplifying assumptions made to obtain estimates of the void fraction and the drag force. In Chapter 3, a cylindrical fluidised bed was modelled using the MFIX and CFDEM open-source CFD-DEM solvers. It was found that the CFDEM model was able to qualitatively reproduce the flow pattern observed in MRI experiments, where bubbles ascended along the central axis of the bed. The MFIX model displayed an offset in the bubbling region. This offset was removed by increasing the coupling between the gas and particle phases such that the drag force and void fraction were calculated at every DEM step. Thus, either simulation package is suitable for simulating gas particle flows considering the congruence between the outputs.

Both codes underestimated the magnitude of the vertical particle velocity in the bubbling region. This discrepancy was attributed to the simulated spherical particles incorrectly modelling the packing, contacts and drag experienced by the poppy seeds of the experiment. The effective diameter method was used to specify a void fraction diameter to match the empirical voidage at minimum fluidisation, while a drag diameter was specified to match the empirical minimum fluidisation gas velocity. Suitable values for the voidage and drag

diameters were estimated from theory and validated against CFD-DEM simulations. Applying the effective diameters to the cylindrical fluidised bed improved the quantitative agreement with experiments.

The effect of the method used to calculate the local void fraction was studied in Chapter 4. A square bubbling fluidised bed was simulated using the MFIX CFD-DEM code. It was found that the void fraction scheme had a minimal effect on the particle velocity field for grid sizing of ~$3d_p$. Sub-scale features such as the jets of air from the gas distributor were modelled by approximating the inlet as spatially uniform. With this boundary condition, agreement with the MRI experiment was improved. However, this boundary condition required reducing the grid size to $1.6d_p$ to resolve the jets as distinct entities. For this refined grid, particle centering was unable to provide physically sensible estimates of the void fraction. The diffusive smoothing method was able to reduce the run time without affecting the flow field.

Magnetic resonance imaging is a well-established measurement technique for studying granular dynamics. Past work has successfully measured the local velocity distribution of granules in fluidised beds, rotating drums, hoppers and shear cells. MRI velocimetry exploits the attenuation of the MR signal caused by net dephasing of spins moving during acquisition. However, previous work has not considered how the rotation of granules may distort measurements. In Chapter 5, a model was developed to describe the MR signal from PFG experiments in terms of the angular velocity distribution of the granules. The model was verified and validated for annular Couette flow by simulating the MR signal using a satellite point method to incorporate the contribution of spins rotating about particle centroids. This approach to validation was advantageous since it allowed the translational and rotational components of the signal to be isolated for analysis. The verification studies demonstrated that the model was in excellent agreement with MRI simulations. The angular velocity variance was estimated from the simulated signal by the model and was in good agreement with the DEM averages, although it is advised that fitting the model to the measured signal is limited to low values of reciprocal velocity space. This new model demonstrates that MRI can be used to measure the angular velocity distribution of granules provided that translation effects are removed from the signal.

There is uncertainty in the veracity of MRI volume fraction measurements due to the possibility of signal attenuation caused by the motion of granules. This effect would cause faster moving regions to appear more dilute than in reality. In Chapter 6, MRI simulation was employed to measure the spatially resolved signal intensity of the annular Couette system. A

model was developed to perform simulations more rapidly than for the satellite point method used in Chapter 5. Velocity compensated phase encoding gradients and a velocity compensated slice selection gradient were used. It was confirmed by simulations and physical experiments that the gradient sequence was able to inhibit signal attenuation due to motion. Low-resolution images were distorted by Gibbs ringing, making them unsuited for quantitative analysis without further processing. However, if Gibbs ringing is removed, low-resolution images were in excellent agreement with the exact volume fraction. High-resolution images were less susceptible to Gibbs ringing and therefore were also in excellent quantitative agreement with the exact volume fraction.

The annular shear cell system was analysed in Chapter 7 using a coarse-graining method to validate kinetic theory and nonlocal fluidity rheology models. DEM simulations confirmed that an inverse square relation between the stress and the radial coordinate was valid, provided that there was no friction between the confining walls. The kinetic theory model of Bocquet et al. [1] was able to accurately model the decay in the granular temperature away from the moving wall. The velocity profile was in excellent agreement with the DEM data across the entire gap. The nonlocal fluidity models were able to describe the system with reasonable accuracy; however the model fluidity and velocity profiles decayed more rapidly across the annular gap than observed with the DEM simulations. The microscopic definition of the granular fluidity proposed by Zhang and Kamrin [2] was not applicable to the annular shear system studied here because the form of $F(\varepsilon_s)$ found from coarse graining differed from their model.

The findings from this thesis improve the characterisation of granular flows as follows: The multiscale modelling framework is strengthened by increasing the predictive accuracy of the unresolved CFD-DEM method. Thus, the predictive accuracy of TFM simulations is enhanced by improved constitutive relations derived from CFD-DEM data. Velocity distribution measurements using MRI were improved by identifying that granule rotation introduces additional signal attenuation; hence existing measurements systematically overestimate the velocity variance. The signal attenuation model can be used to measure the angular velocity variance and to correct measurements of linear velocity variance, which is a new application for MRI. MRI was found to give quantitative estimates of the volume fraction, thus granular flow models that depend on shear, velocity fluctuations and particle concentration can all be assessed using MRI measurements.

8.2. Future work

The results from Chapter 3 demonstrated that the effective diameter method has the potential to improve quantitative agreement with experiments compared to using spherical diameters. However, the model outlined in this work differs from previous work [3] as to where the effective diameter for the drag force calculation is applied. How the model differences affect the fluidised bed hydrodynamics is unknown since these models have not been compared using the same reference system. It is advised that such simulations are performed in order to ascertain whether it is advantageous to give preference to one of the model definitions.

The model introduced in Chapter 5 that relates granule rotation to the MR signal was validated using discrete element simulations of spherical particles and was found to estimate the angular velocity variance with good agreement to the local averaging of the DEM data. However, this validation approach was only possible due to the ability to isolate the translational and rotational contributions to the simulated MR signal. The signal cannot be separated in this fashion for physical experiments. If rotation and translation occurred on different time scales, then imaging sequences on the order of the short time scale would facilitate isolating the components, however no such timescale separation exists for dense granular flows. Instead, it is proposed that the translational velocity variance is measured independently, and the multiplicative relationship between the translation and rotation components can be exploited to easily infer the rotational signal component. One suitable method is the dynamic magnetic resonance scattering proposed by Herold et al. [4]. This method records the signal at a constant value in k-space over time. The correlation function of the signal is related to the velocity distribution of the nuclei within the sample. The authors developed this method to measure the motion of objects smaller than the imaging resolution; however it appears in principle to be possible to measure the linear velocity variance in the presence of granule rotation effects. Experiments would measure the linear velocity variance using DMRS. The PGSE signal attenuation due to linear velocity fluctuations can be estimated using the DMRS data. The total signal attenuation is measured using PGSE. The difference between the measured PGSE signal and the estimated linear motion signal attenuation is the signal attenuation from granule rotation. The angular velocity variance can be estimated from this partial signal attenuation according to the model developed in this work.

There were discrepancies between the velocity variance measurements from the simulations and the physical experiments of Fabich et al. [5]. While the simulations assumed that granules were spherical, the experiments used nonspherical plant seeds. The different contact dynamics exhibited by nonspherical particles influence the motion of granules and hence the velocity distribution. Nonspherical particles can be modelled using multisphere and superquadric approaches. Recent updates have been made to the LIGGGHTS DEM code [6] that includes algorithms for these methods. Therefore it is feasible to perform annular shear simulations of nonspherical particles by making small modifications to the LIGGGHTS cases designed during this thesis.

MRI was shown in Chapter 6 to be an effective measurement technique for the solid volume fraction, however it is limited by Gibbs ringing artifacts induced by the image reconstruction process that are especially dominant at low resolutions. These artifacts were removed by coarse-mapping high resolution simulated images. In practice, prior knowledge of high-resolution images is not available due to the unacceptably long experiment times. Instead, it is hypothesised that Gibbs ringing can be removed by employing an algorithm that does not assume zero signal beyond the sampled region. Future work should consider developing a suitable algorithm for this purpose.

In addition, the experiments predicted that the volume fraction near the inner wall was considerably lower than the DEM simulations. The origin of this discrepancy is unclear, although it is hypothesised that the configuration of particles affixed to the moving wall has some influence. Wall roughness is quantified either by the spacing between wall particles, or the size of the wall particles. Conflicting results were obtained for studies of wall roughness. simulated inclined flows predict a dilute region near the base when the wall particles are smaller than the particles in the bulk (i.e. the base is smooth) [7]. Pseudo-2D annular shear experiments have shown for increased wall particle spacing (the wall is rougher) that the solid volume fraction near the moving wall decreases [8]. Thus, 3D annular shear simulations where the spacing between the wall particles, or the size of the wall particles, is varied should be performed.

The nonlocal rheology models were validated for annular shear flow, however the microscale relation for fluidity proposed by [2] was in poor agreement with the coarse-grained DEM data. A description for the fluidity in terms of particle packing and velocity fluctuations is required to understand the scaling relation between shear and granular temperature. Thus, there is also a need to develop a more comprehensive definition for fluidity that captures the

observations in literature in addition to the results collected in this thesis. These developments would allow the nonlocal granular fluidity rheology model to describe the full annular shear system and hence improve its applicability to general granular flows.

8.3. References

1. Bocquet, L., et al., *Granular shear flow dynamics and forces: Experiment and continuum theory.* Physical Review E, 2001. **65**(1)
2. Zhang, Q. and K. Kamrin, *Microscopic Description of the Granular Fluidity Field in Nonlocal Flow Modeling.* Physical Review Letters, 2017. **118**(5)
3. Boyce, C.M., et al., *Effective particle diameters for simulating fluidization of non-spherical particles: CFD-DEM models vs. MRI measurements.* AIChE Journal, 2017. **63**(7): p. 2555-2568
4. Herold, V., T. Kampf, and P.M. Jakob, *Magnetic Resonance Probing Ensemble Dynamics.* eprint arXiv:1805.05723, 2018: p. arXiv:1805.05723
5. Fabich, H.T., et al., *Measurements of the velocity distribution for granular flow in a Couette cell.* Physical Review E, 2018. **98**(6)
6. Podlozhnyuk, A., S. Pirker, and C. Kloss, *Efficient implementation of superquadric particles in Discrete Element Method within an open-source framework.* Computational Particle Mechanics, 2017. **4**(1): p. 101-118
7. Weinhart, T., et al., *Closure relations for shallow granular flows from particle simulations.* Granular Matter, 2012. **14**(4): p. 531-552
8. Jasti, V. and C.F. Higgs III, *Experimental study of granular flows in a rough annular shear cell.* Physical Review E, 2008. **78**(4): p. 041306

9. Appendices

9.1. Appendix A: MFIX input script for fluidised bed simulation

In this section, an example MFIX input script is supplied for the fluidised bed CFD-DEM simulations performed in Chapters 3 and 4. The script is known as "mfix.dat" and contains information about the fluid domain, particle properties, initial conditions, boundary conditions and solver settings. This script is written for use with the 2015.1 version of the MFIX software. To run this case, an executable built from the MFIX source code (known as "mfix.exe") is placed in the same directory as mfix.dat and a file called "particle_input.dat", which contains information about the particle positions, diameters, densities, and velocities.

```
  RUN_NAME = '3DSQ_FB'
  DESCRIPTION = '3D square CFD-DEM fluidized bed.'

#_____________________________________________________________________________
# RUN CONTROL SECTION

  RUN_TYPE = 'NEW'
  UNITS = 'SI'

  TIME =   0.0
  TSTOP =  5.0

  DT =     5.0d-4
  DT_MAX = 5.0d-4

  ENERGY_EQ = .F.

  SPECIES_EQ(0:1) = .F.  .F.
  DISCRETIZE(1:6) = 2 2 2 2 2 2

  MOMENTUM_X_EQ(1) = .F.
  MOMENTUM_Y_EQ(1) = .F.
  MOMENTUM_Z_EQ(1) = .F.
  DES_CONTINUUM_COUPLED = .T.
  DES_EXPLICITLY_COUPLED = .T.

  DRAG_TYPE = 'BVK'

  DES_INTERP_ON = .T.
  DES_INTERP_MEAN_FIELDS = .T.
  DES_INTERP_SCHEME = 'SQUARE_DPVM'
  DES_INTERP_WIDTH = 0.00107

  GRAVITY_X = 0.0
  GRAVITY_Y = 0.0
  GRAVITY_Z = -9.81

#_____________________________________________________________________________
# NUMERICAL SECTION

  MAX_NIT = 50
  TOL_RESID = 1.0d-3

#_____________________________________________________________________________
# GEOMETRY SECTION

  COORDINATES = 'CARTESIAN'
  imax = 10
```

```
  xlength = 0.037
  jmax = 10
  ylength = 0.037
  kmax = 32
  zlength = 0.12

#_____________________________________________________________________________
# MATERIAL SECTION

! GAS SECTION
!-----------------------------------------------------------------------//

  RO_g0 = 1.17       ! kg/m^3
  MU_g0 = 1.800E-5    ! kg/(m.s)

! PARTICLE SECTION
!-----------------------------------------------------------------------//
  MMAX = 1

  PARTICLES = 38415        ! Number of particles.
  D_p0(1) =   0.00107      ! (m)
  RO_s0(1)=   1050       ! (kg/m^3)


! Solids phase 1
!-----------------------------------------------------------------------//
  SOLIDS_MODEL(1) = 'DEM'

! Particle-particle:
  KN =   1000                  ! Normal collision spring constant
  MEW =  0.1                  ! Friction coefficient

! Particle-wall
  KN_W =  1000               ! Normal collision spring constant
  MEW_W = 0.1                ! Friction coefficient

! Restitution coefficients
  DES_EN_INPUT = 0.93         ! e11
  DES_EN_WALL_INPUT = 0.93    ! e1w

  DES_NEIGHBOR_SEARCH =  4     ! Grid based neighbor search
  NEIGHBOR_SEARCH_N   = 20     ! Steps between neighbor search

  NFACTOR = 500                ! DEM settling period in no. of loops

#_____________________________________________________________________________
# INITIAL CONDITIONS SECTION

  ! 1: Freeboard
  ic_x_w(1) = 0.0
  ic_x_e(1) = 0.037
  ic_y_s(1) = 0.0
  ic_y_n(1) = 0.037
  ic_z_b(1) = 0.0
  ic_z_t(1) = 0.12
  ic_u_g(1) = 0.0
  ic_v_g(1) = 0.0
  ic_w_g(1) = 0.3
  ic_ep_g(1) = 1.0

#_____________________________________________________________________________
# BOUNDARY CONDITIONS SECTION

! Inlet (uniform):
!-----------------------------------------------------------------------//
  bc_x_w(1) = 0.0037
  bc_x_e(1) = 0.0333
  bc_y_s(1) = 0.0037
  bc_y_n(1) = 0.0333
  bc_z_b(1) = 0.0
  bc_z_t(1) = 0.0
  bc_type(1) = 'MI'
  bc_u_g(1) = 0.0
  bc_v_g(1) = 0.0
  bc_w_g(1) = 0.754
  bc_ep_g(1) = 1.0
  bc_p_g(1) = 0.0
```

```
bc_x_w(2) = 0.0
bc_x_e(2) = 0.037
bc_y_s(2) = 0.0
bc_y_n(2) = 0.037
bc_z_b(2) = 0.12
bc_z_t(2) = 0.12
bc_type(2) = 'PO'
bc_p_g(2) = 0.0

bc_x_w(3) = 0.0
bc_x_e(3) = 0.0037
bc_y_s(3) = 0.0
bc_y_n(3) = 0.0037
bc_z_b(3) = 0.0
bc_z_t(3) = 0.0
bc_type(3) = 'MI'
bc_u_g(3) = 0.0
bc_v_g(3) = 0.0
bc_w_g(3) = 0.159
bc_ep_g(3) = 1.0
bc_p_g(3) = 0.0

bc_x_w(4) = 0.0
bc_x_e(4) = 0.0037
bc_y_s(4) = 0.0037
bc_y_n(4) = 0.0333
bc_z_b(4) = 0.0
bc_z_t(4) = 0.0
bc_type(4) = 'MI'
bc_u_g(4) = 0.0
bc_v_g(4) = 0.0
bc_w_g(4) = 0.346
bc_ep_g(4) = 1.0
bc_p_g(4) = 0.0

bc_x_w(5) = 0.0
bc_x_e(5) = 0.0037
bc_y_s(5) = 0.0333
bc_y_n(5) = 0.037
bc_z_b(5) = 0.0
bc_z_t(5) = 0.0
bc_type(5) = 'MI'
bc_u_g(5) = 0.0
bc_v_g(5) = 0.0
bc_w_g(5) = 0.159
bc_ep_g(5) = 1.0
bc_p_g(5) = 0.0

bc_x_w(6) = 0.0037
bc_x_e(6) = 0.0333
bc_y_s(6) = 0.0
bc_y_n(6) = 0.0037
bc_z_b(6) = 0.0
bc_z_t(6) = 0.0
bc_type(6) = 'MI'
bc_u_g(6) = 0.0
bc_v_g(6) = 0.0
bc_w_g(6) = 0.346
bc_ep_g(6) = 1.0
bc_p_g(6) = 0.0

bc_x_w(7) = 0.0333
bc_x_e(7) = 0.037
bc_y_s(7) = 0.0
bc_y_n(7) = 0.0037
bc_z_b(7) = 0.0
bc_z_t(7) = 0.0
bc_type(7) = 'MI'
bc_u_g(7) = 0.0
bc_v_g(7) = 0.0
bc_w_g(7) = 0.159
bc_ep_g(7) = 1.0
bc_p_g(7) = 0.0

bc_x_w(8) = 0.0333
bc_x_e(8) = 0.037
```

```
  bc_y_s(8) = 0.0037
  bc_y_n(8) = 0.0333
  bc_z_b(8) = 0.0
  bc_z_t(8) = 0.0
  bc_type(8) = 'MI'
  bc_u_g(8) = 0.0
  bc_v_g(8) = 0.0
  bc_w_g(8) = 0.346
  bc_ep_g(8) = 1.0
  bc_p_g(8) = 0.0

  bc_x_w(9) = 0.0333
  bc_x_e(9) = 0.037
  bc_y_s(9) = 0.0333
  bc_y_n(9) = 0.037
  bc_z_b(9) = 0.0
  bc_z_t(9) = 0.0
  bc_type(9) = 'MI'
  bc_u_g(9) = 0.0
  bc_v_g(9) = 0.0
  bc_w_g(9) = 0.159
  bc_ep_g(9) = 1.0
  bc_p_g(9) = 0.0

  bc_x_w(10) = 0.0037
  bc_x_e(10) = 0.0333
  bc_y_s(10) = 0.0333
  bc_y_n(10) = 0.037
  bc_z_b(10) = 0.0
  bc_z_t(10) = 0.0
  bc_type(10) = 'MI'
  bc_u_g(10) = 0.0
  bc_v_g(10) = 0.0
  bc_w_g(10) = 0.346
  bc_ep_g(10) = 1.0
  bc_p_g(10) = 0.0

#_____________________________________________________________________
# OUTPUT CONROL SECTION

  RES_DT = 0.01      ! interval write restart (.RES) file

  NLOG = 25       ! time steps between updates to (.LOG) file
  FULL_LOG = .T.  ! display residuals on screen

! Interval at which .SPX files are written
  SPX_DT(1) = 0.01   ! EP_g
  SPX_DT(2) = 0.05   ! P_g, P_star
  SPX_DT(3) = 0.01   ! U_g, V_g, W_g
  SPX_DT(4) = 0.05   ! U_s, V_s, W_s
  SPX_DT(5) = 100.   ! ROP_s
  SPX_DT(6) = 100.   ! T_g, T_s
  SPX_DT(7) = 100.   ! X_g, X_s
  SPX_DT(8) = 100.   ! theta
  SPX_DT(9) = 100.   ! Scalar


  GROUP_RESID = .T.  ! Group residuals by equation

  PRINT_DES_DATA = .F.  ! write DES vtk files
!=======================================================================
! VTK file options
!=======================================================================
  WRITE_VTK_FILES  = .TRUE.
  TIME_DEPENDENT_FILENAME = .TRUE.

! Save particle data over a small rectangular region
  VTK_FILEBASE(1)    = '023D_DEM'
  VTK_SELECT_MODE(1) = 'C'              ! pick particles which centers are inside
region
  VTK_DT(1)          = 0.01
  VTK_DATA(1)        = 'P'          ! Write particle data (vtp files)
  VTK_X_w(1)         = 0.0
  VTK_X_e(1)         = 0.037
  VTK_Y_s(1)         = 0.0
  VTK_Y_n(1)         = 0.037
  VTK_Z_b(1)         = 0.0
```

```
  VTK_Z_t(1)         = 0.12

  VTK_PART_DIAMETER(1) = .TRUE.
  VTK_PART_VEL(1) = .TRUE.


#_____________________________________________________________________________
# DMP SETUP

  NODESI =  1  NODESJ = 1  NODESK =  1

  ENABLE_DMP_LOG = .T.
  CHK_BATCHQ_END = .F.
```

9.2. Appendix B: CFDEM scripts for fluidised bed simulation

CFDEM simulations are a hybrid of an OpenFOAM case and a LIGGGHTS case. The case directory contains two sub-directories known as “CFD”, which contains the OpenFOAM case information, and “DEM” which contains the LIGGGHTS case information. In the CFD case, there are three directories:

- “0”, which contains the initial and boundary conditions.
- “constant”, which contains the geometry, fluid physical properties, and settings for fluid-solid coupling.
- “system”, which specifies the solver settings.

In CFD/0, there are files which correspond to simulated fluid properties. For example, the file for fluid velocity (CFD/0/u) is:

```
/*--------------------------------*- C++ -*----------------------------------*\
| =========                 |                                                 |
| \\      /  F ield         | OpenFOAM: The Open Source CFD Toolbox           |
|  \\    /   O peration     | Version:  1.6                                   |
|   \\  /    A nd           | Web:      http://www.OpenFOAM.org               |
|    \\/     M anipulation  |                                                 |

\*---------------------------------------------------------------------------*/
FoamFile
{
    version     2.0;
    format      ascii;
    class       volVectorField;
    object      U;
}
// * * * * * * * * * * * * * * * * * * * * * * * * * * * * * * * * * * * * * *

dimensions      [0 1 -1 0 0 0 0];

internalField   uniform (0 0 0.0);

boundaryField
{

    wall
    {
        //type            fixedValue;
        //value           uniform (0 0 0);
        type            slip;
    }

    inlet
    {
        type               groovyBC;
        valueExpression     "(pow(pow((pos().x-xc),2)+pow((pos().y-yc),2),0.5)<r) ?
vector(0,0,0.73) : vector(0,0,0.3)";
        variables          "r=0.02;xc=0.0;yc=0.0;";

    }

    outlet
    {
        type               pressureInletOutletVelocity;
        phi                phi;
        value              $internalField;
    }
}
```

```
// ************************************************************************
```

Here, the initial velocity within the entire bed (internalField) is set to zero. A slip boundary condition is applied to the walls. The non-uniform inlet boundary condition is specified using the groovyBC library. The pressureInletOutletVelocity boundary condition is applied at the outlet that specifies $\frac{du}{dx}$ as zero.

The geometry is defined by CFD/constant/polyMesh/blockMeshDict. The mesh is generated by running the blockMesh utility in the CFD directory. The blockMeshDict code for a hybrid mesh of a cylindrical fluidised bed is:

```
/*--------------------------------*- C++ -*----------------------------------*\
| =========                 |                                                 |
| \\      /  F ield         | OpenFOAM: The Open Source CFD Toolbox           |
|  \\    /   O peration     | Version:  2.0                                   |
|   \\  /    A nd           | Web:      http://www.OpenFOAM.org               |
|    \\/     M anipulation  |                                                 |
\*---------------------------------------------------------------------------*/
FoamFile
{
version  2.0;
format   ascii;
class       dictionary;
object      blockMeshDict;
}
// ************************************

   meshGenApp blockMesh;
   convertToMeters 1;

    //64 mm column diameter
    //15 cm length

   vertices
   (
    ( 0.009428571429 0.009428571429 0.0  ) // Vertex fiveoclocksqb = 0
    (-0.009428571429 0.009428571429 0.0  ) // Vertex sevenoclocksqb = 1
    (-0.009428571429 -0.009428571429 0.0 ) // Vertex elevenoclocksqb = 2
    ( 0.009428571429 -0.009428571429 0.0 ) // Vertex oneoclocksqb = 3

    ( 0.015556349 0.015556349 0.0 ) // Vertex fiveoclockcb = 4
    (-0.015556349 0.015556349 0.0) // Vertex sevenoclockcb = 5
    (-0.015556349 -0.015556349 0.0) // Vertex elevenoclockcb = 6
    ( 0.015556349 -0.015556349 0.0) // Vertex oneoclockcb = 7

    ( 0.009428571429 0.009428571429 0.12) // Vertex fiveoclocksqt = 8
    (-0.009428571429 0.009428571429 0.12) // Vertex sevenoclocksqt = 9
    (-0.009428571429 -0.009428571429 0.12) // Vertex elevenoclocksqt = 10
    ( 0.009428571429 -0.009428571429 0.12) // Vertex oneoclocksqt = 11

    ( 0.015556349 0.015556349 0.12) // Vertex fiveoclockct = 12
    (-0.015556349 0.015556349 0.12) // Vertex sevenoclockct = 13
    (-0.015556349 -0.015556349 0.12) // Vertex elevenoclockct = 14
    ( 0.015556349 -0.015556349 0.12) // Vertex oneoclockct = 15
   );

   blocks
   (
    //square block
    hex (
       2 3 0 1
       10 11 8 9
       )
    (6 6 32)
    simpleGrading (1 1 1)

    //slice1
    hex (
```

```
       1 0 4 5
       9 8 12 13
       )
    (6 4 32)
    simpleGrading (1 1 1)

    //slice2
    hex (
       6 2 1  5
       14 10 9   13
       )
   ( 4 6 32)
simpleGrading (1 1 1)

   //slice3
   hex (
         6 7 3 2
         14 15 11 10
       )
   (6 4 32)
simpleGrading (1 1 1)

   //slice4
   hex (
         3 7 4 0
         11 15 12 8
       )
   (4 6 32)
simpleGrading (1 1 1)

   );

   //create the quarter circles
   edges
   (
    arc 4 5 (0.0 0.022 0.0 )
    arc 5 6 (-0.022 0.0 0.0)
    arc 6 7 (0.0 -0.022 0.0 )
    arc 7 4 (0.022 0.0 0.0)

    arc 12 13 (0.0 0.022 0.12 )
    arc 13 14 (-0.022 0.0 0.12)
    arc 14 15 (0.0 -0.022 0.12 )
    arc 15 12 (0.022 0.0 0.12 )

   );

   patches
   (
    patch inlet
    (
     (0 3 2 1)
     (0 4 7 3)
     (4 0 1 5)
     (1 2 6 5)
     (3 7 6 2)
    )
    patch outlet
    (
     (8 11 10 9)
     (8 12 15 11)
     (12 8 9 13)
     (9 10 14 13)
     (11 15 14 10)
    )
    wall wall
    (
     (5 4 12 13)
     (5 13 14 6)
     (6 14 15 7)
     (7 15 12 4)
    )
);

mergePatchPairs
(
);
```

The interphase coupling settings are defined in CFD/constant/couplingProperties. Important settings in this file include the coupling interval, drag model and void fraction scheme.

```
/*---------------------------------------------------------------------------*\
| =========                 |                                                 |
| \\      /  F ield         | OpenFOAM: The Open Source CFD Toolbox           |
|  \\    /   O peration     | Version:  1.4                                   |
|   \\  /    A nd           | Web:      http://www.openfoam.org               |
|    \\/     M anipulation  |                                                 |
\*---------------------------------------------------------------------------*/

FoamFile
{
    version         2.0;
    format          ascii;

    root            "";
    case            "";
    instance        "";
    local           "";

    class           dictionary;
    object          couplingProperties;
}

// * * * * * * * * * * * * * * * * * * * * * * * * * * * * * * * * * * * * * * * * * * * * //

//===========================================================================//
// sub-models & settings

syncMode false;

modelType "A"; // A or B

couplingInterval 100;

voidFractionModel divided;//centre;//

locateModel engine;//turboEngineM2M;//

meshMotionModel noMeshMotion;

regionModel allRegion;

IOModel basicIO;

probeModel off;

dataExchangeModel twoWayMPI;//twoWayM2M;//twoWayFiles;//oneWayVTK;//

averagingModel dense;//dilute;//

clockModel standardClock;//off;

smoothingModel off;// localPSizeDiffSmoothing;// constDiffSmoothing; //

forceModels
(
    BeetstraDrag
    gradPForce
    viscForce
);

momCoupleModels
(
    implicitCouple
);

turbulenceModelType "RASProperties";//"LESProperties";//

//===========================================================================//
// sub-model properties


implicitCoupleProps
```

```
{
    velFieldName "U";
    granVelFieldName "Us";
    voidfractionFieldName "voidfraction";
}

gradPForceProps
{
    pFieldName "p";
    voidfractionFieldName "voidfraction";
    velocityFieldName "U";
    interpolation true;
}

viscForceProps
{
    velocityFieldName "U";
    interpolation true;
}
volWeightedAverageProps
{
    scalarFieldNames
    (
        voidfraction
    );
    vectorFieldNames
    (
    );
    upperThreshold 0.999;
    lowerThreshold 0;
    verbose true;
}
totalMomentumExchangeProps
{
    implicitMomExFieldName "Ksl";
    explicitMomExFieldName "none";
    fluidVelFieldName "U";
    granVelFieldName "Us";
}
DEMbasedDragProps
{
    velFieldName "U";
    voidfractionFieldName "voidfraction";
}

BeetstraDragProps
{
    velFieldName "U";
    voidfractionFieldName "voidfraction";
    interpolation true;
    implForceDEM true;
    scale 1.0; // diameter divided by scale in drag calculation
}


particleCellVolumeProps
{
    upperThreshold 0.999;
    lowerThreshold 0.;
    verbose true;
}

fieldStoreProps
{
    scalarFieldNames
    (
    );

    vectorFieldNames
    (
        "U"
    );
}

dividedProps
{
    alphaMin 0.01;
```

```
    scaleUpVol 1.0;
    weight 1.0; // particle volume multiplied by weight in voidage calculation
}

twoWayMPIProps
{
    liggghtsPath "../DEM/in.liggghts_run";
}
// ************************************************************************* //
```

Run and write settings are included in CFD/system/controlDict

```
/*--------------------------------*- C++ -*----------------------------------*\
| =========                 |                                                 |
| \\      /  F ield         | OpenFOAM: The Open Source CFD Toolbox           |
|  \\    /   O peration     | Version:  1.6                                   |
|   \\  /    A nd           | Web:      www.OpenFOAM.org                      |
|    \\/     M anipulation  |                                                 |
\*---------------------------------------------------------------------------*/
FoamFile
{
    version     2.0;
    format      ascii;
    class       dictionary;
    location    "system";
    object      controlDict;
}
// * * * * * * * * * * * * * * * * * * * * * * * * * * * * * * * * * * * * * //

application     pisoFoam;
startFrom       startTime;
startTime       0;
stopAt          endTime;
endTime         5.0;
deltaT          0.0001;
writeControl    adjustableRunTime;
writeInterval   0.01;
purgeWrite      0;
writeFormat     ascii;
writePrecision  6;
writeCompression uncompressed;
timeFormat      general;
timePrecision   6;
runTimeModifiable yes;
adjustTimeStep  no;
maxCo 0.1;
libs ( "libgroovyBC.so");

// ************************************************************************* //
```

The settings for the finite volume discretisation and solution are specified in the files CFD/system/fvSchemes and CFD/system/fvSolution, respectively.

The particle-side simulation settings are defined in the “DEM” directory are specified by a LIGGGHTS input script as follows:

```
log             ../DEM/log.liggghts
thermo_log      ../DEM/post/thermo.txt

atom_style      granular
atom_modify     map array
communicate     single vel yes

boundary        m m m
newton          off

units           si
processors      2 2 1

# read the restart file
read_restart    ../DEM/post/restart/liggghts.restart
```

```
neighbor        0.00107 bin
neigh_modify    delay 0

# Material properties required for granular pair styles

fix         m1 all property/global kn peratomtypepair 1 1000
fix         m2 all property/global kt peratomtypepair 1 285.71
fix         m3 all property/global gamman peratomtypepair 1 0.000932
fix         m4 all property/global gammat peratomtypepair 1 0.000466
fix         m5 all property/global coefficientFriction peratomtypepair 1 0.1

# pair style
pair_style    gran  model  hooke/stiffness  tangential  history  #  Hookean  without
cohesion
pair_coeff  * *

# timestep, gravity
timestep    0.000001
fix         gravi all gravity 9.81 vector 0.0 0.0 -1.0

# walls
fix              zwalls1  all  wall/gran  model  hooke/stiffness  tangential  history
primitive type 1  zplane 0.0
fix              zwalls2  all  wall/gran  model  hooke/stiffness  tangential  history
primitive type 1  zplane 0.12
fix             cylwalls  all  wall/gran  model  hooke/stiffness  tangential  history
primitive type 1 zcylinder 0.022 0. 0.

# change the particles density
set         group all density 1050

# cfd coupling
fix         cfd all couple/cfd couple_every 100 mpi
fix         cfd2 all couple/cfd/force/implicit

# apply nve integration to all particles that are inserted as single particles
fix         integr all nve/sphere

# center of mass
compute     centerOfMass all com

# compute total dragforce
compute     dragtotal all reduce sum f_dragforce[1] f_dragforce[2] f_dragforce[3]

# screen output
compute         rke all erotate/sphere
thermo_style     custom step atoms ke c_rke vol c_centerOfMass[3] c_dragtotal[1] &
c_dragtotal[2] c_dragtotal[3]
thermo          10
thermo_modify   lost ignore norm no
compute_modify  thermo_temp dynamic yes

dump            dmp all custom 10000 ../DEM/post/dump*.liggghts_run id type x y z &
vx vy vz fx fy fz radius

run             1
```

9.3. Appendix C: LIGGGHTS input script for Couette cell simulations

LIGGGHTS simulations are generated from an input script such as the one provided in this section. This script was developed for use with LIGGGHTS 3.6.0. In this script, information is provided about the domain, particle properties, walls, particle insertion, DEM solver settings and output controls. Of note is how the rough moving walls are generated. The "lattice" and "create_atoms" commands are used to generate a single layer of particles. These particles are then arranged into a cylinder by the "set" command. These particles are then assigned to a group with the "group" command. The motion of particles in this group is controlled by the "fix … move rotate" command.

```
## Initialisation ##
echo both
atom_style      granular
atom_modify     map array
communicate     single vel yes
boundary        m m m
newton          off
units           si
processors      2 2 1

# Domain
region          reg block -0.025 0.025 -0.025 0.148 -0.001 0.005 units box
create_box      1 reg

# Neighbour Search
neighbor        0.00044 bin
neigh_modify    delay 0


## Setup ##

# Material properties required for granular pair styles
fix   m1 all property/global kn peratomtypepair 2 1.0e4 1.0e4 1.0e4 1.0e4
fix   m2 all property/global kt peratomtypepair 2 2.85e3 2.85e3 2.85e3 2.85e3
fix   m3 all property/global gamman_abs peratomtypepair 2 3.18e-3 3.18e-3 3.18e-3
3.18e-3
fix   m4 all property/global gammat_abs peratomtypepair 2 0.0 0.0 0.0 0.0
fix   m5 all property/global coefficientFriction peratomtypepair 2 0.1 0.0 0.0 0.0

# pair style
pair_style  gran model hooke/stiffness tangential history absolute_damping on
pair_coeff  * *
# particle distributions and insertion
fix     pts1 all particletemplate/sphere 15485867 atom_type 1 density constant 1050
radius constant 0.00022
fix     pdd1 all particledistribution/discrete 49979687 1 pts1 1.0

# Wall plane region
region wallInsert block 0.0242 0.0243 0.0 0.1019 0.0 0.005
region wallInsert2 block 0.0242 0.0243 0.0 0.1472 0.0 0.005

# Insertion region
region insert1 cylinder z 0.0 0.0 0.02299 0.003 0.005 units box side in
region insert2 cylinder z 0.0 0.0 0.01666 0.003 0.005 units box side out
region insert intersect 2 insert1 insert2

# walls
fix     zwalls1  all wall/gran model hooke/stiffness tangential history primitive &
type 2 zplane 0.0 absolute_damping on
fix     zwalls2  all wall/gran model hooke/stiffness tangential history primitive &
type 2 zplane 0.01 absolute_damping on
fix     cylwall1 all wall/gran model hooke/stiffness tangential history primitive &
type 2 zcylinder 0.025 0.0 0.0 absolute_damping on
```

```
fix     cylwall3 all wall/gran model hooke/stiffness tangential history primitive &
type 1 zcylinder 0.01644 0.0 0.0 absolute_damping on
fix     cylwall4 all wall/gran model hooke/stiffness tangential history primitive &
type 1 zcylinder 0.02321 0.0 0.0 absolute_damping on

# timestep, gravity
timestep    0.000001
fix ts_chk all check/timestep/gran 100000 0.5 0.5
fix         gravi all gravity 9.81 vector 0.0 0.0 -1.0

# screen output
compute         rke all erotate/sphere
thermo_style    custom step atoms ke c_rke vol
thermo          1000
thermo_modify   lost ignore norm no
compute_modify  thermo_temp dynamic yes

# write output
compute     fcxc all stress/atom pair
dump         init all custom 10000 post/dump*.liggghts_run id type x y z vx vy vz &
c_fcxc[1] c_fcxc[2] c_fcxc[3] c_fcxc[4] c_fcxc[5] c_fcxc[6] radius

# Insert gap particles
fix     integr1 all nve/sphere
fix        ins all insert/rate/region seed 15485863 distributiontemplate pdd1 &
nparticles 36000 particlerate 3600000 insert_every 2000 overlapcheck yes vel
constant 0.0 0.0 -1 region insert ntry_mc 10000
run         500000

unfix ins
unfix integr1
unfix cylwall3
unfix cylwall4

# Create Inner Wall atoms and place in cylindrical arrangement

lattice fcc 6.223e-4
create_atoms 1 region wallInsert
variable newx atom 0.01622*cos(2*PI/0.1019*y)
variable newy atom 0.01622*sin(2*PI/0.1019*y)
set region wallInsert x v_newx y v_newy diameter 0.00044 density 1050

# Create Outer Wall atoms and place in cylindrical arrangement

create_atoms 1 region wallInsert2
variable newx2 atom 0.02343*cos(2*PI/0.1472*y)
variable newy2 atom 0.02343*sin(2*PI/0.1472*y)
set region wallInsert2 x v_newx2 y v_newy2 diameter 0.00044 density 1050

# set up inner moving particle wall group
region in60 cylinder z 0. 0. 0.01644 0. 0.01 units box side in
region in56 cylinder z 0. 0. 0.016  0. 0.01 units box side out
region wall2 intersect 2 in56 in60
group inner region wall2
neigh_modify exclude group inner inner

# set up outer particle wall group
region out94 cylinder z 0. 0. 0.02365 0. 0.01 units box side in
region out90 cylinder z 0. 0. 0.02321 0. 0.01 units box side out
region wall intersect 2 out90 out94
group outer region wall
neigh_modify exclude group outer outer

group gap subtract all inner outer

## Detailed Settings ##

# apply nve integration to gap particles, rotate to inner wall particles
fix     mvinner inner move rotate 0. 0. 0. 0. 0. 1. 587.9 units box
fix     mvouter outer nve/noforce
fix     integr2 gap nve/sphere

# Apply load to top wall particles
fix cad all mesh/surface/stress/servo file topPlate.stl type 1 scale 1.0 move 0.0 &
0.0 0.0049 com 0.0 0.0 0.0 ctrlPV force axis 0.0 0.0 1.0 target_val -0.16866 &
vel_max 100
```

```
fix topServo all wall/gran model hooke/stiffness tangential history primitive mesh&
n_meshes 1 meshes cad absolute_damping on

#shear
run   10000000
write_restart   post/liggghts.restart
```

9.4. Appendix D: Matlab code for satellite point MRI simulation

The code presented in this section was used to calculate the phase shift incurred by each of the satellite points constituting each particle. The complex signal of the sample is then calculated for each voxel.

```
function [Sp] = particleMRI(count,a,b)
% Calculate signal using cluster of points to represent particle.
% Inputs: count. identifier for liggghts sump file
%         a. flag to turn on granular rotation (0 or 1)
%         b. flag to turn on granular translation (0 or 1)
load('partC.mat'); % file that contains x,y,z coordinates of satellite
% points relative to particle centroid.

% divide domain into voxels
y_start = 0.016;
y_stop = y_start + 0.00765;
ny = 13;
y = linspace(y_start,y_stop,ny+1);
dy = (y_stop-y_start)/ny;
y_cent = y_start+dy/2:dy:y_stop-dy/2;
y = [-fliplr(y),y];
y_cent = [-fliplr(y_cent),0,y_cent];
ny = length(y_cent);

% MRI parameters (typical values)
G_array = zeros(1,64);
G_array(1) = -0.3515;
for ig = 2:1:64
    G_array(ig) = G_array(ig-1)+(-1)*G_array(1)/32; %T/m
end
nGrads = length(G_array);
gamma = 2.6753e8; %rad/s/T
delta = 1e-3; %little delta in s
Delta = 3.5e-3; %big delta in s
%time increment
dt = 0.1e-3; %s
ts = 100; % increment between file names

t = 0:dt:(Delta+delta);
%num time pts
numT = length(t); % during gradent pair application
% Set gradient sequence array. The specific gradient value will
nG = delta/dt; % number of time steps that a gradient is applied for
Grad = zeros(1,numT);
Grad(1:nG) = -1;
Grad(end-nG:end-1) = 1;

% Arrays without zero gradient
Grad2 = Grad(Grad~=0);
numTG = length(Grad2);
count2 = 1; % initialise counter for phi0 array index. only includes
%values at non zero gradients to save on RAM.

% Read particle data files
[ID,np] = dump_read_init(count);
nsp = length(partC(1,:));
```

```
% repeat gradient array so that the phase can be calculated
% element-wise.
Grad2 = repmat(Grad2,[np,1,nsp]);
Grad2 = permute(Grad2,[1,3,2]);

% initialize change in angular displacement (rad)
thx = zeros(np,1);
thy = zeros(np,1);
thz = zeros(np,1);

% partCi gives i component displacement from particle centre
% extend array
partCx = repmat(partC(1,:),np,1);
partCy = repmat(partC(2,:),np,1);
partCz = repmat(partC(3,:),np,1);

% Initialize phase, point-cell index and signal arrays
phi = zeros(np,nsp,nGrads);
phi0 = zeros(np,nsp,numTG);
pijk0 = zeros(np,1);
delta_yL = zeros(np,1);
delta_yR = zeros(np,1);
Sp = zeros(length(y_cent),nGrads);

% time loop
for it = 1:numT;
    [XP,VP,omega] = dump_read(count,ID); %reads number of steps needed.
    % dump_read called here to prevent running out of RAM for long
    % sequences.

    % Attain initial translational velocity components (m/s)
    velx = VP(1,:)';
    vely = VP(2,:)';
    velz = VP(3,:)';
    % Attain initial angular velocity components (rad/s)
    omx = omega(1,:)';
    omy = omega(2,:)';
    omz = omega(3,:)';
    if it == 1
        % Attain initial translational positions of particle centres (m)
        xp = XP(1,:)'; % initial x position
        yp = XP(2,:)'; % initial y position
        zp = XP(3,:)'; % initial z position
        disp('reading initial positions')
    end
    % Turn particle into a cluster of points. Start with long array of
    % particle centres then add partCi to get locations of satellite
    % points.
    xp2 = repmat(xp,1,nsp);
    xp2 = xp2 + partCx;
    yp2 = repmat(yp,1,nsp);
    yp2 = yp2 + partCy;
    zp2 = repmat(zp,1,nsp);
    zp2 = zp2 + partCz;

    if Grad(it)~=0
        %simple flow MRI pulse sequence. Phase at each time step without
gradient.
```

```
        phi0(:,:,count2) = gamma*dt*xp2;  %calculate contribution to signal
from x-direction only
        count2 = count2 + 1;
    end

    % update particle positions using velocity
    xp = xp + velx*dt*b;
    yp = yp + vely*dt*b;
    zp = zp + velz*dt*b;

    % Update angular displacements using angular velocity. Note this is
    % the change in displacement over dt
    thx = omx*dt*a;
    thy = omy*dt*a;
    thz = omz*dt*a;
    %calculate rotation matrix (assumes constant rotational velocity)
    for ip = 1:1:np
        % get co-ordinates of satellite points about centre of particle
        % ip.
        partC = [partCx(ip,:); partCy(ip,:); partCz(ip,:)];
        % calculate rotation matrix
        Rx = [1 0 0;0 cos(thx(ip)) -sin(thx(ip));0 sin(thx(ip))
cos(thx(ip))];
        Ry = [cos(thy(ip)) 0 sin(thy(ip));0 1 0; -sin(thy(ip)) 0
cos(thy(ip))];
        Rz = [cos(thz(ip)) -sin(thz(ip)) 0;sin(thz(ip)) cos(thz(ip)) 0; 0 0
1];
        Rot = Rx*Ry*Rz;
        %rotate pseudo particles relative to COM
        partC = Rot*partC;
        % Separate into components. This is used to rotate the
        % satellite points during the next iteration before the phase
        % is calculated.
        partCx(ip,:) = partC(1,:);
        partCy(ip,:) = partC(2,:);
        partCz(ip,:) = partC(3,:);
    end
    % Iterate to next step
    count = count + ts;
end
% Identify which cell each particle centre lives in at end of sequence.
pijk0 = getpijk(yp2(:,1),y);
pijk0 = repmat(pijk0,1,nsp);
delta_yL = zeros(np,1);
delta_yR = zeros(np,1);
for ip = 1:1:np
    delta_yL(ip) = y(pijk0(ip,1)) - yp2(ip,1);
    delta_yR(ip) = y(pijk0(ip,1)+1) - yp2(ip,1);
end
delta_yL = repmat(delta_yL,1,nsp);
delta_yR = repmat(delta_yR,1,nsp);
B = zeros(np,nsp);
B(partCy<delta_yL) = -1;
B(partCy>delta_yR) = 1;
pijk = pijk0 + B;

for ig = 1:1:nGrads
    % for loop to multiply ungradiented phase by each gradient value in
    % the sequence.
    G = G_array(ig);
    % set value of gradient
```

```
    Grad1 = Grad2*G;
    % multiply pre-phase by gradient
    phi1 = phi0.*Grad1;
    % sum phase steps to  obtain phase for each pseudo-particle at
    % gradient G
    phi = sum(phi1,3);
    phi = exp(1i*phi);
    for iy = 1:1:ny
        Sp(iy,ig) = sum(sum(phi(pijk==iy)));
    end
end
disp('signals calculated');
end
```

9.5. Appendix E: Matlab codes for DEM averaging and coarse-graining

Averaging DEM data is performed with the code supplied in this section. The driver function contains information specific to the system, namely the spatial domain over which averaging is to be performed. The particle-weighted averaging of the DEM data is done by the "VP_pavg" function. The fraction of a particle in a cell is calculated by the "calc_weight" function.

```
function cubeWeightVoid
% Author: Daniel Clarke
% Driver function to calculate void fraction using the method of Khawaja et
% al. (2012). The system here is a test case for a single particle in a
% small domain.
XP = [0.0001,0.0001,0.0005]';
VP = [0,0,0]';
dp = 0.001;
xw = linspace(-0.002,0.002,5);
dx = xw(2)-xw(1); % walls
xc = linspace(-0.002+dx/2,0.002-dx/2,4); % centres
yw = xw; yc = xc;
zw = xw; zc = xc;
pijk = getPijk(xw,yw,zw,XP);
[fijk,cellid] = getFijk(xc,yc,zc);
[v,n] = VP_pavg(xw,yw,zw,XP,VP,dp,pijk,fijk,cellid);
imagesc(xc,yc,n(:,:,3)); axis square;
hold on
plot(XP(1)+dp/2*cos(0:0.01:2*pi),XP(2)+dp/2*sin(0:0.01:2*pi),'w')
end

function [VPZ,np]=VP_pavg (x,y,z,XP,VP,diam,pijk,fijk,cellid)
%%% Computes the particle weighted time averaged hydrodynamic velocity %%%
% x, y, and z are edges of bins.
% XP is 3 x Nparticles x Nsteps array of particle coordinates
% diam is an array of diameters.
% pijk is a 3 x Nparticles x Nsteps array identifying which cell the
% particle is in.
% fijk is an identifier for the bin based on its pijk coordinates
% yslice is the lower and upper limits of the slice
nz = length(z) -1; % number of z bins
nx = length(x) -1; % number of x bins
ny = length(y) -1; % number of y bins
npart = size(XP,2);
VPZ=zeros(nx,ny,nz);
np=zeros(nx,ny,nz);
[filtcell, filtweight] = calc_weight(x,y,z,XP,diam,pijk,fijk);
for ip=1:1:npart % loop over particle
    % Conditional test to see if particle lies within slice dy. If
    % so it is counted (wp = 1). Otherwise wp = 0. This is
    % essentially a "top hat" weighting function.
    for idx = 1:1:27
        ix = cellid(1,filtcell(idx,ip));
        iy = cellid(2,filtcell(idx,ip));
        iz = cellid(3,filtcell(idx,ip));
        VPZ(ix,iy,iz)=VPZ(ix,iy,iz)+VP(3,ip)*filtweight(idx,ip);
        np(ix,iy,iz)=np(ix,iy,iz)+filtweight(idx,ip);
    end
end
end
%%% End of VP_pavg %%%

function [filtcell, filtweight] = calc_weight(x,y,z,XP,diam,pijk,fijk)
% x, y, and z are edges of bins.
% XP is 3 x Nparticles x Nsteps array of particle coordinates
% diam is diameter.
% pijk is a 3 x Nparticles x Nsteps array identifying which cell the
% particle is in.
% fijk is an identifier for the bin based on its pijk coordinates
% yslice is the lower and upper limits of the slice
%
```

```
% filtcell is a bin identifier that corresponds to a weighting, filtweight.
sq_width_x = zeros(1,3);
sq_width_y = zeros(1,3);
sq_width_z = zeros(1,3);
np = size(XP,2);
filtcell = zeros(27,max(np));
filtweight = zeros(27,max(np));
for ip = 1:1:np % loop over particles
    i = pijk(ip,1);
    j = pijk(ip,2);
    k = pijk(ip,3);
    for kc = -1:1:1 % loop over neighbouring z bins
        kb = kc + 2;
        for jc = -1:1:1 % loop over neighbouring y bins
            jb = jc + 2;
            for ic = -1:1:1 % loop over neighbouring x bins
                ib = ic + 2;
                % calculate whether the edges of the particle exceed
                % the bin edges, this gives the amount of the particle that
                % is in the current bin.
                max_x = min(x(i+ic+1),(XP(1,ip)+diam/2));
                min_x = max(x(i+ic),(XP(1,ip)-diam/2));
                sq_width_x(1,ib) = max_x - min_x;
                if (sq_width_x(1,ib) < 0)
                    sq_width_x(1,ib) = 0;
                end
                max_y = min(y(j+jc+1),(XP(2,ip)+diam/2));
                min_y = max(y(j+jc),(XP(2,ip)-diam/2));
                sq_width_y(1,jb) = max_y - min_y;
                if (sq_width_y(1,jb) < 0)
                    sq_width_y(1,jb) = 0;
                end
                max_z = min(z(k+kc+1),(XP(3,ip)+diam/2));
                min_z = max(z(k+kc),(XP(3,ip)-diam/2));
                sq_width_z(1,kb) = max_z - min_z;
                if (sq_width_z(1,kb) < 0)
                    sq_width_z(1,kb) = 0;
                end
            end
        end
    end
    idx = 1;
    for kc = -1:1:1 % loop over neighbouring z bins
        for jc = -1:1:1 % loop over neighbouring y bins
            for ic = -1:1:1 % loop over neighbouring x bins
                ib = ic + 2;
                jb = jc + 2;
                kb = kc +2;
                % calculate the cuboidal volume of the partial particle
                % in the current bin
                cubevol = sq_width_x(1,ib)*sq_width_y(1,jb)*sq_width_z(1,kb);
                weight = cubevol/(diam^3); % scale to particle volume
                % correction from Khawaja et al. (2012)
                newweight = -0.8457*weight^3 + 1.6625*weight^2 + 0.1832*weight;
                ijkc = fijk(i+ic,j+jc,k+kc); % get cell identifier
                filtcell(idx,ip) = ijkc;
                filtweight(idx,ip) = newweight; % assign weighting
                idx = idx + 1;
            end
        end
    end
    sumweight = sum(filtweight(:,ip));
    filtweight(:,ip)    =    filtweight(:,ip)/sumweight;    %    normalise    so    that
sum(filtweight) = 1

end
end

function [fijk,cellid] = getFijk(x,y,z)
%%% Assign fluid cell IDs based on position. %%%
% fijk is single identifier for each cell
% cellid indicates the identifier for each cell in each direction
% e.g. left to right: 1,2,3,..,nx
index = 0;
nx = length(x); ny = length(y); nz = length(z);
fijk = zeros(nx,ny,nz);
cellid = zeros(3,ny*nx*nz);
```

```
for k = 1:1:nz
    for j = 1:1:ny
        for i = 1:1:nx
            index = index + 1;
            fijk(i,j,k) = index;
            cellid(1,index) = i;
            cellid(2,index) = j;
            cellid(3,index) = k;
        end
    end
end
end

function [pijk] = getPijk(x,y,z,XP)
% %%% Identify cell where each particle is located and the cell co-ords
npart = size(XP,2);
pijk = zeros(npart,3);
nx = length(x); ny = length(y); nz = length(z);
for ip=1:1:npart
    for iz=1:1:nz
        if (XP(3,ip)>=z(iz)) && (XP(3,ip)<z(iz+1))
            pijk(ip,3) = iz;
            break
        end
    end
    for iy=1:1:ny
        if (XP(2,ip)>=y(iy)) && (XP(2,ip)<y(iy+1))
            pijk(ip,2) = iy;
            break
        end
    end
    for ix=1:1:nx
        if (XP(1,ip)>=x(ix)) && (XP(1,ip)<x(ix+1))
            pijk(ip,1) = ix;
            break
        end
    end
end
end
```

For the coarse-graining averaging technique, a similar file structure is used, where the average is calculated using “smoothCGspace”, and the weightings are calculated with the “weightCG” function. The driver function is this case is specific for annular shear flow, where data was averaged over the entire azimuth. The vector and tensor variables are converted into cylindrical coordinates using the “convVectorToRadial” and “convTensorToRadial” functions.

```
function smoothCG
% smoothCG: Code to produce fields for void fraction,
% velocity distribution and stress using CG method.
%
% Averages along a line are taken. To improve the sample size, the positions are
% rotated about the axis to sample the full couette without any double counting.
%
% Particle properties
rhos = 1050; % granule density, kg/m^3
% Define spatial grid
zlow = 0.003; zhigh = 0.007; zlim = [zlow, zhigh]; z = mean(zlim); % z limits, m
dz = zhigh-zlow; % slice thickness, m
%x-direction
x_start = 0.015; x_stop = 0.025; % r limits, m
nx = 40; % number of bins
dx = (x_stop-x_start)/nx; % bin size, m
x = linspace(x_start+dx/2,x_stop-dx/2,nx); % bin centre positions
xw = linspace(x_start,x_stop,nx+1); % bin centre positions
% y-direction
y = 0;
% time direction
```

```
ns = 100;
count = 8.6e6;
ts = 1e4; % number of DEM steps btw file outputs
th = 0:0.1:2*pi-0.1; nrep = length(th);
% loop over each file
for ii = 1:1:ns
    % read DEM output data:
   [xp,vp,fc,dp]=dumpRead(count,zlim);
   % convert velocity to cylindrical coordiantes
   vpc = convVectorToRadial(vp,xp);
   fc = convTensorToRadial(fc,xp);
   for jj = 1:1:nrep
       xp = posRotate(xp,th(jj));
   % calculate instantaneous CG fields
       [rho(:,jj),v(:,:,jj),T(:,:,jj),Sn(:,jj),S(:,jj)]                                    =
smoothCGspace(x,y,z,xp,vpc,fc(4,:),1/3*(fc(1,:)+fc(2,:)+fc(3,:)),mean(dp));
   end
   phi(:,ii) = squeeze(mean(rho,2))/rhos;
   V(:,:,ii) = mean(v,3);
   VV(:,:,ii) = mean(T,3);
   sigRT(:,ii) = squeeze(mean(S,2));
   P(:,ii) = squeeze(mean(Sn,2));
% Iterate to next file
count = count + ts;
fprintf('completed step %i of %i\n',ii,ns);
end
save('LFCG_w=1dp.mat','x','phi','V','VV','P','sigRT')
end

function [rhoCG,v,T,P,sigc4CG] = smoothCGspace(x,y,z,rp,vp,Fxy,p,dp)
%smoothCG code to generate 1D continuum variables from discrete data.
%   The local mean density is calculated according to:
%_____________________________________________________________________
%   rho = sum(m_i*W(r-r_i));
%_____________________________________________________________________
%   m_i is the mass of particle i,
%   r_i is the position of the centroid of particle i
%   r is the position of the bin centre.
%   W(r) is a weighting function that is Gaussian in form.
w = 1*dp; % CG width should be close to particle diameter
c = 3*w; % cut off length, m
xl = 0.016; xr = 0.02365; % couette cell boundaries, m
rhos = 1050; % granule density, kg/m^3
m = rhos*pi/6*dp^3; % particle mass, kg
% Initialise CG variables
rhoCG = zeros(size(x));
pxCG = zeros(size(x)); pyCG = zeros(size(x)); pzCG = zeros(size(x));
vx = zeros(size(x)); vy = zeros(size(x)); vz = zeros(size(x));
sigkxx = zeros(size(x)); sigkyy = zeros(size(x)); sigkzz = zeros(size(x));
sigc4CG = zeros(size(x));
P = zeros(size(x));
Tx = zeros(size(x)); Ty = zeros(size(x)); Tz = zeros(size(x));
% decompose particle position vector
xp = rp(1,:); yp = rp(2,:); zp = rp(3,:);
vpx = vp(1,:); vpy = vp(2,:); vpz = vp(3,:);
for ii = 1:1:length(x)
    % id particles within cut-off distance
    flag = xp>(x(ii)-c)&xp<(x(ii)+c)&yp>(y-c)&yp<(y+c)&zp>(z-c)&zp<(z+c);
     % single out local data
    xploc = sqrt((xp(flag)-x(ii)).^2+(yp(flag)-y).^2+(zp(flag)-z).^2);
    vxloc = vpx(flag); vyloc = vpy(flag); vzloc = vpz(flag);
    Fxyloc = Fxy(flag); ploc = p(flag);
    W = weightCG(xploc,w); % calculate weightings
    if x(ii) < xl+c
        xploc2 = sqrt((xl-(xp(flag)-xl)-x(ii)).^2+(yp(flag)-y).^2+(zp(flag)-z).^2);
        W2 = weightCG(xploc2,w);
        W = W+W2;
    end
    if x(ii) > xr-c
        xploc2 = sqrt((xr-(xp(flag)-xr)-x(ii)).^2+(yp(flag)-y).^2+(zp(flag)-z).^2);
        W2 = weightCG(xploc2,w);
        W = W+W2;
    end
    rhoCG(ii) = sum(m*W); % local coarse grained density, kg/m^3
% local coarse grained momentum = kg m/s
    pxCG(ii)   =   sum(m*vxloc.*W);   pyCG(ii)   =   sum(m*vyloc.*W);   pzCG(ii)   =
sum(m*vzloc.*W);
```

```
% local coarse grained velocity
    vx(ii)   =   pxCG(ii)/rhoCG(ii);   vy(ii)   =   pyCG(ii)/rhoCG(ii);   vz(ii)   =
pzCG(ii)/rhoCG(ii);
% local fluctuation velocity, m/s
    vxf = vxloc-vx(ii); vyf = vyloc-vy(ii); vzf = vzloc-vz(ii);
% coarse grained kinetic stress, Pa
    sigkxx(ii)  =  sum(m*vxf.^2.*W);  sigkyy(ii)  =  sum(m*vyf.^2.*W);  sigkzz(ii)  =
sum(m*vzf.^2.*W);
% coarse grained velocity variance, m^2/s^2
    Tx(ii)  =  sigkxx(ii)/rhoCG(ii);  Ty(ii)  =  sigkyy(ii)/rhoCG(ii);  Tz(ii)  =
sigkzz(ii)/rhoCG(ii);
    sigc4CG(ii) = sum(Fxyloc.*W); % coarse grained shear stress, Pa
    P(ii) = sum(ploc.*W); % coarse grained pressure, Pa
end
v = [vx;vy;vz];
T = [Tx;Ty;Tz];
end

function W = weightCG(ri,w)
%weightCG function to calculate weighting for particle contribution to bin
% INPUTS: ri is the particle position relative to bin centre, w is the CG
% width (recommended to be 1dp)
% OUTPUTS: W is the array of weightings for particles i within the bin
c = 3*w; % cut off length, m
Vw   =   2*sqrt(2)*pi^(3/2)*w^3*erf(sqrt(2)*c/(2*w))^3;   %   constant   for   mass
conservation
W = 1/Vw*exp(-(ri).^2/(2*w^2));
end

%+++++++++++++++++++++++++++++++++++++++++++++++++++++++++++++++++++++++++++++++
% CODE TO READ DEM OUTPUT DATA
%+++++++++++++++++++++++++++++++++++++++++++++++++++++++++++++++++++++++++++++++
function [XP,VP,FCXC,dp] = dumpRead(count,z)
% Reads files where particles may disappear. This code can handle missing
% particles between time steps.
filename = sprintf('files/dump%d.liggghts_run',count);
A = dlmread(filename,' ',9,0);
A = purge(A,z); % remove particles outside of a slice region.
A = sortrows(A); % rearrange matrix so that IDs are in ascending order

% read positions
XP(1,:) = A(:,3); XP(2,:) = A(:,4); XP(3,:) = A(:,5);
% read velocities
VP(1,:) = A(:,6); VP(2,:) = A(:,7); VP(3,:) = A(:,8);
% % read atom-wise stresses
FCXC(1,:) = A(:,9); FCXC(2,:) = A(:,10); FCXC(3,:) = A(:,11);
FCXC(4,:) = A(:,12); FCXC(5,:) = A(:,13); FCXC(6,:) = A(:,14);
% read ID
ID = A(:,1);
%read radius
dp = 2*A(:,15);
end

function [A1] = purge(A,z)
% Purge file removes particles that are outside of slice boundaries
% called by dump_read function
% define z limits
zlo = z(1);
zhi = z(2);
A1 = A;
np = length(A(:,1));
Az = zeros(1,np);
% Identify the particles which exceed the boundaries.
Az(A(:,5)<zlo) = 1; Az(A(:,5)>zhi) = 1;
% Remove rows where the particle coordinates exceed the box limits.
A1(Az~=0,:) = [];
end

%+++++++++++++++++++++++++++++++++++++++++++++++++++++++++++++++++++++++++++++++
% CODE TO CONVERT FROM CARTESIAN TO POLAR CYLINDRICAL COORDINATES
%+++++++++++++++++++++++++++++++++++++++++++++++++++++++++++++++++++++++++++++++
function [FCRC] = convTensorToRadial(FCXC,XP)
% function to convert atom-wise tensor elements from cartesian coordinate system to
% polar cylindrical system.
np = length(XP(1,:));
FCRC = zeros(6,np);
for i = 1:1:np
```

```
    % populate tensor components as 3x3
    sCart = [FCXC(1,i) FCXC(4,i) FCXC(5,i);
        FCXC(4,i) FCXC(2,i) FCXC(6,i);
        FCXC(5,i) FCXC(6,i) FCXC(3,i)];
    % define angle
    theta = atan2(XP(2,i),XP(1,i));
    % calculate transform matrices
    A = [cos(theta) sin(theta) 0;
        -sin(theta) cos(theta) 0;
        0 0 1];
    B = [cos(theta) -sin(theta) 0;
        sin(theta) cos(theta) 0;
        0 0 1];
    % calculate cylindircal tensor
    sCyl = A*sCart*B;
    % rewrite tensor in 6-element format
    FCRC(1,i) = sCyl(1,1); FCRC(2,i) = sCyl(2,2); FCRC(3,i) = sCyl(3,3); % normal
components
    FCRC(4,i) = sCyl(1,2); FCRC(5,i) = sCyl(1,3); FCRC(6,i) = sCyl(2,3); % deviator
components
end
end

function [vCyl] = convVectorToRadial(VP,XP)
% function to convert atom-wise velocity vector from cartesian system to polar
% cylindrical system
np = length(XP(1,:));
vCyl = zeros(3,np);
for i = 1:1:np
    vCart = [VP(1,i);VP(2,i);VP(3,i)];
    % define angle
    theta = atan2(XP(2,i),XP(1,i));
    % calculate transform matrix
    A = [cos(theta) sin(theta) 0;
        -sin(theta) cos(theta) 0;
        0 0 1];
    % convert from cartesian to cylindrical
    v = A*vCart;
    % store in array
    vCyl(1,i) = v(1);
    vCyl(2,i) = v(2);
    vCyl(3,i) = v(3);
end
end

%+++++++++++++++++++++++++++++++++++++++++++++++++++++++++++++++++++++++++++++++
% CODE TO ROTATE GRANULES ABOUT AXIS
%+++++++++++++++++++++++++++++++++++++++++++++++++++++++++++++++++++++++++++++++
function xp2 = posRotate(xp,dth)
% posRotate: code to move particles in the azimuth by angle dth.
[th,r,z] = cart2pol(xp(1,:),xp(2,:),xp(3,:));
th = th + dth;
[x,y,z] = pol2cart(th,r,z);
xp2 = [x;y;z];
end
```

9.6. Appendix F: Microscale fluidity for planar shear with gravity

The planar shear with gravity system studied by Zhang and Kamrin was replicated to verify that their proposed microscale definition for fluidity could be obtained using the DEM simulation and averaging methods developed in this thesis. Here, particle contacts were simulated with a Hertzian model, where the particle diameter was 0.0008 m, the elastic modulus was 10^8 Pa, the Poisson ratio was 0.33, the restitution coefficient was 0.1 and the friction coefficient was 0.4. The coarse-graining method described in Section 7.3.2 was used where $w = 1.3d_p$. The dimensionless fluidity is plotted against the volume fraction in Figure 9.1. The agreement between the DEM simulation and the model is reasonable and demonstrates that the deviation between the Couette simulations and the model is not the result of the coarse graining scheme.

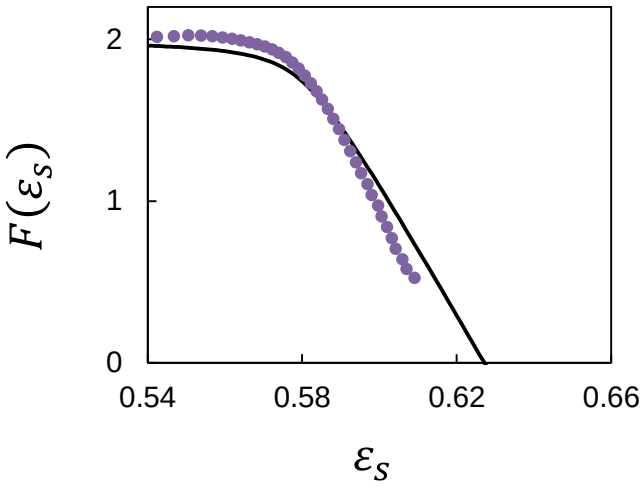

Figure 9.1. Dimensionless fluidity against solid volume fraction. DEM simulation of planar shear with gravity: ●. Equation 7.24: solid line.